Development of methods for high-throughput viscoelastic analysis for suspension as well as adherent cells

Inauguraldissertation

zur

Erlangung des akademischen Grades eines

Doktors der Naturwissenschaften (Dr. rer. nat.)

der

Mathematisch-Naturwissenschaftlichen Fakultät

der

Universität Greifswald

vorgelegt von
Bob Fregin

Greifswald, September 2021

Dekan:	Prof. Dr. Gerald Kerth
1. Gutachter:	Prof. Dr. Oliver Otto
2. Gutachter:	Prof. Dr. Ben Fabry
3. Gutachter:	Prof. Dr. Ulrich F. Keyser

Tag der Promotion: 13. Januar 2022

Contents

1. Introduction

Cell mechanical properties are linked to cell state, fate, and function revealing comprehensive and fundamental information on a cell. In the first section of this chapter, I will introduce cell mechanics as label-free biomarker and show the high relevance of cell mechanical techniques for basic research in cell biology as well as for applied science in medical applications. I will point out some open questions which I will address in this thesis. While in the second part, basic principles of viscoelastic material properties will be introduced, the third section focuses on tools for assessing mechanical properties from cells and tissue. Digital holography will be introduced in section four which is the basis for a novel method I developed and which will be introduced in detail in the second chapter. In the last section of this chapter, I will give a brief overview on the statistical methods used in this thesis.

1.1. Cell mechanics

The importance of cell mechanics for cell biology

In our day-to-day life, cells and tissues in our body are subjected to stress and elongation. Our beating heart, inflating lung, and peristalsis of the gut are only some examples highlighting the importance of mechanical stimuli and responses for fundamental biological functioning [1]. For the heart, lung, bone, cartilage, blood vessel, as well as skeletal and cardiac muscles a link between structure, mechanical responses, and biological function of the tissues and organs could be established [2]. Based on a mechanical analysis, diverse biomedical applications can be addressed, as e.g., diagnosis and treatment of orthopedic, cardiovascular, and respiratory diseases [2–4]. *In vivo* mechanical tissue analysis allows for the detection of brain anomalies and diseases [5]. Elongation or strain and stress response are also important on a single-cell level and is understood as a stimulus for cell growth, differentiation, migration, remodeling, and gene expression [1, 6, 7]. The ability of cells to respond to forces is crucial for embryonic development and homeostasis in adults [8], while cell-generated forces are driving tissue morphogenesis and organ formation in the embryo [9, 10].

In cell biology, fluorescent and chemical labels are employed to investigate the spatial and temporal organization of proteins as well as their activities [11, 12]. However, molecular labeling requires *a priori* knowledge on the target protein. In contrast, the cells' ability to reply to external loads can be used as an intrinsic biophysical marker. While studying biochemical signaling pathways (e.g., by kinetic or localization microscopy, Western blot, immunofluorescence) is a bottom-up approach with an

enormous number of involved actors and potential compensation effects between the regulatory networks, cell mechanical properties provide a comprehensive measure of cells' state (top-down) [3, 4, 13–15]. As an example for the complex biochemical signaling: more than 100 genes in 12 different classes are affected if endothelial cells are exposed to a shear stress [7]. Recently, first studies established a link between cell mechanical changes and genes involved in the regulation [16]. If the specificity of molecular markers is required, e.g., by targeting a specific molecular effect, techniques are available for bridging the gap between the biochemical domain and cell mechanics [17].

Cells are able for mechanosensing, i.e., they can sense their mechanical microenvironment by external forces and translate them into biochemical signaling, and are able to alter their ability to sense and their mechanical response upon biological and biochemical signals [2, 6, 18–20]. The mechanosensing feature of cells was studied, e.g., on the tumor suppressor protein merlin, acting as a mechanochemical transducer and linking intercellular forces to collective cell movements in migrating epithelial cells by a distinct molecular mechanism [21]. Cells were also shown to reveal a mechanical memory effect which plays a role when cell collectives migrate through tissue of different stiffness, e.g., in morphogenesis and cancer metastasis [22].

Cell mechanical properties can be used as an inherent biomarker for determining cell state, fate, and function [3, 4, 13–15]. Cell mechanical behavior has not only been shown to depend on the cell type and can be interpreted as mechanical fingerprint [23], but changes when cells are treated with drugs [24], causing e.g., an altered contractility [25], or when cells are diseased [26]. Dysregulated adherent cells reveal aberrant high contraction forces [25] and dead cells are stiffer than viable ones – a fact that can be utilized for label-free sorting [27]. As a consequence, diseases can be studied by monitoring cell mechanical properties, e.g., diagnosing cancer or spherocytosis [3, 4]. Deformability and velocity are crucial factors for cancer cells during metastasis since reduced friction is required for migration through tight constrictions [28]. Monitoring cell immune states by mechanical means can be used, e.g., for cell preparation in regenerative medicine [4]. Differentiation has also been shown to impact on cell's contractility and mechanical properties [24, 25], and mechanical properties change over cell-cycle phase [24].

Cell mechanical properties are governed by the cytoskeleton [16, 30–32], which consists of three main polymers: actin filaments, microtubules, and intermediate filaments [7, 31] (bold-faced organelles in Figure 1.1). While actin has the strongest impact on cell mechanics, intermediate filaments are contributing as well, in particular, for high strains [16]. Microtubules have been shown to also play a role for cell mechanical behavior at high strains, a direct investigation, however, is difficult since drug-induced disassembly leads to compensation by actin filaments and contractility [16].

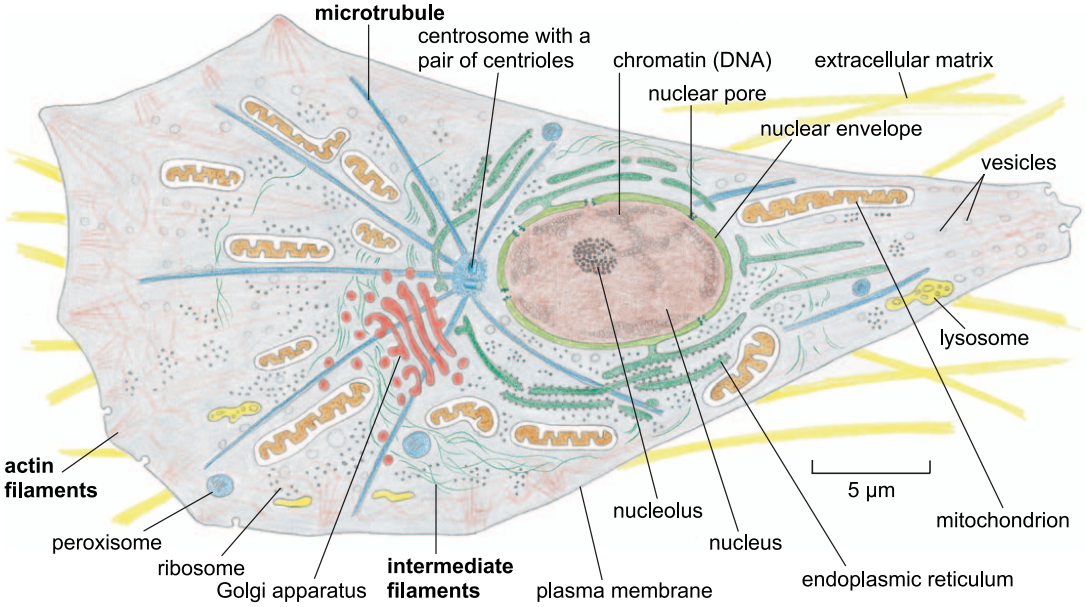

Figure 1.1.: Schematic of an animal cell with labeled organelles. The mechanical properties of a cell are mainly determined by the cytoskeleton. Organelles belonging to the cytoskeleton are bold-faced: actin filaments, microtubules, and intermediate filaments. Adapted from [29].

Cell mechanical properties are nonlinear concerning stress magnitude as well as frequency [7, 31, 32] and cells show viscoelastic as well as plastic behavior [33] which has to be considered when used as marker. At short times of mechanical characterization, mainly passive cytoskeletal material properties are probed while for slow mechanical tests, remodeling of cross-linked semiflexible polymer networks can occur [32].

Development of cell mechanical technologies

At the intersection of cell biology and physics, cell mechanics has been an emerging field for several decades, indicated by an increasing number of publications focusing on development of methods and principles as well as their application (Figure 1.2). Cell mechanical techniques can be categorized for methods applicable to cells in suspension and adherent cells. Typical methods for suspension cells are optical tweezers [35], the optical stretcher [36], micropipette aspiration [37] among others (introduced in Section 1.3.1) while the atomic force microscope (AFM) [38], microplate rheology [39], magnetic twisting cytometry [40], particle tracking microrheology [41], magnetic tweezers [42], traction force microscopy [10], and deformation by ferrofluid microdroplets [43] are some of the techniques for mechanical characterization of adherent cells (introduced in Section 1.3.2). Most of these methods are, however, limited by accessible material parameters, available throughput or the need for time-consuming post processing [44]. Utilizing an AFM as one of the most prominent techniques (Figure 1.2), adherent cells can be investigated in great detail but the method is not suited for suspended cells

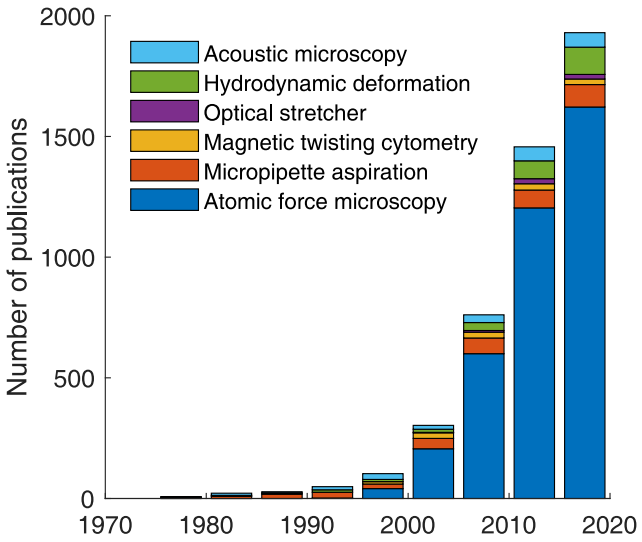

Figure 1.2.: Number of publications on different techniques or principles to determine cell mechanical properties. Data was gathered from PubMed [34], search string: ((cell mechanics) OR (cell rheology)) AND (<name of the technique as it appears in the legend>), from January 2021.

(only via immobilization), is not contact-free, and has a low throughput. In particular for studying large cell populations, high-throughput methods are important since they allow for fast mechanical phenotyping [14, 15, 24, 45]. With deformability cytometry, a method based on hydrodynamic deformation, cell deformability can be analyzed at rates of $\approx$ 1000 cells/s while data analysis is performed off-line [14, 46]. With real-time deformability cytometry (RT-DC), another technique using hydrodynamic cell deformation, cell elasticity can be determined in real-time at analysis rates of more than 100 cells/s [24]. While cell deformability is captured in RT-DC in real-time during the experiment, a Young's modulus can be calculated for each single cell in a postprocessing step [47]. Both approaches access the elastic components of a cell (either by deformability or a Young's modulus) but not its viscous properties. This limitation, I overcame by developing dynamic real-time deformability cytometry (dRT-DC) assessing viscoelastic properties of cells in suspension at high throughput and in real-time [48] (Article III, concluded in Section 3.3).

Cell mechanical tests are typically performed by application of a stress while monitoring its deformation or strain. In a manuscript on shape descriptors, I address the question, which shape descriptors can be used as strain parameters in a microfluidic system utilizing hydrodynamic cell deformation and which analysis techniques are effective (Manuscript IV, concluded in Section 3.4).

While a number of mechanical methods have been introduced, translational applications, however, remain at an early stage. We came up with an assay for quality analysis of blood products in transfusion medicine by utilizing RT-DC [49] (Article I, concluded in Section 3.1).

High-throughput mechanophenotyping is not only important for suspension cells but also for adherent cells since most of the cells are aggregated into tissues, e.g., in our human body. We introduced the concept of virtual channels which allows for adjusting the cross-section of a microfluidic system to the size of the analyte and hence, for high-throughput single-cell and tissue mechanics within one experimental method (RT-DC) [50] (Article II, concluded in Section 3.2).

Characterization of adherent cells on surfaces at high throughput and contact-free is achieved by a novel method that I developed within this thesis: holographic vibration spectroscopy (HVS). The fundamental working principle is introduced in Section 2.3 of the subsequent chapter.

1.2. Viscoelastic material properties

Phenomenologically, cells reveal elastic as well as viscous material properties [7, 30, 51, 52]. Both are covered by the concept of viscoelasticity. Since the aim of this thesis is to analyze the viscoelastic properties of suspension and adherent cells, a theoretical description is required for their quantification.

In this section, first, the material properties elasticity and viscosity will be introduced, followed by an introduction of several commonly used linear viscoelastic models: the Kelvin-Voigt model, the Maxwell-Wiechert model, and the model of standard linear solid. Within this thesis, I am going to use solely linear viscoelastic models since they are simple and it has been shown that they can be used for living matter [8, 51]. Last, I will briefly discuss nonlinear models, as e.g., power-law rheology.

Opposing to a simple phenomenological description, three classical models have been developed for investigating the physical origin of cells' viscoelastic behavior: the sol-gel hypothesis, the tensegrity model, and the soft glassy rheology model [7, 53]. Since the models were developed to explain a certain set of rheological experiments, they cannot reproduce all the observed cellular effects. The models are either limited to properties of the cytoskeleton, do not include thermal and nonthermal fluctuations, cannot explain the nontrivial frequency dependency, or do not allow for linking the observed phenomena to molecular processes and existing biochemical data. As a consequence, new models have been developed, e.g., a model of dynamic cross-links [7].

1.2.1. Elasticity

According to Hook's law for a linear elastic solid, the strain ϵ is directly proportional to an applied stress σ [54, 55]. If a linear elastic solid of surface area A is elongated by a

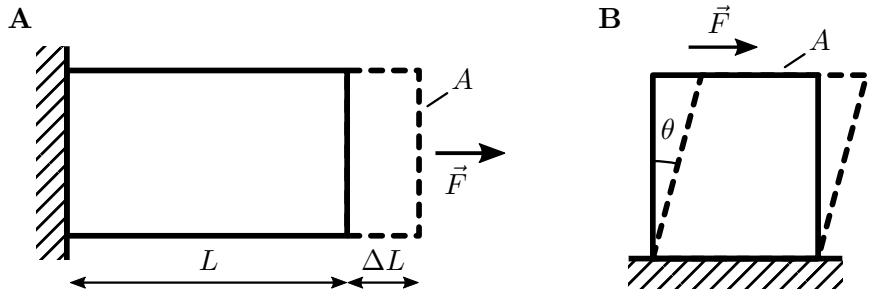

Figure 1.3.: Definition of extensional and shear strain. **A** Extensional strain $\epsilon = \Delta L/L$ and **B** shear strain $\gamma = \theta$ of a linear elastic solid in response to an extensional stress $\sigma = F/A$ and shear stress $\tau_s = F/A$, respectively. Adapted from [54].

force F, the applied extensional stress is given by $\sigma = F/A$ yielding a strain $\epsilon = \Delta L/L$, where L is the length of the unloaded body and ΔL its elongation in response to the applied stress (Figure 1.3A). The same is true for a compression of the body. The Young's modulus E is a one-dimensional material parameter of a linear elastic solid given by the ratio of extensional stress σ and strain ϵ along the same axis

$$E = \frac{\sigma}{\epsilon} \ . \tag{1.1}$$

The more rigid, i.e. the stiffer, a material is, the higher its Young's modulus is.

If the applied force F is not perpendicular, but parallel to the free surface of area A, the linear elastic solid is sheared (Figure 1.3B). In response to shear stress $\tau_s = F/A$, the elastic solid is sheared by an angle θ, defined as shear strain $\gamma = \theta$. Similar to the Young's modulus, the shear modulus G of that solid is defined as a ratio of shear stress τ_s and strain γ

$$G = \frac{\tau_s}{\gamma} \ . \tag{1.2}$$

The shear modulus G and Young's modulus E are coupled via the Poisson's ratio ν, a ratio of the strain perpendicular and the strain parallel to the direction of the applied force [54]

$$G = \frac{E}{2(1+\nu)} \ . \tag{1.3}$$

Usually, cells are assumed to be incompressible, corresponding to a Poisson's ratio of $\nu = 0.5$. This implies that elongating a cell in one direction leads to a contraction with a strain of 50 % in the other two directions in space.

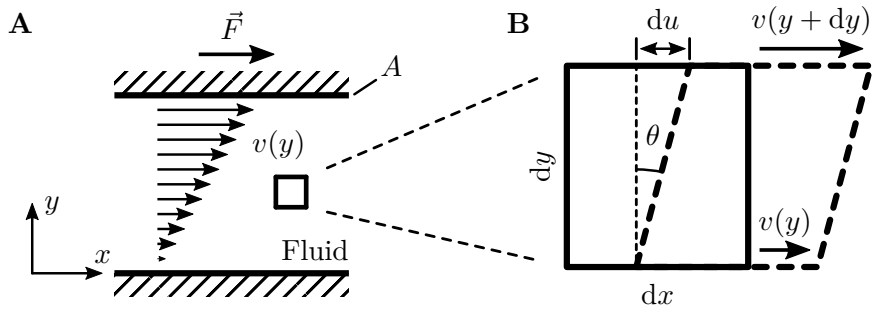

Figure 1.4.: Definition of dynamic viscosity η. **A** Sketch of two plates with a fluid in between for the introduction of viscosity describing frictional forces between layers of that fluid moving with different velocities. **B** An infinitely-small volume of the fluid in (A) is moving with a velocity v and is sheared due to a velocity gradient. A adapted from [54].

1.2.2. Viscosity

Viscosity is a measure of the fluidity of a material and is a phenomenon describing frictional forces between molecular layers of a fluid moving at different velocities. According to Newton's law of viscosity, the viscosity of a fluid is the proportionality constant relating the velocity gradient and the shear stress, originating from those frictional forces. In order to introduce (dynamic) viscosity, we assume two plates with a fluid in between where the upper plate of area A is moving due to a force F (Figure 1.4A). The shear stress $\tau_s = F/A$ forces the fluid to move with a velocity $v(y)$ which decreases linearly from its maximum at the top plate to zero at the fixed bottom plate. With the resulting velocity gradient in direction of y, perpendicular to the direction of flow x, Newton's law of viscosity can be written as

$$\tau_s = \eta \frac{\partial v}{\partial y} \ . \tag{1.4}$$

If an infinitely-small square of side lengths $\mathrm{d}x$ and $\mathrm{d}y$ is considered in detail, one can find that it moves with velocity $v(y)$ (Figure 1.4B). However, the top edge is moving with a slightly higher velocity $v(y + \mathrm{d}y) = v(y) + \mathrm{d}v$ than the bottom edge, and the square is therefor sheared yielding a small displacement $\mathrm{d}u$ (in the direction of x) of the upper edge with respect to the bottom one. The velocity difference is the change in displacement over time t, $\mathrm{d}v = \frac{\partial}{\partial t}\mathrm{d}u$. The shear angle θ can be described by $\tan\theta = \mathrm{d}u/\mathrm{d}y$ and, since angles are very small, approximated to $\theta \approx \mathrm{d}u/\mathrm{d}y$. Shear strain γ is equal to this angle θ, as introduced earlier (Figure 1.3).

Consequently, Newton's law from Equation 1.4 can be re-written to

$$\begin{aligned} \tau_s &= \eta \frac{\partial}{\partial y}\frac{\mathrm{d}u}{\partial t} = \eta \frac{\mathrm{d}}{\mathrm{d}t}\frac{\mathrm{d}u}{\mathrm{d}y} = \eta \frac{\mathrm{d}}{\mathrm{d}t}\theta = \eta \frac{\mathrm{d}}{\mathrm{d}t}\gamma \\ &= \eta\dot{\gamma} \ . \end{aligned} \tag{1.5}$$

Equation 1.5 shows that a dynamic viscosity η is the proportionality constant relating shear stress τ_s and the first derivative of shear strain which is also called shear velocity or shear rate $\dot{\gamma}$.

1.2.3. Linear material models

Linear material models are utilized to describe the cell's mechanical properties [51]. Composed of at least one elastic and one viscous element, i.e., a spring (purely elastic) and a dashpot (purely viscous), a network of these two elements defines the relationship between stress σ and strain ϵ, which are external parameters defining material properties (Figure 1.5). In the following, a generalized stress σ and strain ϵ are considered independent of whether they describe an extensional stress and strain or a shear stress and strain.

Whereas in a purely elastic element, energy from an applied stress or strain is stored internally, causing the element to release the same amount of energy as uptaken, a purely viscous material cannot store energy and, hence, is a dissipative structure. Since the rheological representation of a viscoelastic material consists of both elastic and viscous elements, the absorbed energy is partially stored and partially dissipated. While a spring reflects a linear dependency of stress and strain according to Equation 1.1: $\sigma = E \cdot \epsilon$, a dashpot induces a stress if strain changes following Equation 1.5: $\sigma = \eta \cdot \dot{\epsilon}$.

Material models consisting of two and three elements are considered here. However, more complex networks of four and more basic elements exist as well. The most general form is given by the generalized Kelvin-Voigt model or the equivalent generalized Maxwell-Wiechert model [55]. While the first consists of a spring in series to a sequence of several parallel springs and dashpots, the generalized Maxwell-Wiechert model contains a spring in parallel to several elements of a spring in series with a dashpot.

In analogy to electrical circuits, the strain of the material ϵ is described by the potential while the stress σ represents the current through the whole network. Following network theory and the strain-stress relationship of a single element allows for calculation of overall strain or stress of the network, or any internal parameter.

Kelvin-Voigt model

A Kelvin-Voigt solid consists of a spring in parallel to a dashpot (Figure 1.5A, top). Its stress-strain relation can be described by the following ordinary differential equation

$$\dot{\epsilon} + \frac{1}{\tau}\epsilon = \frac{1}{\eta}\sigma \ , \quad \tau = \frac{\eta}{E_K} \ , \tag{1.6}$$

where τ, defined by the ratio of viscosity η and Young's modulus E_K, is a characteristic time.

If a rectangular stress function of magnitude σ_0 is applied (Figure 1.5A, bottom, upper sketch), a Kelvin-Voigt model shows a strain of exponential behavior with a

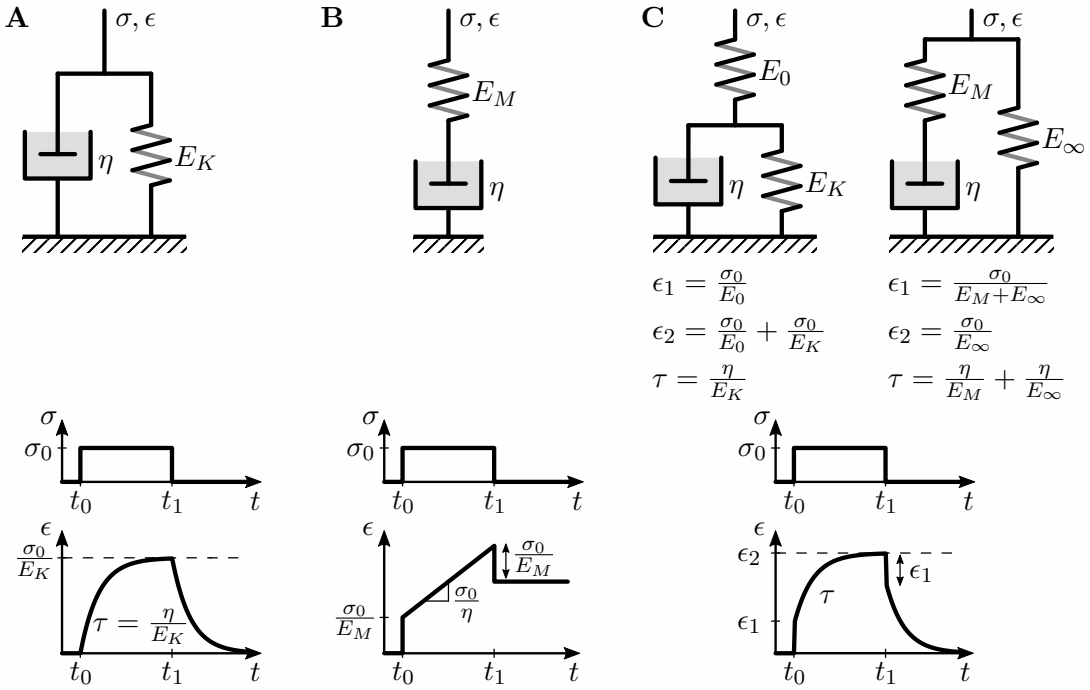

Figure 1.5.: Viscoelastic material models. **A** Kelvin-Voigt model, **B** Maxwell-Wiechert model and **C** Standard linear solid model in Kelvin-Voigt representation (left) and Maxwell-Wiechert representation (right). Each network consists of springs with a Young's modulus E and dashpots of viscosity η. After application of a constant stress σ_0 at time t_0 and release at t_1 (bottom, upper sketch), the network reveals a characteristic strain function ϵ (bottom, lower sketch). Adapted from [55].

steady-state of σ_0/E_K and a time constant τ (Figure 1.5A, bottom, lower sketch). The strain response is finite, i.e., it reaches a plateau after a long time t with respect to τ ($t/\tau \gg 1$), and is reversible, meaning that the strain tends again to zero if the stress is completely released.

Maxwell-Wiechert model

In contrast, in a Maxwell-Wiechert fluid, the spring and dashpot are connected in series (Figure 1.5B, top). The network can be described by the following ordinary differential equation

$$\dot{\epsilon} = \frac{1}{E_M}\dot{\sigma} + \frac{1}{\eta}\sigma \ . \tag{1.7}$$

Applying a rectangular stress function (Figure 1.5B, bottom, upper sketch) results in an immediate elastic response, i.e., a step in strain by σ_0/E_M caused by the spring, followed by a linearly increasing strain with a slope of σ_0/η originating from the dashpot (Figure 1.5B, bottom, lower sketch). Since both elements are connected in

series, the strain is increasing as long as the stress is applied, a property of a perfect fluid without surface tension. After stress release, the strain decreases instantaneously by the amplitude of the elastic part and stays constant at the level previously reached from the viscous response.

Standard linear solid

The standard linear solid is a structure with three elements, consisting of a Kelvin-Voigt model in series to a spring of Young's modulus E_0 (Figure 1.5C, top left) or a Maxwell-Wiechert model in parallel to a spring of Young's modulus E_∞ (Figure 1.5C, top right). Both networks are mechanically equivalent. For the Kelvin-Voigt and Maxwell-Wiechert representation, stress and strain follow a relationship described by Equations 1.8 and 1.9, respectively

$$E_0 E_K \epsilon + E_0 \eta \dot{\epsilon} = (E_0 + E_K)\sigma + \eta \dot{\sigma} \ , \tag{1.8}$$

$$E_M E_\infty \epsilon + (E_M + E_\infty)\eta \dot{\epsilon} = E_M \sigma + \eta \dot{\sigma} \ . \tag{1.9}$$

From a comparison of the coefficients after normalization, one can derive the following equations for parameter conversion

$$E_0 = E_M + E_\infty \ , \qquad \frac{1}{E_K} = \frac{1}{E_M} + \frac{1}{E_\infty} \ . \tag{1.10}$$

The viscosity η is independent of the selected representation.

Applying a rectangular stress function of magnitude σ_0 (Figure 1.5C, bottom, upper sketch) yields an instantaneous step strain $\epsilon_1 = \sigma_0/E_0$ originating from spring E_0 followed by an exponential strain response with the characteristic time $\tau = \eta/E_K$, both derived from the Kelvin-Voigt representation (Figure 1.5C, bottom, lower sketch). For sufficiently long times t ($t/\tau \gg 1$), time-dependent effects vanish and the steady-state strain $\epsilon_2 = \sigma_0/E_\infty$ is reached which is solely defined by the Young's modulus E_∞ from the Maxwell-Wiechert representation. The strain response is symmetric when releasing the stress. The quantities of ϵ_1, ϵ_2 and τ can be converted appropriately (Equations 1.10 and Figure 1.5C).

1.2.4. Nonlinear viscoelasticity

So far, only linear viscoelastic models have been considered. A very prominent nonlinear method is power-law rheology. In power-law rheology, the creep function $J(t)$, defined by deformation d divided by the applied force F, follows a power law

$$J(t) = \frac{d(t)}{F} = j_0 \left(\frac{t}{t_0} \right)^\beta \tag{1.11}$$

with a prefactor j_0 representing the inverse of the elasticity, time t_0 for reference, usually set to $t_0 = 1\,\mathrm{s}$, and a power-law exponent β describing the fluidity [52]. While the fluidity β is equal to zero or one for a purely elastic or a purely viscous material,

respectively, a viscoelastic material yields a fluidity between zero and unity. Cells reveal a fluidity around 0.25 [39, 52].

Power-law rheology is a useful tool for describing a cell's creep response if deformation is captured over several decades in time. Furthermore, it enables a straightforward comparison to experiments performed at different conditions due its scalability. A power-law decay function can be approximated by, e.g., several Maxwell-Wiechert models, if one model with a timescale per decade in time is added [52].

Within the concept of power-law rheology, the cytoskeleton of a living cell can be described as a soft glassy material [7, 32, 56]. Soft glassy materials are characterized by a very low elastic or storage modulus in the range of Pa to kPa [56]. Furthermore, storage and loss modulus reveal the same weak power-law dependency over frequency range and the loss tangent or hysteresivity, the ratio of loss and storage modulus, is frequency insensitive and on the order of 0.1 [56]. The storage and loss modulus, both combined in the complex modulus, are another representation of viscoelasticity, where the storage modulus (real-valued) represents elastic properties (equal to the Young's modulus) while the loss modulus (complex-valued) reflects the viscous properties (dissipative structures).

1.3. Technologies to assess cell mechanical properties

Multiple techniques have been developed over the last decades for the quantification of cell mechanical properties. However, living matter is mechanically far more complex than engineered materials such as metals, polymers or semiconductors, since it is active, dynamic and contain integrated functions including metabolism, control, sensing, communication, growth, remodeling, reproduction, and apoptosis [2]. The mechanical analysis of a rod of metal, for example, is much simpler because the material is homogeneous, isotropic, and linear, which is not true for a cell and its complex system of compartments. Consequently, techniques for mechanical probing on cells need to account for these characteristics.

As an active system, a cell can change its mechanical properties and, in turn, adapt to its environment. Since the process of adaption requires time, only passive properties are probed on short time scales (milliseconds range) while active internal processes of the cell can play a role on long time scales (seconds to minutes) and may impact the measurement result [32, 57]. Measurements on short time scales are mainly sensitive to cell's cytoskeleton, as they are not affected by remodeling [23]. The cytoskeleton generally has a major impact on the mechanical properties, consisting of actin filaments, microtubuli, intermediate filaments, cross-linkers, and molecular motors (Figure 1.1). If a nucleus exists, and especially if its size is comparable to cell size or strains are high during the mechanical test, it can contribute to the cell's mechanical stress response as well [14, 58, 59].

The Young's modulus of cells is in the range of 100 Pa to 100 kPa, which is low compared to engineered materials [2, 19, 52]. The size of the analyte ranges from one up to several tens of micrometer when focusing on single cells and small cell clusters, or

up to several millimeter when observing entire tissues. Targeting the lateral resolution, cell mechanical methods span a range from subcellular to single cells all the way up to an ensemble of cells or tissues. When combining a high force resolution due to low forces on soft materials, and a high lateral resolution, the measurement tools need to be very sensitive. Most of these techniques allow for a combination with online imaging of the cell(s) of interest during mechanical characterization.

State-of-the-art techniques can be classified by the type, direction, and regime of forces applied to cells or tissue [8]. If forces are applied normally to cell surface, they lead to elongation or compression while parallel forces, i.e. tangential to the cell's boundary, lead to shear. Depending on the direction of stress, different types of strain will be observed (see Section 1.2.1). Some of the techniques are probing the cells with a combination of both. Depending on how stress is applied over time, one distinguishes between a creep compliance test in which a constant stress is applied while strain is monitored, and a dynamic test during which stress is a function of time – a harmonic one in most cases [8]. Additionally, a strain can be applied while monitoring retention forces and the stress in a stress relaxation experiment.

Another classification of measurement techniques is given by their biological applicability: *ex vivo*, *in vitro*, and some of which can even be used for *in vivo* characterization, e.g., magnetic resonance elastography (MRE), demonstrated in measurements on breast [60], liver [61], and inside the brain [5], or optical coherence elastography (OCE) used in ophthalmology [62]. The focus of this thesis is on methods used for *ex vivo* and *in vitro* samples.

In the following, some prominent cell mechanical techniques will be briefly described. They are classified for characterization of cells in suspension and adherent cells. However, an adherent cell can be detached from its surface, e.g., by trypsinization (enzymatic dissociation), brought into suspension, and measured utilizing corresponding tools, while a cell in suspension can be immobilized and probed by a technique primarily for adherent cells.

1.3.1. Cell mechanical tools for suspension cells

An overview of methods for cells in suspension is depicted in Figure 1.6.

Since the cells of interest are suspended in a liquid, mechanical probing can be integrated into flow cytometry setups, providing a cell analysis in a continuous flow, reaching very high analysis rates. Miniaturization can be achieved by integration of rheological measurements into microfluidic devices. Due to microchannels with a small cross sectional area, high flow velocities and even parallelization [63] on a small footprint can be achieved yielding a high number of analyzed cells per time.

Optical tweezers

Optical tweezers, or single-beam gradient force traps, utilize a single focused light beam to trap a particle or a cell [2, 35] (Figure 1.6A). The light of the divergent beam with an intensity gradient is refracted on the change in refractive index between the

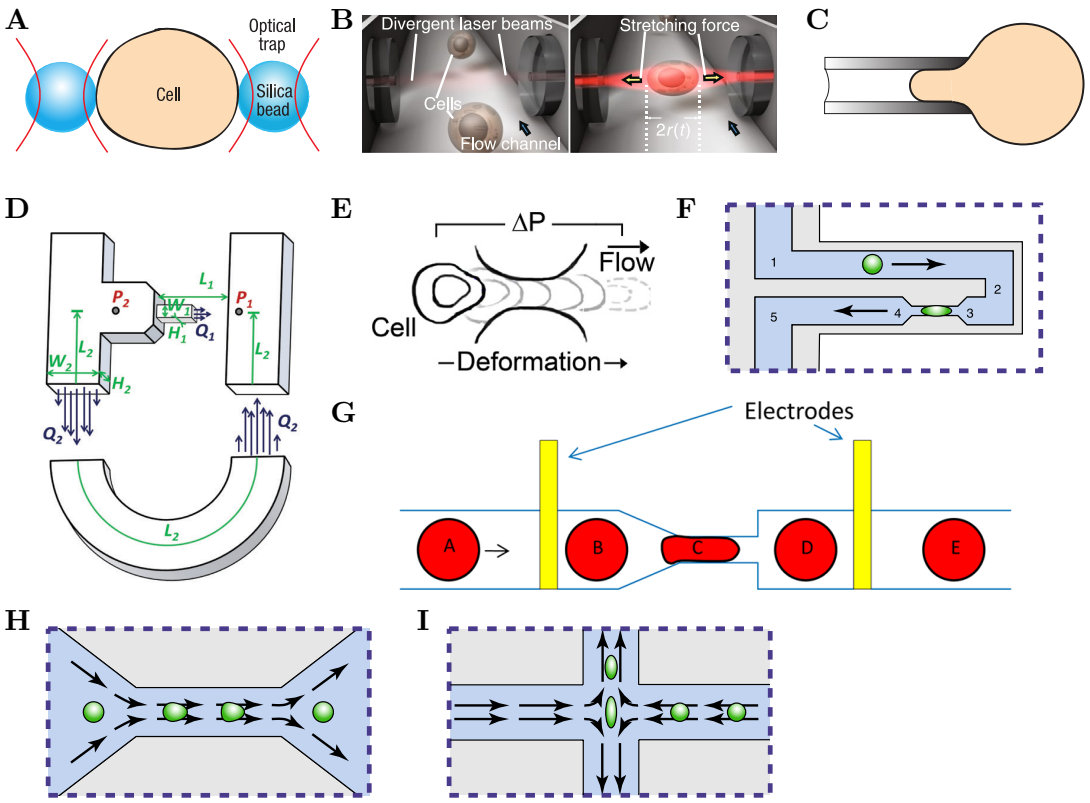

Figure 1.6.: Sketches of techniques for the assessment of mechanical properties of cells in suspension. **A** Optical tweezers, **B** optical stretcher, **C** micropipette aspiration, **D** integration of parallelized micropipettes into a microfluidic device, **E**, **F**, **G** squeezing a cell through a narrow constriction while detecting the translocation time optically (E), within a suspended microchannel resonator (F) or electrically by a change in the impedance over the channel (G). **H**, **I** Cells are deformed hydrodynamically in a shear flow (H) or in an extensional flow (I). A adapted from [2], B from [8], C from [2], D from [63], E from [64], F, H, I from [15], G from [26].

particle or cell and its surrounding which leads to an attractive force centralizing the object close to beam waist. Since the bead is trapped in a harmonic potential, the trap stiffness k_{trap} can be determined from an initial characterization by relating the force F_{trap} acting on the bead and its lateral shift Δx out of trap center, following $F_{\text{trap}} = -k_{\text{trap}} \cdot \Delta x$. When two microbeads are attached to the opposing sides of a cell and trapped optically with one beam each, a compressive force onto the cell can be exerted when moving the beads closer together. Moving the beads closer together applies a force onto the cell while a counterforce pushes the beads slightly out of their trap center (Δx). From cell deformation, the displacement of the beads and the trap stiffness, the mechanical properties of a cell can be derived, corresponding to a stress-strain experiment (Equation 1.1).

Optical stretcher

The optical stretcher is a dual-beam optical trap, where two diverging laser beams are directed opposite to each other [8, 36] (Figure 1.6B). The optical force onto the cell originating from light-matter interaction cancels because of the symmetric setup. However, from every beam results a momentum pointing outwards the optical denser material, i.e., the cell. These contributions are additive from both beams leading to a stretching force while centering the cell between the beams. The cell can be stretched depending on the intensity of the laser beams. From beam size, the optical power, cell size and refractive indices of the cells and their surrounding medium, the stress acting on the cells can be calculated [36]. Their strain is derived from a cell contour fit based on simultaneously acquired video microscopy images. Relating stress and strain provides the mechanical properties of a single cell. After a cell is characterized, it is released by switching off the optical trap. Due to an external flow of suspended cells perpendicular to the two laser beams, a new cell can be trapped and subsequently characterized.

Micropipette aspiration

Micropipette aspiration is a technique for accessing the mechanical properties of a single cell by suction of a cell fraction into a narrow glass capillary [2, 37] (Figure 1.6C). Since the cell is larger than the capillary, it raises retention forces against the negative pressure inside the capillary. Relating the negative pressure and the distance of the fraction a cell is sucked into the capillary, obtained from online imaging, the mechanical properties of the cell can be derived.

Microfluidic micropipette array

The combination of mechanical single-cell characterization by micropipette aspiration and a microfluidics approach allows for high-throughput analysis. Many cells can be characterized in parallel utilizing an array of micropipettes integrated into a microfluidic chip [63] (Figure 1.6D). Due to a flow of suspended cells through the system cells are automatically trapped into the micropipettes and mechanically probed by a pressure difference.

Squeezing a cell through a constriction

Cells are forced by an external flow to squeeze through a channel while the cell is larger than the cross section of the constriction (Figure 1.6E-G). The target value for the determination of single-cell mechanical properties is the passage time, the time a cell needs from approaching the channel entrance until leaving the constriction, which can be accessed optically, mechanically or electrically [15]. Video microscopy allows for an optical determination of the passage time [64–66] (Figure 1.6E), while the change in resonance frequency of a suspended microchannel resonator (SMR) allows for a mechanical readout [28] (Figure 1.6F). If electrodes are integrated into the system,

one before channel inlet and one after the outlet, a change in the electrical resistance can be detected while a cell passes the channel, from which the passage time can be determined [26] (Figure 1.6G). From the pressure applied to the fluid, a stress onto the cell can be calculated. The strain can be derived, e.g., from video microscopy. Using these parameters or by a calibration, cell mechanical properties can be extracted [64, 66].

Hydrodynamic deformation

In contrast to cell deformation by squeezing cells through a constriction, hydrodynamic methods use a channel with a diameter larger than the cells. Here, cells are deformed due to hydrodynamic normal and shear forces on their periphery [14, 15, 24] (Figure 1.6H and I). While cells in channels with constant cross section deform mainly due to shear forces [24] (Figure 1.6H), normal forces are dominating in a cross-channel configuration where cells follow an extensional flow [14] (Figure 1.6I). Since the cells are passing the channel without having contact to its boundaries, high velocities up to a range of meters per second, can be reached. With a high throughput of up to 2,000 cells per second, these setups approach rates comparable to traditional flow cytometers [14, 46].

Combining mechanical characterization in a microfluidic system with a fluorescent readout, new application fields can be addressed [17]. The mechanical properties of, e.g, a stained subpopulation from a heterogeneous sample can be accessed, if the targeted fraction cannot be discriminated exclusively by mechanical means.

Real-time deformability cytometry (RT-DC) as one of the techniques based on hydrodynamic deformation will be explain in more detail, since it is a prerequisite for this work [24] (Figure 1.7). Cells in suspension are deformed by hydrodynamic shear and normal stresses in a Poiseuille flow in a narrow constriction of constant cross section (Figure 1.7A). A sheath flow consisting of the same medium as the carrier fluid of the cells is used as co-flow, focusing the cells in channel center (not shown in Figure 1.7A). An alignment of the cells is required since the stress distribution experienced by a cell depends on its position perpendicular to the direction of flow. The focusing is achieved by a ratio of volumetric flow rates between sample and sheath of 1:3, dosed by a syringe pump. Both flows are connected to a microfluidic chip made of polydimethylsiloxane (PDMS) by soft lithography bonded to a glass cover slip which contains a constriction of quadratic cross-section with a side length of 20 μm or 30 μm and of 300 μm length. The outlet is connected to a waste reservoir. Cells translocating through the microchannel are imaged by a high-speed CMOS camera with 2000 frames per second while illuminated by a pulsed high-power LED (Figure 1.7B). From the projection images, the cell contour is determined by background subtraction, image binarization using a gray-value threshold and subsequent contour fitting utilizing a convex hull algorithm. Circularity c, a parameter relating cell contour area A and perimeter P, and subsequently, rescaled circularity c^* is calculated as a measure of

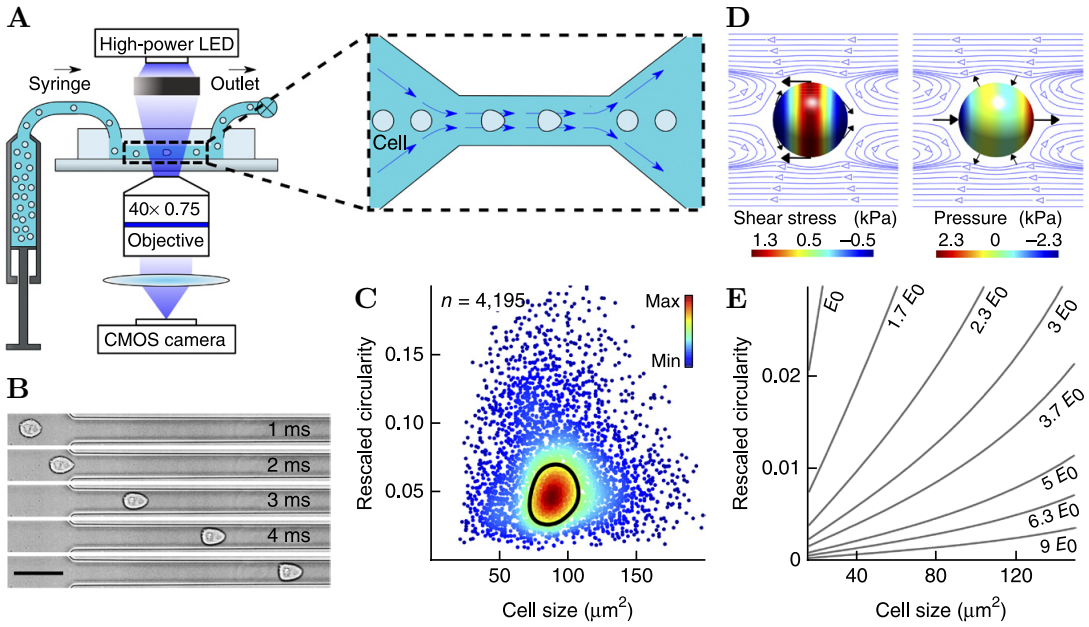

Figure 1.7.: Real-time deformability cytometry (RT-DC). **A** Schematic of the setup. **B** Time series of a cell deforming in the constriction. **C** Scatter plot of rescaled circularity versus cell size (projected area) for more than 4000 cells. **D** Numerical simulation of shear (left) and normal forces (right) acting on a cell's surface (modeled as a sphere). **E** Lines of equal elasticity in a rescaled circularity versus cell size graph. Adapted from [24].

deformation d for each single cell[1] (Figure 1.7C)

$$c^* = 1 - c = 1 - \frac{2\sqrt{\pi A}}{P} \,. \tag{1.12}$$

Rescaled circularity is zero for a circle and between zero and one for any other shape. Contour fitting and calculation of the deformation parameter is done in real time during the experiment. Within a mathematical framework, a model was developed predicting shear and normal stresses in equilibrium acting on a cell modeled as a sphere of a given diameter and Young's modulus, and under a set of external conditions: channel size, flow velocity and fluid viscosity [47, 67] (Figure 1.7D). By calculating iso-elasticity lines from the model, rescaled circularity and cell size can be decoupled (Figure 1.7E). The Young's modulus can be estimated from cell's rescaled circularity and size for given experimental conditions.

[1] Within the context of RT-DC, $1 - c$ with c being the circularity of a cell contour is typically referred to as deformation d. But since cell deformation d can be described by other parameters as well, which were investigated in manuscript IV of this thesis (concluded in Section 3.4), here, $1 - c$ is introduced as rescaled circularity c^*.

1.3.2. Cell mechanical tools for adherent cells

In contrast to cells in suspension, adherent cells are attached to other cells of the same or a different type by cell-cell junctions. In *ex vivo* and *in vitro* studies, cells are usually adhered to a surface and immobilized.

Particular attention has to be paid to the mechanosensitivity of adherent cells. Cells can sense the mechanical properties of the material they adhere to and adapt appropriately [20]. In essence, a cell attached to, e.g., a soft hydrogel will behave differently from the exact same cell adhered to a glass surface, and consequently, different mechanical properties will be determined from that cell. Cells have also been shown to reveal a mechanical memory effect [22].

Most of the techniques for measuring the mechanical properties of adherent cells have the disadvantage of low throughput [52], while some of the methods allow for a parallelized measurement of many cells in a tissue at a time. However, often tracer need to be integrated into the tissue, either magnetic particles [40], beads [68, 69], fluorescently labeled beads [70], oil droplets [9] or ferrofluid microdroplets [43], which potentially influence tissue integrity.

Figure 1.8 gives an overview of most frequently used methods for mechanical analysis of adherent cells.

Microplate rheometer

A single cell is kept between two parallel plates and compressed either statically or dynamically [7, 8, 39, 52] (Figure 1.8A). With online optical microscopy, the strain of the cell can be determined while from the bending of the flexible plate, the force applied to the cell can be extracted. From the stress-strain relationship, cell mechanical properties can be derived. Since only one cell is characterized at a time, the throughput of this method is low.

Atomic force microscopy

The gold standard for determination of cell mechanical properties on adherent cells is the atomic force microscope (AFM) [2, 7, 8, 38, 52] (Figure 1.8B). To this day, the AFM is utilized in most of the studies related to cell mechanics (Figure 1.2). A cantilever of known spring constant (from calibration) is brought in contact with a cell and bends under pressure. The bending is detected with a position-sensitive detector via deflecting a laser beam directed to the back side of the cantilever. In most cases, a bead of given diameter is attached to the cantilever and used as a probe. The interaction between a round bead and the surface under analysis, i.e., the dependency of indentation depth and force applied to the indenter, is described by the framework of Hertz models [73, 74]. From a force distance curve, cell mechanical properties can be derived by fitting with a model taking into account the characteristics of the setup. Depending on the size of the bead, a cell is measured as a whole or subcellular

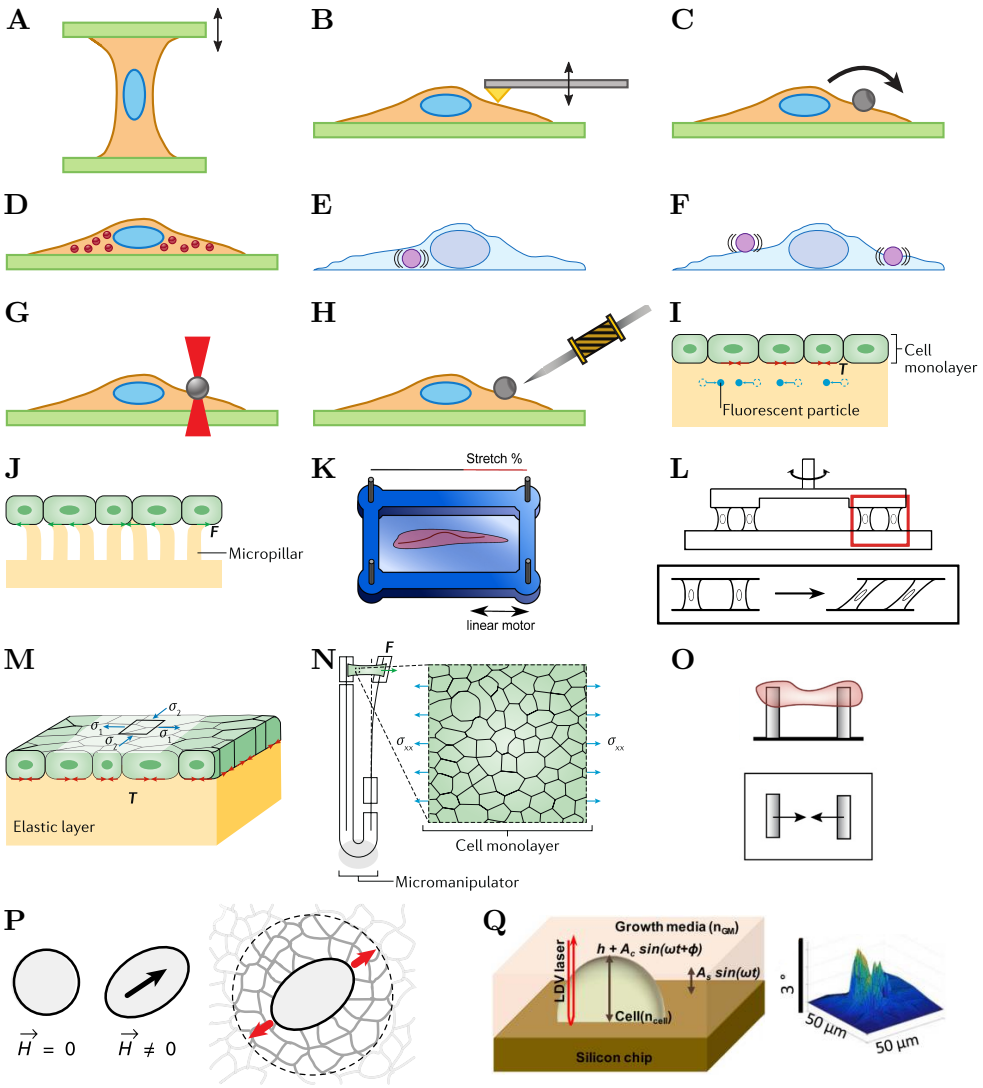

Figure 1.8.: Sketches of techniques for the assessment of mechanical properties of adherent cells. The methods are briefly described in the text. **A** Microplate rheology, **B** atomic force microscopy, **C** magnetic twisting cytometry, **D** particle tracking microrheology, **E** internal laser tracking microrheology, **F** external laser tracking microrheology, **G** optical tweezers, **H** magnetic tweezers, **I** traction force microscopy, **J** micropillars, **K** cell stretcher, **L** cell monolayer rheology, **M** monolayer stress microscopy, **N** suspended-monolayer stretching, **O** tissue pillars, side view (top) and top view of bending pillars (bottom), **P** ferrofluid microdroplets as mechanical actuators, **Q** single-cell vibrometer with optical readout. A, B adapted from [52], C, D, G, H from [52], E, F from [7], I, J, M, N from [71], K from [42], L adapted from [8], O from [10], P from [43], Q from [72].

structures are accessed. To overcome the low throughput of the scanning-probe method, a new high-speed AFM was developed with force distance curve velocities of up to 850 μm/s [75]. This fast AFM allows for observing dynamics in living adherent cells.

Magnetic twisting cytometry

Magnetic twisting cytometry is a technique of active microrheology based on magnetized beads which are first attached to the cell surface and subsequently rotated in a controlled external magnetic field [2, 7, 8, 40, 52] (Figure 1.8C). The torque acting on the bead can be calculated from the magnetic field magnitude, the angle of bead's magnetic moment and its volume [40]. Bead displacement is extracted from video microscopy synchronized to the oscillatory exciting magnetic field. From the corresponding Fourier transformation, viscoelastic moduli can be derived. Within a single measurement, a mechanical characterization of cells in a tissue with approximately 100 beads can be performed [40, 52].

Particle tracking microrheology

Particle tracking or two-point microrheology is a method of passive rheology [7, 8, 41, 52] (Figure 1.8D). Small beads of submicrometer size are ballistically injected into cells and after cell recovery, their movement is observed over time without external excitation. Their mean square displacement caused by Brownian motion is recorded and translated into a cellular strain function. From the corresponding power spectrum and the thermal energy (k_BT), viscoelastic properties are calculated [68, 69]. In two-point rheology, highly inhomogeneous soft viscoelastic materials can be analyzed by cross correlating bead displacements of pairs of embedded beads [41]. Further strengths of the method are the ability to access both bulk rheological properties and those of the microenvironment around a bead, since many tracer particles can be imaged at the same time [41]. Independent of the implementation, dynamics can be observed [69].

Laser tracking microrheology

Laser tracking microrheology is broadly similar to particle tracking microrheology (Figure 1.8E and F). Differences can be observed from particle density and detection method. For laser tracking microrheology a laser of low power is used in conjunction with a quadrant photodiode. Since the laser power is low, induced forces can be neglected and thus, a tracked particle solely responds to Brownian motion. Due to the monochromatic illumination, fluorescently labeled beads can be used [70]. Depending on whether beads are endocytosed or attached to cell surface [76], the method is classified for internal (Figure 1.8E) or external (Figure 1.8F) laser tracking microrheology [7]. An advantage of this technique is the very high frequency range of up to 100 kHz which can be reached due to the single-point detection [52]. Also, optically refractile granules within the cytoplasm can be tracked which has the advantage that no beads need to be injected and cells do not need to recover from the injection [77].

Optical tweezers

The method was already introduced for suspension cells where two beads are trapped optically to exert a controlled deformation on the cell. The same method can be applied to adherent cells, while only one bead is necessary since the counterforce comes from the substrate [52] (Figure 1.8G). With a bead in an optical trap of calibrated stiffness, a force can be applied onto a cell while monitoring its deformation. Relating stress and strain, yields the material properties. A strength of the method is the opportunity to reach subcellular resolution, if a small probing bead is used, with a low throughput on the other hand.

Magnetic tweezers

Similar to optical tweezers, there is another technique based on superparamagnetic beads called magnetic tweezers [42, 52] (Figure 1.8H). A magnetic field is generated by a solenoid surrounding a ferromagnetic core with a tip. Mounted on a micromanipulator, the tip is moved close to a cell containing a magnetic bead. While the field exerts a force onto the bead within a cell, images are captured by a microscope to track bead's displacement. Cell deformation is calculated from bead displacement. From force and deformation, mechanical properties can be obtained. The throughput of the method is limited by the fact that only one bead, i.e., one cell, can be analyzed at a time.

Traction force microscopy

When a cell or tissue is attached to an elastic substrate, e.g., polyacrylamide, of defined stiffness with embedded fluorescent tracer particles, cellular forces acting on the surface can be extracted by tracking the particles [10, 42, 71] (Figure 1.8I). First, a microscopic image with attached cells or tissue is recorded representing the stressed or contracted state, or an image sequence is acquired, if dynamics are of interest. From a second image, the resting position of the markers is detected by removing the cellular forces, either by cell lysis, detachment, or myosin inhibition [10]. From the displacement of the markers and substrate stiffness, the 2-dimensional in-plane shear forces exerted by the cells and ultimately, the strain energy field are computed. Further development of the method allowed for analysis without knowledge on the locations of cell's focal adhesions to the substrate [42]. Strengths of the technique are the very high spatial resolution of down to 10 nm [42], the wide range of adjustable substrate stiffness and the quick as well as repeatable measurements once the system is established [10]. If subcellular resolution is not required, a monolayer tissue can be mechanically characterized with single-cell resolution [71]. However, characterized cells cannot be easily processed further due to their detachment or even their lysis. In principle, the method can be applied to analyze 3-dimensional force fields as well [10].

Micropillars

This method is similar to traction force microscopy with the difference that the cell substrate is structured [10, 71] (Figure 1.8J). Cells are attached on top of an array of vertical pillars with a diameter in the micrometer range. The pillars are fabricated with silicone rubber, usually polydimethylsiloxane (PDMS), and are serving as cantilevers. Cellular traction forces can be accessed from the bending of micropillars by optical microscopy. Since the spring constant of the micropillars is known by calibration or is estimated from pillar design, the measured displacement of the pillar's free facet can be translated into forces exerted by a cell. Both single cells and monolayer tissues can be mechanically characterized. As the micropillars bend independently and do not interact with each other, no further model assumptions are necessary to extract force fields and since the resting position of the pillars is known, no cell detachment or lysis is required [10]. Many cells can be mechanically characterized in parallel, including cell-cell interaction forces.

Cell stretcher

Cells attached to an elastomeric membrane coated with external matrix proteins are exposed to an uniaxial stress [2, 42] (Figure 1.8K). Cell viability under external loading is analyzed using a viability stain and by determining the fraction of dead cells in dependence of the mechanical stress. If the elasticity of the substrate is systematically tuned, the interactions of cells with the substrate can be investigated [2]. Although the method is not quantitative with respect to mechanical properties, effects under mechanical loading can be analyzed. Micropatterned substrates allow for studying contractile forces during the stretching as well as the interdependence between applied stress and focal adhesions points.

Cell monolayer rheology

Cell monolayer rheology is a technique for probing the mechanical properties of a thin tissue layer attached to a surface [8] (Figure 1.8L). A ring-like structure is stacked on top of the cells causing some of the cells to attach to two contact surfaces. The ring is slightly rotated harmonically in both directions and from relating rotation angle and torque, a shear modulus can be calculated. An ensemble of the rheological properties of many cells is accessed within one experiment.

Monolayer stress microscopy

The internal stress field of a tissue can be accessed by attachment of a cell monolayer to an elastic surface [71] (Figure 1.8M). Modeling the monolayer as thin flat plate, from cell trajectories, the in-plane stress within an expanding monolayer can be calculated by mathematical models based on simple force-equilibrium arguments. The only *a priori* information required for stress calculation is the Poisson's ratio of the monolayer. An advantage of the technique is the non-invasive accessibility of the internal stress

distribution rather than the interaction with a substrate. Disadvantages are the assumption of a uniform tissue height, the limitation to in-plane stress excluding, e.g., tissue bending and the description by an elastic constitutive equation which might not hold completely true for cells [71].

Suspended-monolayer stretching and tissue pillars

In a macroscopic technique, the ensemble mechanical properties of a whole tissue can be analyzed. Either a suspended monolayer of *ex vivo* or *in vitro* tissue is stretched actively between two rods by increasing their distance with a micromanipulator [71] (Figure 1.8N) or the tissue is attached to two pillars, which are fixed in position, holding the tissue in between [10] (Figure 1.8O). While contractile forces of, e.g., cardiomyocytes can be analyzed with the method based on two passive pillars, a piece of tissue can be actively stretched while monitoring force and strain in the first realization. From bending of the flexible rod (Figure 1.8N) or of both flexible rods (Figure 1.8O), the applied torque can be calculated when the elasticity of the rod material is known. Bending, or strain, is observed from optical microscopy. Compared to the simplicity of the mechanical characterization of a complete tissue, sample preparation is time-consuming and has low throughput.

Ferrofluid microdroplets

Biocompatible ferrofluid microdroplets integrated into a tissue can be used as mechanical actuators [43] (Figure 1.8P). The microdroplets have a round shape when no external magnetic field is applied while they elongate if magnetic forces are induced by a magnet (Figure 1.8P, left). Due to the exerted force dipole and the resulting strain, the mechanical properties in close vicinity can be probed (Figure 1.8P, right). Generating a controlled uniform magnetic field allows for calculating the acting forces while the local strain in tissues can be determined from microscopy. Switching the stress on and off, and following the strain over time, allows for extraction of viscoelastic material properties. The method is able to perform spatially resolved and time-dependent mechanical measurements *in vivo* as well as *in situ* on 3D tissues and was used to determine viscoelastic properties of developing 3D tissues [43].

Single-cell vibrometer with optical readout

Adherent cells are mechanically excited on a vertically vibrating substrate while a laser Doppler vibrometer (LDV) is used for a point-wise analysis [72] (Figure 1.8Q). Due to the viscoelastic properties, cells respond to the exciting vibration with a retardation in phase angle. This vibration-induced phase shift (VIPS) is measured with the LDV while a measurement spot is rastered over the cell. From the VIPS measured at multiple vibration frequencies, the Young's modulus of the adherent cells can be estimated with the help of a simulation modeling induced phase shifts under given cell mechanical properties. The method is label free but has a low throughput due to the need to scan the region of interest.

1.4. Digital holography

Holography, introduced in 1948 by Dennis Gabor [78] and acknowledged with the Nobel Prize in Physics in 1971, is an optical technique for acquiring and storing the entire parameter space of an electromagnetic wave, i.e., amplitude and phase. The hologram, a spatially resolved map of optical amplitude and phase, e.g., reflected from an object of interest, can be recorded on an analog film (photosensitive material) or by a digital camera – the first is used in analog, the latter in digital holography. Within this thesis, I will focus on digital holography. The combination of fast digital cameras with small pixel sizes as well as high sensitivity and digital hologram reconstruction allows for many applications in the fields of 3D imaging, microscopy, lithography, metrology, profilometry and tomography [79]. Once acquired, a digital hologram, discretized in position and intensity, can be reconstructed and evaluated depending on the measurement system within short times on modern computers, rendering digital holography a powerful tool. A unique feature of holography is its sensitivity towards the phase of light which is of importance for holographic vibration spectroscopy, a technique I developed for non-contact mechanical characterization of adherent cells and tissue at high throughput, introduced in Section 2.3.

First, basic principles for hologram recording and reconstruction are addressed in Section 1.4.1. In Sections 1.4.2, the angular spectrum method for reconstruction of a real object image will be introduced. Third, phase-shifting holography, a method for time-dependent hologram recording and reconstruction will be described in Section 1.4.3.

1.4.1. Holographic principles

Two fundamental optical setups can be used for hologram recording: inline and off-axis holography. For inline holography, the object of interest is illuminated by a coherent light source, typically a laser, and the wave scattered by the object is directed to a detector where it is overlaid with the incident reference beam (Figure 1.9A). Both beams propagate along one optical axis and create an interference pattern in intensity on the detector (Figure 1.9B).

Inline holography is limited to small objects since a fraction of the incident beam needs to travel to the detector without being disturbed by the object(s) of interest. For too large objects, diffraction is not sufficient to reach the detector behind the object.

In contrast to inline holography, in an off-axis holographic setup, reference and object beam hit the detector under a small angle. Within a Mach-Zehnder interferometer [81, 82] a coherent beam is divided into a reference and an object beam (Figure 1.9C). While the reference beam is guided to the detector directly, the object beam illuminates the object of interest and its reflection is directed to the detector as well. Similar to the setup for inline holography, reference and object beams create an interference pattern on the detector (Figure 1.9D). Due to the angle between both beams, the camera records a regular fringe pattern with a spatial frequency increasing with the

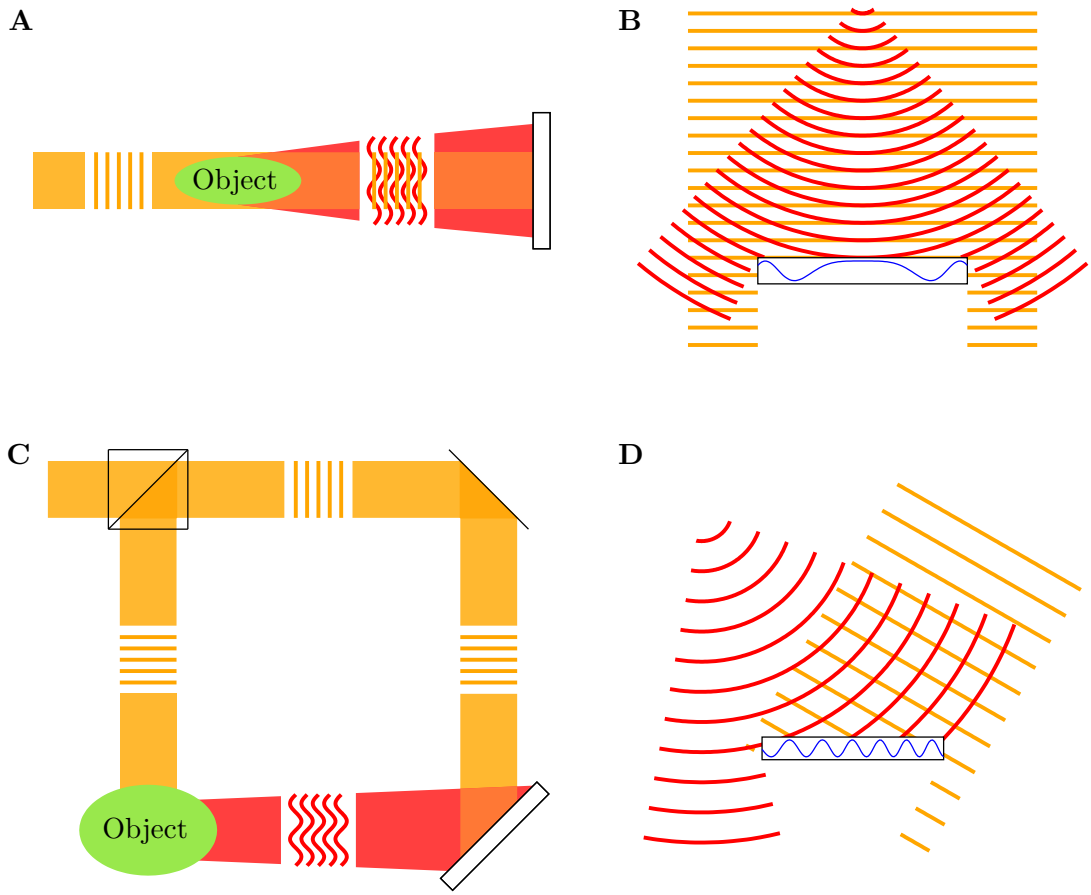

Figure 1.9.: Inline and off-axis hologram recording. **A** Optical setup for inline hologram recording: a monochromatic beam is directed to the object of interest which diffracts the incident beam. Electromagnetic fields from the incident reference beam (yellow) and the object beam (red) overlap on the detector (black box). Lines indicate unperturbed (yellow) and distorted wavefronts (red). **B** Example for the intensity profile (blue) on the detector created by a spherical (red) wave from the object and a plane reference wave (yellow) recorded from the inline setup (A). **C** Optical setup for recording in off-axis configuration: a Mach-Zehnder interferometer is used to divide the coherent beam into reference (yellow) and object beam (red) and combine both on the detector (black box). **D** Exemplary intensity profile (blue) on the detector arisen from a spherical object wave (red) and a plane reference wave (yellow) recorded in off-axis configuration (C). Adapted from [80].

angle. In contrast to inline holography, off-axis holography is not facing the limitation with respect to object size. On the other hand, optical setups are more complex. So far, the configuration for recording a hologram from a reflective object was introduced, but off-axis holography can also be used if the object is transparent. For transparent objects, the transmitted light is directed to the detector and overlaid with the reference beam.

Regardless of the optical setup chosen, reference and object beam interfere on the detector. For simplicity, the two beams are described by plane waves with a complex electric field $\mathbf{E}$

$$\begin{aligned}\mathbf{E}_{\text{ref}} &= E_{\text{ref}} \cdot \exp(j\omega_0 t - j\vec{k}_{\text{ref}}\vec{r} - j\varphi_{\text{ref}}) \\ \mathbf{E}_{\text{obj}} &= E_{\text{obj}} \cdot \exp(j\omega_0 t - j\vec{k}_{\text{obj}}\vec{r} - j\varphi_{\text{obj}}) \ ,\end{aligned} \tag{1.13}$$

as a function of position $\vec{r} = [x\ y\ z]^\intercal$, propagating in the directions of wave vectors $\vec{k}_{\text{ref}}$ and $\vec{k}_{\text{obj}}$ with wave number $k = |\vec{k}| = 2\pi/\lambda$ as well as wavelength λ, and varying over time t at an angular frequency ω_0 of the coherent light source. While j is the imaginary unit ($j^2 = -1$), φ_{ref} and φ_{obj} are phase shifts of the reference and object beam, respectively, and E_{ref} and E_{obj} are real amplitude functions of the electric field, i.e., dependent on the lateral and axial position along the direction of propagation ($E_{\text{ref}}(\vec{r})$ and $E_{\text{obj}}(\vec{r})$).

The superposition of both beams creates an interference intensity pattern on the detector. In general, light intensity I can be derived from an electric field following

$$I = \epsilon c \mathbf{E}^2 \propto \mathbf{E}^2 \ , \tag{1.14}$$

with $\epsilon = \epsilon_0 \epsilon_r$ and c being the permittivity (product of absolute and relative permittivity) and the speed of light, respectively. The permittivity describes the electric polarizability of a dielectric, in this case of the medium of light propagation. The interfered light intensity on the detector follows the equation

$$\begin{aligned} I &= \epsilon c(\mathbf{E}_{\text{ref}} + \mathbf{E}_{\text{obj}})^2 \\ &\propto (\mathbf{E}_{\text{ref}} + \mathbf{E}_{\text{obj}})^2 \\ &\propto (\mathbf{E}_{\text{ref}} + \mathbf{E}_{\text{obj}}) \cdot (\mathbf{E}_{\text{ref}} + \mathbf{E}_{\text{obj}})^* \\ &\propto |\mathbf{E}_{\text{ref}}|^2 + \mathbf{E}_{\text{ref}}\mathbf{E}_{\text{obj}}^* + \mathbf{E}_{\text{ref}}^*\mathbf{E}_{\text{obj}} + |\mathbf{E}_{\text{obj}}|^2 \ , \end{aligned} \tag{1.15}$$

where $\mathbf{E}^*$ represents the complex conjugate of the electrical field $\mathbf{E}$. For the two waves in Equation 1.13, the interference intensity on the detector is

$$\begin{aligned} \frac{I}{\epsilon c} &= E_{\text{ref}}^2 + E_{\text{ref}}E_{\text{obj}} \exp\Big\{ j\Big(\vec{k}_{\text{obj}} - \vec{k}_{\text{ref}}\Big)\vec{r} + j(\varphi_{\text{obj}} - \varphi_{\text{ref}}) \Big\} \\ &\quad + E_{\text{ref}}E_{\text{obj}} \exp\Big\{ j\Big(\vec{k}_{\text{ref}} - \vec{k}_{\text{obj}}\Big)\vec{r} + j(\varphi_{\text{ref}} - \varphi_{\text{obj}}) \Big\} + E_{\text{obj}}^2 \\ &= E_{\text{ref}}^2 + E_{\text{obj}}^2 + 2E_{\text{ref}}E_{\text{obj}} \cos\Big\{ \Big(\vec{k}_{\text{obj}} - \vec{k}_{\text{ref}}\Big)\vec{r} + \Delta\varphi \Big\} \ , \quad \Delta\varphi = \varphi_{\text{obj}} - \varphi_{\text{ref}} \end{aligned} \tag{1.16}$$

following the trigonometric identity $\cos(\alpha) \equiv \frac{1}{2}\Big(\exp(j\alpha) + \exp(-j\alpha)\Big)$. According to Equation 1.16, the intensity on the detector is maximum if both the electric fields of the reference as well as object beam have their maximum magnitude at the detector. Similarly, an intensity maximum is created if the electric field of both beams has the maximal negative magnitude, since intensity is proportional to the squared electric

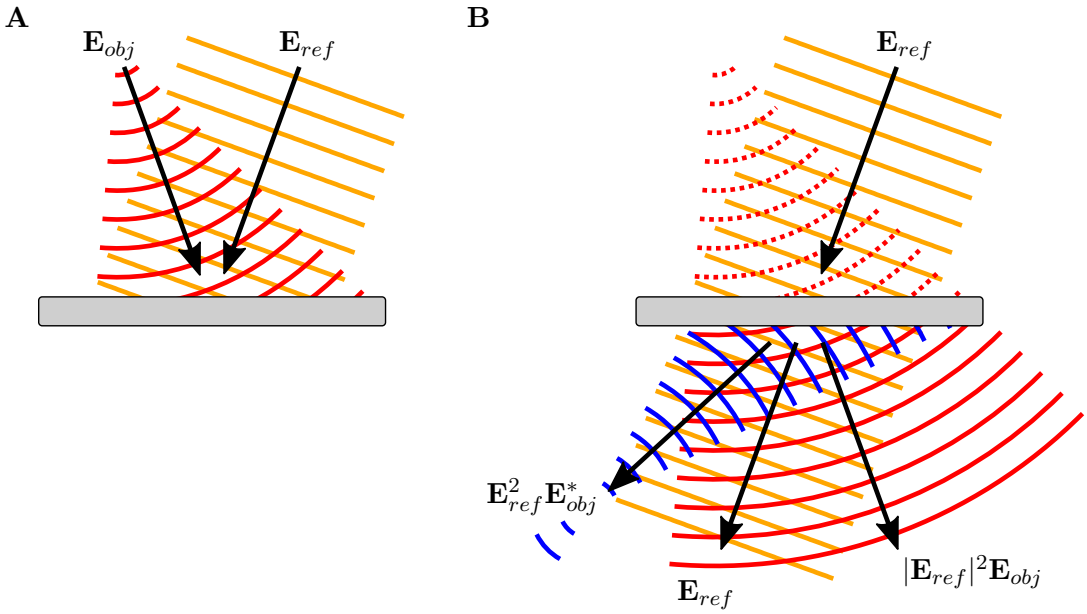

Figure 1.10.: Reconstruction of a hologram. **A** A hologram (gray) recorded from $\mathbf{E}_{\text{ref}}$ (yellow) and $\mathbf{E}_{\text{obj}}$ (red) can be reconstructed by **B** illuminating with the reference beam $\mathbf{E}_{\text{ref}}$ (yellow) under the same angle as used for recording and yields three different components proportional to $|\mathbf{E}_{\text{ref}}|^2\mathbf{E}_{\text{obj}}$ (red), $\mathbf{E}_{\text{ref}}$ (yellow) and $\mathbf{E}^2_{\text{ref}}\mathbf{E}^*_{\text{obj}}$ (blue), representing the real object image, an image of the illumination source and the conjugate object image, respectively. Adapted from [80].

field (Equation 1.14). For any other combination of the two electric fields, the intensity is decreased and yields a minimum if a maximum in electric field of one beam coincides with a minimum of the other. In particular, the sensitivity of the hologram's intensity to the phase of the light $\Delta\varphi$ can be observed. The explained correlations can be seen from the two examples of hologram recordings in Figure 1.9B and Figure 1.9D, where the wavefronts of the two interfering beams are indicted by lines, i.e., the lines reflect, e.g., the positions of maximum electric field amplitude.

Object's amplitude and phase can be reconstructed from the recorded hologram (Figure 1.10A) when illuminating with the reference beam $\mathbf{E}_{\text{ref}}$ under the same angle as used for recording (Figure 1.10B). While reconstruction will be demonstrated for an analog transmissible hologram, the process is transferable to digital holography. The intensity present at the analog hologram during recording is stored by the photosensitive material as modulation in its transmittance. While a high intensity causes high exposure and low transmittance of the film plate, low exposing intensity lead to higher transmittance. Since the interference intensity on the detector from Equation 1.15 defines the transmittance of the hologram, the reference beam used for reconstruction $\mathbf{E}_{\text{ref}}$ is modulated by the position-dependent transmittance and leads to a reconstructed intensity $I_{\text{rec}} \propto I \cdot \mathbf{E}_{\text{ref}}$ with

$$I_{\text{rec}} \propto |\mathbf{E}_{\text{ref}}|^2\mathbf{E}_{\text{obj}} + \Big(|\mathbf{E}_{\text{ref}}|^2 + |\mathbf{E}_{\text{obj}}|^2\Big)\mathbf{E}_{\text{ref}} + \mathbf{E}_{\text{ref}}^2\mathbf{E}_{\text{obj}}^* \ . \tag{1.17}$$

Three different images are generated. While the real object image is stored in the +1. diffraction order, zeroth order yields an image of the reference beam and −1. order contains a conjugated image of the object, corresponding to the first, second and third term in Equation 1.17 as well as to the red, yellow and blue beams shown in Figure 1.10B, respectively. By selecting the correct diffraction order from an off-axis hologram, the real image consisting of phase and amplitude information can be reconstructed. Observing the hologram in Figure 1.10B under the angle in which the red beam propagates, gives the impression of looking at the recorded object represented by the electrical field $\mathbf{E}_{\text{obj}}$. However, only for off-axis holography, the three images are separated by an angle, which is the same angle as for the recording. The three images fall together in the case of inline holography.

1.4.2. Angular spectrum method for hologram reconstruction

Within a hologram, the constant term and the twin object images ($\mathbf{E}_{\text{obj}}$ & $\mathbf{E}_{\text{obj}}^*$) overlap (Equation 1.15). In analog holography, the components can be easily separated by observing the hologram under the correct angle (in the direction of propagating $\mathbf{E}_{\text{obj}}$) during reconstruction (Figure 1.10B). The principle of angular filtering can be transferred to digital holography. First, the angular spectrum $S_H(k_{\text{s},x}, k_{\text{s},y})$, a two-dimensional spectrum containing spatial frequency components $f_{\text{s},x}$, $f_{\text{s},y}$ at corresponding pixel positions $(k_{\text{s},x}, k_{\text{s},y})$ in directions x and y, respectively, of a recorded hologram $H(k_x, k_y)$ (Figure 1.11A) is calculated by a 2D-discrete Fourier transformation (DFT) (implemented as 2D-fast Fourier transformation (FFT))

$$S_H(k_{\text{s},x}, k_{\text{s},y}) = \sum_{k_x=0}^{N_x-1}\sum_{k_y=0}^{N_y-1} \exp\left(-2\pi j\frac{k_x k_{\text{s},x}}{N_x}\right)\exp\left(-2\pi j\frac{k_y k_{\text{s},y}}{N_y}\right)H(k_x, k_y) \ , \tag{1.18}$$

$$f_{\text{s},x} = \frac{k_{\text{s},x}}{N_x\Delta x} \ , \qquad\qquad f_{\text{s},y} = \frac{k_{\text{s},y}}{N_x\Delta y} \ , \tag{1.19}$$

where both pixel maps $H(k_x, k_y)$ and $S_H(k_{\text{s},x}, k_{\text{s},y})$ contain $N_x \times N_y$ pixels and indices k_x and k_y range from 0 to $N_x - 1$ or $N_y - 1$, respectively, while indices $k_{\text{s},x}$ and $k_{\text{s},y}$ are element of $[-N_x/2 + 1, N_x/2]$ and $[-N_y/2 + 1, N_y/2]$, respectively. The fringes in an off-axis hologram (Figure 1.11A) yield three regions, corresponding to the three components [83] (see Figure 1.11B and cf. Equation 1.17 and Figure 1.10B). The twin images are located at the positive and negative spatial frequency of the fringes (bottom right (blue) and top left (red) in Figure 1.11B), while the constant contribution from the reference beam is located at frequency zero (center, yellow). If the spatial frequency of the object image (and its conjugate) is high enough, i.e., the contributions do not overlap in the spectrum, spatial filtering can provide the contribution from the real

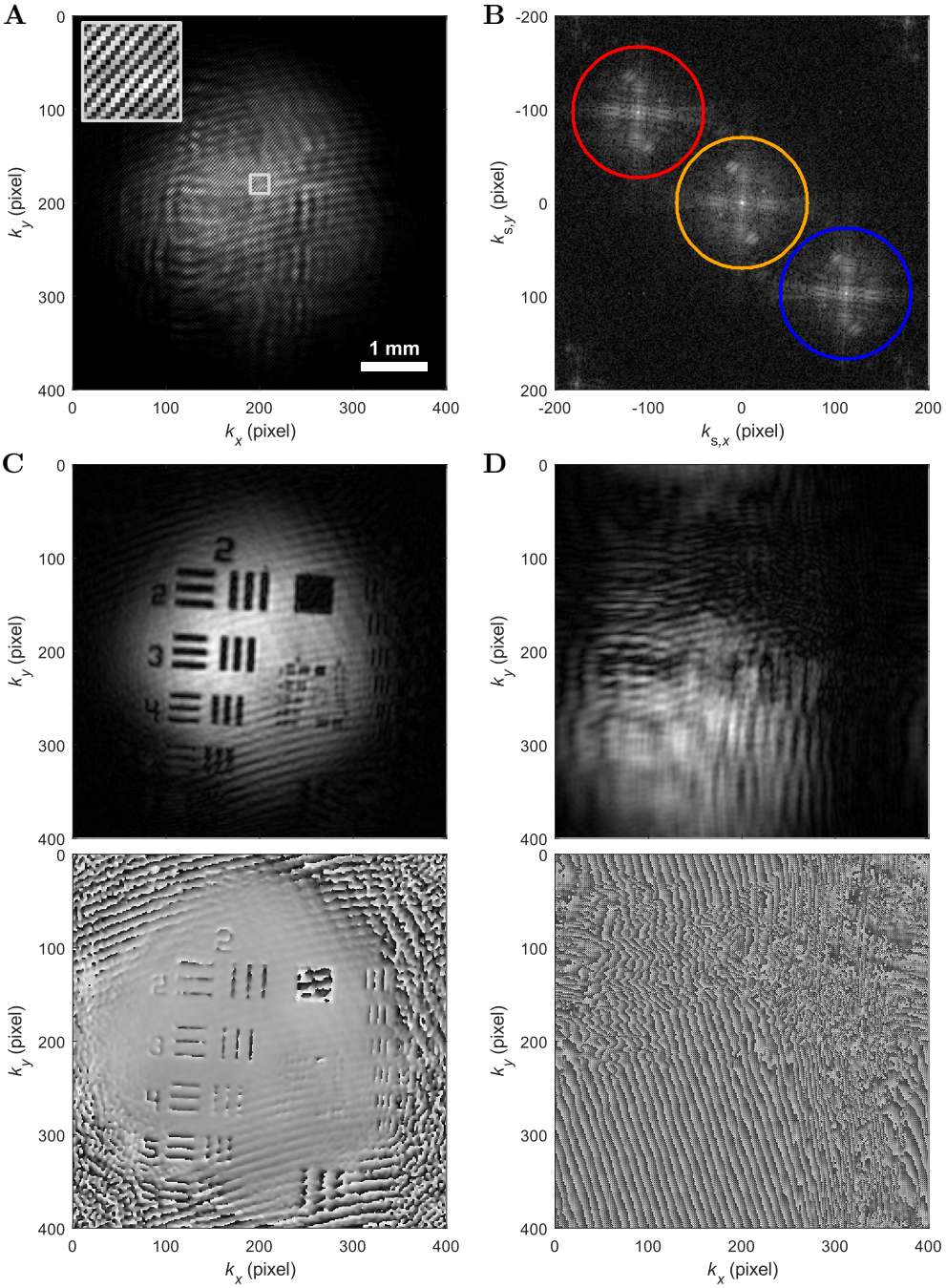

Figure 1.11.: Digital hologram recording in off-axis configuration and reconstruction with the angular spectrum method. **A** Hologram recorded from a resolution test target reveals fringes (inset) originating from an angle between object and reference beam. **B** Angular spectrum with spatial frequency components from the real object image (red), its conjugate (blue) and a constant term from the reference beam (yellow). Intensity is shown on a logarithmic scale. **C** Reconstruction of the real object image, composed of amplitude (top) and phase (bottom) and **D** reconstruction of object image conjugate.

object image. Filtering is achieved by a multiplying the spectrum with a circular mask, i.e., by selecting a certain region of the spectrum (red circle in Figure 1.11B). Next, an optional spatial demodulation can be performed by shifting the center of the filtered spectrum (center position of the mask) to zero frequency (origin of coordinates) which removes the tilted phase originating from the off-axis angle between reference and object beam during hologram recording. An inverse 2D-FFT of the filtered (and demodulated) spectrum $\widetilde{S}_H$ yields object's amplitude $|\widetilde{H}|$ and phase $\angle\widetilde{H}$ from the reconstructed hologram $\widetilde{H}$ (Figure 1.11C).

$$\widetilde{H}(k_x, k_y) = \frac{1}{N_x N_y} \sum_{k_{\mathrm{s},x}=0}^{N_x-1} \sum_{k_{\mathrm{s},y}=0}^{N_y-1} \exp\left(2\pi j \frac{k_x k_{\mathrm{s},x}}{N_x}\right) \exp\left(2\pi j \frac{k_y k_{\mathrm{s},y}}{N_y}\right) \widetilde{S}_H(k_{\mathrm{s},x}, k_{\mathrm{s},y}) \ . \tag{1.20}$$

By angular filtering, the unwanted overlapping contributions from both the reference beam and the conjugated object image could be excluded. Since the light containing the conjugated object image propagates in reverse direction, a reconstruction of the conjugated object image yields defocused amplitude and phase maps in the optical plane of the (real) recorded object (Figure 1.11D).

1.4.3. Phase-shifting holography for hologram recording and reconstruction

Another method for hologram recording and reconstruction is phase-shifting holography. In particular, in heterodyne optical setups, i.e., where reference and object beam share not the same frequency, phase-shifting holography is a straightforward approach since the hologram can be calculated directly from a time series of recorded images without Fourier transformation and spatial filtering. Phase-shifting holography is compatible with both implementations for recording – the off-axis as well as the inline configuration.

A hologram can be composed of multiple images, if the optical phase of the beam which illuminates the object of interest is shifted by a certain amount between consecutive images. For probing the entire phase space of 2π and bijective phase reconstruction, at least three recordings are necessary, or in general N frames ($N \geq 3$). Usually, four images are taken ($N = 4$), leading to a phase shift of $\pi/2$ or 90° between two consecutive images. For very high throughput, the four images can be recorded simultaneously by a synchronized array of four cameras yielding holograms at the frame rate of the cameras. However, processing the images acquired from different detectors requires spatial mapping because the cameras are physically separated.

The hologram recording can also be performed with a single camera while the required phase shift is introduced either spatially or temporally. The required phase can be inserted mechanically by modulating the optical path length of the reference beam, e.g., by moving a mirror on a piezo crystal, synchronized to image acquisition. Connected by the refractive index of the propagation medium and the wave number $k = 2\pi/\lambda$, the change in optical path length can be translated into the required phase shift. A temporal phase shift, i.e., a phase linearly progressing over time, can be

implemented by a defined mismatch in frequency between the object and reference beams. If the frequencies are adjusted following the relationship

$$f_{\text{ref}} - f_{\text{obj}} = \frac{f_{\text{cam}}}{N} \ , \tag{1.21}$$

where f_{ref}, f_{obj} and f_{cam} represent the optical frequencies of reference and object beam light waves as well as the sampling rate of the camera, respectively, N images with a phase shift of $2\pi/N$ between two consecutive images are acquired. The throughput for this method is the camera sampling rate diminished by a factor of $1/N$.

In the following, the commonly chosen case of $N = 4$ is considered. Once four images with a relative phase shift of 90° are acquired, a hologram can be composed. Similar to Equation 1.13 let us consider the electric field of two beams varying over time. In contrast to the homodyne detection used above where both electric fields share the same angular frequency, reference and object beam have slightly different angular frequencies in a heterodyne setup following Equation 1.21. The object beam includes a retardation phase angle field φ depending on the properties of the object

$$\begin{aligned} \mathbf{E}_{\text{ref}} &= E_{\text{ref}} \cdot \exp(j\omega_{\text{ref}} t) \\ \mathbf{E}_{\text{obj}} &= E_{\text{obj}} \cdot \exp(j\omega_{\text{obj}} t - \varphi), \ \text{with} \ \ \omega_{\text{ref}} - \omega_{\text{obj}} = \frac{2\pi f_{\text{cam}}}{4} \ . \end{aligned} \tag{1.22}$$

Calculating the intensity of the two electric fields superpositioned on the detector using Equation 1.15 and the trigonometric identity $\cos(\alpha) \equiv \frac{1}{2}\Big(\exp(j\alpha) + \exp(-j\alpha)\Big)$ yields

$$\begin{aligned} I &\propto E_{\text{ref}}^2 + 2E_{\text{ref}}E_{\text{obj}} \cos\Big((\omega_{\text{ref}} - \omega_{\text{obj}})t + \varphi\Big) + E_{\text{obj}}^2 \\ &\propto E_{\text{ref}}^2 + E_{\text{obj}}^2 + 2E_{\text{ref}}E_{\text{obj}} \cos\left(\frac{2\pi f_{\text{cam}}}{4} t + \varphi\right) \ . \end{aligned} \tag{1.23}$$

Intensity I is sampled by the detector at times $t_i = i/f_{\text{cam}}$ ($i \in \mathbb{N}$) leading to $I_i = I(t_i)$

$$I_i \propto E_{\text{ref}}^2 + E_{\text{obj}}^2 + 2E_{\text{ref}}E_{\text{obj}} \cos\left(i\frac{\pi}{2} + \varphi\right) \ . \tag{1.24}$$

From the cosine argument, the phase shift of $\pi/2$ between two consecutive images with index i can be observed. According to Equation 1.24, four frames have the intensity fields I_i with $i = 0, ..., 3$

$$\begin{aligned} I_0 &= \epsilon c\Big(E_{\text{ref}}^2 + E_{\text{obj}}^2 + 2E_{\text{ref}}E_{\text{obj}} \cos\varphi\Big) \\ I_1 &= \epsilon c\Big(E_{\text{ref}}^2 + E_{\text{obj}}^2 - 2E_{\text{ref}}E_{\text{obj}} \sin\varphi\Big) \\ I_2 &= \epsilon c\Big(E_{\text{ref}}^2 + E_{\text{obj}}^2 - 2E_{\text{ref}}E_{\text{obj}} \cos\varphi\Big) \\ I_3 &= \epsilon c\Big(E_{\text{ref}}^2 + E_{\text{obj}}^2 + 2E_{\text{ref}}E_{\text{obj}} \sin\varphi\Big) \ . \end{aligned} \tag{1.25}$$

Based on the four images $I_{0,\dots,3}$, a hologram H can be created from a linear combination

$$\begin{aligned} H &= I_0 - I_2 - j(I_1 - I_3) \\ &= \epsilon c(4E_{\text{ref}}E_{\text{obj}}\cos\varphi + j4E_{\text{ref}}E_{\text{obj}}\sin\varphi) \ , \end{aligned} \tag{1.26}$$

with the properties

$$|H| = 4\epsilon c E_{\text{ref}}E_{\text{obj}} \ , \tag{1.27}$$

$$\angle H = \varphi \ . \tag{1.28}$$

As the amplitude E_{ref} of the electric field of the reference beam is supposed to be known (it can be accessed for example by acquiring an image exclusively of the reference beam, i.e., by shadowing the object beam), the field amplitude from the object E_{obj} can be reconstructed from the hologram's magnitude $|H|$ while its phase angle $\angle H$ yields the phase field φ of the object of interest.

Figure 1.12 presents an experimental example where a test target was imaged in transmission with phase-shifting holography in off-axis configuration. The first out of four captured images is shown (I_0, Figure 1.12A). Following Equation 1.26, from the four images $I_{0,\dots,3}$, the hologram H is calculated and its magnitude $|H|$ as well as phase $\angle H$ are reconstructed (Figure 1.12B and C). Due to the off-axis angle between reference and object beam, the reconstructed phase is tilted. Tilt removal yields the unwrapped object phase which reveals the structures of the resolution test target (Figure 1.12D).

For the generalized case of N acquired frames ($N \geq 3$), the hologram H can be composed from the frames with intensity maps I_i

$$H = \sum_{i=0}^{N-1} I_i \exp\left(-j\frac{2\pi i}{N}\right) \ . \tag{1.29}$$

With sampled intensity I_i

$$\frac{I_i}{\epsilon c} = E_{\text{ref}}^2 + E_{\text{obj}}^2 + 2E_{\text{ref}}E_{\text{obj}}\cos\left(\frac{2\pi i}{N} + \varphi\right) \ , \tag{1.30}$$

this leads to the properties of H

$$|H| = N\epsilon c E_{\text{ref}}E_{\text{obj}} \ , \tag{1.31}$$

$$\angle H = \varphi \ . \tag{1.32}$$

Also from the general case of N acquired frames, object wave amplitude E_{obj} as well as optical phase φ originating from the object of interest can be reconstructed.

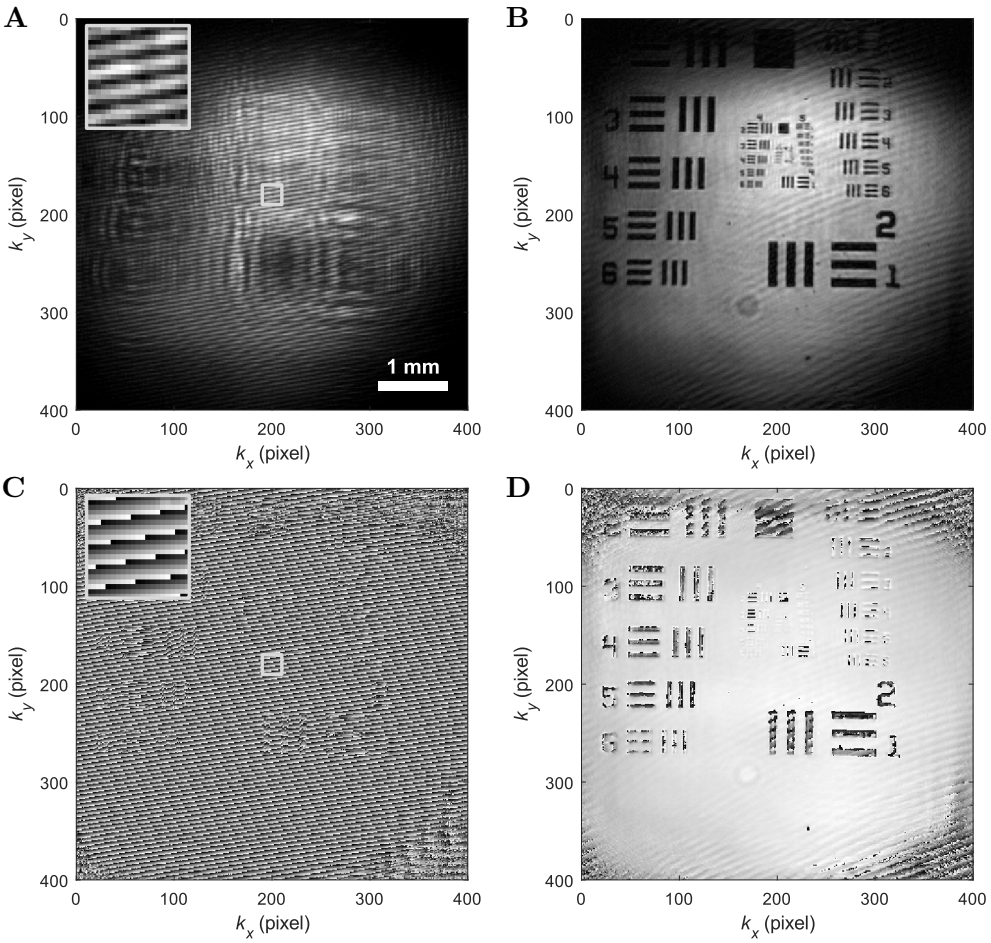

Figure 1.12.: Phase-shifting holography: hologram recording and reconstruction utilizing an off-axis setup. **A** First of four images recorded in a time sequence from a resolution test target. Fringes (inset) originate from the off-axis configuration. **B** Reconstruction from the four consecutive frames yields amplitude, **C** wrapped phase (phase tilt originates from the off-axis angle) and **D** phase after tilt removal. Gray values in phase maps represent the phase space from $-\pi$ (black) to $+\pi$ (white).

1.5. Statistical analysis with linear mixed models

Statistical analysis is used to study an effect observed in an experiment and caused, e.g., by a treatment, as well as to distinguish whether the differences between two experiments are caused by random fluctuations only. To minimize statistical uncertainty, often the experiment is repeated leading to a nested or hierarchical dataset.

In particular, with RT-DC, a sample population is mechanically phenotyped and compared to another condition. In the presented studies, at least three biological replicates are analyzed. This type of multivariate analysis can be performed by linear mixed models (LMMs). In the following, first, LMMs will be introduced and second, compared to the well-established t-test.

Linear mixed models describe a linear relationship of a target variable $\boldsymbol{Y}$ depending on multiple independent variables $\boldsymbol{Z}$

$$\boldsymbol{Y}_i = \boldsymbol{X}_i\boldsymbol{\beta} + \boldsymbol{Z}_i\boldsymbol{b}_i + \boldsymbol{\epsilon}_i \ , \tag{1.33}$$

with a vector $\boldsymbol{Y}_i$ of measurements of the ith subject, covariates matrices $\boldsymbol{X}_i$ and $\boldsymbol{Z}_i$, linear regression coefficients $\boldsymbol{\beta}$ for fixed effects and $\boldsymbol{b}_i$ for subject-specific or random effects, and vector of residuals $\boldsymbol{\epsilon}_i$ [84–86]. The classification into fixed and random effects depends on the experimental design and the research question that is to be answered by the regression model. In particular, for data gathered from RT-DC, the change in target variable between two measurement conditions is considered as fixed effect while changes between biological replicates are represented by a random effect.

In the following, data analysis utilizing LMMs will be compared to the application of a t-test. Since a two-sample t-test compares the means of two sample distributions, it is an appropriate tool for investigating an effect between two conditions. However, for large sample sizes, a t-test yields even for small differences between population means a low p-value of high significance. For high-throughput techniques like RT-DC, datasets can consist of several thousand measurements where a t-test would report a highly significant difference even if the two populations are almost entirely overlapping [87] (Figure 1.13).

To compare the results from a t-test and a LMM, two sets of random numbers $\widetilde{Y}_1$ and $\widetilde{Y}_2$ were generated, both derived from standard normal distribution

$$\begin{aligned} \widetilde{Y}_1 &\sim \mathcal{N}(0,1) \ , \\ \widetilde{Y}_2 &\sim \mathcal{N}(0,1) \ . \end{aligned} \tag{1.34}$$

Each set consists of 1000 samples reflecting a sample count comparable to most of the presented data. Similar to experimental assays, three replicates are generated for both distributions, $\widetilde{Y}_{1,i}$ and $\widetilde{Y}_{2,i}$ with $i = 1, 2, 3$. Each replicate is forced to a mean of zero by subtracting its mean $\overline{\widetilde{Y}}_{1,i}$ or $\overline{\widetilde{Y}}_{2,i}$, which can differ from zero due to the finite

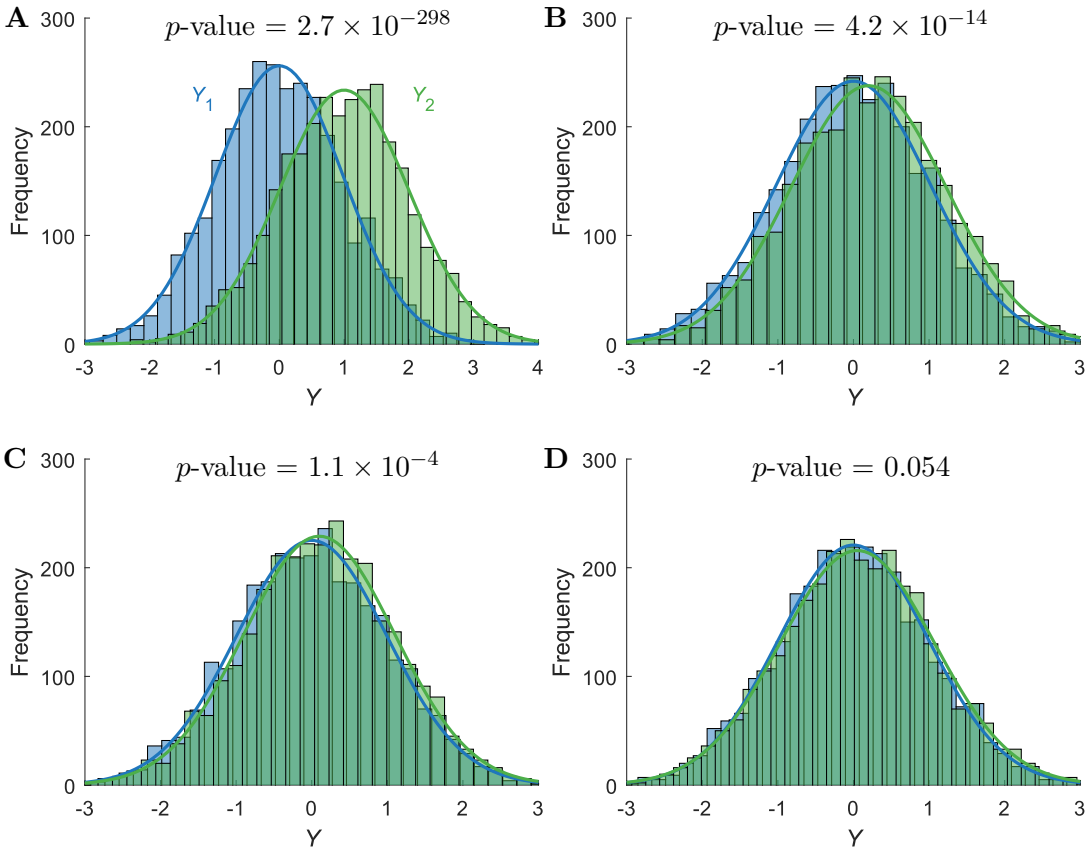

Figure 1.13.: Two-sample t-test applied to two populations Y_1 and Y_2, both derived from the standard normal distribution. The three replicates, consisting of 1000 samples each, are pooled while the distance of the two distributions' means $\Delta\overline{Y} = \overline{Y}_2 - \overline{Y}_1$ is 1 (**A**), 0.2 (**B**), 0.1 (**C**) and 0.05 (**D**). Resulting p-values are indicated above the histograms of both distributions including a Gaussian histogram fit.

number of elements. Then, an arbitrary effect size $\Delta\overline{Y}$ is artificially introduced

$$\begin{aligned} Y_{1,i} &= \widetilde{Y}_{1,i} - \overline{\widetilde{Y}}_{1,i} \ , \\ Y_{2,i} &= \widetilde{Y}_{2,i} - \overline{\widetilde{Y}}_{2,i} + \Delta\overline{Y} \ , \qquad\qquad \Delta\overline{Y} = \overline{Y}_{2,i} - \overline{Y}_{1,i} \ . \end{aligned} \tag{1.35}$$

For analysis by a t-test, the difference between the means of two populations Y_1 and Y_2 is analyzed which are pooled from the replicates $Y_{1,i}$ and $Y_{2,i}$, respectively. Since the t-test is an unbiased test, pooling has no impact on the significance analysis. The test statistic for the two-sample t-test is

$$t = \frac{\overline{Y}_2 - \overline{Y}_1}{\sqrt{\frac{s^2_{Y_1}}{N_{Y_1}} + \frac{s^2_{Y_2}}{N_{Y_2}}}} \ , \tag{1.36}$$

with empirical standard derivation s and sample count N. Since sample counts of both distributions are equal, $N = N_{Y_1} = N_{Y_2}$, their difference in means is the effect size, $\Delta\overline{Y} = \overline{Y}_2 - \overline{Y}_1$, and standard derivations are similar, $s_Y = s_{Y_1} \approx s_{Y_2}$, the test statistic simplifies to

$$t = \frac{\sqrt{N}}{\sqrt{2}s_Y}\Delta\overline{Y} \ . \tag{1.37}$$

According to the exemplary parameters, there are $N_{\text{rep}} = 3$ repetitions with $N_{\text{samples}} = 1000$ samples each, leading to a pooled sample count of $N = N_{\text{rep}}N_{\text{samples}} = 3000$. For $2(N-1) = 5998$ degrees of freedom and a confidence level of 95 %, the (two-sided) Student's t-distribution yields $t \approx 1.96$. If the empirical standard deviation is $s_Y \approx 1$ (standard normal distribution), the effect size has to be at least $\Delta\overline{Y} \approx 0.05$ for being significant (Figure 1.13D). For larger effect sizes, $\Delta\overline{Y} \geq 0.05$, a t-test yields very low p-values since the high number of samples directly enters into the test statistic (Equation 1.37 and Figure 1.13).

In contrast to a t-test, LMMs offer the possibility to incorporate random effects, and hence, the replicates $Y_{1,i}$ and $Y_{2,i}$ derived from the standard normal distribution are not pooled, but their inter-group difference is considered as a random effect. While no differences exist in this simulation study since the means are equal within a group (Equation 1.35), in experimental assays, day-to-day differences or differences between biological or technical replicates are usually considered as random effects.

Statistical analysis based on LMMs is done in R [88] and is performed the exact same way as for experimental data. The datasets consist of three paired replicates for both a control and a treatment condition, which are distinguished by a dummy coded variable "condition"

$$\text{condition} = \begin{cases} 0, & \text{for control group} \\ 1, & \text{for treatment group} \end{cases} \ . \tag{1.38}$$

First, a model is fitted that does not include a fixed effect and consists only of random effects for variances between the biological replicates and between treatment and control group. This model represents the null hypothesis (derived from Equation 1.33)

$$\text{H}_0\text{:} \quad \boldsymbol{Y}_i \sim \beta_0 + \boldsymbol{b}_{0,i} + \boldsymbol{b}_{1,i} \cdot \text{condition} + \boldsymbol{\epsilon}_i \ , \tag{1.39}$$

with replicate index i. A second model is fitted incorporating a fixed effect for the treatment effect

$$\text{H}_1\text{:} \quad \boldsymbol{Y}_i \sim \beta_0 + \beta_1 \cdot \text{condition} + \boldsymbol{b}_{0,i} + \boldsymbol{b}_{1,i} \cdot \text{condition} + \boldsymbol{\epsilon}_i \ , \tag{1.40}$$

representing the alternative hypothesis, with linear regression coefficients $\boldsymbol{\beta} = [\beta_0, \beta_1]^{\text{T}}$ for fixed effects and $\boldsymbol{b}_i = [\boldsymbol{b}_{0,i}, \boldsymbol{b}_{1,i}]^{\text{T}}$ for random effects. Under the hypothesis H_0, β_0 is the grand mean of the entire sample population while under H_1, β_0 is the mean of the control group and β_1 the difference to that of the treatment group.

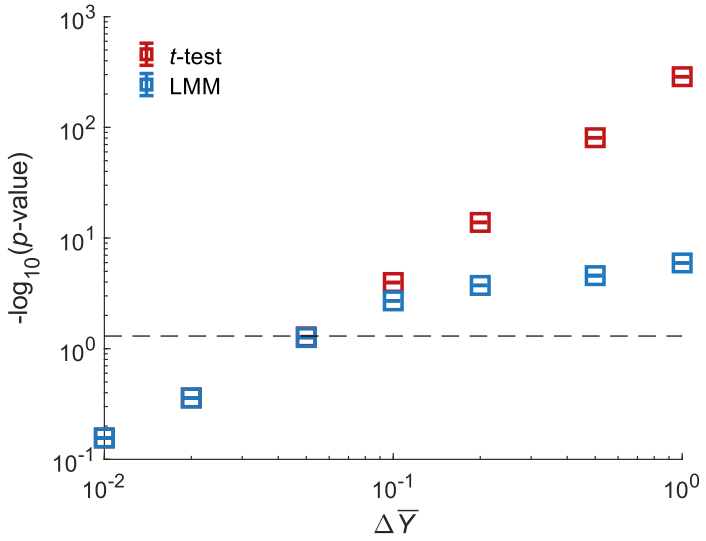

Figure 1.14.: Comparison of p-values from a t-test (red) versus analysis by linear mixed models (LMM) (blue). Three replicates of two populations, $Y_{1,i}$ and $Y_{2,i}$ with $i = 1, 2, 3$, derived from the standard normal distribution, each consisting of 1000 samples, with a distance of their means $\Delta\overline{Y}$ are statistically analyzed by a t-test and linear mixed models. For the t-test, replicates are pooled. Resulting p-values are reported in dependency of $\Delta\overline{Y}$ while the horizontal dashed line indicates $p = 0.05$, i.e., data points below the line are considered non-significant while conditions above are. Simulations were repeated ten times for each parameter condition and their mean is presented while error bars represent the standard error of the mean (SEM).

For both LMMs, the function *lmer* from the package *lme4* [89] is used[2]. From a subsequent likelihood ratio test, the maximum likelihood estimates are compared utilizing Wilks' theorem [90] and a p-value is derived, implemented in R by using the function *anova* from the package *stats* [91].

A comparison of p-values calculated from both statistical methods for varying $\Delta\overline{Y}$ can be observed from Figure 1.14. For very small effect sizes, $\Delta\overline{Y} < 0.05$, a t-test and the statistical analysis based on LMMs yield the same non-significant p-value. For effect sizes $\Delta\overline{Y} > 0.05$, the extracted p-values are increasingly differing. While the t-test reports very low p-values already for population mean distances slightly above $\Delta\overline{Y} = 0.05$, LMM-analysis reveals a reduced slope for p-value decrease with increasing $\Delta\overline{Y}$.

In Summary, LMMs are better suited for datasets with large sample counts. In particular, since the analysis by LMMs interprets the variance between experimental replicates as a random effect, it better reflects the ground truth represented by the fixed effect.

[2] Null hypothesis H_0 is implemented as $Y \sim 1 + (1 + \text{treatment} \,|\, \text{replicate})$ while alternative hypothesis H_1 is modeled as $Y \sim 1 + \text{treatment} + (1 + \text{treatment} \,|\, \text{replicate})$, where treatment and replicate indicate the condition.

2. Materials and Methods

Methods applied and developed within this thesis are introduced in the three sections of this chapter. First, two model systems are briefly described: HL60, a human leukemia cell line as well as induced pluripotent stem cells (iPSCs).

In the second part of this chapter, a shape characterization based on a Fourier decomposition into shape modes will be presented, which I developed as a basis for dRT-DC, a technique for viscoelastic analysis of cells in suspension [48] (see Section 3.3).

I will introduce holographic vibration spectroscopy (HVS) in the third section, a novel method which I developed for label-free and non-contact access to viscoelastic material properties of adherent cells and tissues. This project aims to translate the rapid assessment of mechanical properties from cells in suspension as performed by RT-DC and dynamic RT-DC to adherent cells. Taking the human body as an example, renders the importance of a technique for mechanical phenotyping of adherent cells, as the majority of cells occur aggregated into tissues rather than in suspension. While for cells in suspension, methods for mechanical phenotyping are available with measurement rates of up to 1000 cells per second [15], methods for adherent cells or tissues remain at low throughput (cf. Section 1.3.2). Furthermore, tissues need to be labeled by, e.g., magnetic particles [40], beads [68–70] or oil droplets [9, 43]. To overcome these limitations, a label-free optomechanical method is introduced, which is able to characterize tissues at high throughput.

2.1. Cell culture

For the two methods I establish within this thesis, two cell lines were employed. HL60 cells, a suspension cell line was used for three of the four presented papers in this thesis (see Chapter 3). Initial measurements with HVS, the newly developed method for fast access to tissue viscoelastic properties, were performed on iPSCs grown on a surface.

2.1.1. Suspension cells

As a model system for suspension cells, HL60 cells (courtesy of Dan and Ada Olins) were used, a myeloid precursor cell line. Cells were cultured in RPMI-1640 medium (Biowest) with 10 % fetal calf (or bovine) serum (FCS) (Gibco), 1 % penicillin/streptomycin (Biowest) and 2 mM L-Glutamin (Biowest) in a humidified incubator (CB150(E3/B)O, Binder) at 37 °C, 5 % CO_2 and 95 % air. The cells were split approximately every 48 h by centrifugation for 5 minutes at 200 rcf (Allegra X-15R, Beckman Coulter). Cells are re-suspended in cell medium to a concentration of approximately 1.5×10^5 cells per

milliliter while the supernatant is discarded. Experiments were performed during log phase, approximately 36 h after splitting. Cell viability has been assessed to $\approx 95\,\%$ using Trypan Blue and the cells passed a test for Mycoplasma infection (MycoSPY®, Biontex). Cell culture was carried out by Doreen Biedenweg.

2.1.2. Adherent cells

Induced pluripotent stem cells (iPSCs, Thermo Fisher Scientific) were utilized as modeling system for adherent cells. Cells were maintained in complete mTeSR plus medium (StemCell Technologies) in a humidified incubator (CB150(E3/B)O, Binder) at 37 °C, 5 % CO_2 and 95 % air. Six days prior to the analysis, a silver mirror (PF10-03-P01, Thorlabs) was equipped with a culture insert with 4 wells (Cat.No: 80469, Ibidi) and coated with Matrigel (Corning) for one hour at 37 °C. After removing growth medium, iPSCs were washed with phosphate-buffered saline w/o Mg^{2+}/Ca^{2+} (Biowest) and treated with 0.5 mM ethylenediaminetetraacetic acid (EDTA) (Promega) for 5 minutes at 37 °C. After removal, cells were detached by pipetting growth medium supplemented with 1 % Penicillin/Streptomycin (Biowest) and transferred at a 1:6 ratio to two diagonal wells of the previously attached culture insert, while the other two were filled solely with growth medium. On the following day, after three days and on the day of analysis, cell medium was changed. Cell culture was carried out by Dr. Stefanie Spiegler.

2.2. Cell shape characterization

The shape of single cells and tissue plays a crucial role in biology, e.g., in the early stage of development of life, the gastrulation [92, 93]. The shape of a cell is a consequence of complex internal structures and processes as well as external structures, e.g., the extracellular matrix and neighboring cells, mediated by forces [53, 94–97]. Shape changes can also be actively generated, to induce cell movement [98]. From the internal structures, mostly the cytoskeleton consisting of actin filaments, microtubuli, intermediate filaments, cross-linkers, motors, as well as the nucleus are contributing to cell shape [23, 52, 95, 98, 99].

When cells respond to an external physical stress, they adapt their shape. Techniques for assessing cell mechanical properties make use of shape changes and were introduced in Section 1.3. Shape descriptors can be employed to provide an effective quantification of cell shapes and their deformation under stress in 2D [100–103] as well as 3D [102, 104]. The fourth research article submitted with this thesis (Section 3.4) investigates 2D images of suspension cells and focuses on the following shape descriptors: area, normalized front radius, axes ratio, Taylor deformation, principal axes ratio, rescaled circularity, inverse Haralick's circularity, circular variance and inertia ratio.

The deformation of a cell in suspension depends on its hydrodynamic environment which is used for cell mechanical analysis by RT-DC (see Section 1.3.1). While a cell passes the microfluidic constriction in RT-DC, it first elongates to an ellipsoidal shape (Figure 2.1A, top) responding to a peak stress at the inlet originating from an

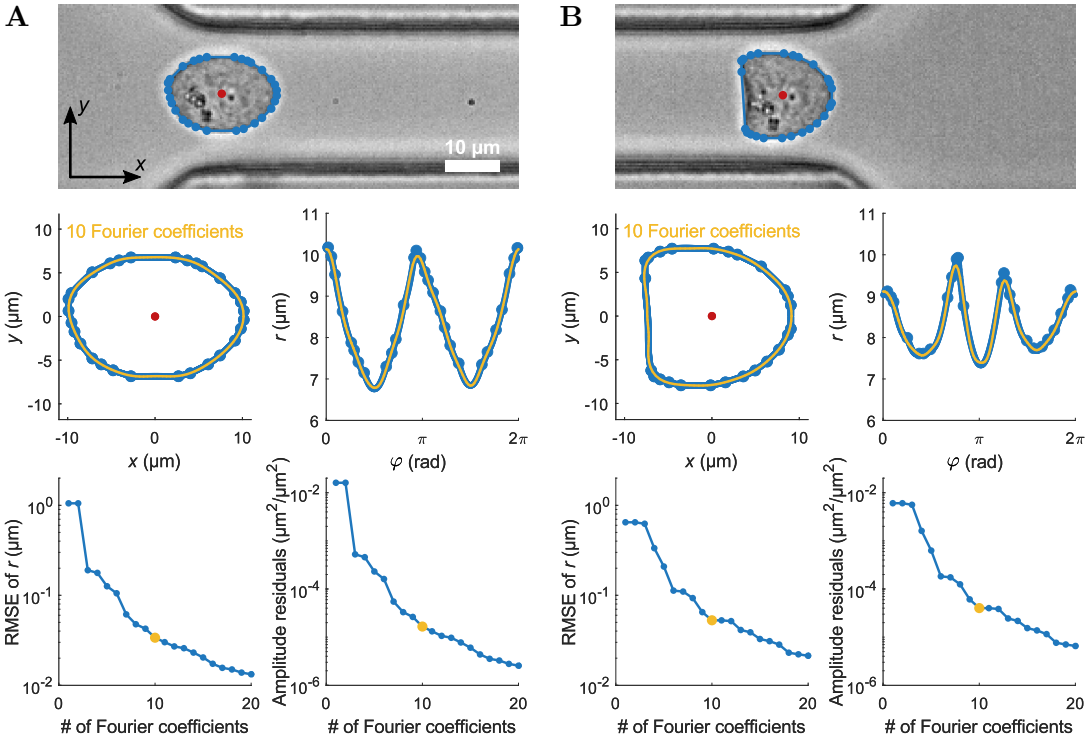

Figure 2.1.: Description of cell contours by ten Fourier shape modes. **A** Raw image with overlaid contour points (blue dots), connecting polygon edges (blue lines), and center of mass (red) for the ellipsoidal shape of a cell approaching the microfluidic channel, i.e., at the inlet (top). Interpolated contour of the cell (blue) and shape estimate from the first 10 Fourier coefficients (yellow) in a Cartesian (center left) and radial representation (center right). Two error measures are presented for approximating the contour by 1 to 20 Fourier coefficient pairs (a_k, b_k) (bottom). Root-mean-square error (RMSE) is calculated for 500 points equidistantly sampled in radial phi-space (bottom left). Amplitude residuals are calculated from the Parseval's theorem (see text). Residuals of squared amplitudes included in the approximation compared to all squared amplitudes are shown (bottom right). **B** Raw cell image of a cell with bullet-like shape close to channel outlet (top), shape representation for estimation by 10 Fourier components (center) and error analysis for shape estimation by 1 to 20 shape modes (bottom). Analysis was carried out as in (A).

acceleration into the channel and second, reveals a bullet-like shape (Figure 2.1B, top) in response to a stress of shear and normal forces, which are constant over the length of the channel (see Section 3.3). In my work, I introduced a method which is able to disentangle the two shape responses, based on a Fourier decomposition and subsequent shape reconstruction [48] (see Section 3.3).

Decomposition of cellular shapes utilizing a Fourier transformation has already been performed for a morphological analysis of living matter [98, 101, 105]. For example, an elliptical Fourier transformation was used for cell shape description more than thirty years ago [106].

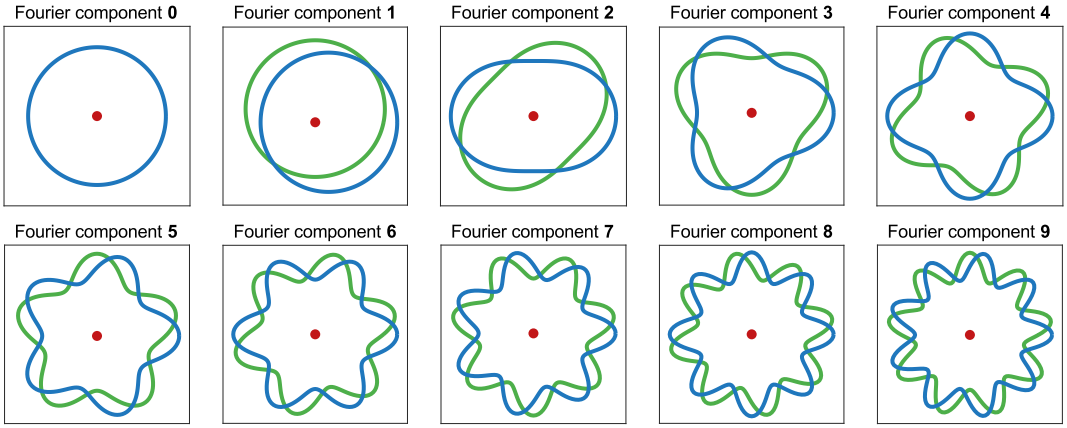

Figure 2.2.: First ten Fourier shape modes. Fourier components a_k (blue) and b_k (green) for $k = 0, 1, ..., 9$ for a radial function $r(\varphi)$. For improved visibility, an amplitude of Fourier coefficient a_0 is added to the components 1 to 9.

Here, the analysis is extended to cells in flow, where a shape reconstruction from two subsets of Fourier components could be linked to the two stress distributions present in a microfluidic channel. Cell shapes are extracted by a contour finding algorithm analyzing brightfield images of cells passing the constriction [24, 48] (Figure 2.1A and B, top). Cell contours, captured in Cartesian coordinates x and y with x pointing in the direction of flow (Figure 2.1A and B, center left), are transformed into polar coordinates represented by radius r over angle φ (Figure 2.1A and B, center right). To ensure that the polygon edges are reproduced in the radial representation, the cell contour polygon is interpolated with 500 points, equidistantly sampled in φ-space, before transforming into polar coordinates. Next, the radius function $r(\varphi)$ of the cell contour is Fourier transformed, i.e., cell shapes are decomposed into a set of coefficients corresponding to amplitudes of shape modes with different radial frequencies (Figure 2.2). Since the first (i.e., lower) Fourier coefficients carry most of the shape information, the radius function $r(\varphi)$ is approximated by a finite Fourier series with $k_{\max} + 1$ elements

$$r(\varphi) \simeq \frac{a_0}{2} + \sum_{k=1}^{k_{\max}} \Big(a_k \cos(k\varphi) + b_k \sin(k\varphi) \Big) \ , \tag{2.1}$$

with Fourier coefficients a_k and b_k being amplitudes of radial cosine and sine functions

$$a_k = \frac{1}{\pi} \int_0^{2\pi} r(\varphi) \cdot \cos(k\varphi) \mathrm{d}\varphi \ , \qquad \text{for} \quad k \geq 0 \ , \tag{2.2}$$

$$b_k = \frac{1}{\pi} \int_0^{2\pi} r(\varphi) \cdot \sin(k\varphi) \mathrm{d}\varphi \ , \qquad \text{for} \quad k \geq 1 \ . \tag{2.3}$$

Since a_k and b_k are amplitudes of an orthogonal set of functions, a phase shift of $90°/k$ or $\pi/(2k)$ can be observed between these coefficients in a reconstruction from Equation 2.1 (Figure 2.2).

Because the angle-dependent contour radius is derived from pixel values it is a discrete function $r_i(\varphi_i)$ and consequently, the integrals can be simplified to sums

$$a_k = \frac{1}{\pi}\sum_{i=0}^{N} r_i(\varphi_i)\cdot\cos(k\varphi_i)\cdot\Delta\varphi \ , \qquad \text{for} \quad k \geq 0 \ , \tag{2.4}$$

$$b_k = \frac{1}{\pi}\sum_{i=0}^{N} r_i(\varphi_i)\cdot\sin(k\varphi_i)\cdot\Delta\varphi \ , \qquad \text{for} \quad k \geq 1 \ , \tag{2.5}$$

with $N = 500$ points and $\Delta\varphi = 2\pi/(N+1)$.

In order to assess the precision of the shape estimate represented by the first $k_{\max}+1$ Fourier coefficients, two quality criteria are calculated for 1 to 20 Fourier coefficient pairs (a_k, b_k) (Figure 2.1A and B, bottom). First, the Root-mean-square error (RMSE) between the interpolated contour and the contour reconstructed from the first $k_{\max}+1$ Fourier coefficients is calculated (Figure 2.1A and B, bottom left). Second, the Fourier amplitude residuals are estimated. The quadratic sum of all Fourier coefficients can be calculated from Parseval's theorem [107]

$$\frac{a_0^2}{2} + \sum_{k=1}^{\infty}\left(a_k^2 + b_k^2\right) = \frac{1}{\pi}\int_0^{2\pi} r^2(\varphi)\mathrm{d}\varphi \simeq \frac{1}{\pi}\sum_{i=0}^{N} r_i^2(\varphi_i)\cdot\Delta\varphi \ . \tag{2.6}$$

Squared amplitude residuals R_{ampl} are derived by relating the squared amplitudes included in the approximation to the entire sum of squared coefficients (Figure 2.1A and B, bottom right)

$$R_{\mathrm{ampl}} = \frac{\dfrac{a_0^2}{2} + \displaystyle\sum_{k=1}^{k_{\max}}\left(a_k^2 + b_k^2\right)}{\dfrac{1}{\pi}\displaystyle\sum_{i=0}^{N} r_i^2(\varphi_i)\cdot\Delta\varphi} \ . \tag{2.7}$$

For an increasing $k_{\max}$, i.e., a higher number of Fourier coefficients included into contour approximation, the RMSE as well as the amplitude residuals decrease. For $k_{\max} = 9$, i.e., considering the first 10 Fourier coefficients, RMSE is below 60 nm while the amplitude residuals are below $5 \times 10^{-5}\,\mu\mathrm{m}^2/\mu\mathrm{m}^2$. This means that less than $5 \times 10^{-3}\,\%$ of squared amplitudes is contained by Fourier coefficients starting from $k = 10$. In further work presented in this thesis, Fourier decomposition is restricted to the first 10 components in all experiments.

2.3. Holographic vibration spectroscopy

For mechanical phenotyping of cells in suspension, very powerful techniques are available with analysis rates of up to 1000 cells per second [15] (cf. Section 1.3.1). In particular,

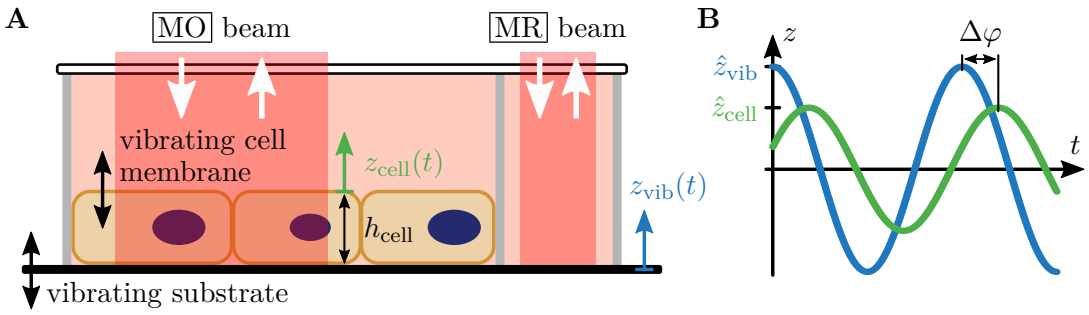

Figure 2.3.: Principle of holographic vibration spectroscopy (HVS). **A** Sketch of the optomechanical setup. Adherent cells attached to a reflective vibrating substrate (deflection $z_{\mathrm{vib}}(t)$) and surrounded by medium respond to the vibration with an oscillation of the upper cell membrane ($z_{\mathrm{cell}}(t)$) summarizing the response of the entire cell. z_{cell} is defined with respect to the vibrating substrate, i.e., to z_{vib}. While one laser beam probes the cells in a chamber including the vibrating cell membrane (moving object beam, MO), a second beam is used to probe the vibrating substrate without cells (moving reference beam, MR). A flat optical access is enabled by a cover slip on top of the chamber. **B** Deflection $z_{\mathrm{vib}}(t)$ and $z_{\mathrm{cell}}(t)$ over time. The viscoelastic properties of cells are thought to induce a phase shift $\Delta\varphi$ and a reduced amplitude $\hat{z}_{\mathrm{cell}}$ of the cell interface response (green) with respect to the exciting agitation (blue) of amplitude $\hat{z}_{\mathrm{vib}}$.

the combination of mechanical cell probing utilizing hydrodynamic deformations with microfluidic platforms enables such high analysis rates. Techniques targeting the mechanical properties of adherent cell, however, reach much lower throughputs and often require for labeling, e.g., by particles integrated into cells and tissue (cf. Section 1.3.2).

Contrary to this imbalance in technical capabilities, most of the cells in our human body are adherent cells aggregated into tissues and organs. Suspension cells, mainly blood cells, form only a small fraction with respect to the overall quantity. This shows the biological importance of cell mechanical tools to analyze adherent cells and reveals the demand for high-throughput and label-free techniques to investigate fundamental principles of living matter.

A recently introduced method uses microcavities to access displacements, forces and stresses of adherent cells at high throughput [108]. Real-time imaging of the interference pattern from the microcavities measured at two wavelengths enables to determine cellular forces which locally alter cavity lengths. The method was used to investigate the beating behavior of cardiomyocytes in response to drug treatment. However, the method is limited to force and stress detection, no material properties of the cells are derived. Besides, sample preparation is sophisticated.

Another possibility is to analyze the response of adherent cells on a vibrating surface. Optical analysis of their oscillation in cell height h_{cell} provides access to the mechanical properties of adherent cells and tissue at non-contact and high throughput (Figure 2.3A). Mechanical vibration excitation of single cells based on a MEMS (micro-electro-

mechanical system) was demonstrated already, and used for mass and growth analysis by evaluating the shift in resonance frequency caused by cells attached to vibrating micro-platforms of 60 μm $\times$ 60 μm size [109]. The ratio of resonance amplitude with an attached cell and without a cell was used to predict the viscoelastic material properties of the cell with the help of an analytical model, a mass-spring-damper system [110] (cf. Section 1.2). However, the mapping between resonance amplitude damping and viscoelastic properties, i.e., the Young's modulus as well as the viscosity, is not unique and only probability maps can be created. Besides resonance frequency and amplitude, the phase shift between the exciting vibration and the induced cellular response was investigated. It could be demonstrated within experiments and simulations that this vibration-induced phase shift (VIPS, $\Delta\varphi$ in Figure 2.3B) depends on cell mechanical properties [111]. The VIPS was analyzed for different mechanical conditions of the attached cells (live, fixed and for various treatments) as well as over a frequency range of vibration from 50 kHz to 130 kHz. The results could be converted to a Young's modulus of an adhered cell with the help of a finite element method (FEM) simulation [72] (cf. paragraph: Single-cell vibrometer with optical readout in Section 1.3.2). As sample preparation is sophisticated for the MEMS, the method is still restricted to single-cell analysis and the readout is performed at a single point using a laser Doppler vibrometer (LDV) while spatial resolution is achieved by scanning the surface, leading to low throughput.

Here, I introduce an imaging vibrometry technique for non-contact viscoelastic phenotyping of adherent cells and tissues at high throughput. Adherent cells are incubated in a chamber surrounded by growth medium while they are attached to a vibrating reflective substrate (Figure 2.3A, see Section 2.1.2). In response to a harmonic vibration $z_{\mathrm{vib}}(t)$ of the substrate with amplitude $\hat{z}_{\mathrm{vib}}$, the cells show an oscillation in height due to their elastic behavior. Time-varying cell height consists of a static contribution h_{cell} (height without vibration excitation) and height fluctuations $z_{\mathrm{cell}}(t)$ of amplitude $\hat{z}_{\mathrm{cell}}$ which summarize the vibrational response of the entire cell and are present at the upper cell membrane (Figure 2.3B). The viscous components of the cell introduce a phase lag $\Delta\varphi$ between excitation and response (VIPS). In my approach, readout of vibrational parameters is done optically, while the detection is spatially resolved over several single cells or a tissue, utilizing a high-speed camera instead of a photo diode. An optical access for detection is provided by an anti-reflex coated cover slip (Figure 2.3A). The cover slip does not cover the cell chamber completely, to allow air exchange and an unconstrained response to the vibration. Two laser beams are used to probe two separated regions within the chamber, one with cells, seen by the MO (moving object) beam carrying the information of the object of interest, and one without cells, probed by the MR (moving reference) beam. For resolving small differences in vibration amplitude and phase, holography was selected as interferometric optical method since it is sensitive to the optical phase containing all information on vibration parameters (see Section 1.4). Ultimately, from a comparison of cell vibration amplitude and phase to those of the exciting vibration, viscoelastic material properties of the adherent cells and tissue can be derived.

2.3.1. Holographic laser Doppler vibrometry on a vibrating surface

First, the method is established on a vibrating surface without cells. The principle bases on an LDV which was used previously for single point measurements as introduced above [72, 109–111]. Within an LDV, a laser beam is divided into a reference and an object beam. While the reference is guided to a photo detector directly, the object beam is shifted in its frequency by an acousto-optic modulator (AOM), directed to the vibrating surface and its backscattered light is overlaid with the reference beam on the photo detector. The AOM uses the acousto-optic effect to induce a frequency shift in light by a sound wave at radio frequency [112, 113]. Caused by the Doppler effect, another frequency shift is introduced in the object beam path which originates from the vibrating surface and is proportional to its velocity over time. From the interference signal of both beams on a point detector, the beat frequency is determined, that is direct proportional to surface' out-of-plane (perpendicular to the surface) velocity at the point of analysis. The frequency shift introduced by the AOM contributes to the beat frequency as well and defines the frequency at rest, i.e., without vibration. A beat frequency above zero at rest enables for a measurement of negative velocities, i.e., when the surface is moving away from the LDV, lowering the frequency reflected by the surface. In summary, in an LDV the intensity measured by the detector is a frequency modulated (FM) signal with a carrier frequency defined by the AOM. From the frequency modulation, the out-of-plane velocity of a surface can be accessed.

In contrast to a standard LDV, the method introduced within this thesis should extend this approach towards a spatially resolved 2D measurement in high throughput and shall provide access to vibration amplitude as well as phase by utilizing holographic laser Doppler vibrometry (HLDV). Therefore, I implemented an optical setup for characterizing an out-of-plane vibration of a reflective surface (Figure 2.4). A fiber-pigtailed linearly polarized laser emitting at wavelength $\lambda_0 = 660\,\mathrm{nm}$ (Cobolt Flamenco 04-51-0100, HÜBNER) is collimated and divided into a reference (R) and an object beam (O) using a polarizing beam splitter (PBS1). The PBS in combination with a $\lambda/2$-retardation plate and a polarizer (P) provides the possibility to adjust the total intensity of both laser beams as well as their intensity ratio. With an AOM (MT80-B30A1,5-VIS, AA OPTO-ELECTRONIC) in each beam path, different frequency shifts around a center frequency of 80 MHz are added to the frequency of light $f_0 = c/\lambda_0$ in the AOMs' first diffraction order, where c is the speed of light. By driving the AOMs with different radio frequencies $\Delta\omega_{\mathrm{ref}}$ and $\Delta\omega_{\mathrm{obj}}$, a controlled mismatch in light frequency between the two beams can be established, which means that the setup is working in the heterodyne regime. After the beams are expanded (BE), the object beam is guided to a vertically vibrating reflective surface and its reflection is superimposed with the reference beam on the detector, a high-speed complementary metal-oxide-semiconductor (CMOS) camera (MC1362, Mikrotron). The polarizing beam splitter (PBS2) in conjunction with a $\lambda/4$-retardation plate in the object beam path is used to collect the entire reflected light from the vibrating surface by rotating its polarization. The linearly polarized light exiting the beam splitter (PBS2) is converted

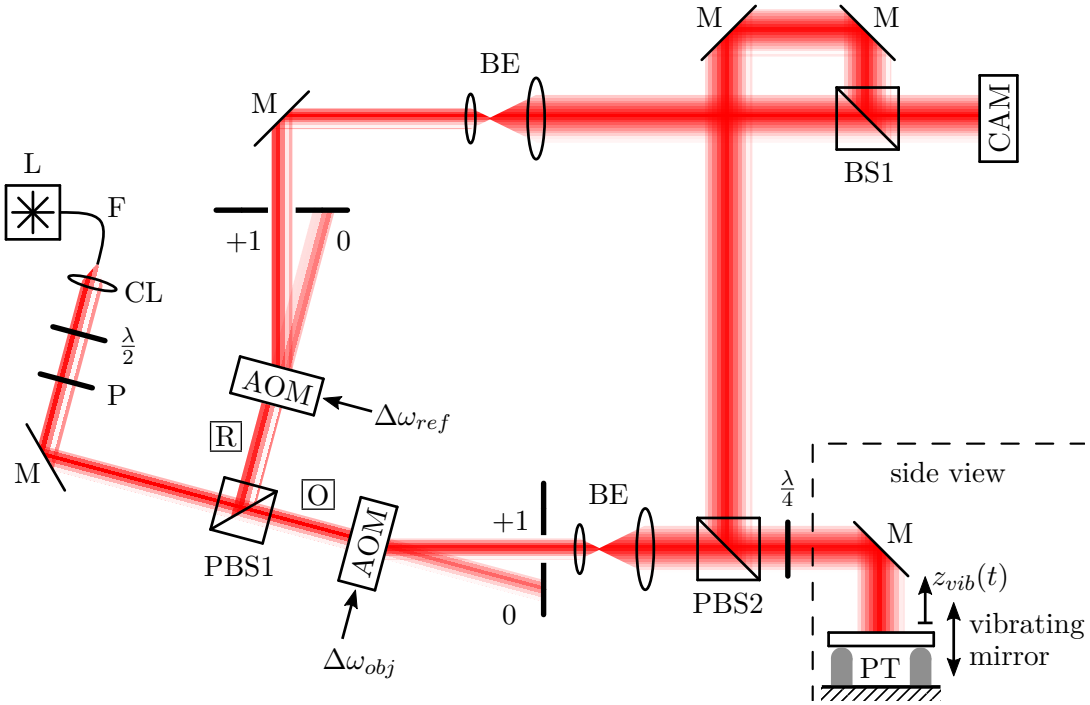

Figure 2.4.: Sketch of the optical setup for 2D analysis of a vibrating surface (top view). L: fiber-pigtailed laser emitting at $\lambda_0 = 660\,\mathrm{nm}$, F: optical fiber, CL: collimating lens, $\frac{\lambda}{2}$ & $\frac{\lambda}{4}$: retardation wave plates, P: polarizer, M: mirror, PBS: polarizing beam splitter, AOM: acousto-optic modulator, BE: beam expander, BS: beam splitter, PT: piezoelectric transducer, CAM: CMOS camera. The vibrating mirror is mounted horizontally. Adapted from [114].

to circular polarization by the $\lambda/4$-plate. The light backscattered from the surface has a circular polarization but with inverted rotation direction and is converted back to a linear polarization but perpendicular to its original polarization when traveling back through the $\lambda/4$-plate and hence, exits PBS2 on the exit perpendicular to the incoming beam. Since off-axis holography enables for separation of the real object image and its conjugate, this technique is selected for detection, and consequently, both beams hit the detector under a small angle (cf. Section 1.4).

A mirror (PF10-03-P01, Thorlabs) was chosen as reflective surface while its vibration is generated by a piezoelectric transducer (PT) consisting of three single-crystal piezoelectric stacks (PQ9FC1, Thorlabs) which are rated for a stationary displacement of $5\,\mu\mathrm{m}$ at $500\,\mathrm{V}$ with no load and a resonance frequency at $85\,\mathrm{kHz}$. The three piezoelectric stacks are covered by ceramic hemispheres to guarantee single contact points to the mirror and avoid shear forces which can damage the crystals. The stacks are arranged in an equilateral triangle on top of a rigid metal plate while the contact points to the mirror are close to its outer edge. Electrically, the three piezos are connected in parallel to a power amplifier (MX200, PiezoDrive) with a voltage gain of $20\,\mathrm{V/V}$. The input signal of the driver V_{vib} for the piezoelectric transducer as well as the trigger signal for the camera are synthesized by an arbitrary function generator

(33522B, Keysight), while the harmonic signals for the AOMs are generated by another two-channel function generator (33622A, Keysight), which are phase-locked using the same reference clock. Generated signals for the AOMs are amplified by one power amplifier each (AMPB-B-30-10.500, AA OPTO-ELECTRONIC).

Interference intensity field on the detector

The camera measures the intensity field of both beams superimposed on the detector. In order to derive spatially resolved vibration amplitude and phase maps (depending on the lateral position on the detector) from these intensity fields, the optical system will be modeled first. For temporal and spatial propagation, the electric field $\mathbf{E}$ of both beams can be described by optical waves. For simplicity, the plane wave equation is selected for description

$$\mathbf{E} = E \cdot \exp(j\omega t - jkz) \ , \tag{2.8}$$

with real amplitude field E, angular frequency ω, time t, wave number $k = 2\pi/\lambda$, with $c = \lambda\omega/(2\pi)$, a spatial coordinate z along direction of propagation and imaginary unit j (cf. Equation 1.13). Although Gaussian beams are used in experiments a simplification to a plane wave is sufficient for modeling. This restriction can be overcome by replacing the real amplitude field E by an amplitude function depending on lateral and axial position within the beam.

All the vibration parameters which will be introduced as well as electric field amplitudes E_{ref} and E_{obj} of the reference and object beam, respectively, are dependent on the lateral position (x, y) on the detector as mentioned above. For the sake of simplicity, the parameters are represented without the functional dependency on x and y.

The path length of the reference beam z_{ref}, measured from the point of beam division to the detector, stays constant over time

$$z_{\mathrm{ref}} = z_{\mathrm{ref},0} = const \ . \tag{2.9}$$

In contrast, the path length of the object beam z_{obj} is modulated by the time-dependent deflection $z_{\mathrm{vib}}(t)$ of the reflective surface (Figure 2.4) and can be described as follows

$$z_{\mathrm{vib}} = \hat{z}_{\mathrm{vib}} \cos(\omega_{\mathrm{vib}} t - \varphi_{\mathrm{vib}}) \tag{2.10}$$

$$\begin{aligned} z_{\mathrm{obj}} &= z_{\mathrm{obj},0} - 2z_{\mathrm{vib}} \\ &= z_{\mathrm{obj},0} - 2\hat{z}_{\mathrm{vib}} \cos(\omega_{\mathrm{vib}} t - \varphi_{\mathrm{vib}}) \ , \end{aligned} \tag{2.11}$$

where $z_{\mathrm{obj},0}$ indicates the propagation distance constant over time which is shortened by twice (due to reflection) the deflection of the harmonically oscillating surface with vibration amplitude $\hat{z}_{\mathrm{vib}}$, an angular frequency ω_{vib}, and with phase angle φ_{vib}. Please note that the motion of $z_{\mathrm{vib}}(t)$ is counted positive towards the incoming beam (see Figure 2.4).

For light propagating in a medium, the optical path length has to be considered which is the product of the geometrical path length and the refractive index of the medium. Here, the beams are propagating in air with a refractive index of $n_{\text{air}} = 1.000\,292$ under normal conditions, which is approximated to 1 and neglected in the following derivations.

The two AOMs introduce an angular frequency shift $\Delta\omega_{\text{ref}}$ and $\Delta\omega_{\text{obj}}$ with respect to laser light frequency $\omega_0 = 2\pi f_0$ in the reference and object beam path, respectively

$$\begin{aligned} \omega_{\text{ref}} &= \omega_0 + \Delta\omega_{\text{ref}} \\ \omega_{\text{obj}} &= \omega_0 + \Delta\omega_{\text{obj}} \ . \end{aligned} \tag{2.12}$$

With the electric field amplitudes E_{ref} and E_{obj}, the path lengths z_{ref} and z_{obj} (Equations 2.9 and 2.11) as well as the two optical frequencies ω_{ref} and ω_{obj} (Equation 2.12) in the heterodyne setup, the electric fields of both beams read (Equation 2.8)

$$\begin{aligned} \mathbf{E}_{\text{ref}} &= E_{\text{ref}} \cdot \exp(j\omega_{\text{ref}} t - jkz_{\text{ref},0}) \\ \mathbf{E}_{\text{obj}} &= E_{\text{obj}} \cdot \exp\Big(j\omega_{\text{obj}} t - jkz_{\text{obj},0} + j\Phi_{\text{vib}} \cos(\omega_{\text{vib}} t - \varphi_{\text{vib}})\Big) \ , \end{aligned} \tag{2.13}$$

$$\text{with } \Phi_{\text{vib}} = 2k\hat{z}_{\text{vib}} = 4\pi \frac{\hat{z}_{\text{vib}}}{\lambda_0} \ . \tag{2.14}$$

While the phase of light in the reference beam is linearly progressing over time with angular frequency ω_{ref}, object beam's phase increases with ω_{obj}. Additionally, it is harmonically modulated with an amplitude of phase modulation Φ_{vib} that is proportional to vibration amplitude $\hat{z}_{\text{vib}}$.

Of note, for the calculation of Φ_{vib}, the laser wavelength λ_0 is used although wavelength is altered by approximately the center frequency f_{AOM} of the AOMs. However, the difference between laser wavelength and the modified wavelength λ can be neglected according to

$$\lambda = \frac{c}{\frac{c}{\lambda_0} + f_{\text{AOM}}} = 660\,\text{nm} - 0.1\,\text{pm} \approx \lambda_0 \ , \tag{2.15}$$

with $\lambda_0 = 660\,\text{nm}$ and $f_{\text{AOM}} = 80\,\text{MHz}$.

Interfering the electrical fields of both beams (Equation 2.13) on the detector, yields an intensity I according to Equation 1.15 and utilizing the trigonometric identity $\cos(\alpha) \equiv \frac{1}{2}\Big(\exp(j\alpha) + \exp(-j\alpha)\Big)$

$$\begin{aligned} \frac{I}{\epsilon c} = E_{\text{ref}}^2 + E_{\text{obj}}^2 + 2E_{\text{ref}}E_{\text{obj}} \cos\Big((\omega_{\text{ref}} - \omega_{\text{obj}})t - kz_{\text{ref},0} + kz_{\text{obj},0} \\ - \Phi_{\text{vib}} \cos(\omega_{\text{vib}} t - \varphi_{\text{vib}})\Big) \ . \end{aligned} \tag{2.16}$$

The constant products of geometrical path length and the wave number $-kz_{\text{ref},0}$ and $kz_{\text{obj},0}$ can be summarized into a time-independent phase φ_{const}, leading to

$$\frac{I}{\epsilon c} = E_{\text{ref}}^2 + E_{\text{obj}}^2 + 2E_{\text{ref}}E_{\text{obj}} \cos\Big((\omega_{\text{ref}} - \omega_{\text{obj}})t + \varphi_{\text{const}} - \Phi_{\text{vib}} \cos(\omega_{\text{vib}} t - \varphi_{\text{vib}})\Big) \ . \tag{2.17}$$

Since vibration parameters $\hat{z}_{\text{vib}}$ and φ_{vib}, the constant phase φ_{const} as well as electric field amplitudes E_{ref} and E_{obj} are dependent on the lateral position (x, y) on the detector, I is a representation of the intensity measured at each single pixel of the camera.

Frequency-domain representation of the intensity field on the detector

The frequency of light in the object beam path is shifted by the vibration frequency due to the Doppler effect. As introduced above, LDVs are based on that frequency shift. However, light backscattered by a harmonically vibrating surface does not only contain a frequency shift by that of the vibration but also higher orders. To get the complete frequency response, the time-dependent intensity signal can be translated into a frequency-domain representation utilizing the Jacobi-Anger expansion as proposed earlier [79]

$$\exp(j\Phi\cos\theta) \equiv \sum_{m=-\infty}^{\infty} j^m J_m(\Phi)\exp(jm\theta)\ , \tag{2.18}$$

with $J_m(\Phi)$ being the mth-order Bessel function of the first kind of argument Φ, where $J_{-m}(\Phi) = (-1)^m J_m(\Phi)$, and an angle θ. The electric field $\mathbf{E}_{\text{obj}}$ in the object beam path from Equation 2.13 can be rewritten to

$$\begin{aligned}\mathbf{E}_{\text{obj}} &= E_{\text{obj}}\cdot\exp(j\omega_{\text{obj}}t - jkz_{\text{obj},0})\exp\Big(j\Phi_{\text{vib}}\cos(\omega_{\text{vib}}t-\varphi_{\text{vib}})\Big) \\ &= E_{\text{obj}}\cdot\exp(j\omega_{\text{obj}}t - jkz_{\text{obj},0})\sum_{m=-\infty}^{\infty} J_m(\Phi_{\text{vib}})\exp\left(jm\left(\omega_{\text{vib}}t-\varphi_{\text{vib}}+\frac{\pi}{2}\right)\right)\ ,\end{aligned} \tag{2.19}$$

utilizing the identity $j^m \equiv \exp(jm\frac{\pi}{2})$. Depending on the amplitude of phase modulation Φ_{vib}, frequency components $m\cdot\omega_{\text{vib}}$ are contributing to the backscattered electric field with amplitudes defined by the Bessel functions $J_m(\Phi_{\text{vib}})$. With the electric field of the reference beam path $\mathbf{E}_{\text{ref}}$ from Equation 2.13, the intensity field I present on the detector can be described by

$$\begin{aligned}\frac{I}{\epsilon c} = E_{\text{ref}}^2 + E_{\text{obj}}^2 + E_{\text{ref}}E_{\text{obj}}\cdot\Bigg[& \\ \exp\Big(j(\omega_{\text{ref}}-\omega_{\text{obj}})t + j\varphi_{\text{const}}\Big)\sum_{m=-\infty}^{\infty} J_m(\Phi_{\text{vib}})\exp\left(-jm\left(\omega_{\text{vib}}t-\varphi_{\text{vib}}+\frac{\pi}{2}\right)\right) + & \\ \exp\Big(-j(\omega_{\text{ref}}-\omega_{\text{obj}})t - j\varphi_{\text{const}}\Big)\sum_{m=-\infty}^{\infty} J_m(\Phi_{\text{vib}})\exp\left(jm\left(\omega_{\text{vib}}t-\varphi_{\text{vib}}+\frac{\pi}{2}\right)\right)\Bigg]\ , &\end{aligned} \tag{2.20}$$

with $\varphi_{\text{const}} = -kz_{\text{ref},0} + kz_{\text{obj},0}$. Sums' prefactors are not dependent on m, but can be integrated into the summands, leading to

$$\frac{I}{\epsilon c} = E_{\text{ref}}^2 + E_{\text{obj}}^2 + E_{\text{ref}}E_{\text{obj}} \cdot \Bigg[\sum_{m=-\infty}^{\infty} J_m(\Phi_{\text{vib}}) \exp\Bigg(j(\omega_{\text{ref}} - \omega_{\text{obj}})t + j\varphi_{\text{const}} - jm\Big(\omega_{\text{vib}}t - \varphi_{\text{vib}} + \frac{\pi}{2}\Big)\Bigg) + \sum_{m=-\infty}^{\infty} J_m(\Phi_{\text{vib}}) \exp\Bigg(-j(\omega_{\text{ref}} - \omega_{\text{obj}})t - j\varphi_{\text{const}} + jm\Big(\omega_{\text{vib}}t - \varphi_{\text{vib}} + \frac{\pi}{2}\Big)\Bigg)\Bigg] . \tag{2.21}$$

Subsequently, the two sums can be combined into one.

$$\frac{I}{\epsilon c} = E_{\text{ref}}^2 + E_{\text{obj}}^2 + E_{\text{ref}}E_{\text{obj}} \sum_{m=-\infty}^{\infty} J_m(\Phi_{\text{vib}}) \cdot \Bigg[\exp\Bigg(j(\omega_{\text{ref}} - \omega_{\text{obj}})t + j\varphi_{\text{const}} - jm\Big(\omega_{\text{vib}}t - \varphi_{\text{vib}} + \frac{\pi}{2}\Big)\Bigg) + \exp\Bigg(-j(\omega_{\text{ref}} - \omega_{\text{obj}})t - j\varphi_{\text{const}} + jm\Big(\omega_{\text{vib}}t - \varphi_{\text{vib}} + \frac{\pi}{2}\Big)\Bigg)\Bigg] \tag{2.22}$$

The two exponential functions within the sum represent a complex number and its complex conjugate. Utilizing the trigonometric identity $\cos(\alpha) \equiv \frac{1}{2}\Big(\exp(j\alpha) + \exp(-j\alpha)\Big)$ leads to the frequency-domain representation of I

$$\begin{aligned}\frac{I}{\epsilon c} &= E_{\text{ref}}^2 + E_{\text{obj}}^2 + 2E_{\text{ref}}E_{\text{obj}} \sum_{m=-\infty}^{\infty} J_m(\Phi_{\text{vib}}) \cos\Bigg((\omega_{\text{ref}} - \omega_{\text{obj}})t + \varphi_{\text{const}} - m\Big(\omega_{\text{vib}}t - \varphi_{\text{vib}} + \frac{\pi}{2}\Big)\Bigg) \\ &= E_{\text{ref}}^2 + E_{\text{obj}}^2 + 2E_{\text{ref}}E_{\text{obj}} \sum_{m=-\infty}^{\infty} J_m(\Phi_{\text{vib}}) \cos(\omega t + \varphi) \\ &\text{with } \omega = \omega_{\text{ref}} - \omega_{\text{obj}} - m\omega_{\text{vib}} \text{ and } \varphi = \varphi_{\text{const}} - m\frac{\pi}{2} + m\varphi_{\text{vib}} \ (m \in \mathbb{Z}) ,\end{aligned} \tag{2.23}$$

which is equivalent to the time-domain representation in Equation 2.17, but reveals its components of the frequency spectrum.

The intensity I on the detector consists of a constant contribution (DC, $f = 0$) of $\epsilon c(E_{\text{ref}}^2 + E_{\text{obj}}^2)$ and a frequency comb (Equation 2.23). Discrete angular frequency lines of the frequency comb can be found at ω and have a magnitude of $2\epsilon c|E_{\text{ref}}E_{\text{obj}}J_m(\Phi_{\text{vib}})|$ (Figure 2.5A). The sideband ($m \neq 0$) intensity magnitudes are increasing with Φ_{vib}, i.e., with increasing vibration amplitudes $\hat{z}_{\text{vib}}$ (Equation 2.14), while the intensity amplitude at the baseband ($m = 0$), i.e., without a shift in frequency from the

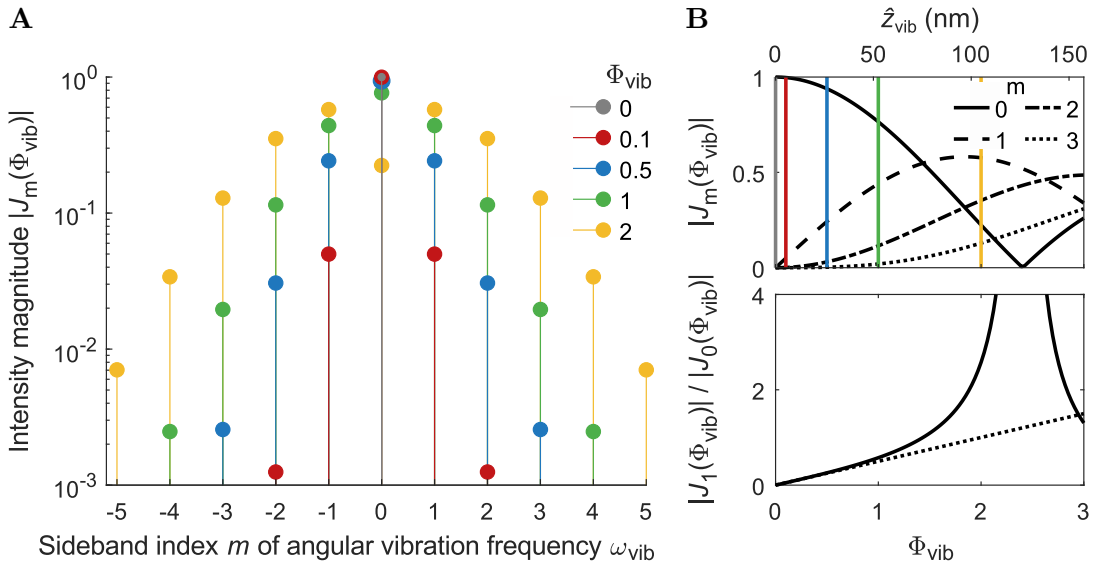

Figure 2.5.: Simulation of Bessel mode magnitude on the detector. **A** Intensity magnitude $|J_m(\Phi_{vib})|$ for frequency components $m \cdot \omega_{vib}$ with $m \in \mathbb{Z}$ in Equation 2.23 for an amplitude of phase modulation Φ_{vib} of 0 (gray), 0.1 (red), 0.5 (blue), 1 (green) and 2 (yellow), equivalent to vibration amplitudes $\hat{z}_{vib}$ of 0 nm, 5.3 nm, 26.3 nm, 52.5 nm and 105.0 nm, respectively, for $\lambda_0 = 660\,\text{nm}$ (Equation 2.14). **B** Bessel function magnitude $|J_m(\Phi_{vib})|$ for the modes $m = 0, ..., 3$ and $\Phi_{vib} \in [0, 3]$ (top). Equivalent vibration amplitudes $\hat{z}_{vib}$ are shown for $\lambda_0 = 660\,\text{nm}$. Levels of Φ_{vib} in (A) are indicated by vertical lines. Ratio of $|J_1(\Phi_{vib})|$ and $|J_0(\Phi_{vib})|$ which is used for reconstruction of Φ_{vib} and $\hat{z}_{vib}$ from intensity measurements (bottom). For small Φ_{vib}, the ratio can be approximated by $\frac{1}{2}\Phi_{vib}$ (dotted line).

vibration, is decreasing (Figure 2.5A and B, top). This means that the optical power is transferred from the baseband into higher-order sidebands for increasing amplitude of phase modulation Φ_{vib}. Since the vibration amplitude $\hat{z}_{vib}$ is encoded via Φ_{vib} in the intensity of all bands, it can be accessed by measuring the intensity magnitude of an arbitrary spectral band on the detector. Previously, measurements on vibrating surfaces were performed based on the intensity of a single band [115, 116]. However, a measurement of intensity requires for an intensity reference and can be easily distorted, e.g., by varying ambient light. A reference-free and more robust approach is achieved by a ratiometric intensity measure [79, 117, 118]. From the intensity ratio of the first sideband $|J_1(\Phi_{vib})|$ and the baseband $|J_0(\Phi_{vib})|$, Φ_{vib} and the vibration amplitude $\hat{z}_{vib}$ can be derived (Figure 2.5B, bottom). Besides the baseband, the first sideband is selected since it reveals the steepest gradient over Φ_{vib} and has a higher magnitude than higher bands ($m \geq 2$) for low Φ_{vib} (Figure 2.5B, top). Selecting those two bands yields the highest signal-to-noise ratio (SNR) available for low vibration amplitudes. From previous work, vibration amplitudes in the lower nanometer range are expected [72, 111].

Since $|J_0(\Phi_{\text{vib}})|$ is exclusively unique for $\Phi_{\text{vib}} \lessapprox 2.4$ and is zero at $\Phi_{\text{vib}} \approx 2.4$ (Figure 2.5B, top), the ratiometric method is limited to $\Phi_{\text{vib}} < 2.4$ because the ratio $|J_1(\Phi_{\text{vib}})|/|J_0(\Phi_{\text{vib}})|$ converges to infinity for $\Phi_{\text{vib}} \approx 2.4$ (Figure 2.5B, bottom). For $\lambda_0 = 660\,\text{nm}$, vibration amplitudes of up to $\hat{z}_{\text{vib, max}} = 126\,\text{nm}$ can therefore be reconstructed.

Sampled intensity on the detector

In an experiment using HLDV on a vibrating mirror, I could reproduce the developed theory and extract vibration amplitudes in the lower nanometer range (Figure 2.6). Sampling the interference intensity I from Equation 2.23 (or Equation 2.17) with the camera at a sampling rate f_{cam}, discretizes the signal over time t. Sampled intensity I_i recorded from one pixel of the camera is shown for increasing driving voltages V_{vib} (measured before the piezo driver) of the piezoelectric transducer (Figure 2.6A). Setting the driving voltage to $V_{\text{vib}} = 0$, leads to no induced vibration ($\Phi_{\text{vib}} = 0$) and results in a pure harmonic signal with an angular frequency of $\omega = \omega_{\text{ref}} - \omega_{\text{obj}}$ (Figure 2.6A, red). This can be seen from Equation 2.17 by setting $\Phi_{\text{vib}} = 0$, or from Equation 2.23, where $J_m(0)$ is zero for all m, except for $m = 0$ (cf. Figure 2.5B, top). Only one spectral component ($m = 0$) as well as a DC ($f = 0$) term is present in case of no vibration (Figure 2.6B, red). For increasing vibration amplitudes, the intensity signal is increasingly modulated by higher frequency components (Figure 2.6A, blue, green and yellow). All signals can be well described by fits to the time-dependent intensity from Equation 2.17. In agreement to the spectra of bands discussed above (Figure 2.5A), the sampled intensity signals reveal increasing spectral magnitudes of the sidebands ($m \geq 1$) for increasing driving voltages V_{vib} (Figure 2.6B).

The sampled intensity $I_i = I(t_i)$ on the camera in frequency-domain representation (Equation 2.23) at time points $t_i = i/f_{\text{cam}}$ ($i \in \mathbb{N}$) reads

$$\begin{aligned} \frac{I_i}{\epsilon c} = E_{\text{ref}}^2 + E_{\text{obj}}^2 + 2E_{\text{ref}}E_{\text{obj}} \sum_{m=-\infty}^{\infty} J_m(\Phi_{\text{vib}}) \\ \cdot \cos\left(2\pi i \frac{f_{\text{ref}} - f_{\text{obj}} - m f_{\text{vib}}}{f_{\text{cam}}} + \varphi_{\text{const}} - m\frac{\pi}{2} + m\varphi_{\text{vib}}\right) . \end{aligned} \tag{2.24}$$

To optically lock-in to a selected band m_{sel} of vibration frequency f_{vib}, the following constraint for the frequency mismatch between the reference and object beam has to be fulfilled for analysis by phase-shifting holography with N frames (refer to Equation 1.21)

$$f_{\text{ref}} - f_{\text{obj}} = m_{\text{sel}} \cdot f_{\text{vib}} - \frac{f_{\text{cam}}}{N} , \tag{2.25}$$

which can be adjusted utilizing the two AOMs. In contrast to the frequency constraint in Equation 1.21 introduced for phase-shifting holography (Section 1.4.3) where the technique was used for imaging of static objects, here, the object of interest is vibrating

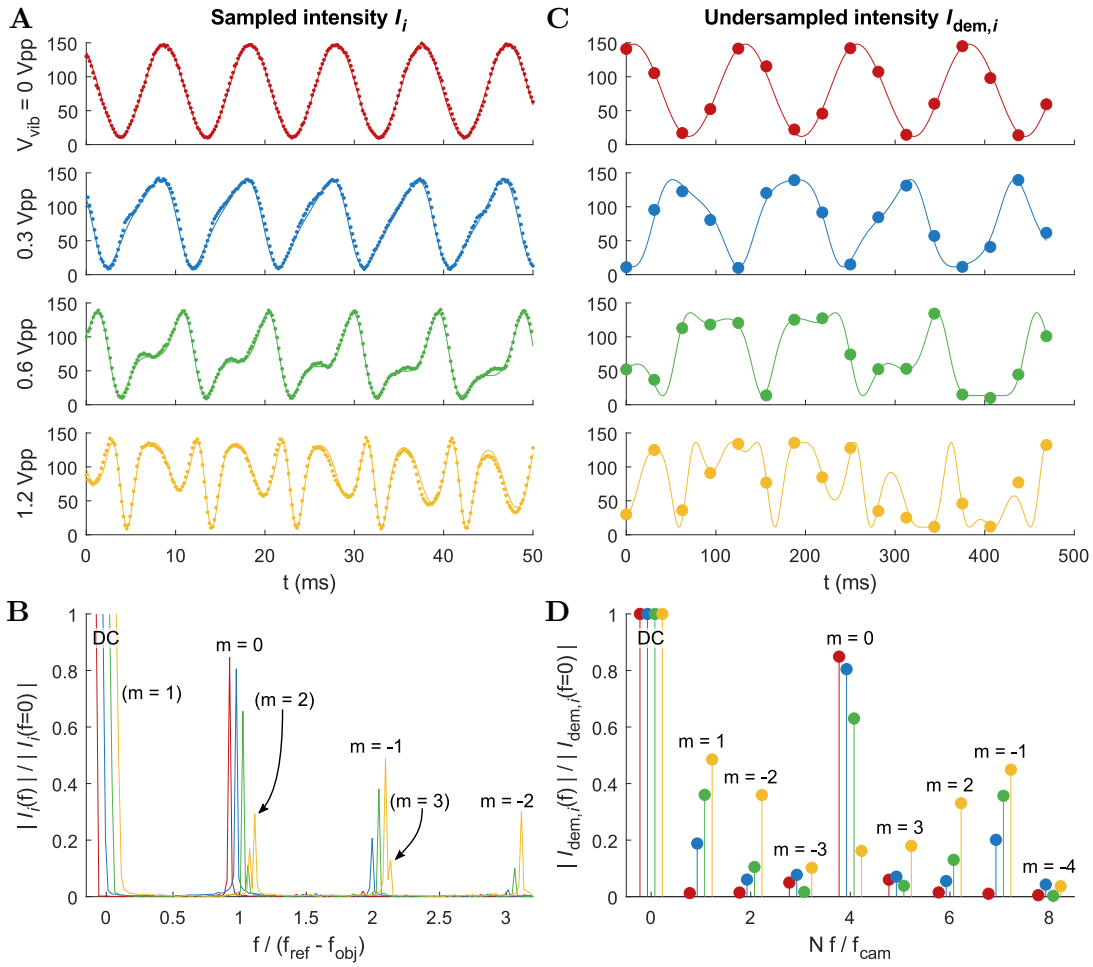

Figure 2.6.: Experiment using holographic laser Doppler vibrometry (HLDV) on a vibrating mirror. **A** Sampled intensity signal I_i from a mirror vibrating at $f_{\mathrm{vib}} = 264\,\mathrm{Hz}$ sampled with $f_{\mathrm{cam}} = 2.64\,\mathrm{kHz}$ (first 50 ms are shown), observed for 0.5 s with a shutter time of $T_{\mathrm{int}} = 10\,\mu\mathrm{s}$ and $f_{\mathrm{ref}} - f_{\mathrm{obj}} = 262\,\mathrm{Hz}$ at one pixel of the camera for the driving voltages V_{vib} of 0 Vpp (red), 0.3 Vpp (blue), 0.6 Vpp (green) and 1.2 Vpp (yellow) connected to the piezo driver. Data points and fits (lines) to Equations 2.17 are shown. **B** One-sided power spectra of the sampled intensity signals in (A) from all acquired samples, $N = 1320$. Spectrum is normalized to the DC magnitude. Baseband ($m = 0$) and sidebands are referenced by text above, text in brackets indicate bands which are hidden since they are located very close in frequency to another band with higher magnitude (with the exception of $m = 2$ for $V_{\mathrm{vib}} = 1.2\,\mathrm{Vpp}$). For improved visibility, the four spectra are slightly shifted in frequency to have no overlap. **C** Intensity signals from (A) undersampled with $f_{\mathrm{cam}} = 32\,\mathrm{Hz}$ and fits (lines) to the demodulated intensity $I_{\mathrm{dem},i}$ from Equation 2.29. **D** One-sided power spectra similar to (B) of all samples ($N = 16$) from signals in (C). From the demodulated spectrum, amplitudes of phase modulation Φ_{vib} of 0.03, 0.45, 1.00 and 2.06 were reconstructed (see text for details), corresponding to vibration amplitudes $\hat{z}_{\mathrm{vib}}$ of 1.6 nm, 23.9 nm, 52.3 nm and 108.0 nm, respectively.

and the constraint focuses the detection on one arbitrary vibration frequency band m_{sel}. The optical selection is equivalent to a down- or demodulation of the m_{sel}-th band of vibration frequency to the sampling frequency of the camera f_{cam} and allows for optical investigation of one specific vibration band $m_{\mathrm{sel}} \cdot f_{\mathrm{vib}}$.

Incorporating the frequency constraint into Equation 2.24, the sampled intensity I_i reads

$$\frac{I_i}{\epsilon c} = E_{\mathrm{ref}}^2 + E_{\mathrm{obj}}^2 + 2E_{\mathrm{ref}}E_{\mathrm{obj}} \sum_{m=-\infty}^{\infty} J_m(\Phi_{\mathrm{vib}}) \cdot \cos\left(2\pi i(m_{\mathrm{sel}} - m)\frac{f_{\mathrm{vib}}}{f_{\mathrm{cam}}} - \frac{2\pi i}{N} + \varphi_{\mathrm{const}} - m\frac{\pi}{2} + m\varphi_{\mathrm{vib}}\right) . \tag{2.26}$$

Two terms depending on the running image index i are contributing to the cosine argument, representing the time-dependent part in Equation 2.26, i.e., its frequency. While the term $-2\pi i/N$ is related to phase-shifting holography (cf. Equation 1.30), the other term depends on the ratio of vibration frequency and camera's sampling rate $f_{\mathrm{vib}}/f_{\mathrm{cam}}$.

The vibration frequency is expected to be in the range of 100 kHz for a detectable VIPS from the cells [72, 111]. However, sampling rates of the camera are much lower for real-time data transfer to a computer and online frame analysis, they are approximately in the range of 1 kHz to 10 kHz [24, 48]. Hence, $f_{\mathrm{vib}} \gg f_{\mathrm{cam}}$.

In general, for $f_{\mathrm{vib}} > f_{\mathrm{cam}}$, the ratio $f_{\mathrm{vib}}/f_{\mathrm{cam}}$ can be decomposed into an integer e and its fractional part δ

$$\frac{f_{\mathrm{vib}}}{f_{\mathrm{cam}}} = e + \delta \ , \qquad e = \left\lfloor \frac{f_{\mathrm{vib}}}{f_{\mathrm{cam}}} \right\rfloor \in \mathbb{N} \ , \qquad \delta = \frac{f_{\mathrm{vib}}}{f_{\mathrm{cam}}} - e \ , \tag{2.27}$$

with floor function $\lfloor\,\rfloor$. Replacing $f_{\mathrm{vib}}/f_{\mathrm{cam}}$ by $e + \delta$, Equation 2.26 reads

$$\frac{I_i}{\epsilon c} = E_{\mathrm{ref}}^2 + E_{\mathrm{obj}}^2 + 2E_{\mathrm{ref}}E_{\mathrm{obj}} \sum_{m=-\infty}^{\infty} J_m(\Phi_{\mathrm{vib}}) \cdot \cos\left(2\pi ei(m_{\mathrm{sel}} - m) + 2\pi\frac{i}{N}\Big(\delta N(m_{\mathrm{sel}} - m) - 1\Big) + \varphi_{\mathrm{const}} - m\frac{\pi}{2} - m\varphi_{\mathrm{vib}}\right) . \tag{2.28}$$

Since $2\pi ei(m_{\mathrm{sel}} - m)$ is an integer multiple of 2π under all conditions for e, i, m_{sel} and m, this term can be neglected, as it has no impact on the result of the cosine. By removing this high-frequency term (reflected by e, it carries the major part of the vibration frequency), the slowly varying component represented by δ remains, equivalent to a demodulation (by removing the high-frequency carrier) of intensity signal frequencies into the bandwidth of the camera (or low-pass filtering). The demodulated intensity $I_{\mathrm{dem},i}$ is then

$$\frac{I_{\mathrm{dem},i}}{\epsilon c} = E_{\mathrm{ref}}^2 + E_{\mathrm{obj}}^2 + 2E_{\mathrm{ref}}E_{\mathrm{obj}} \sum_{m=-\infty}^{\infty} J_m(\Phi_{\mathrm{vib}}) \cdot \cos\left(2\pi\frac{i}{N}\Big(\delta N(m_{\mathrm{sel}} - m) - 1\Big) + \varphi_{\mathrm{const}} - m\frac{\pi}{2} - m\varphi_{\mathrm{vib}}\right) . \tag{2.29}$$

Because the intensity signal is repetitive, it can be digitized by sampling rates lower than the vibration frequency under certain conditions (as used, e.g., in equivalent-time sampling in digital oscilloscopes).

In an experiment, I could confirm the reconstruction from an undersampled intensity signal (Figure 2.6C). Optically, the sideband $m_{\mathrm{sel}} = +1$ was selected and the intensity of a vibration at $f_{\mathrm{vib}} = 264\,\mathrm{Hz}$ was sampled at $f_{\mathrm{cam}} = 32\,\mathrm{Hz}$ over 0.5 s, i.e., $N = 16$ frames were captured for phase-shifting holographic evaluation. According to Equation 2.25, the frequency difference between reference and object beam path was set to $f_{\mathrm{ref}} - f_{\mathrm{obj}} = 262\,\mathrm{Hz}$ with the AOMs. The experiment was performed for different driving voltages V_{vib}, inducing a vibration of amplitude $\hat{z}_{\mathrm{vib}}$. The fits to acquired data points according to Equation 2.29 (lines in Figure 2.6C) reveal low frequency contributions compared to the intensity signal digitized with sufficiently high sampling rate (Figure 2.6A). This means that it is sufficient, to sample the signal with 16 instead of 1320 points over 0.5 s for representing the slowly varying intensity which contains the vibration parameters of interest, a reduction by a factor of 82.5 in sample size and required sampling rate.

Spectral intensity analysis

The spectrum of the (over-) sampled intensity signal (Equation 2.26) contains a DC term and the following frequency components (depending in sample index i in Equation 2.26)

$$\frac{f}{f_{\mathrm{cam}}} = (m_{\mathrm{sel}} - m)\frac{f_{\mathrm{vib}}}{f_{\mathrm{cam}}} - \frac{1}{N}\ . \tag{2.30}$$

Normalizing the frequency components to the frequency mismatch $f_{\mathrm{ref}} - f_{\mathrm{obj}}$, which is adjusted to approximately $m_{\mathrm{sel}} f_{\mathrm{vib}}$ (Equation 2.25), leads to

$$\frac{f}{f_{\mathrm{ref}} - f_{\mathrm{obj}}} = \frac{(m_{\mathrm{sel}} - m)\frac{f_{\mathrm{vib}}}{f_{\mathrm{cam}}} - \frac{1}{N}}{m_{\mathrm{sel}}\frac{f_{\mathrm{vib}}}{f_{\mathrm{cam}}} - \frac{1}{N}} \approx 1 - \frac{m}{m_{\mathrm{sel}}}\ , \tag{2.31}$$

since $f_{\mathrm{vib}}/f_{\mathrm{cam}} \gg 1/N$, and for $m_{\mathrm{sel}} \neq 0$. For the experimental example of $m_{\mathrm{sel}} = +1$, frequency components $f/(f_{\mathrm{ref}} - f_{\mathrm{obj}})$ can be found approximately at $1 - m$, i.e., at integers (Figure 2.6B). Please note that due to the sampling, frequency components are mirrored at $f = 0$, because a real harmonic signal reveals a positive and negative frequency line, demonstrated by the identity $\cos(\alpha) \equiv \frac{1}{2}\Big(\exp(j\alpha) + \exp(-j\alpha)\Big)$, leading to $f/(f_{\mathrm{ref}} - f_{\mathrm{obj}}) \approx |1 - m|$. Some frequency components cannot be obtained from Figure 2.6B (but are part of the spectrum) because they are located very close to another contribution of higher magnitude (corresponding band index m is shown in brackets). An exception can be observed for high vibration amplitudes (yellow trace)

where the spectral magnitude at $m = 2$ is higher than the one at baseband $m = 0$ (cf. Figure 2.5 for $\Phi_{\mathrm{vib}} = 2$, yellow). Corresponding normalized frequencies $f/(f_{\mathrm{ref}} - f_{\mathrm{obj}})$ are both around 1 but are slightly different and hence, two peaks can be observed (Figure 2.6B).

In the demodulated intensity signal $I_{\mathrm{dem},i}$ (Equation 2.29), frequency components f_{dem} are occurring at (time-dependent part depending on sample index i)

$$N\frac{f_{\mathrm{dem}}}{f_{\mathrm{cam}}} = \delta N(m_{\mathrm{sel}} - m) - 1 \ . \tag{2.32}$$

However, frequency components are mirrored at frequencies $f = 0$ and $f = N/2$ due to sampling at f_{cam} (Nyquist-Shannon sampling theorem). Consequently, a DFT yields the frequency components at

$$\begin{aligned} N\frac{f_{\mathrm{DFT}}}{f_{\mathrm{cam}}} &= \left| \left(N\frac{f_{\mathrm{dem}}}{f_{\mathrm{cam}}} + \frac{N}{2} \right) \% N - \frac{N}{2} \right| \\ &= \left| \left(\delta N(m_{\mathrm{sel}} - m) - 1 + \frac{N}{2} \right) \% N - \frac{N}{2} \right| , \end{aligned} \tag{2.33}$$

with modulo operator %. A complete derivation of the DFT of the intensity signal from Equation 2.29 can be found in Section A.1.1 in the Appendix.

For the experiment, $m_{\mathrm{sel}} = +1$, $N = 16$ and $\delta = \frac{5}{16}$ were selected, leading to the frequency components at (Figure 2.6D)

$$N\frac{f_{\mathrm{DFT}}}{f_{\mathrm{cam}}} = \left| (12 - 5m) \% 16 - 8 \right| \ . \tag{2.34}$$

In Section A.1.2 in the Appendix, I demonstrate that these acquisition parameters are advantageous for spectral analysis and vibration parameter extraction and show, how to select experimental parameters.

Although the sampling rate f_{cam} is reduced by a factor of 82.5 for sampling the demodulated intensity signal, the frequency modes with band index m could be reconstructed and agree well with the spectral response of the (over-) sampled signal (Figure 2.6B and D). However, the parameters for the undersampling have to be carefully selected. Due to the sampling, spectral components are folded into $f_{\mathrm{DFT}}/f_{\mathrm{cam}} \in [0, 1/2]$, as mentioned above. This can lead to overlap and misinterpretation of the bands. If two or more bands are overlapping, no distinct amplitude and phase parameters of the contributing bands can be extracted, which can be seen from the following two-tone signal, to which two harmonic signals with the same frequency ω but different amplitudes (A_1 & A_2) and phase angles (φ_1 & φ_2) are contributing

$$A_1\cos(\omega t-\varphi_1)+A_2\cos(\omega t-\varphi_2)=A\cos(\omega t-\varphi) \tag{2.35}$$
$$\text{with } A=\sqrt{A_1^2+A_2^2+2A_1A_2\cos(\varphi_1-\varphi_2)}\ ,$$
$$\varphi=\arctan\left(\frac{A_1\sin\varphi_1+A_2\sin\varphi_2}{A_1\cos\varphi_1+A_2\cos\varphi_2}\right).$$

From the ensemble amplitude A and phase φ one cannot conclude the amplitudes A_1 and A_2 nor phases φ_1 and φ_2.

Spectral vibration parameter readout

As introduced earlier, from a ratiometric intensity measure of the first sideband $|J_1(\Phi_{\text{vib}})|$ and the baseband $|J_0(\Phi_{\text{vib}})|$, the vibration amplitude $\hat{z}_{\text{vib}}$ can be derived. Hence, it is required to have minimal overlap at bands $m=0$ and $m=+1$ or $m=-1$. Since the signal is not band-limited but consists of an infinite number of bands (Equation 2.29), except for $\hat{z}_{\text{vib}}=0$, no overlap-free configuration can be achieved. However, because the intensity magnitude of bands with higher order ($|m|\geq 2$) decrease drastically with order $|m|$ (Figure 2.5A), there are parameter sets which minimize the impact of overlapping bands. For a more detailed analysis and a table of advantageous acquisition parameters, see Section A.1.2 in the Appendix.

The bands m which are found at frequencies according to Equation 2.33, have a magnitude of $|J_m(\Phi_{\text{vib}})|$ (Equation 2.29). The vibration amplitude $\hat{z}_{\text{vib}}$ can be calculated from these intensity magnitudes of the power spectrum $I_{\text{dem},i}(f)$ at baseband ($m=0$) and first sideband ($m=\pm1$)

$$\frac{|I_{\text{dem},i}(f)|_{m=\pm1}}{|I_{\text{dem},i}(f)|_{m=0}}=\frac{J_1(\Phi_{\text{vib}})}{J_0(\Phi_{\text{vib}})}\ ,\quad \hat{z}_{\text{vib}}=\frac{\Phi_{\text{vib}}}{4\pi}\lambda\quad\text{for } J_0(\Phi_{\text{vib}})>0, \Phi_{\text{vib}}\lessapprox 2.4\ , \tag{2.36}$$

by first, determining Φ_{vib} from the curve $J_1(\Phi_{\text{vib}})/J_0(\Phi_{\text{vib}})$ of the two Bessel modes' ratio (Figure 2.5B, bottom) and by second, deriving $\hat{z}_{\text{vib}}$. For small Φ_{vib}, the ratio $J_1(\Phi_{\text{vib}})/J_0(\Phi_{\text{vib}})$ can be approximated by $\Phi_{\text{vib}}/2$ (Figure 2.5B, bottom, dotted line). If $\Phi_{\text{vib}}\leq 0.62$ ($\hat{z}_{\text{vib}}\leq 32.6\,\text{nm}$ for $\lambda_0=660\,\text{nm}$) the estimation error is below 5 %. Since the ratio $J_1(\Phi_{\text{vib}})/J_0(\Phi_{\text{vib}})$ is only unique for $\Phi_{\text{vib}}\lessapprox 2.4$ (Figure 2.5B, bottom), vibration amplitude reconstruction is limited to $\hat{z}_{\text{vib, max}}=126\,\text{nm}$ for $\lambda_0=660\,\text{nm}$ (Equation 2.14).

Following this approach for the experiments, amplitudes of phase modulation of $\Phi_{\text{vib}}=0.03$ ($V_{\text{vib}}=0\,\text{Vpp}$), 0.45 ($V_{\text{vib}}=0.3\,\text{Vpp}$), 1.00 ($V_{\text{vib}}=0.6\,\text{Vpp}$) and 2.06 ($V_{\text{vib}}=1.2\,\text{Vpp}$) could be reconstructed from the spectral bands of the demodulated intensity measurements (Figure 2.6D), corresponding to vibration amplitudes $\hat{z}_{\text{vib}}$ of 1.6 nm, 23.9 nm, 52.3 nm and 108.0 nm, respectively. This means that the mirror responds with increasing vibration amplitudes to the increasing driving voltages of the piezoelectric transducer. Demonstrated for a single pixel of the camera, the procedure can be carried out for reconstruction of spatially resolved vibration amplitude maps.

The phase $\angle I_{\mathrm{dem},i}(f)$ of spectral bands m can be written as (Equation 2.29)

$$\angle I_{\mathrm{dem},i}(f) = \begin{cases} \varphi_{\mathrm{const}} - m\frac{\pi}{2} - m\varphi_{\mathrm{vib}} + \pi(J_m(\Phi_{\mathrm{vib}}) < 0), & \text{if } N\frac{f_{\mathrm{dem}}}{f_{\mathrm{cam}}}\%N \in \left[0, \frac{N}{2}\right] \\ -\varphi_{\mathrm{const}} + m\frac{\pi}{2} + m\varphi_{\mathrm{vib}} + \pi(J_m(\Phi_{\mathrm{vib}}) < 0), & \text{else} \end{cases} . \tag{2.37}$$

The sign of phase angle observed from the spectrum depends on the frequency mirroring of band m under investigation and acquisition parameters δ and N (cf. Equation 2.33). Furthermore, if band amplitude $J_m(\Phi_{\mathrm{vib}})$ is negative, a phase shift of π has to be considered ($\pi(J_m(\Phi_{\mathrm{vib}}) < 0)$). Phase at the baseband $m = 0$ is independent of vibration phase and is $\pm\varphi_{\mathrm{const}}$. While the baseband yields φ_{const}, φ_{vib} can be determined from one of the first sidebands $m = \pm 1$ by solving Equation 2.37.

For $m_{\mathrm{sel}} = +1$, the two phases can be reconstructed as follows

$$\varphi_{\mathrm{const}} = \begin{cases} \angle I_{\mathrm{dem},i}(f)_{m=0}, & \text{if } \delta \leq \frac{1}{2} + \frac{1}{N} \\ -\angle I_{\mathrm{dem},i}(f)_{m=0}, & \text{else} \end{cases} , \tag{2.38}$$

$$\varphi_{\mathrm{vib}} = \begin{cases} \angle I_{\mathrm{dem},i}(f)_{m=1} + \angle I_{\mathrm{dem},i}(f)_{m=0} - \frac{\pi}{2}, & \text{if } \delta \leq \frac{1}{2} + \frac{1}{N} \\ \angle I_{\mathrm{dem},i}(f)_{m=1} - \angle I_{\mathrm{dem},i}(f)_{m=0} - \frac{\pi}{2}, & \text{else} \end{cases} . \tag{2.39}$$

Within this section, I developed a method for reconstructing the vibration parameters amplitude $\hat{z}_{\mathrm{vib}}$ and phase φ_{vib} from a spectral intensity analysis of specific vibration bands. I demonstrated that due to a downmodulation, high vibration frequencies f_{vib} can be accessed by much lower sampling rates f_{cam} of the camera (Figure 2.6D). When evaluating each pixel of the acquired intensity maps, two-dimensional fields $\hat{z}_{\mathrm{vib}}(x, y)$, $\varphi_{\mathrm{vib}}(x, y)$ and $\varphi_{\mathrm{const}}(x, y)$ can be measured. The acquisition parameters N and δ have to be carefully selected since they guarantee minimal band overlap, i.e., minimize analysis errors. The method is calibration-free as vibration amplitudes are measured directly with respect to wave number k or wavelength λ.

However, the method only yields precise results, if the integration (or shutter) time T_{int} of the detector is a small fraction of the vibration period f_{vib}^{-1}. Hence, the method is limited by the minimal shutter time of the camera and optical power available from the object during short shutter times. For high vibration frequencies, the camera integrates over a significant fraction of vibration period, lowering the intensity signal contrast, i.e., the SNR. If the shutter time is equal to or longer than the vibration period ($T_{\mathrm{int}} \geq f_{\mathrm{vib}}^{-1}$), vibration parameters cannot be extracted from the spectrum of the recorded intensity signal any more since sidebands are averaged out due to integration. If such high vibration frequencies are subject to be analyzed, time-averaged holography can be used to extract the vibration parameters.

Time-averaged holography

Time-averaged holography was introduced by pioneering measurements from Powell and Stetson in 1965 on reflective vibrating surfaces utilizing analog holography [119]. Filtering of specific vibration bands was further investigated and analysis strategies were developed, e.g., for small or large vibrations, by temporally modulating the reference or object beam [120].

From digital holograms, time-averaged holography is able to extract numerically amplitude and phase of a vibration [121]. Even simultaneous characterization of in-plane (parallel to the surface) and out-of-plane (perpendicular to the surface) components of a vibrating surface is possible, utilizing spatial multiplexing and polarized light for image separation [122].

The basic principle of the technique is to integrate with the detector over a long time T_{int} compared to vibration period f_{vib}^{-1}, i.e., $T_{\mathrm{int}} \cdot f_{\mathrm{vib}} \gg 1$. Due to integration, only the selected band m_{sel} can be accessed and all other bands are suppressed.

Selecting optically the m_{sel}-th band of the vibration (Equation 2.25) constrains the time-dependent intensity signal present on the detector (Equation 2.23) to

$$\frac{I}{\epsilon c} = E_{\mathrm{ref}}^2 + E_{\mathrm{obj}}^2 + 2E_{\mathrm{ref}}E_{\mathrm{obj}} \sum_{m=-\infty}^{\infty} J_m(\Phi_{\mathrm{vib}}) \cos(\omega t + \varphi) \tag{2.40}$$

$$\text{with} \quad \omega = (m_{\mathrm{sel}} - m)\omega_{\mathrm{vib}} - \frac{\omega_{\mathrm{cam}}}{N} \ , \quad \varphi = \varphi_{\mathrm{const}} - m\frac{\pi}{2} + m\varphi_{\mathrm{vib}} \ (m \in \mathbb{Z}) \ .$$

For the spectral analysis, the time-dependent intensity I from Equation 2.40 was sampled with a shutter time which is short with respect to vibration period f_{vib}^{-1}, equivalent to a snapshot in time, where the effect from the integration can be neglected. Here, the integration over a longer time T_{int} at times t_i gives the intensity $\widetilde{I}_i$

$$\widetilde{I}_i = \frac{1}{T_{\mathrm{int}}} \int_{t_i}^{t_i+T_{\mathrm{int}}} \frac{I}{\epsilon c} \mathrm{d}t \tag{2.41}$$

$$= E_{\mathrm{ref}}^2 + E_{\mathrm{obj}}^2 + \frac{2E_{\mathrm{ref}}E_{\mathrm{obj}}}{\omega T_{\mathrm{int}}} \sum_{m=-\infty}^{\infty} J_m(\Phi_{\mathrm{vib}}) \Big[\sin(\omega t_i + \omega T_{\mathrm{int}} + \varphi) - \sin(\omega t_i + \varphi)\Big]$$

$$= E_{\mathrm{ref}}^2 + E_{\mathrm{obj}}^2 + \frac{4E_{\mathrm{ref}}E_{\mathrm{obj}}}{\omega T_{\mathrm{int}}} \sum_{m=-\infty}^{\infty} J_m(\Phi_{\mathrm{vib}}) \cos\left(\omega t_i + \frac{\omega T_{\mathrm{int}}}{2} + \varphi\right) \sin\left(\frac{\omega T_{\mathrm{int}}}{2}\right)$$

$$= E_{\mathrm{ref}}^2 + E_{\mathrm{obj}}^2 + 2E_{\mathrm{ref}}E_{\mathrm{obj}} \sum_{m=-\infty}^{\infty} J_m(\Phi_{\mathrm{vib}}) \cos\left(\omega t_i + \frac{\omega T_{\mathrm{int}}}{2} + \varphi\right) \mathrm{sinc}\left(\frac{\omega T_{\mathrm{int}}}{2}\right) \ , \tag{2.42}$$

utilizing the trigonometric identity $\sin\alpha - \sin\beta \equiv 2\cos\left(\frac{x+y}{2}\right)\sin\left(\frac{x-y}{2}\right)$ and with the unnormalized sinc function $\mathrm{sinc}(\alpha) = \frac{\sin\alpha}{\alpha}$, also called sampling function $\mathrm{Sa}(\alpha)$.

The argument of the unnormalized sinc function is

$$\frac{\omega T_{\mathrm{int}}}{2} = \frac{1}{2}(m_{\mathrm{sel}} - m)\omega_{\mathrm{vib}}T_{\mathrm{int}} - \frac{1}{2N}\omega_{\mathrm{cam}}T_{\mathrm{int}} \ . \tag{2.43}$$

Selecting an integration time equal to vibration period ($T_{\mathrm{int}} = f_{\mathrm{vib}}^{-1}$) yields

$$\frac{\omega T_{\mathrm{int}}}{2} = \pi(m_{\mathrm{sel}} - m) - \pi\frac{f_{\mathrm{cam}}}{N f_{\mathrm{vib}}} \ . \tag{2.44}$$

For $\frac{f_{\mathrm{cam}}}{N f_{\mathrm{vib}}} \to 0$ ($f_{\mathrm{vib}} \gg f_{\mathrm{cam}}$)

$$\mathrm{sinc}\left(\frac{\omega T_{\mathrm{int}}}{2}\right) \approx \begin{cases} 0, & \text{if } m \neq m_{\mathrm{sel}} \\ 1, & \text{if } m = m_{\mathrm{sel}} \end{cases} , \tag{2.45}$$

since the remaining part of the argument $\pi(m_{\mathrm{sel}} - m)$ is an integer multiple of π and the unnormalized sinc function yields a value of one for an argument of zero and has zeros at multiples of π. For $T_{\mathrm{int}} > f_{\mathrm{vib}}^{-1}$, ideally multiples of the vibration period f_{vib}^{-1}, the same selective behavior for $m = m_{\mathrm{sel}}$ exists, with the advantage of reduced noise due to the longer integration time.

The cosine term of the integrated intensity $\widetilde{I}_i$ from Equation 2.42 yields for $T_{\mathrm{int}} = f_{\mathrm{vib}}^{-1}$, sampled at times $t_i = i/f_{\mathrm{cam}}$

$$\begin{aligned} \cos\left(\omega t_i + \frac{\omega T_{\mathrm{int}}}{2} + \varphi\right) = \cos\Bigg(&2\pi i(m_{\mathrm{sel}} - m)\frac{f_{\mathrm{vib}}}{f_{\mathrm{cam}}} - 2\pi\frac{i}{N} \\ &+\pi(m_{\mathrm{sel}} - m) - \pi\frac{f_{\mathrm{cam}}}{N f_{\mathrm{vib}}} + \varphi\Bigg) \ . \end{aligned} \tag{2.46}$$

Due to the selection of band $m = m_{\mathrm{sel}}$ by the sinc function, only the corresponding cosine term contributes to the intensity spectrum, which is

$$\cos\left(\omega\frac{i}{f_{\mathrm{cam}}} + \frac{\omega f_{\mathrm{vib}}^{-1}}{2} + \varphi\right)\Bigg|_{m=m_{\mathrm{sel}}} = \cos\left(-2\pi\frac{i}{N} - \pi\frac{f_{\mathrm{cam}}}{N f_{\mathrm{vib}}} + \varphi\right) \ . \tag{2.47}$$

The term $-2\pi i/N$ in the cosine argument is a propagating phase from phase shifting holography probing the 2π phase space, which allows for reconstruction of φ (cf. Equation 1.30). The other contributing phase tends to zero ($\pi f_{\mathrm{cam}}/(N f_{\mathrm{vib}}) \to 0$). But since this term is constant over sampling index i (or time), it contributes to φ_{const} within φ and does not impact on vibration parameter extraction.

The intensity accessed from time-averaged holography for integration times of at least $T_{\mathrm{int}} = f_{\mathrm{vib}}^{-1}$, ideally long times, can be reformulated to (Equations 2.42, 2.45, 2.47 and φ from Equation 2.40)

$$\widetilde{I}_i \approx E_{\mathrm{ref}}^2 + E_{\mathrm{obj}}^2 + 2E_{\mathrm{ref}}E_{\mathrm{obj}}J_{m_{\mathrm{sel}}}(\Phi_{\mathrm{vib}})\cos\left(-2\pi\frac{i}{N} + \varphi_{\mathrm{const}} - m_{\mathrm{sel}}\frac{\pi}{2} + m_{\mathrm{sel}}\varphi_{\mathrm{vib}}\right) . \tag{2.48}$$

From this intensity, the magnitude $|2E_{\mathrm{ref}}E_{\mathrm{obj}}J_{m_{\mathrm{sel}}}(\Phi_{\mathrm{vib}})|$ and phase $\varphi_{\mathrm{const}} - m_{\mathrm{sel}}\frac{\pi}{2} + m_{\mathrm{sel}}\varphi_{\mathrm{vib}}$ for the selected band m_{sel} can be extracted utilizing phase-shifting holography (see Section 1.4.3).

Time-averaged holography provides access to one specific vibrational band while integration times of the detector are chosen longer than vibration period, allowing for investigation of very high-frequency vibrations in the range of 100 kHz or even beyond. The integration is equivalent to applying a band-pass filter in the spectrum around the selected band of a width indirect proportional to integration time [120]. An advantage of the long integration times is the low required laser power and hence, low light exposure of the cells. For high vibration frequencies, as subject of analysis in the targeted application, even integration times long compared to vibration period, lead to high-throughput readout.

Dual local oscillator

As introduced earlier, for a robust extraction of vibration parameters, the bands $m_{\mathrm{sel}} = 0$ and $m_{\mathrm{sel}} = +1$ or $m_{\mathrm{sel}} = -1$ are required. Time-averaged holography provides access to one band while it is very insensitive against noise, i.e., has a high SNR. For a complete measurement, two steps are required selecting two different bands with the AOMs in a time sequence (cf. Equation 2.25). However, time-division multiplexing lowers the throughput of the method and has the disadvantage that changes between both steps (either from the environment or the sample) are not covered by the measurement but contribute to as error. But, selection of both bands can be performed at the same time by frequency-division multiplexing [117]. Therefor, a positive as well as negative frequency shift matched to the sampling rate of the camera are used, containing the information from one band each. In this case, the reference beam, or local oscillator, consists of two frequency components, i.e., it is a dual local oscillator. While for one frequency component f_{ref0}, the frequency constraint is set as already introduced (Equation 2.25)

$$f_{\mathrm{ref0}} - f_{\mathrm{obj}} = m_{\mathrm{sel0}} \cdot f_{\mathrm{vib}} - \frac{f_{\mathrm{cam}}}{N} \ , \tag{2.49}$$

selecting band m_{sel0}, the inverse frequency shift of the sampling rate is set for the second reference beam frequency f_{ref1}, which selects band m_{sel1}

$$f_{\mathrm{ref1}} - f_{\mathrm{obj}} = m_{\mathrm{sel1}} \cdot f_{\mathrm{vib}} + \frac{f_{\mathrm{cam}}}{N} \ . \tag{2.50}$$

A superposition of both frequency lines in the electric field of the reference beam can be achieved by exciting the AOM with a two-tone signal, synthesized by the function generator.

In Equations 2.49 and 2.50, the selected bands m_{sel0} and m_{sel1} of vibration frequency f_{vib} are downmodulated to camera's sampling rate divided by N, $-f_{\mathrm{cam}}/N$ and f_{cam}/N, respectively. Hence, a frequency spectrum yields these two components. However, since all frequencies corresponding to the real object image overlap with the negated frequencies in its complex conjugate, it is required to filter the recorded off-axis holograms for the real object image utilizing the angular spectrum method (Section 1.4.2).

To minimize cross-talk between both frequency lines (and the twin object images), their frequency magnitude should be different [118]. This can be achieved by demodulation of the bands m_{sel0} and m_{sel1} to frequencies $-e_0 f_{\mathrm{cam}}/N$ and $+e_1 f_{\mathrm{cam}}/N$ with two integers e_0 and e_1

$$f_{\mathrm{ref0}} - f_{\mathrm{obj}} = m_{\mathrm{sel0}} \cdot f_{\mathrm{vib}} - \frac{e_0 f_{\mathrm{cam}}}{N} \ , \tag{2.51}$$

$$f_{\mathrm{ref1}} - f_{\mathrm{obj}} = m_{\mathrm{sel1}} \cdot f_{\mathrm{vib}} + \frac{e_1 f_{\mathrm{cam}}}{N} \ , \tag{2.52}$$

$$\text{with } e_0, e_1 \in \mathbb{N},\ e_0, e_1 \in \left[1, \frac{N}{2}\right] \text{ and } e_0 \neq e_1 \ . \tag{2.53}$$

Although a spectral evaluation is only applicable for short integration times with respect to vibration period, it can be used for time-averaged holography with two local oscillators since it filters for two independent bands. Consequently, from the frequency spectrum of the real object image (after twin-image separation), spectral amplitude and phase of bands m_{sel0} and m_{sel1} can be extracted as introduced before from the frequency components at

$$N\frac{f_{\mathrm{DFT,0}}}{f_{\mathrm{cam}}} = -e_0 \qquad \text{and} \qquad N\frac{f_{\mathrm{DFT,1}}}{f_{\mathrm{cam}}} = +e_1 \ , \tag{2.54}$$

respectively (or at inverse frequencies from the complex conjugate object image).

For vibration amplitude and phase reconstruction, $m_{\mathrm{sel0}} = 0$ is set for accessing the baseband with corresponding Bessel mode J_0 and $m_{\mathrm{sel1}} = +1$ for the first sideband with mode J_1. Following the reconstruction procedure introduced earlier, vibration amplitude and phase can be derived.

Vibrating mirror experiment

In an experiment, I looked at an oscillating mirror without cells. Based on the optical setup presented in Figure 2.4 and the theoretical principles developed above, the vibrating mirror was analyzed and vibration amplitude $\hat{z}_{\mathrm{vib}}$ and phase φ_{vib} as well as constant setup phase φ_{const} were reconstructed (Figure 2.7).

The piezoelectric transducer was pre-stressed by two screws exerting pressure on the mirror from above, mediated by rubber rings. To achieve high vibration amplitudes at high frequencies, measurements were performed close to resonance of the loaded piezoelectric transducer. Resonance frequency was found at $f_{\mathrm{vib}} = 85\,\mathrm{kHz}$ (piezo stacks are rated for a resonance frequency of 85 kHz) by maximizing the current through the loaded piezo stacks, accessed via the voltage drop over a shunt resistor of $1\,\Omega$ connected in series to the piezos and measured with an oscilloscope.

Camera frame rate was set to 1 kHz while $N = 10$ frames were selected for one 2π phase cycle within phase-shifting holography. The frequency mismatch between the object beam and both reference beam frequencies was adjusted with the AOMs selecting $e_0 = 2$ and $e_1 = 3$, probing the baseband at $-200\,\mathrm{Hz}$ and the first vibration

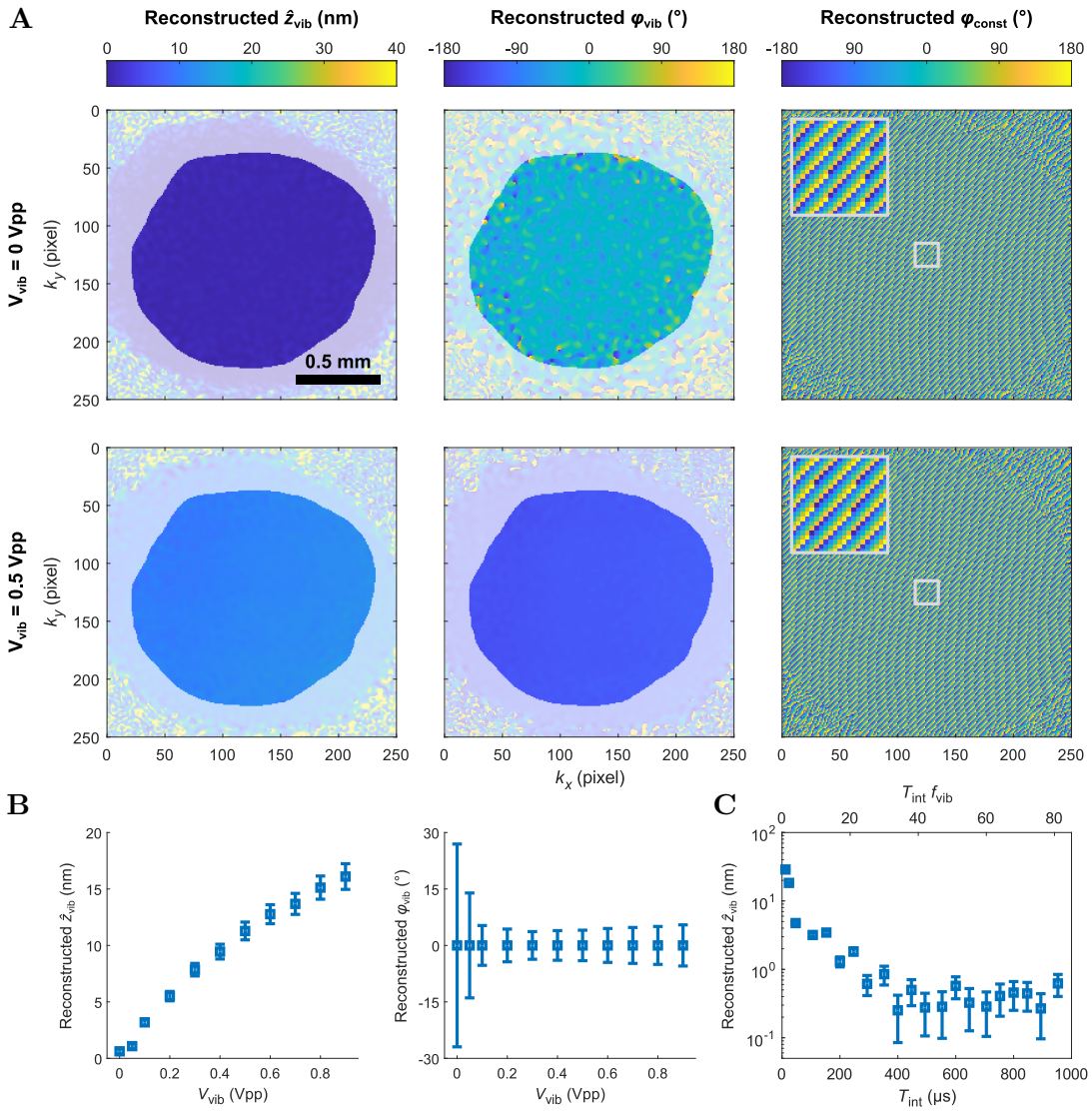

Figure 2.7.: Holographic laser Doppler vibrometry (HLDV) on a vibrating mirror. **A** Reconstructed vibration amplitude $\hat{z}_{\mathrm{vib}}$ (left), vibration phase φ_{vib} (center) and time-independent setup phase φ_{const} (right) for no vibration ($V_{\mathrm{vib}} = 0\,\mathrm{Vpp}$, top) and for a driving voltage of $V_{\mathrm{vib}} = 0.5\,\mathrm{Vpp}$ (bottom) connected to the piezo driver. **B** Vibration amplitude (left) and phase response (right) for different driving voltages. Mean ± standard deviation are shown over all valid pixels (non-transparent) in (A), determined from a smoothed $\exp(-2) \approx 13.5\,\%$-intensity contour around interference intensity maximum. Since reconstructed φ_{vib} has no reference in time, its mean is random and was set to zero for statistical analysis (right). **C** Dependency of the reconstructed vibration amplitude on camera shutter time T_{int}, or number of integration cycles $T_{\mathrm{int}} f_{\mathrm{vib}}$, for zero driving voltage ($V_{\mathrm{vib}} = 0\,\mathrm{Vpp}$) determines the noise floor. All experiments were carried out at $f_{\mathrm{vib}} = 85\,\mathrm{kHz}$ (close to resonance), $f_{\mathrm{cam}} = 1\,\mathrm{kHz}$, $N = 10$, $T_{\mathrm{int}} = 953\,\mu\mathrm{s}$ (A, B) while 100 frames were analyzed for parameter extraction.

band at +300 Hz simultaneously using the principle of a dual local oscillator (Equation 2.54).

Vibration amplitude $\hat{z}_{\mathrm{vib}}$ and phase φ_{vib} as well as the time-independent phase φ_{const} were reconstructed from 100 acquired frames and are presented for piezo driving voltages V_{vib} of 0 Vpp (no vibration) and 0.5 Vpp (Figure 2.7A). For the increased driving voltage, an increased vibration amplitude can be observed. While reconstructed vibration phase φ_{vib} is noisy for $V_{\mathrm{vib}} = 0$ Vpp, a homogeneous phase was reconstructed for $V_{\mathrm{vib}} = 0.5$ Vpp. Reconstructed time-independent phase φ_{const} reveals a wrapped tilted phase, originating from the angle under which reference and object hit the detector in the off-axis holography setup (see Section 1.4).

Reconstructed vibration amplitude $\hat{z}_{\mathrm{vib}}$ and phase φ_{vib} maps were investigated for further driving voltages within a range of 0 Vpp to 0.9 Vpp (images not shown). Since the laser beams do not entirely illuminate the selected region of 250 × 250 pixels on the camera, for statistical analysis, a subregion was selected from a smoothed $\exp(-2) \approx 13.5\,\%$-intensity contour around the interference intensity maximum (Figure 2.7A, non-transparent regions). A fraction of $\exp(-2)$ was chosen since this level is commonly used for defining a Gaussian beam's diameter.

For increasing piezo driving voltages V_{vib}, an increase in reconstructed vibration amplitudes $\hat{z}_{\mathrm{vib}}$ can be found (Figure 2.7B, left). Reconstructed vibration phase φ_{vib} is randomly distributed over time since a reference is missing. The phases can only be compared within an acquisition series, i.e., not between the measurements performed at different driving voltages. For statistical analysis, the mean of reconstructed phase maps is set to zero and solely the standard deviation of all valid pixels is evaluated (Figure 2.7B, right). From the low standard deviation, one can conclude that the phase is homogeneous which means that the vibration of the mirror reveals no position-dependent phase delay within the region of analysis. The in-phase movement of the mirror, which could be confirmed here, is guaranteed by the three-point bearing of simultaneously moving piezoelectric stacks as well as the selection of a thick mirror which effectively suppresses in-plane vibrations. However, extracted vibration phase yields large standard deviations for small vibration amplitudes, in case of driving voltages of $V_{\mathrm{vib}} = 0$ Vpp and 50 mVpp (Figure 2.7A, top center and B, right). This can be explained by the fact that for a vibration amplitude $\hat{z}_{\mathrm{vib}} = 0$, the phase angle φ_{vib} is not defined (cf. Equation 2.17) and hence, extracted phase maps reveal a high noise level for small vibration amplitudes.

In a final set of experiments on the vibrating mirror, the effects of the integration time used in time-averaged holography were studied. So far, for parameter reconstruction, a long integration time of $T_{\mathrm{int}} = 953\,\mu$s was used, equivalent to an integration over $T_{\mathrm{int}} f_{\mathrm{vib}} = 81$ vibration periods. As described above, spectral filtering on the selected vibration band depends on the integration time. Here, integration time was varied experimentally while reconstructing vibration amplitudes $\hat{z}_{\mathrm{vib}}$ for $V_{\mathrm{vib}} = 0$ Vpp (no vibration), which defines the noise floor (Figure 2.7C). Integration times close to an integer multiple of vibration period f_{vib}^{-1} were selected. Although the vibration frequency has no effect on the vibration since its amplitude is zero, it still contributes

to the frequency mismatch between reference and object beam for the mode $m_{\mathrm{sel}} = +1$. For integration times below 30 μs, equivalent to one or two vibration periods, amplitudes above 10 nm are reconstructed. This high noise level can be reduced to below 1 nm if integration time is prolonged to at least 400 μs or 34 vibration cycles. The noise floor cannot be further reduced by increasing integration times.

Within experiments on a vibrating mirror, I demonstrated that the developed method enables to extract 2D maps of vibration amplitudes $\hat{z}_{\mathrm{vib}}$ on the lower nanometer range and vibration phases φ_{vib} at low noise from a single acquisition series using two independent reference frequency lines. I could confirm that the established mechanical setup is suited for vibration excitation, even around a frequency of 85 kHz, and showed that in-plane vibrations are suppressed which is essential for an unbiased readout of the out-of-plane components.

2.3.2. Vibrating cell monolayer

After establishing a contact-free method for spatially resolved characterization of vibrating surfaces in Section 2.3.1, the method is applied to a cell monolayer adhered to a coated mirror.

The optical setup for characterization of a vibrating surface (Figure 2.4) is extended towards mechanical analysis of adherent cells (Figure 2.8). The light beam of a linearly polarized and fiber-pigtailed laser emitting at $\lambda_0 = 660$ nm is collimated and passes a $\lambda/2$-retardation plate as well as a polarizer before it is divided by a polarizing beam splitter (PBS1) into reference (R) and object (O) beam path. The retardation plate in combination with a rotatable polarizer is used for an adjustment of overall intensity and the ratio between both beam paths. The reference beam is rotated in its polarization angle by 90° using a $\lambda/2$-wave plate to match the polarization of the object beam path. The first diffraction order of two AOMs is used to shift the frequency of light in both beams by $\Delta\omega_{\mathrm{ref}}$ and $\Delta\omega_{\mathrm{obj}}$, respectively, while the remaining light in zeroth order is shadowed by a diaphragm.

Using a further beam splitter (BS1), reference and object beam are combined and doubled. One pair of both beams (static reference beam, SR and static object beam, SO[1]) is expanded by a Kepler telescope with an optical magnification of 2, consisting of two convex lenses of focal lengths $f_1 = 150$ mm and $f_2 = 300$ mm. The beams pass a $\lambda/2$-retardation plate for polarization adjustment (to compensate for polarization effects introduce by the sample) and are subsequently separated. By a beam splitter mounted on a linear translation stage (BS3, direction is indicated by a double-headed arrow), they are combined again while their distance can be varied, in order to match the distance of two beams with which they are superimposed later.

The other pair of reference and object beam from BS1 passes PBS2, is circularly polarized by a $\lambda/4$-wave plate and directed to the sample of interest (moving reference

[1] Although the SO beam does not hit the sample it is called an object beam since it carries the frequency shift $\Delta\omega_{\mathrm{obj}}$, while "static" in this terminology indicates that the beam does not hit the vibrating sample.

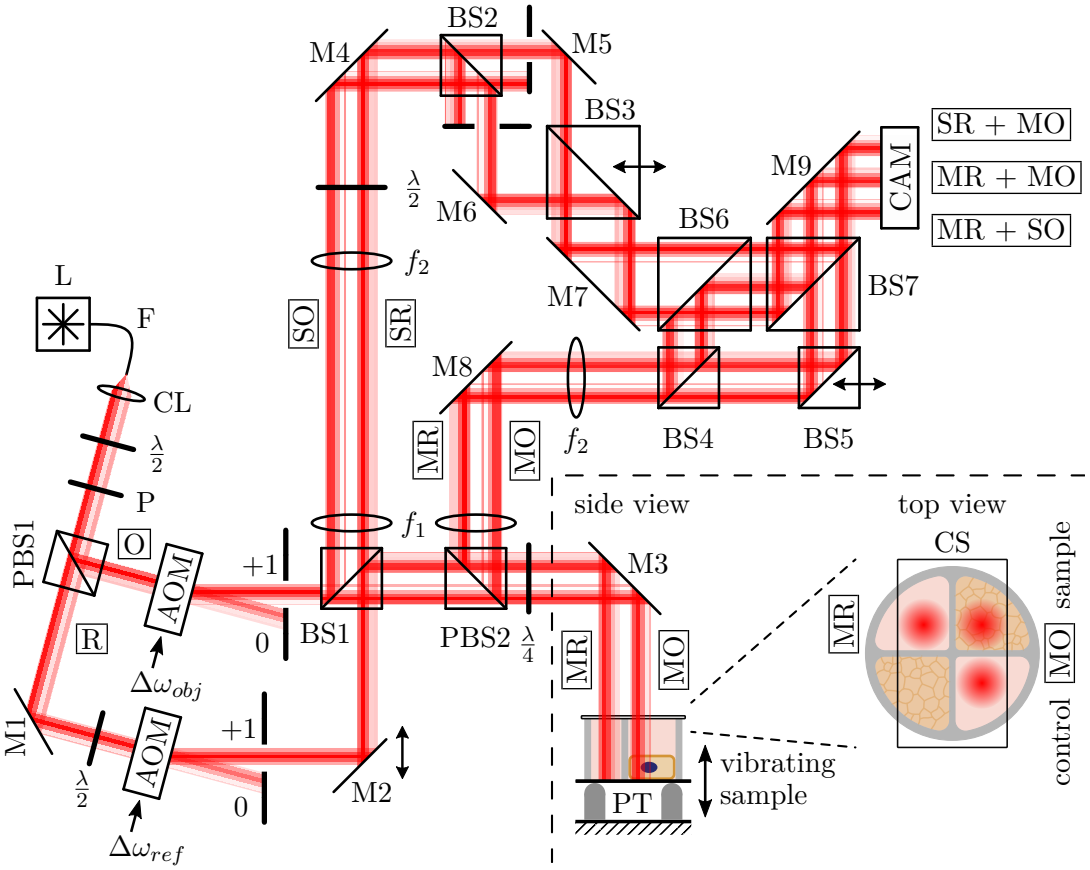

Figure 2.8.: Holographic vibration spectroscopy (HVS). Top-down view of the optical setup for analyzing vibrating adherent cells. L: fiber-pigtailed laser emitting at 660 nm, F: optical fiber, CL: collimating lens, $\frac{\lambda}{2}$ & $\frac{\lambda}{4}$: retardation wave plates, P: polarizer, M: mirror, PBS: polarizing beam splitter, AOM: acousto-optic modulator, BS: beam splitter, lenses $f_1 = 150$ mm and $f_2 = 300$ mm, CS: cover slip, PT: piezoelectric transducer, CAM: CMOS camera. The vibrating mirror is mounted horizontally. Optical components with a double-headed arrow next to them are mounted on a translation stage for beam distance adjustment. For improved readability only the used beam paths are shown at beam splitters.

beam, [MR] and moving object beam, [MO]). The reflected light passes the $\lambda/4$-plate again, i.e., it is rotated in polarization by 90° after the second pass and hence, the entire reflected light exits the polarizing beam splitter (PBS2) towards detection, where the beam pair is expanded by a Kepler telescope similar to the beam pair first described ([SR] & [SO]). For the [MR] & [MO] beam pair, the vibrating sample is located in the focal plane of lens f_1, while the focal plane of f_2 falls together with the imaging plane of the camera, which maps the sample onto the camera with an optical magnification of 2. Both beams are duplicated using beam splitter BS4 and combined by BS7. With a beam splitters in between, mounted on a linear translation stage (BS5, direction indicated by a double-headed arrow), the beam pairs are translated to each other by a variable distance. With BS5, the duplicated [MO] beam is shifted to

coincide with the MR beam. Over beam splitter BS6, the beam pair first described (SR & SO) is coupled in and beams are superimposed with the MO and duplicated MR beam. In summary, on the camera, three pairs of two overlapping beams are recorded simultaneously: SR + MO, MR + MO, MR + SO (from top to bottom). Since intensity fields are recorded with off-axis holography, a small angle between all three pairs is introduced and carefully adjusted by orientations of mirrors and beam splitters.

Induced pluripotent stem cells (iPSCs) were cultured on a mirror coated with Matrigel in two out of four wells of an attached culture insert (see Section 2.1.2 for details). For a sample measurement, the reference beam (MR) is directed to a chamber without cells while the object beam (MO) travels through a part of the chamber with adherent cells (see right inset in Figure 2.4). In a control measurement, the MO beam is targeted to a well without cells, i.e., both the MR and MO beam are probing two wells without cells in that case. With a linear translation stage shifting the mirror M2 (direction indicated) in the reference beam path, the separation distance of those two beams can be adapted to the sample.

The beam pairs were implemented to capture several aspects of the vibrating sample at the same time, which will be investigated theoretically in the following. All combinations of a reference with an object beam were selected for analysis, except for the interference of both static beams (SR + SO), which contains no sample information. Due to the required frequency mismatch between two beams for heterodyne analysis, a reference beam can only be combined with an object beam.

SR + MO beam pair

Similar to the interference intensity field developed in Section 2.3.1 and used for characterization of vibrating surfaces, interference intensity can be derived from the optical path lengths of the SR and MO beam. Differently from before, the object beam probes the chamber with cells in this case (see Figures 2.3 and 2.8).

Static reference beam path length z_{SR} is constant over time

$$z_{\mathrm{SR}} = z_{\mathrm{SR},0} = const\ . \tag{2.55}$$

Moving object beam path length z_{MO} is modulated by the deflection $z_{\mathrm{vib}}(t)$ of the reflective surface as well as by the induced vibration of the cell interface $z_{\mathrm{cell}}(t)$ to surrounding cell medium (Figure 2.3) and can be described as follows

$$z_{\mathrm{MO}} = z_{\mathrm{MO},0} - 2kz_{\mathrm{vib}} - 2kz_{\mathrm{cell}} \tag{2.56}$$

$$\text{with } z_{\mathrm{vib}} = \hat{z}_{\mathrm{vib}} \cos(\omega_{\mathrm{vib}} t - \varphi_{\mathrm{vib}})\ , \tag{2.57}$$

$$z_{\mathrm{cell}} = (n_{\mathrm{cell}} - n_{\mathrm{med}}) \hat{z}_{\mathrm{cell}} \cos(\omega_{\mathrm{vib}} t - \varphi_{\mathrm{cell}})\ , \tag{2.58}$$

with refractive indices n_{cell} and n_{med} of the cells and cell medium, respectively.

Similar to the derivation in Equations 2.12 to 2.17, the interference intensity $I_{\mathrm{SR+MO}}$ can be formulated to

$$\frac{I_{\mathrm{SR+MO}}}{\epsilon c} = E_{\mathrm{ref}}^2 + E_{\mathrm{obj}}^2 + 2E_{\mathrm{ref}}E_{\mathrm{obj}}\cos\Big((\omega_{\mathrm{ref}} - \omega_{\mathrm{obj}})t + \varphi_{\mathrm{const}} - 2k\hat{z}_{\mathrm{vib}}\cos(\omega_{\mathrm{vib}}t - \varphi_{\mathrm{vib}}) - 2k(n_{\mathrm{cell}} - n_{\mathrm{med}})\hat{z}_{\mathrm{cell}}\cos(\omega_{\mathrm{vib}}t - \varphi_{\mathrm{cell}})\Big)\ . \tag{2.59}$$

Since the intensity signal contains the responses from the vibrating mirror $z_{\mathrm{vib}}(t)$ as well as from the cells $z_{\mathrm{cell}}(t)$ at the same frequency ω_{vib}, both contributions overlap and the intensity can be reformulated (Equation 2.35)

$$\frac{I_{\mathrm{SR+MO}}}{\epsilon c} = E_{\mathrm{ref}}^2 + E_{\mathrm{obj}}^2 + 2E_{\mathrm{ref}}E_{\mathrm{obj}} \cdot \cos\Big((\omega_{\mathrm{ref}} - \omega_{\mathrm{obj}})t + \varphi_{\mathrm{const}} - 2k\hat{z}_{\Sigma}\cos(\omega_{\mathrm{vib}}t - \varphi_{\Sigma})\Big)\ , \tag{2.60}$$

$$\text{with } \hat{z}_{\Sigma} = \sqrt{\hat{z}_{\mathrm{vib}}^2 + (n_{\mathrm{cell}} - n_{\mathrm{med}})^2\hat{z}_{\mathrm{cell}}^2 + 2(n_{\mathrm{cell}} - n_{\mathrm{med}})\hat{z}_{\mathrm{vib}}\hat{z}_{\mathrm{cell}}\cos(\varphi_{\mathrm{vib}} - \varphi_{\mathrm{cell}})}\ ,$$

$$\varphi_{\Sigma} = \arctan\left(\frac{\hat{z}_{\mathrm{vib}}\sin\varphi_{\mathrm{vib}} + (n_{\mathrm{cell}} - n_{\mathrm{med}})\hat{z}_{\mathrm{cell}}\sin\varphi_{\mathrm{cell}}}{\hat{z}_{\mathrm{vib}}\cos\varphi_{\mathrm{vib}} + (n_{\mathrm{cell}} - n_{\mathrm{med}})\hat{z}_{\mathrm{cell}}\cos\varphi_{\mathrm{cell}}}\right)\ . \tag{2.61}$$

The frequency-domain representation, derived similarly to Equations 2.20 to 2.23, reads

$$\frac{I_{\mathrm{SR+MO}}}{\epsilon c} = E_{\mathrm{ref}}^2 + E_{\mathrm{obj}}^2 + 2E_{\mathrm{ref}}E_{\mathrm{obj}}\sum_{m=-\infty}^{\infty} J_m(\Phi_{\Sigma}) \cdot \cos\Big((\omega_{\mathrm{ref}} - \omega_{\mathrm{obj}} - m\omega_{\mathrm{vib}})t + \varphi_{\mathrm{const}} - m\frac{\pi}{2} + m\varphi_{\Sigma}\Big) \tag{2.62}$$

$$\text{with } \Phi_{\Sigma} = 4\pi\frac{\hat{z}_{\Sigma}}{\lambda_0}\ .$$

From $I_{\mathrm{SR+MO}}$, only the ensemble vibration amplitude $\hat{z}_{\Sigma}$ and phase φ_{Σ} can be accessed from experiments but no distinct readout from the exciting vibration and cell interface vibration is available. Since $\hat{z}_{\Sigma}$ depends also on the phases and amplitudes contribute to φ_{Σ} (Equation 2.61), the ensemble parameters reconstructed from the SR + MO beam pair are not separated for amplitude and phase.

MR + MO beam pair

To be able to access the vibration response solely from the cells, a beam pair with a moving instead of a static reference is analyzed. While the object beam path length is described above (Equation 2.56), the path length of moving reference z_{MR} is

$$z_{\mathrm{MR}} = z_{\mathrm{MR},0} - 2z_{\mathrm{vib}} \tag{2.63}$$

$$\text{with } z_{\mathrm{vib}} = \hat{z}_{\mathrm{vib}}\cos(\omega_{\mathrm{vib}}t - \varphi_{\mathrm{vib}})\ , \tag{2.57}$$

consisting of a constant path length $z_{\mathrm{MR},0}$ modulated by mirror vibration z_{vib}.

The interfered intensity of the $\boxed{\text{MR + MO}}$ beam pair is

$$\begin{aligned}\frac{I_{\text{MR+MO}}}{\epsilon c} &= E_{\text{ref}}^2 + E_{\text{obj}}^2 + 2E_{\text{ref}}E_{\text{obj}} \qquad (2.64)\\ &\quad \cdot \cos\Big((\omega_{\text{ref}} - \omega_{\text{obj}})t + \varphi_{\text{const}} + 2kz_{\text{vib}} - 2kz_{\text{vib}} - 2kz_{\text{cell}}\Big)\ .\\ &= E_{\text{ref}}^2 + E_{\text{obj}}^2 + 2E_{\text{ref}}E_{\text{obj}} \qquad (2.65)\\ &\quad \cdot \cos\Big((\omega_{\text{ref}} - \omega_{\text{obj}})t + \varphi_{\text{const}} - 2k(n_{\text{cell}} - n_{\text{med}})\hat{z}_{\text{cell}}\cos(\omega_{\text{vib}}t - \varphi_{\text{cell}})\Big)\ .\end{aligned}$$

Equation 2.65 demonstrates that the intensity solely depends on the cells' vibration and therefore, it can be used to analyze their response independent of the exciting vibration.

Of note, since the frequency of light is altered in reference and object beam path differently with the AOMs, also corresponding wave numbers k_{ref} and k_{obj} differ. Since the terms $2kz_{\text{vib}} - 2kz_{\text{vib}}$ in Equation 2.64, one from the reference and one from the object beam, cancel only in case of equal wave numbers $k = k_{\text{ref}} = k_{\text{obj}}$, the impact on the intensity $I_{\text{MR+MO}}$ in Equation 2.65 has to be estimated.

For a laser of wavelength λ_0, a center frequency f_{AOM} of the AOMs and a frequency difference $\Delta f = f_{\text{ref}} - f_{\text{obj}}$ between reference and object beam (cf. Equation 2.25), wave numbers k_{ref} and k_{obj} read

$$f_{\text{ref}} = \frac{c}{\lambda_0} + f_{\text{AOM}} + \Delta f\ , \qquad f_{\text{obj}} = \frac{c}{\lambda_0} + f_{\text{AOM}}\ , \qquad (2.66)$$

$$k_{\text{ref}} = 2\pi\left(\frac{1}{\lambda_0} + \frac{f_{\text{AOM}} + \Delta f}{c}\right)\ , \qquad k_{\text{obj}} = 2\pi\left(\frac{1}{\lambda_0} + \frac{f_{\text{AOM}}}{c}\right)\ . \qquad (2.67)$$

The sum of both terms in Equation 2.64 is

$$2k_{\text{ref}}\hat{z}_{\text{vib}} - 2k_{\text{obj}}\hat{z}_{\text{vib}} = 4\pi\frac{\Delta f}{c}\hat{z}_{\text{vib}} = 4.2 \times 10^{-3}\,\text{m}^{-1} \cdot \hat{z}_{\text{vib}}\ , \qquad (2.68)$$

for $\Delta f \approx f_{\text{vib}} \approx 100\,\text{kHz}$. On the other hand, the contributing amplitude from cell interface vibration can be estimated to (Equation 2.65)

$$\begin{aligned}2k_{\text{obj}}(n_{\text{cell}} - n_{\text{med}})\hat{z}_{\text{cell}} &= 4\pi\left(\frac{1}{\lambda_0} + \frac{f_{\text{AOM}}}{c}\right)(n_{\text{cell}} - n_{\text{med}})\hat{z}_{\text{cell}} \qquad (2.69)\\ &= 9.5 \times 10^5\,\text{m}^{-1} \cdot \hat{z}_{\text{cell}}\ ,\end{aligned}$$

with $\lambda_0 = 660\,\text{nm}$, $f_{\text{AOM}} = 80\,\text{MHz}$ and a difference in refractive indices of $n_{\text{cell}} - n_{\text{med}} \approx 0.05$ [123, 124].

By comparing Equations 2.68 and 2.69, one can clearly see that the contribution from cell membrane vibrations are much higher than the one from exciting vibrations, even if cell vibration amplitudes are smaller than the exciting ones. In conclusion, this means that the approximation of $I_{\text{MR+MO}}$ in Equation 2.65 is valid under the experimental conditions.

Following the derivation in Equations 2.20 to 2.23, from Equation 2.65 a frequency-domain representation can be derived

$$\begin{aligned}\frac{I_{\mathrm{MR+MO}}}{\epsilon c} &= E_{\mathrm{ref}}^2 + E_{\mathrm{obj}}^2 + 2E_{\mathrm{ref}}E_{\mathrm{obj}} \sum_{m=-\infty}^{\infty} J_m(\Phi_{\mathrm{cell}}) \\ &\quad \cdot \cos\Big((\omega_{\mathrm{ref}} - \omega_{\mathrm{obj}} - m\omega_{\mathrm{vib}})t + \varphi_{\mathrm{const}} - m\frac{\pi}{2} + m\varphi_{\mathrm{cell}}\Big) \\ \text{with } \Phi_{\mathrm{cell}} &= 4\pi\frac{(n_{\mathrm{cell}} - n_{\mathrm{med}})\hat{z}_{\mathrm{cell}}}{\lambda_0} \ .\end{aligned} \tag{2.70}$$

Analyzing the MR + MO beam pair interference intensity provides a very sensitive access to the induced cell vibrations due to its differential beam configuration.

MR + SO beam pair

While the moving reference beam is probing the vibrating mirror and a well without cells, the static object beam does not hit the vibrating surface. Since a reference beam with corresponding frequency shift introduced by an AOM is used to probe the mirror's surface, the object beam has to be used as static reference in order to maintain the frequency mismatch between both beams (which is essential for vibration band selection). Moving reference beam path length is given by Equation 2.63 and static object beam path length can be described by

$$z_{\mathrm{SO}} = z_{\mathrm{SO},0} = const \ . \tag{2.71}$$

Interference intensity for the MR + SO beam pair is

$$\begin{aligned}\frac{I_{\mathrm{MR+SO}}}{\epsilon c} &= E_{\mathrm{ref}}^2 + E_{\mathrm{obj}}^2 + 2E_{\mathrm{ref}}E_{\mathrm{obj}} \\ &\quad \cdot \cos\Big((\omega_{\mathrm{ref}} - \omega_{\mathrm{obj}})t + \varphi_{\mathrm{const}} + 2k\hat{z}_{\mathrm{vib}}\cos(\omega_{\mathrm{vib}}t - \varphi_{\mathrm{vib}})\Big) \ ,\end{aligned} \tag{2.72}$$

which is similar to the intensity signal gained from the setup for vibrating surface analysis (Equation 2.17), but with inverted sign of vibration z_{vib} due to the exchanged reference and object beams.

The inverse sign of phase modulation leads to the reverse direction of frequency and phase shift induced by the vibration, observed from the frequency-domain representation (derived similarly to Equations 2.20 to 2.23)

$$\begin{aligned}\frac{I_{\mathrm{MR+SO}}}{\epsilon c} &= E_{\mathrm{ref}}^2 + E_{\mathrm{obj}}^2 + 2E_{\mathrm{ref}}E_{\mathrm{obj}} \sum_{m=-\infty}^{\infty} J_m(\Phi_{\mathrm{vib}}) \\ &\quad \cdot \cos\Big((\omega_{\mathrm{ref}} - \omega_{\mathrm{obj}} + m\omega_{\mathrm{vib}})t + \varphi_{\mathrm{const}} + m\frac{\pi}{2} - m\varphi_{\mathrm{vib}}\Big) \\ \text{with } \Phi_{\mathrm{vib}} &= 4\pi\frac{\hat{z}_{\mathrm{vib}}}{\lambda_0} \ .\end{aligned} \tag{2.73}$$

This is equivalent to the frequency-domain representation of vibrating surface analysis in Equation 2.23 but the Bessel mode amplitude which is $J_{-m}(\Phi_{\mathrm{vib}})$ in this case (this can be obtained from Equation 2.23 by replacing m with $-m$).

The MR + SO beam pair gives access to the exciting vibration z_{vib} and thus, provides a control for the extracted cell vibrations.

In summary, the interference intensities of the three beam pairs provide different vibration parameters. While the MR + SO beam pair gives access solely to the exciting vibration of the mirror, cell vibrations are captured by the MR + MO beam pair. Interference from SR + MO carries an ensemble of both vibration responses, a superposition of both vibration amplitudes and phases. For an experiment, the MR + MO and MR + SO beam pair will be most useful.

Cell monolayer experiment

In the previous paragraphs, I first introduced a method for contact-free characterization of reflective surfaces vibrating at high frequencies (HLDV) and extracted vibration parameters from a mirror vibrating at 85 kHz with amplitudes in the lower nanometer range. Second, I extended the optical setup towards mechanical analysis of adherent cells with vibrational excitation and optical readout (HVS) and investigated three analysis beam pairs for their information content and demonstrated mathematically that vibration parameters of cellular responses can be derived from the measurements.

In a measurement, I applied the developed method to a confluent monolayer of iPSCs adhered to a vibrating surface. Utilizing a coating, the cells were attached to a mirror within a four well silicone insert (see Figure 2.8). While two wells contain a cell monolayer, the two others do not. All wells were completely filled with cell growth medium and a glass slide with anti-reflex coating (WG11010R-A, Thorlabs) covers the four wells partially, providing a planar optical access and allowing for unconstrained vibration as well as air exchange. In advance to the measurement, resonance frequency of piezoelectric system loaded with the mirror and sample chamber was found at 83 kHz as described earlier. Sampling parameters $f_{\mathrm{cam}} = 1\,\mathrm{kHz}$, $N = 10$, $e_0 = 2$ and $e_1 = 3$ were selected, i.e., the baseband $m_{\mathrm{sel0}} = 0$ is demodulated to $-200\,\mathrm{Hz}$ while the first sideband $m_{\mathrm{sel1}} = +1$ is demodulated to $+300\,\mathrm{Hz}$ (Equation 2.54). The piezoelectric transducer was gently pre-stressed with two screws and rubber spacers pressing on the cover slip on top of the cell chamber.

Two independent measurement series were performed where frames were acquired for increasing excitation amplitudes. In a first experiment, a control measurement series, both the MO as well as MR beam were probing two wells without cells (Figure 2.9A). In the second series, the position of the MO beam was changed in order to probe a well with cells (Figure 2.9B). Since not only the vibrating mirror is included into the reference measurement, all potential vibration effects from cell medium, culture insert and cover slip are contributing to the control measurement which allows for a comparison of the vibration response solely originating from the cell monolayer.

Reconstructed vibration amplitudes $\hat{z}_{\Sigma}$, $\hat{z}_{\mathrm{cell}}$ and $\hat{z}_{\mathrm{vib}}$ were masked for interference

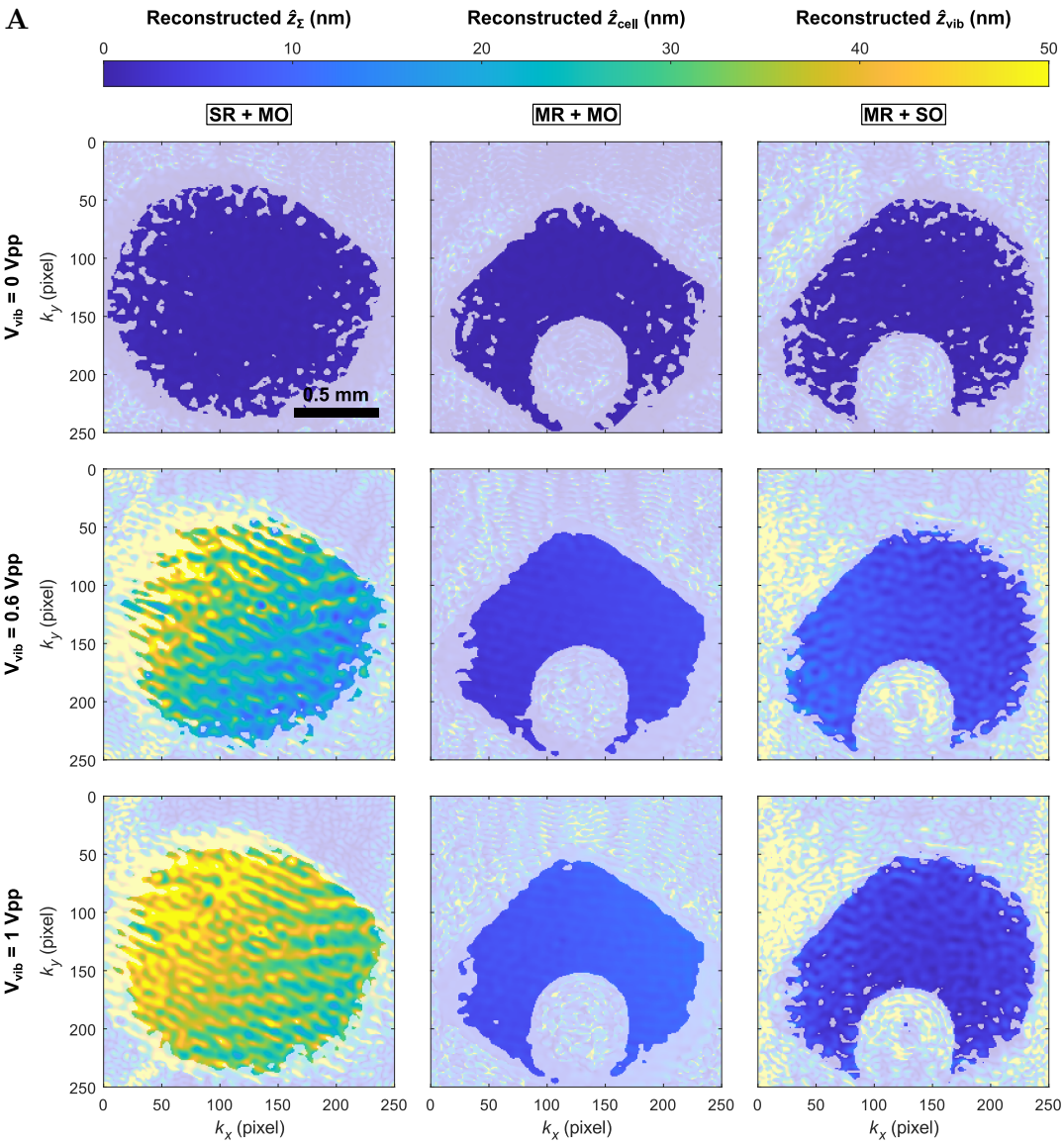

Figure 2.9.: Holographic vibration spectroscopy (HVS) on induced pluripotent stem cells (iPSCs). **A** Control measurement at two wells without cells. Vibration amplitudes $\hat{z}_\Sigma$ (left), $\hat{z}_{\mathrm{cell}}$ (center) and $\hat{z}_{\mathrm{vib}}$ (right) reconstructed from the SR + MO, MR + MO and MR + SO beam pair, respectively, for no vibration ($V_{\mathrm{vib}} = 0\,\mathrm{Vpp}$, top), $V_{\mathrm{vib}} = 0.6\,\mathrm{Vpp}$ (center) and $V_{\mathrm{vib}} = 1\,\mathrm{Vpp}$ (bottom). Vibration frequency was $f_{\mathrm{vib}} = 83\,\mathrm{kHz}$ (close to resonance) while a sampling rate of $f_{\mathrm{cam}} = 1\,\mathrm{kHz}$, an integration time of $T_{\mathrm{int}} = 988\,\mu\mathrm{s}$, $N = 10$ frames were selected for acquisition and analysis was performed over 100 frames. A validity criterion is derived from interference beam intensity. Transparent regions indicate that beam intensity was below $\exp(-2) \approx 13.5\,\%$ of its maximum. An air bubble in the MR beam led to an invalid region of reconstructed amplitude maps in the bottom center. **B** Reconstructed amplitudes from a measurement on a confluent monolayer of iPSCs arranged as in (A). Experimental conditions were the same as in (A).

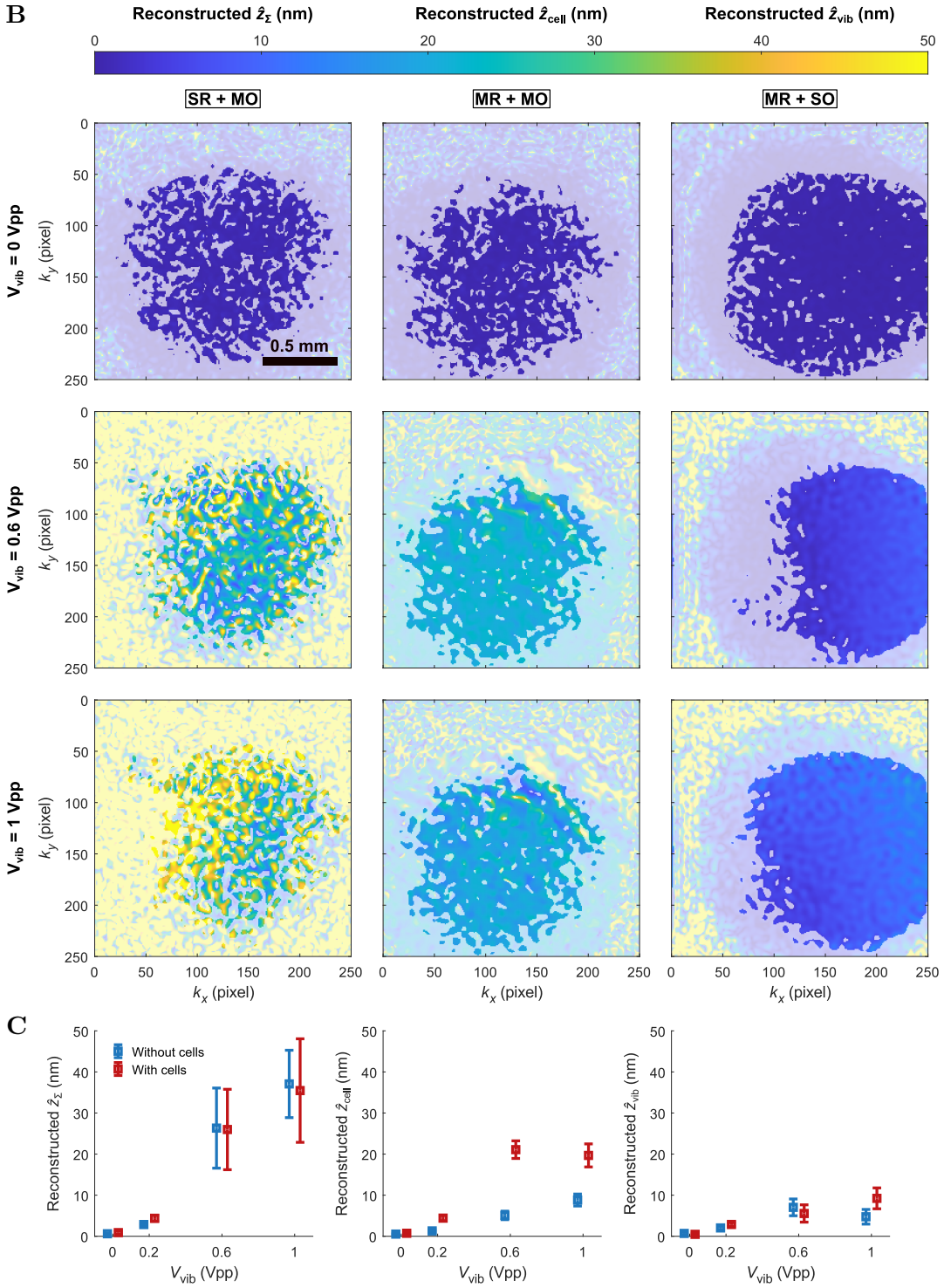

Figure 2.9.: Continued. **C** Comparison of reconstructed vibration amplitudes for driving voltages $V_{\mathrm{vib}} = 0\,\mathrm{Vpp}$, $0.2\,\mathrm{Vpp}$ (images not shown), $0.6\,\mathrm{Vpp}$ and $1\,\mathrm{Vpp}$ from (A) and (B). Mean $\pm$ standard deviation of all valid pixels are shown.

beam intensity, a measure of single strength. Only if intensity at a specific pixel is at least $\exp(-2) \approx 13.5\,\%$ of the maximum intensity of both the reconstructions, for $m_{\mathrm{sel0}} = 0$ as well as for $m_{\mathrm{sel1}} = +1$, derived data is considered to be valid. Since the intensity backscattered from the sample contains speckles, in particular for the cell measurements, validity maps are discontiguous. If excluded, calculated amplitude values are presented transparently (Figure 2.9A and B) and are not considered in the statistical comparison between measurements of the empty chamber and measurements on cells (Figure 2.9C). To assess differences, the mean and standard deviation over the populations of valid pixels are presented.

While no clear differences can be observed from the $\boxed{\text{SR + MO}}$ beam (Figure 2.9C, left), representing a superposition of mirror and cell vibrations, an increased cell vibration amplitude is assessed from the differential measurement beam pair $\boxed{\text{MR + MO}}$ (Figure 2.9C, center). With increasing driving voltage, the measured interface amplitude of wells without cells increases as well, which may originate from an increasing noise level, but the cell measurements reveal a more pronounced increase while they show a saturation starting from $V_{\mathrm{vib}} = 0.6\,\mathrm{Vpp}$. For driving voltages of $V_{\mathrm{vib}} = 0.6\,\mathrm{Vpp}$ and $V_{\mathrm{vib}} = 1\,\mathrm{Vpp}$ there is a clear response from cell monolayer vibrations of amplitude $\hat{z}_{\mathrm{cell}}$. The reconstructed amplitudes from the $\boxed{\text{MR + SO}}$ beam pair (Figure 2.9C, right), assessing solely vibrations of the mirror, show an increase with driving voltage as well, but amplitudes are much smaller in total. No clear differences between measurements with and without cells can be observed, except for $V_{\mathrm{vib}} = 1\,\mathrm{Vpp}$. This means, that the exciting vibration amplitudes $\hat{z}_{\mathrm{vib}}$ are comparable between measurements with and without cells. Since the amplitudes measured from the $\boxed{\text{MR + SO}}$ beam are smaller than the ones from the other two beam pairs and are also smaller than those from the vibrating mirror without the cell chamber in the previous experiment at the same piezo driving voltages, it is likely that vibration amplitudes accessed from the $\boxed{\text{MR + SO}}$ beam are underestimated (Figure 2.7). One difference between this beam pair compared to the other two beams as well to the measurements in the previous experiment is the analyzed vibration band, which is here $m_{\mathrm{sel1}} = -1$ in contrast to the other conditions where it is $m_{\mathrm{sel1}} = +1$. Although it was shown from theory that vibration magnitudes are the same and phases are inverse to each other (plus a phase of π), the experiments reveal a difference. Comparing the reconstructed amplitudes $\hat{z}_{\Sigma}$ from the $\boxed{\text{SR + MO}}$ beam pair to $\hat{z}_{\mathrm{cell}}$, $\hat{z}_{\mathrm{vib}}$ and amplitudes from characterizations of the bare mirror (Figure 2.7), the reconstructed amplitudes $\hat{z}_{\Sigma}$ seem to be overestimated, which can originate from the impact of vibration phases reflected by the third summand in amplitude superposition (Equation 2.61) which deviates from the geometrical mean of $\hat{z}_{\mathrm{cell}}$ and $\hat{z}_{\mathrm{vib}}$.

Reconstructed constant phase of the optical setup φ_{const} shows a tilted phase as observed from experiments utilizing off-axis holography earlier (data not shown). Phases associated to the sample φ_{Σ}, φ_{cell} and φ_{vib} reconstructed from the $\boxed{\text{SR + MO}}$, $\boxed{\text{MR + MO}}$ and $\boxed{\text{MR + SO}}$, respectively, reveal a random pattern since they lack a reference in time (data not shown).

In summary, the experiment on adherent cells reveals a clear difference in vibration amplitude which are related to cell mechanical properties as introduced earlier. I could demonstrate that the developed contact-free optical technique is able to detect a vibration response from a cell monolayer. In particular, the side-by-side comparison to measurements without the cell monolayer but including the chamber provides evidence that the observed differences originate from a vibration response in cell height.

3. Conclusions

The focus of this thesis is the development of methods to measure the mechanical properties of suspension cells as well as adherent cells. In the following, I will present the main results from four peer-reviewed research articles targeting this aim: two first-author and two co-author publications.

In the first research article, an application of RT-DC, which is a high-throughput method for mechanical phenotyping of cells in suspension (cf. Section 1.3.1), for quality assessment of peripheral blood products in transfusion medicine will be presented. The second and third publications introduce extensions of RT-DC towards high-throughput tissue mechanics and high-throughput dynamic mechanical probing yielding a complete viscoelastic parameter set for every single cell. In the fourth article, I will present a fundamental comparison of shape descriptors used as strain parameters for cells in suspension which are deformed and dynamically tracked within RT-DC.

Two of the articles were published in the journal Nature Communications, one in Lab on a Chip, and one has been submitted to the Biophysical Journal.

3.1. I. Article: Label-free on-chip quality assessment of cellular blood products using real-time deformability cytometry

For safety reasons, the highest standards of quality control have to be maintained for blood products in transfusion medicine. Since the product release for transfusion depends on quality parameters of the product, the analysis is required to be fast and quality assessment should have a minimal impact on the blood cells, which is still an unresolved challenge. Cell function is crucial for the integrity of the blood product and can be impacted, e.g., by minor variations in production and storage protocol. As of today, there is no robust technique available for cell quality assessment directly before transfusion or transplantation.

Since cell function can be linked to cell mechanical properties, high-throughput mechanical phenotyping utilizing RT-DC can address this issue, providing further advantages of low required sample volume and real-time analysis. In this publication, we used label-free mechanical analysis for fast online quality control of the blood products: platelet concentrates, red blood cell concentrates, and hematopoietic stem cells.

Platelet concentrates are usually stored at room temperature. Under this condition, however, there is a risk for bacterial contamination during the shelf time. As an alternative to room temperature, we investigated storage at 4 °C. While established

assays for platelet metabolism, activation, and aggregation did not show differences compared to storage at 4 °C, the deformation decreased significantly starting from the first day of storage. We also demonstrated that mechanical characterization reveals a significantly decreased deformation after platelet activation. Both effects render RT-DC a tool for monitoring the quality of platelets during storage.

In clinical trials, it is necessary to distinguish between the patient's own and transfused platelets to trace platelet survival which can be done by labeling with nanoparticles. We confirmed with RT-DC that platelets treated with nanoparticles do not behave mechanically different from non-labeled platelets, which is an outcome of high importance for patients' safety. Having no impact on the mechanical properties of labeled platelets, qualifies magnetic nanoparticles for an introduction to clinical use as an alternative to radioactive labeling.

For storage of red blood cell concentrates, two blood bags containing different plasticizers were investigated for their impact on the blood product. The standard di(2-ethylhexyl)phthalate (DEHP) bags have potentially harmful effects: hormone-like and toxic effects. Utilizing RT-DC, we compared red blood cell deformation over 49 days from blood stored in the standard DEHP bags to a new generation of bags based on the plasticizer diisononyl cyclohexane-1,2-dicarboxylate (DINCH) which minimizes the potentially harmful effects. DINCH, however, is known to increase hemolysis which we monitored during the storage as well. We found a lower red blood cell deformation, i.e., a higher stiffness, for cells stored in blood bags based on DINCH with a clear correlation to a slight increase in hemolysis, which highlights the potential of RT-DC to be used for rapid quality assessment of red blood cell concentrates of clinical relevance.

Finally, we investigated hematopoietic stem cells, which are cryopreserved with dimethyl sulfoxide (DMSO) for long-term storage. We compared their properties before freezing and directly after thawing the cryopreserved cells with 5 % or 10 % DMSO. Our results suggest that the viability of hematopoietic stem cells is linked to their mechanical properties: the higher the viability, the lower their deformation. This means that RT-DC can also be used for a label-free access to stem cell viability.

In summary, label-free mechanical characterization on affordable disposable microfluidic chips used in RT-DC allows for monitoring the quality of platelet, red blood cell, and stem cell products. This highlights the potential of RT-DC as an easy to integrate and powerful technoloy for clinical application.

3.2. II. Article: High-throughput cell and spheroid mechanics in virtual fluidic channels

The mechanical characterization of cells in suspension has the advantage of very high throughput, allowing for screening of cell populations providing high statistical power. Up to recently, mechanical phenotyping in microfluidic systems has been limited to

single cells. Typically, the constriction geometry has to be well chosen, i.e., channel width must not be too small, ensuring that cells are solely deformed by the hydrodynamic stress distribution and not by contact to constriction boundaries. On the other hand, the width of the channel must not be too large since forces acting on the cells get too small if the cell covers a small cross-sectional area of the constriction leading to low deformation levels and, ultimately, to a low signal-to-noise ratio (SNR). A cell should cover approximately between 55 % and 90 % of the channel width to observe a finite deformation [47]. In essence, the cross-sectional area of the channel has to be adapted to the size of the cells of interest. Within this publication, we overcame these limitations by introducing the concept of virtual channels in microfluidic and mesofluidic systems.

We established virtual fluidic channels in microfluidic chips made of PDMS using two different media for sample and sheath flow in RT-DC that are immiscible within the experimental contact time (cf. Section 1.3.1). Due to a high viscous sheath medium, a channel for the sample flow forms in its center confined by the virtual channel walls. Interestingly, the virtual channel size is defined solely by volumetric flow rates and the viscosities of the two media. We demonstrated that virtual channels can be utilized equally well to generate cell deformation, which was proven by equal results for mechanical cell characterization. In the 2.5D microfluidic design, virtual channels are confined in one dimension only. Within the square-shaped cross-section of the microchannels, the sample flow is shaped to a rectangular cross-section if two different media are used for sample and sheath flow.

We transferred the concept to the mesofluidic length scale and established virtual channels of a complete 2D confinement in a glass cuvette used in flow cytometers (side lenghts of 360 μm and length of 20 mm). The sample flow is shaped to a circular cross-section surrounded by the sheath flow although the outer dimensions of the channel have a quadratic cross-section. The virtual channel width solely depends on the volumetric flow rates and viscosities of the coflowing solutions. However, within a mesofluidic system, the adjustable range of virtual channel width extends greatly. In our system, channels ranging from a few micrometer up to more than 100 μm in diameter can be established providing a greatly increased flexibility concerning the size of the analyte. We observed two different steady-state shapes originating from two modes of deformation. If the width of a virtual channel is smaller than the average cell size, cells are predominantly deformed due to interfacial forces exerted by the liquid-liquid interface. For diameters of the virtual channel larger than those of the cells, shear and normal forces of the Poiseuille flow dominate, yielding a bullet-like cell shape if shear rates are high enough.

Material properties, i.e., a Young's modulus, can be extracted from cell shapes governed by shear and normal stresses utilizing a model introduced earlier [47]. In this paper, we extended the analysis and showed that for dominating interfacial stress, a Young's modulus can be derived from an area strain of the cells assuming volume

conservation [125] as well as an initially round-shaped cell and a calculated interfacial stress [126]. As the stress only acts in one dimension (the radial one), simple linear model assumptions are valid leading to a direct proportional dependency of interfacial stress σ_i and area strain ϵ_A connected by a cell's Young's modulus E: $\sigma_i = E\epsilon_A$. We introduced a guide for selecting the appropriate model for analysis by performing numerical finite element method (FEM) simulations.

In this publication, we demonstrated for the first time that spheroids as a 3D tissues model can be mechanically characterized at high throughput within a cuvette from flow cytometry enabled by the concept of virtual channels. Spheroids, round cell clusters grown from a few single cells in microwells and which consisted between 600 and 900 single cells each, were deformed in a virtual channel of appropriate size. Interestingly, a comparison of single HEK293T cells to spheroids consisting of approximately 650 HEK293T cells on average reveals a Young's modulus for spheroids of one order of magnitude lower than the one of single cells. The distinct mechanical behavior suggests that cell-cell interactions, the extracellular matrix and cell organization in tissues, may contribute to the probed mechanical response under external stress. Utilizing virtual channels in mesofluidic systems would allow for an investigation of those mechanical interactions.

A strength of virtual channels is their outstanding scalability. We showed that within seconds, the channel width can be tuned from a few micrometer all the way up to more than 100 μm, allowing for mechanical characterization of single cells as well as *in vitro* 3D tissue models within one experimental setup. In doing so, we provide the ability to study mechanical keys in a natural cell environment including cell-cell and cell-matrix interactions in cytometric systems at high throughput and a label-free manner. Specifically, the comparison between single cells, cells isolated from tissue, and tissues of different structures and complexity allows for a deep insight into cellular organization and function as well as mechanical adaptation and interaction. The integration into flow cytometers, which are well established in scientific and clinical routines, renders mechanical phenotyping in virtual channels a technology which is easy to use in laboratories around the world.

3.3. III. Article: High-throughput single-cell rheology in complex samples by dynamic real-time deformability cytometry

By introducing dynamic real-time deformability cytometry (dRT-DC) I extended the method RT-DC by another material parameter, the cell's viscosity, and therefor provided a complete viscoelastic description of a cell (see Section 1.2). While within RT-DC, the Young's modulus can be derived from a single snapshot of a stress-strain experiment in equilibrium, viscosity relies on a time-dependent measurement. To capture the complete dynamics of a cell while passing a constriction and to extract viscoelastic properties, video microscopy is required to track the moving cells.

In the article, we demonstrated a dynamic tracking of up to 100 cells per second while capturing at least 10 images per cell inside the channel. We found that the cell deformation is a superposition of two responses. While a cell approaches the channel, it first responds to a high peak stress at the inlet due to an acceleration into the constriction. Starting from the inlet position, the cell also responds to a lower and constant stress acting on the cell as normal and shear forces originating from the Poiseuille flow inside the channel. As the two stress distributions overlap, cells reveal a superimposed stress response curve. I introduced a shape mode decomposition utilizing a Fourier transformation applied to the cell contour in a polar representation (see Section 2.2). The peak stress at the inlet elongates the cell in the direction of flow revealing an ellipsoidal shape that is symmetric both parallel as well as perpendicular to the direction of flow. Inside the channel, the cell mimics the Poiseuille flow profile progressing towards a bullet-like shape with only one symmetry axis in the direction of flow. Even Fourier components reflect shapes with symmetries along two axes while odd components are only symmetrical in one direction. A shape reconstruction separated into the subset of even and odd Fourier components and subsequent calculation of the deformation parameter (Equation 1.12) yields two distinct cell responses to inlet and channel stress, respectively.

We extracted cell material properties after separation of both stress contributions. Focusing solely on the response to channel stress allows for a straightforward analysis since the stress distribution is constant within the channel and close to zero before the inlet, representing a simple step-stress experiment. Assuming a Kelvin-Voigt model (see Section 1.2.3), yields an exponentially increasing strain for an applied step stress. A characteristic relaxation time and the steady-state deformation are extracted from an exponential fit to cell response traces to channel stress. The cell's Young's modulus can be derived from steady-state deformation as introduced earlier [24, 47]. In conjunction with the characteristic time, which represents the ratio of viscosity and Young's modulus (Equation 1.6), the viscous component can also be calculated yielding a complete viscoelastic description for every single cell.

Since the response to the inlet stress reflects also a relaxation process, deformation magnitude and characteristic time were extracted from an exponential fit to the inlet response as well. But since the analytical stress is unknown for the inlet, no material properties were derived.

We used dRT-DC to extract viscoelastic material properties from more than 3000 HL60 cells, a human leukemia cell line (cf. Section 2.1.1). Young's moduli are in agreement with values reported earlier [64] while median viscosity is almost two orders of magnitude lower than previously published results [13]. However, due to the high throughput and low translocation times, defining the time of a cell in the constriction, experimental shear rates are higher in dRT-DC. The difference might originate from the shear-thinning effects of the cytoskeleton [13] since cytoplasmic viscosity has been shown to be shear-rate dependent [127].

Additionally, we confirmed a decrease in elasticity and viscosity for HL60 cells treated with cytochalasin D, a compound that inhibits the polymerization of filamentous actin leading to a weakening of the cytoskeleton.

With dRT-DC, I also introduced a method for determining viscoelastic properties independent of cell shape since the deformation reconstructed from the odd Fourier components representing the channel response is always close to zero at channel inlet. Originating from symmetry arguments only, zero deformation at the beginning of the channel response is a requirement for simple mechanical models [67]. Therefore, dRT-DC can be applied to cells with a shape deviating from a circle, allowing for the analysis of complex samples such as blood consisting of different cell types with diverse shapes and properties. We demonstrate the potential of the technique in a characterization of the major subpopulations of peripheral human blood within the same experimental setup and find that the subpopulations reveal a distinct mechanical fingerprint. Interestingly, two subpopulations of the lymphocytes fraction, B- and T-cells, could be shown to have significantly different mechanical properties.

In summary, dynamic RT-DC gives access to the elastic as well as viscous mechanical components of single cells at high throughput and in real time. With dRT-DC, complex samples can be analyzed independent of cell shape.

The interdisciplinary importance of this publication is also reflected by its acknowledgement as the paper of the month in March 2019 by the German Center for Cardiovascular Research (DZHK).

3.4. IV. Manuscript: Cellular shape descriptors determine the outcome of viscoelastic analyses in microfluidic systems

A mechanical test is based on the application of stress while monitoring the strain or vice versa. The shape of deforming cells or tissue is a key parameter, since stress is applied in deformability cytometry and many other techniques for assessing mechanical properties of cells and tissues (cf. Section 1.3). Beyond shape analysis for mechanical interpretation, morphological analysis of cells is generally of high relevance in biomedical research, which can be seen from approximately 1000 publications over the last 20 years using image-based cell analysis [128].

Shape descriptors provide an effective quantification of cell shapes and are used as strain parameters. Fundamental comparisons of shape descriptors are available for adherent cells but are lacking for cells in suspension. To fill this gap, I compared the following shape descriptors and applied them to stress response traces from more than 4800 HL60 cells acquired by dynamic RT-DC: area, normalized front radius, axes ratio, Taylor deformation, principal axes ratio, rescaled circularity, inverse Haralick's circularity, circular variance and inertia ratio. Except for area, all shape descriptors are used as a measure of cell deformation.We investigated stress relaxation times

(as introduced in Article III, Section 3.3) which represent cell material properties (Equation 1.6) and which can be derived from an exponential fit to the stress response curves, assuming a Kelvin-Voigt model (see Section 1.2.3).

I introduced stress relaxation time analyses on several levels of data aggregation. The analysis with the least computational effort is performed by overlaying all acquired deformation-time traces into a master curve and subsequent exponential fitting. Since the deformation response of a cell passing the constriction is a superposition of responses to the inlet and channel stress (see Section 3.3), not all shape descriptors reveal a monotonic behavior but show a minimum. We showed that from the ensemble response of rescaled circularity, inverse Haralick's circularity, and circular variance no relaxation time can be extracted.

In a second approach, we analyzed relaxation times from ensemble responses reconstructed from the even and odd Fourier coefficient subsets, i.e., separated for inlet and channel effects, respectively. Axes ratio and Taylor deformation reveal no relaxation to the channel stress within this analysis.

The most detailed picture one can get when fitting deformation-time traces after Fourier decomposition on a single-cell level. Since a pair of inlet and channel relaxation times can be fitted for every single cell, this strategy results in characteristic time distributions for each shape descriptor.

We showed that the extracted relaxation times depend on the employed shape descriptor as well as the selected analysis strategy, while all extracted relaxation times are on the lower milliseconds timescale and span a range of less than one order of magnitude for HL60 cells.

Not all of the deformation-time traces reach the equilibrium within the channel. One single measurement in equilibrium is required to extract elastic material parameters. Since cells are tracked dynamically, i.e., a time-dependent measurement is performed, it is no longer necessary to capture the steady-state deformation. We demonstrated that the relaxation time as well as steady-state deformation can be extracted from the fit, even if the steady-state is not captured. However, a significant fraction of deformation amplitude must be reached at the end of the channel, to guarantee a stable parameter readout. Here, I introduced an amplitude fraction, a ratio of deformation reached at channel end and steady-state deformation, and translated it to the time-domain to be applied as a cut-off criterion directly to relaxation times. I proposed an amplitude fraction of 50 % and demonstrated within simulations that errors of relaxation times from single-cell analyses as well as on an ensemble level are lower than approximately 10 % if the mean translocation time of cells in the channel is at least twice the median relaxation time of a cell population.

We studied the sensitivity of shape descriptors for cytoskeletal modifications by treating HL60 cells with cytochalasin D inhibiting the polymerization of filamentous actin. An effect size was calculated relating relaxation times from treated HL60 cells to their vehicle (dimethyl sulfoxide (DMSO) treatment). To rank the shape descriptors

and their sensitivity, I introduced a score from the effect sizes and their p-values of significance against an effect size of one, meaning it has no effect. We found that, in general, shape descriptors evaluating the inlet effects yield higher scores, which might originate from the higher probing stress. However, mechanical properties can only be extracted from the channel response since the stress at the inlet is unknown. We observed the highest scores for channel stress response from the shape descriptors inverse Haralick's circularity, normalized front radius, and rescaled circularity (Equation 1.12).

We provided with the manuscript a guide for the selection of a shape descriptor and data analysis strategy, and thereby rule out arbitrariness in the data analysis routine. We further compared the sensitivity of each combination of shape descriptor and analysis strategy for HL60 cells with a modified cytoskeleton. The fact that the steady-state deformation does not need to be reached for dynamic measurements, allows for a speed-up in throughput since the translocation time of a cell within the constriction can be shortened.

4. Summary

Cell mechanical properties reveal substantial information on cell state and function. Utilizing mechanics as a label-free biomarker allows for investigation of fundamental cellular processes as well as biomedical applications, e.g., disease diagnosis. High-throughput methods for accessing the elastic properties of cells in suspension from hydrodynamic deformation in a microfluidic constriction are available with real-time analysis rates of up to 1000 cells per second. However, accessing elastic as well as viscous properties of cells and multicellular systems in suspension as well as adhered to surfaces at high throughput has not been possible so far. In this thesis, I approached this question and developed as well as applied microfluidic and holographic technologies to analyze the viscoelastic properties of single cells and multicellular aggregates, respectively.

First, I demonstrated that real-time deformability cytometry (RT-DC) can be applied in transfusion medicine, where the highest quality standards have to be maintained while blood product release is time-critical. We showed for platelet and red blood cell concentrates as well as for hematopoietic stem cells that their mechanical properties can be used for label-free quality assessment. The results have been published in *Lab on a Chip* [49] (Article I, concluded in Section 3.1).

For RT-DC and many other methods based on hydrodynamic deformation, the constriction size has to be adapted to the objects of interest to allow for a shear-induced deformation. We introduced virtual fluidic channels, which are established by two co-flowing aqueous polymer solutions. Virtual fluidic channels can be precisely adjusted in their cross section, allowing for mechanical phenotyping of single cells as well as cell clusters or tissue spheroids in one microfluidic system. Importantly, measurements can also be performed in standard microfluidic geometries beyond soft lithography, e.g., in the cuvette of a flow cytometer. For cell spheroids as a model system for multicellular aggregates, we show a 10-fold lower Young's modulus of the tissue compared to single-cell mechanics, suggesting cell-cell and cell-matrix interactions being potential contributors to the mechanics of multicellular aggregates. Our work on virtual fluidic channels has been published in *Nature Communications* [50] (Article II, concluded in Section 3.2).

Within this thesis, I expanded the high-throughput elastic phenotyping performed by RT-DC towards viscoelastic cell properties by developing dynamic real-time deformability cytometry (dRT-DC). Dynamic tracking of cells while passing the microfluidic constriction allows to access steady-state (elasticity) and time-dependent (viscosity)

material properties for a complete viscoelastic characterization of cells in suspension at high throughput. I introduced a shape mode decomposition based on a Fourier transformation, which allows to disentangle the superimposed stress responses to an extensional stress at the channel inlet and a constant shear stress in the channel. These hydrodynamic stress distributions are present in almost every microfluidic channel geometry. From the separated stress responses, viscoelastic material properties can be determined independent of cell shape.

We demonstrated experimentally the sensitivity of dRT-DC to cytoskeletal alterations and confirmed the validity of the method by reference measurements on calibrated hydrogel beads. In our work, we also presented a viscoelastic fingerprint of the major subpopulations of peripheral blood: erythrocytes, granulocytes, and peripheral blood mononuclear cells (PBMCs) (e.g., lymphocytes and monocytes), all characterized by the same method. The technique and the results have been published in *Nature Communications* [48] (Article III, concluded in Section 3.3).

In cell mechanical methods based on hydrodynamic deformation, cell shape is usually monitored while a stress is applied. For extraction of material properties as well as for studying shape dynamics, it is essential to describe cell shape yielding highest strain differences for a given microfluidic system and experimental setting. Using dRT-DC, I compared nine different shape descriptors to analyze cell deformation in an extensional as well as shear flow. A relaxation time analysis was performed on different levels of data aggregation from single cells to an ensemble scale. I demonstrated that the steady-state deformation can be predicted from stress response curves without them reaching the steady-state. This is important for cell mechanical measurements in microfluidic systems as the characteristic times are unknown in general and as the channel length is fixed. In addition, by introducing a cut-off criterion for how much of the response trace needs to be captured within the channel, the analysis time per cell can be reduced while material properties can still be extracted. Performing simulations, I compared the accuracy of relaxation times extracted from ensemble and single-cell studies under experimental conditions. Introducing a scoring system to evaluate which combinations of shape descriptors and analysis strategies provide biggest effect size, we concluded that single-cell analyses in an extensional flow are most sensitive to cytoskeletal modifications independent of shape parametrization. The manuscript was submitted to the *Biophysical Journal* (Manuscript IV, concluded in Section 3.4).

Finally, I translated the fast non-contact cell mechanical probing from suspension to adherent cells. No such technology has been available and with the majority of cells being adherent, a robust label-free method for mechanophenotyping at high-throughput is required. Within this thesis, I have introduced and realized a new concept: holographic vibration spectroscopy (HVS), where adherent cells are mechanically excited on a vibrating surface while their height oscillations are measured optically. Analysis is done in an interferometric heterodyne setup by using frequency multiplexing and time-averaged holography in off-axis configuration. Based on interference images captured by a high-speed complementary metal-oxide-semiconductor (CMOS) camera,

I established a mathematical model to reconstruct the vibration amplitude of adherent cells as well as their retardation phase compared to the exciting vibration. From the amplitude and phase response, viscoelastic parameters can be derived, which have to be investigated in subsequent studies. The method was introduced in detail and first results were presented in Section 2.3.

In summary, I introduced in my work two high-throughput methods for the viscoelastic characterization of suspended as well as adherent cells while highlighting applications in tissue mechanics and transfusion medicine that are relevant not only in basic but also in translational research.

5. Outlook

With the methods developed in this thesis, multiple applications can be targeted. In Section 5.1, I will present preliminary data on a comparison of red blood cell mechanics between humans and a bat species able for hibernation. Since these animals are mammals as we are but can survive at body temperatures close to 0 °C, they might behave differently in blood circulation as well as regulation processes.

In Section 5.2, I will suggest further developmental steps and will give some perspectives on potential applications of the new method holographic vibration spectroscopy (HVS) for high-throughput mechanophenotyping of adherent cells, which I introduced in Section 2.3.

5.1. Red blood cell viscoelasticity as key regulator for hibernation in bats

Hibernating mammals are unique in their ability to survive at body temperatures close to zero degree celsius in torpor while having a body temperature around 37 °C in euthermy [129]. The common noctule (*Nyctalus noctula*) is a species of bats that is able to hibernate. In its awake state, *Nyctalus noctula* has a body temperature of 36.5 °C whereas a body temperature below 6 °C could be measured during hibernation at an ambient temperature of 3 °C [130]. When awaking, the temperature can rise by more than 20 °C in 60 min, regulated by the heart rate. This was measured at an ambient temperature of 8 °C and is accelerated for higher ambient temperatures [130].

While hibernating animals can maintain cardiac function, blood flow, respiration, and metabolism, in humans, the shivering response fails, their heart begins to fibrillate, and ultimately, the respiration ceases if body temperature is decreased [129]. To investigate the role of viscoelastic material properties in hibernation, I measured red blood cells of bats (*Nyctalus noctula*) from ten animals utilizing dRT-DC at three different temperatures and compared the results to the samples from ten human donors. Besides room temperature (≈ 23 °C), the samples were measured in a cold (≈ 10 °C) and warm (≈ 37 °C) environment. Since the blood was drawn at room temperature, no regulatory effects inside the body are contributing to the measurement.

While red blood cells from both species undergo similar shape changes, a clear difference in cell size can be observed (Figure 5.1A and B, left). Both the steady-state deformation inside the channel $\hat{d}_{\text{channel}}$ as well as the corresponding relaxation time τ_{channel} show different trends over temperature for humans and bats (Figure 5.1B, center and left). While $\hat{d}_{\text{channel}}$ of red blood cells from bats is independent of the temperature, erythrocytes from humans show an increasing deformation with temperature.

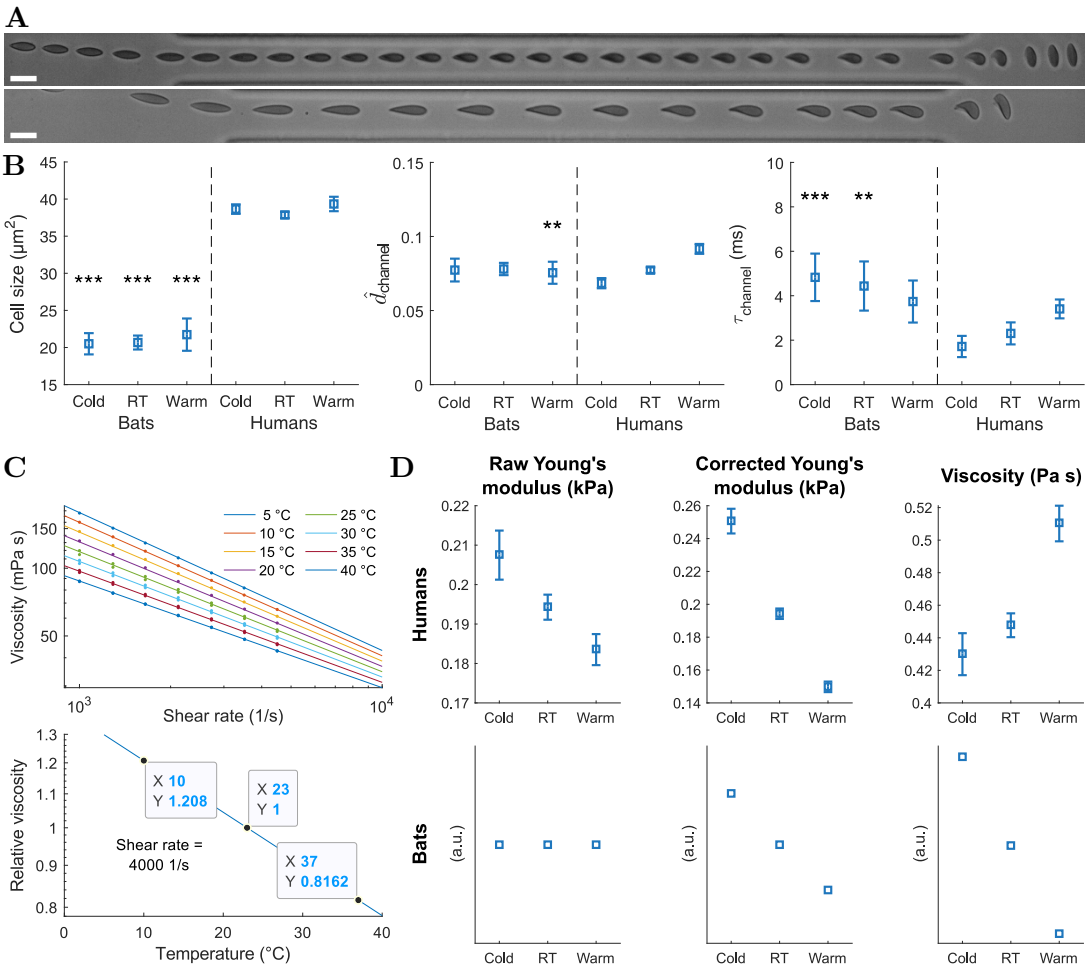

Figure 5.1.: Temperature-dependent rheology of red blood cells from humans and bats (*Nyctalus noctula*). **A** Time series of shape changes of an exemplary red blood cell from bats (top) and humans (bottom). To avoid overlap in the stitched image, 30 out of 45 frames (top) and 15 out of 32 captured frames (bottom) are shown. Scale bar is 10 μm. **B** Temperature-dependent comparison of red blood cells from 10 bats and 10 humans: cell size (left), deformation amplitude (center) and characteristic time of the deformation (right) within the channel. Measurements were carried out in a microchannel of 20 × 20 μm cross section and of 300 μm length at a flow rate of 8 nls^{-1}. Temperature is kept constant during measurements at approximately 10 °C (cold), 23 °C (RT, room temperature) or 37 °C (warm). Mean ± SEM is presented. Significances are derived from linear mixed models (LMMs) comparing bats and humans at each temperature level (**$p < 0.01$; ***$p < 0.001$). **C** Temperature-dependent rheological characterization of the measurement buffer. Dynamic viscosity over shear rate, lines represent a fit to the data points (top). Derived relative viscosity, which is normalized to a temperature of 23 °C, at a shear rate of 4000 s^{-1}, present in the experiments. **D** Raw Young's modulus (left), Young's modulus corrected for the temperature-dependent cell buffer viscosity (center) and cell viscosity (right) for humans (top) and bats (bottom). Mean ± SEM is presented for human samples.

Relaxation times τ_{channel} have a negative or positive trend over temperature for bats and humans, respectively.

Since measurements were carried out in a cell buffer, composed of methylcellulose (1.0 % w/v) dissolved in phosphate buffered saline, with rheological characteristics depending on the temperature as well, results have to be corrected for this dependency. Therefore, I characterized the cell carrier with a rheometer (MCR502, Anton Paar) using a cone-plate system (modules CP50-2/TG and P-PTD200/TG, Anton Paar) (Figure 5.1C). Subsequently, the following model was fitted to the data points and resulted in scaling factors p_1 to p_4

$$\begin{aligned}\log_{10}(\text{viscosity (mPa s)}) = {} & p_1 + p_2 \cdot \log_{10}\Big(\text{shear rate } \left(\text{s}^{-1}\right)\Big) \\ & + p_3 \cdot (\text{temperature } (^\circ\text{C})) \\ & + p_4 \cdot \log_{10}\Big(\text{shear rate } \left(\text{s}^{-1}\right)\Big) \cdot (\text{temperature } (^\circ\text{C})) \\ \text{with } p_1 = {} & +4.18882 \\ p_2 = {} & -0.632717 \\ p_3 = {} & -0.0205908 \\ p_4 = {} & +0.00396732\ .\end{aligned} \tag{5.1}$$

For a shear rate of $4000\,\text{s}^{-1}$, estimated from the experiments (velocity of the cells is $\approx 4\,\text{cm/s}$ and channel radius is $\approx 10\,\mu\text{m}$), a relative viscosity is derived, which is normalized to the viscosity at 23 °C, since the subsequent calculation of the Young's modulus is performed for room temperature.

From cell deformations of human red blood cells, a Young's modulus could be extracted as described earlier [48] (Figure 5.1D, left). However, no Young's modulus could be calculated for the erythrocytes from bats. Due to their low level of channel deformation and their small size, the cells are outside of the range from which Young's moduli are predictable. But since channel deformation and cell size reveal almost no temperature dependency in the experiments, a constant Young's modulus is assumed for a qualitative analysis. According to the scaling law $E_0' = \eta'/\eta \cdot E_0$ with rescaled viscosity η' and Young's modulus E_0' as well as initial viscosity η and Young's modulus E_0 [47], Young's moduli are corrected for the temperature-dependent viscosity of the cell carrier (Figure 5.1D, center). Cell viscosity is the product of the Young's modulus and the characteristic time [48] (Figure 5.1D, right).

While the Young's modulus, i.e., the stiffness, of erythrocytes shows the same negative trend over temperature for humans and bats, their viscosity reveals an opposite effect. Intuitively, the viscosity of fluids is decreasing for increasing temperatures since a material gets thinner if temperature is increased, as it is the case for the bats. A higher viscosity of erythrocytes from bats at low temperatures in combination with a potentially reduced delivery rate of the heart in hibernation leads to an increased circulation time. This would give the cells more time for oxygen uptake in the lungs

as well as for oxygen release in the organs. Strikingly, for human erythrocytes, the apparent viscosity increases with temperature. Of note, from dRT-DC the viscoelastic properties of the cells are accessed and not the bulk properties of the entire blood.

I demonstrated in preliminary experiments that human erythrocytes behave mechanically different from those of the hibernating bat species *Nyctalus noctula*. In further experiments, we would like to study another bat species which is not able to hibernate. This could further clarify whether the species *Nyctalus noctula* behaves differently from human blood cells or whether the effect may arise from its ability of hibernation.

5.2. Holographic vibration spectroscopy

In this thesis, I introduced a non-contact and spatially resolved method for mechanical phenotyping of adherent cells and tissue at high throughput. In Section 2.3 of this thesis on holographic vibration spectroscopy, a change in vibration amplitude originating from a monolayer of induced pluripotent stem cell was demonstrated. Elastic material properties can be derived from cells' vibrational amplitude with respect to the excitation amplitude, while the retardation phase represents their viscous properties.

For an estimation of cell vibration amplitude, the change in refractive indices between cells and surrounding cell medium is required, as seen from Equations 2.65 and 2.70. This dependency can be circumvented by measuring at two different laser wavelengths [131]. However, polarization optics such as wave retarders depend on the wavelength. Therefore, Fresnel rhombs are used in the current optical setup as wave retarders, which shift the light wave by $\lambda/4$ or $\lambda/2$ independent of the wavelength, which allows for a straightforward extension of the setup by another laser. By using dichroic mirrors, the beams from both lasers can be separated, before directed to the camera, and detected simultaneously. If the difference between both wavelengths is small, such that wavelength-dependency of refractive indices can be neglected, the change in refractive indices between the cells and cell medium can be determined and hence, the cell vibration amplitude.

Phases extracted from the cell measurement have not been presented in this work since they have no reference in time and hence, they need to be compared to each other (subtracted), which requires algorithms that do not disturb the phase during analysis. The angular spectrum method, used for twin image separation and noise suppression, however, does impact the phase since it demodulates the spatial frequency of the fringes from off-axis holograms and the demodulation is done for each beam pair separately which makes a comparison between beams impossible. A potential solution is, to enlarge the MO beam such that also the well without cells is imaged (no overlap with the MR beam should be ensured). In this case, the phases could be compared within the image stack recorded from one beam pair.

Based on the parameters extracted from experiments (amplitude ratio and retardation phase), viscoelastic material properties of cells can be determined by comparing the measured parameters to the expected parameters modeled from known material

properties (equivalent to solving the inverse problem). Both the solid model or the power-law structural damping model are candidates for the mechanical dynamics of adherent cells [51]. In previous studies utilizing vibrational excitation of cells, models consisting of springs, dashpots, and masses were used [109–111] as well as FEM simulations [72], which could be employed here too.

To study tissue rheology over frequency, a vibration frequency response of cells can be recorded by excitation at multiple vibration frequencies, either in a time sequence or at once from a superposition of multiple vibration modes. The different modes could be demodulated and decoupled by the sampling rate of the camera. In this scenario, no multiples of vibration frequencies are allowed since they would overlap with the sidebands of another exciting frequency. An alternative could be the recording of a step response and extraction of the rheological frequency-dependency from the time spectrum. However, the strong dependency of vibration amplitude on frequency of the piezoelectric actuators have to be considered for that or another implementation of vibration excitation has to be found.

For improved applicability of the technique for biological and biomedical research, adherent cells in a multi-well plate could be mechanically screened by pressing a vibrating mirror against the bottom of a well and optically determine the parameters from above. Also a changed setup geometry is conceivable – instead of using the reflection from a mirror beneath the cells, a measurement in transmission could be performed. In this case, cells would be illuminated from the top while the light which passed through the tissue is directed to the detector. Since the optical path length of a transmission beam only changes when the cells' height is modulated and does not change by the vibration itself (as the case in the current setup), no moving reference beam (MR) would be required. However, for the reference measurement of the exciting vibrating, a reflecting interface has to be found. Still, adherent cells in a multi-well plate could be phenotyped within the modified setup, e.g., by using a ring-shaped vibration actuator.

While I already demonstrated the new method on a monolayer of adherent cells, it can be expanded to multi-layered cell tissues as well. However, the thicker the sample, the more the probing beam is aberrated due to laser-tissue interaction or speckling. To overcome aberrations introduced by the sample, adaptive optics, in particular, phase correction by a phase modulator, could be applied.

After having the method established, diverse biomedical applications can be targeted. Tissue mechanics could be studied over time as well as mechanical cell communication in tissues. Differentiation assays could be performed on adherent cells, e.g., by capturing the mechanical properties of differentiating cells surrounded by other cells and depending on the extracellular matrix. Also, the impact of drugs on a tissue can be monitored over time as well as diseases diagnosed on primary tissue samples.

6. Bibliography

1. Trepat, X. *et al.* Universal physical responses to stretch in the living cell. *Nature* **447,** 592–595. doi:10.1038/nature05824. arXiv: NIHMS150003 (May 2007).
2. Bao, G. & Suresh, S. Cell and molecular mechanics of biological materials. *Nat. Mater.* **2,** 715–725. doi:10.1038/nmat1001 (Nov. 2003).
3. Di Carlo, D. A Mechanical Biomarker of Cell State in Medicine. *J. Lab. Autom.* **17,** 32–42. doi:10.1177/2211068211431630 (Feb. 2012).
4. Darling, E. M. & Di Carlo, D. High-Throughput Assessment of Cellular Mechanical Properties. *Annu. Rev. Biomed. Eng.* **17,** 35–62. doi:10.1146/annurev-bioeng-071114-040545 (Dec. 2015).
5. Zorgani, A. *et al.* Brain palpation from physiological vibrations using MRI. *Proc. Natl. Acad. Sci.* **112,** 12917–12921. doi:10.1073/pnas.1509895112 (Oct. 2015).
6. Orr, A. W., Helmke, B. P., Blackman, B. R. & Schwartz, M. A. Mechanisms of Mechanotransduction. *Dev. Cell* **10,** 11–20. doi:10.1016/j.devcel.2005.12.006 (Jan. 2006).
7. Hoffman, B. D. & Crocker, J. C. Cell Mechanics: Dissecting the Physical Responses of Cells to Force. *Annu. Rev. Biomed. Eng.* **11,** 259–288. doi:10.1146/annurev.bioeng.10.061807.160511 (Aug. 2009).
8. Wu, P.-H. *et al.* A comparison of methods to assess cell mechanical properties. *Nat. Methods* **15,** 491–498. doi:10.1038/s41592-018-0015-1 (July 2018).
9. Campàs, O. *et al.* Quantifying cell-generated mechanical forces within living embryonic tissues. *Nat. Methods* **11,** 183–189. doi:10.1038/nmeth.2761. arXiv: arXiv:1011.1669v3 (Feb. 2014).
10. Polacheck, W. J. & Chen, C. S. Measuring cell-generated forces: a guide to the available tools. *Nat. Methods* **13,** 415–423. doi:10.1038/nmeth.3834 (May 2016).
11. Lippincott-Schwartz, J. Development and Use of Fluorescent Protein Markers in Living Cells. *Science (80-.).* **300,** 87–91. doi:10.1126/science.1082520 (Apr. 2003).
12. Marks, K. M. & Nolan, G. P. Chemical labeling strategies for cell biology. *Nat. Methods* **3,** 591–596. doi:10.1038/nmeth906 (Aug. 2006).
13. Ekpenyong, A. E. *et al.* Viscoelastic Properties of Differentiating Blood Cells Are Fate- and Function-Dependent. *PLoS One* **7** (ed Lam, W.) e45237. doi:10.1371/journal.pone.0045237 (Sept. 2012).

14. Gossett, D. R. *et al.* Hydrodynamic stretching of single cells for large population mechanical phenotyping. *Proc. Natl. Acad. Sci.* **109,** 7630–7635. doi:10.1073/pnas.1200107109 (May 2012).

15. Urbanska, M. *et al.* A comparison of microfluidic methods for high-throughput cell deformability measurements. *Nat. Methods* **17,** 587–593. doi:10.1038/s41592-020-0818-8 (June 2020).

16. Urbanska, M. *et al.* De novo identification of universal cell mechanics regulators. *bioRxiv,* 45. doi:10.1101/2021.04.26.441418 (2021).

17. Rosendahl, P. *et al.* Real-time fluorescence and deformability cytometry. *Nat. Methods* **15,** 355–358. doi:10.1038/nmeth.4639 (May 2018).

18. Discher, D. E. Tissue Cells Feel and Respond to the Stiffness of Their Substrate. *Science (80-.).* **310,** 1139–1143. doi:10.1126/science.1116995 (Nov. 2005).

19. Janmey, P. A. & McCulloch, C. A. Cell Mechanics: Integrating Cell Responses to Mechanical Stimuli. *Annu. Rev. Biomed. Eng.* **9,** 1–34. doi:10.1146/annurev.bioeng.9.060906.151927 (Aug. 2007).

20. Ogneva, I. V. Cell Mechanosensitivity: Mechanical Properties and Interaction with Gravitational Field. *Biomed Res. Int.* **2013,** 1–17. doi:10.1155/2013/598461 (2013).

21. Das, T. *et al.* A molecular mechanotransduction pathway regulates collective migration of epithelial cells. *Nat. Cell Biol.* **17,** 276–287. doi:10.1038/ncb3115 (Mar. 2015).

22. Nasrollahi, S. *et al.* Past matrix stiffness primes epithelial cells and regulates their future collective migration through a mechanical memory. *Biomaterials* **146,** 146–155. doi:10.1016/j.biomaterials.2017.09.012 (Nov. 2017).

23. Rigato, A., Miyagi, A., Scheuring, S. & Rico, F. High-frequency microrheology reveals cytoskeleton dynamics in living cells. *Nat. Phys.* **13,** 771–775. doi:10.1038/nphys4104 (Aug. 2017).

24. Otto, O. *et al.* Real-time deformability cytometry: on-the-fly cell mechanical phenotyping. *Nat. Methods* **12,** 199–202. doi:10.1038/nmeth.3281 (Mar. 2015).

25. Pushkarsky, I. *et al.* Elastomeric sensor surfaces for high-throughput single-cell force cytometry. *Nat. Biomed. Eng.* **2,** 124–137. doi:10.1038/s41551-018-0193-2 (Feb. 2018).

26. Adamo, A. *et al.* Microfluidics-Based Assessment of Cell Deformability. *Anal. Chem.* **84,** 6438–6443. doi:10.1021/ac300264v. arXiv: NIHMS150003 (Aug. 2012).

27. Islam, M. *et al.* Microfluidic Sorting of Cells by Viability Based on Differences in Cell Stiffness. *Sci. Rep.* **7,** 12. doi:10.1038/s41598-017-01807-z (Dec. 2017).

28. Byun, S. *et al.* Characterizing deformability and surface friction of cancer cells. *Proc. Natl. Acad. Sci.* **110,** 7580–7585. doi:10.1073/pnas.1218806110. arXiv: arXiv:1408.1149 (May 2013).

29. Alberts, B. *et al. Essential cell biology* 4th ed. (Garland Publishing, 2014).

30. Kasza, K. E. *et al.* The cell as a material. *Curr. Opin. Cell Biol.* **19,** 101–107. doi:10.1016/j.ceb.2006.12.002 (Feb. 2007).

31. Fletcher, D. A. & Mullins, R. D. Cell mechanics and the cytoskeleton. *Nature* **463,** 485–492. doi:10.1038/nature08908 (Jan. 2010).

32. Mulla, Y., MacKintosh, F. C. & Koenderink, G. H. Origin of Slow Stress Relaxation in the Cytoskeleton. *Phys. Rev. Lett.* **122,** 218102. doi:10.1103/PhysRevLett.122.218102. arXiv: 1810.08165 (May 2019).

33. Bonakdar, N. *et al.* Mechanical plasticity of cells. *Nat. Mater.* **15,** 1090–1094. doi:10.1038/nmat4689 (Oct. 2016).

34. https://pubmed.ncbi.nlm.nih.gov/. (accessed: Jan 25, 2021).

35. Ashkin, A., Dziedzic, J. M., Bjorkholm, J. E. & Chu, S. Observation of a single-beam gradient force optical trap for dielectric particles. *Opt. Lett.* **11,** 288. doi:10.1364/OL.11.000288 (May 1986).

36. Guck, J. *et al.* The Optical Stretcher: A Novel Laser Tool to Micromanipulate Cells. *Biophys. J.* **81,** 767–784. doi:10.1016/S0006-3495(01)75740-2 (Aug. 2001).

37. Hochmuth, R. M. Micropipette aspiration of living cells. *J. Biomech.* **33,** 15–22. doi:10.1016/S0021-9290(99)00175-X (Jan. 2000).

38. Dufrêne, Y. F., Viljoen, A., Mignolet, J. & Mathelié-Guinlet, M. ¡scp¿AFM¡/scp¿ in cellular and molecular microbiology. *Cell. Microbiol.* **23,** 1–12. doi:10.1111/cmi.13324 (July 2021).

39. Desprat, N., Richert, A., Simeon, J. & Asnacios, A. Creep Function of a Single Living Cell. *Biophys. J.* **88,** 2224–2233. doi:10.1529/biophysj.104.050278 (Mar. 2005).

40. Fabry, B. *et al.* Selected Contribution: Time course and heterogeneity of contractile responses in cultured human airway smooth muscle cells. *J. Appl. Physiol.* **91,** 986–994. doi:10.1152/jappl.2001.91.2.986 (Aug. 2001).

41. Crocker, J. C. *et al.* Two-Point Microrheology of Inhomogeneous Soft Materials. *Phys. Rev. Lett.* **85,** 888–891. doi:10.1103/PhysRevLett.85.888 (July 2000).

42. Bonakdar, N. *et al.* Measuring mechanical properties in cells: three easy methods for biologists. *Cell Biol. Int.* **38,** 1227–1232. doi:10.1002/cbin.10303 (Oct. 2014).

43. Serwane, F. *et al.* In vivo quantification of spatially varying mechanical properties in developing tissues. *Nat. Methods* **14,** 181–186. doi:10.1038/nmeth.4101 (Feb. 2017).

44. Guck, J. & Chilvers, E. R. Mechanics Meets Medicine. *Sci. Transl. Med.* **5,** 212fs41–212fs41. doi:10.1126/scitranslmed.3007731 (Nov. 2013).

45. Deng, Y. *et al.* Inertial Microfluidic Cell Stretcher (iMCS): Fully Automated, High-Throughput, and Near Real-Time Cell Mechanotyping. *Small* **13,** 1700705. doi:10.1002/smll.201700705 (July 2017).

46. Tse, H. T. K. *et al.* Quantitative Diagnosis of Malignant Pleural Effusions by Single-Cell Mechanophenotyping. *Sci. Transl. Med.* **5,** 212ra163–212ra163. doi:10.1126/scitranslmed.3006559 (Nov. 2013).

47. Mietke, A. *et al.* Extracting Cell Stiffness from Real-Time Deformability Cytometry: Theory and Experiment. *Biophys. J.* **109,** 2023–2036. doi:10.1016/j.bpj.2015.09.006 (Nov. 2015).

48. Fregin, B. *et al.* High-throughput single-cell rheology in complex samples by dynamic real-time deformability cytometry. *Nat. Commun.* **10,** 415. doi:10.1038/s41467-019-08370-3 (Dec. 2019).

49. Aurich, K. *et al.* Label-free on chip quality assessment of cellular blood products using real-time deformability cytometry. *Lab Chip* **20,** 2306–2316. doi:10.1039/D0LC00258E (2020).

50. Panhwar, M. H. *et al.* High-throughput cell and spheroid mechanics in virtual fluidic channels. *Nat. Commun.* **11,** 2190. doi:10.1038/s41467-020-15813-9 (Dec. 2020).

51. Lim, C., Zhou, E. & Quek, S. Mechanical models for living cells—a review. *J. Biomech.* **39,** 195–216. doi:10.1016/j.jbiomech.2004.12.008. arXiv: 28444433394 (Jan. 2006).

52. Kollmannsberger, P. & Fabry, B. Linear and Nonlinear Rheology of Living Cells. *Annu. Rev. Mater. Res.* **41,** 75–97. doi:10.1146/annurev-matsci-062910-100351 (Aug. 2011).

53. Ingber, D. E. Tensegrity I. Cell structure and hierarchical systems biology. *J. Cell Sci.* **116,** 1157–1173. doi:10.1242/jcs.00359 (Apr. 2003).

54. Ward, I. M. & Sweeney, J. *An introduction to the mechanical properties of solid polymers, 2nd Edition* 394. doi:10.5860/CHOICE.42-2247 (John Wiley & Sons Ltd, Mar. 2004).

55. Gutierrez-Lemini, D. *Engineering Viscoelasticity* 1–353. doi:10.1007/978-1-4614-8139-3 (Springer US, Boston, MA, 2014).

56. Fabry, B. *et al.* Time scale and other invariants of integrative mechanical behavior in living cells. *Phys. Rev. E* **68,** 041914. doi:10.1103/PhysRevE.68.041914 (Oct. 2003).

57. Broedersz, C. P. *et al.* Cross-Link-Governed Dynamics of Biopolymer Networks. *Phys. Rev. Lett.* **105,** 238101. doi:10.1103/PhysRevLett.105.238101. arXiv: 1006.3940 (Nov. 2010).

58. Serrano-Alcalde, F., García-Aznar, J. M. & Gómez-Benito, M. J. The role of nuclear mechanics in cell deformation under creeping flows. *J. Theor. Biol.* **432,** 25–32. doi:10.1016/j.jtbi.2017.07.028 (Nov. 2017).

59. Pagliara, S. *et al.* Auxetic nuclei in embryonic stem cells exiting pluripotency. *Nat. Mater.* **13,** 638–644. doi:10.1038/nmat3943 (June 2014).

60. Sinkus, R. *et al.* Viscoelastic shear properties of in vivo breast lesions measured by MR elastography. *Magn. Reson. Imaging* **23,** 159–165. doi:10.1016/j.mri.2004.11.060 (Feb. 2005).

61. Venkatesh, S. K., Yin, M. & Ehman, R. L. Magnetic Resonance Elastography of Liver. *J. Comput. Assist. Tomogr.* **37,** 887–896. doi:10.1097/RCT.0000000000000032 (2013).

62. Kirby, M. A. *et al.* Optical coherence elastography in ophthalmology. *J. Biomed. Opt.* **22,** 1. doi:10.1117/1.JBO.22.12.121720 (Dec. 2017).

63. Lee, L. M. & Liu, A. P. A microfluidic pipette array for mechanophenotyping of cancer cells and mechanical gating of mechanosensitive channels. *Lab Chip* **15,** 264–273. doi:10.1039/C4LC01218F (2015).

64. Nyberg, K. D. *et al.* Quantitative Deformability Cytometry: Rapid, Calibrated Measurements of Cell Mechanical Properties. *Biophys. J.* **113,** 1574–1584. doi:10.1016/j.bpj.2017.06.073 (Oct. 2017).

65. Rosenbluth, M. J., Lam, W. A. & Fletcher, D. A. Analyzing cell mechanics in hematologic diseases with microfluidic biophysical flow cytometry. *Lab Chip* **8,** 1062. doi:10.1039/b802931h (2008).

66. Lange, J. R. *et al.* Microconstriction Arrays for High-Throughput Quantitative Measurements of Cell Mechanical Properties. *Biophys. J.* **109,** 26–34. doi:10.1016/j.bpj.2015.05.029 (July 2015).

67. Mokbel, M. *et al.* Numerical Simulation of Real-Time Deformability Cytometry To Extract Cell Mechanical Properties. *ACS Biomater. Sci. Eng.* **3,** 2962–2973. doi:10.1021/acsbiomaterials.6b00558 (Nov. 2017).

68. Mason, T. G., Ganesan, K., van Zanten, J. H., Wirtz, D. & Kuo, S. C. Particle Tracking Microrheology of Complex Fluids. *Phys. Rev. Lett.* **79,** 3282–3285. doi:10.1103/PhysRevLett.79.3282 (Oct. 1997).

69. Lee, J. S. H. Ballistic intracellular nanorheology reveals ROCK-hard cytoplasmic stiffening response to fluid flow. *J. Cell Sci.* **119,** 1760–1768. doi:10.1242/jcs.02899 (May 2006).

70. Jonas, M., Huang, H., Kamm, R. D. & So, P. T. Fast Fluorescence Laser Tracking Microrheometry, I: Instrument Development. *Biophys. J.* **94,** 1459–1469. doi:10.1529/biophysj.106.098111 (Feb. 2008).

71. Gómez-González, M., Latorre, E., Arroyo, M. & Trepat, X. Measuring mechanical stress in living tissues. *Nat. Rev. Phys.* **2,** 300–317. doi:10.1038/s42254-020-0184-6 (June 2020).

72. Mehrnezhad, A. & Park, K. Multifrequency Optomechanical Stiffness Measurement of Single Adherent Cells on a Solid Substrate with High Throughput. *Anal. Chem.* **89,** 10841–10849. doi:10.1021/acs.analchem.7b02356 (Oct. 2017).

73. Hertz, H. Über die Berührung fester elastischer Körper. *Journal für die reine und angewandte Mathematik* **92,** 156–171 (1882).

74. Lin, D. C., Dimitriadis, E. K. & Horkay, F. Robust Strategies for Automated AFM Force Curve Analysis—I. Non-adhesive Indentation of Soft, Inhomogeneous Materials. *J. Biomech. Eng.* **129,** 430–440. doi:10.1115/1.2720924 (June 2007).

75. Braunsmann, C., Seifert, J., Rheinlaender, J. & Schäffer, T. E. High-speed force mapping on living cells with a small cantilever atomic force microscope. *Rev. Sci. Instrum.* **85,** 073703. doi:10.1063/1.4885464 (July 2014).

76. Jonas, M., Huang, H., Kamm, R. D. & So, P. T. Fast Fluorescence Laser Tracking Microrheometry, II: Quantitative Studies of Cytoskeletal Mechanotransduction. *Biophys. J.* **95,** 895–909. doi:10.1529/biophysj.107.120303 (July 2008).

77. Yamada, S., Wirtz, D. & Kuo, S. C. Mechanics of living cells measured by laser tracking microrheology. *Biophys. J.* **78,** 1736–1747. doi:10.1016/S0006-3495(00)76725-7 (2000).

78. D., G. A New Microscopic Principle. *Nature* **161,** 777–778. doi:10.1038/161777a0 (May 1948).

79. Picart, P. *New Techniques in Digital Holography* (ed Picart, P.) doi:10.1002/9781119091745 (John Wiley & Sons, Inc., Hoboken, NJ, USA, Mar. 2015).

80. Fregin, B. *Untersuchung der adaptiven Optik zur Strömungsmessung durch diffuse Phasengrenzflächen* Diplomarbeit (Technische Universität Dresden, Fakultät Elektrotechnik und Informationstechnik, Institut für Grundlagen der Elektrotechnik und Elektronik, Professur für Mess- und Sensorsystemtechnik, Feb. 25, 2016).

81. Zehnder, L. Ein neuer Interferenzrefraktor. *Zeitschrift für Instrumentenkunde* **11,** 275–285 (1891).

82. Mach, L. Ueber einen Interferenzrefraktor. *Zeitschrift für Instrumentenkunde* **12,** 89–93 (1892).

83. Cuche, E., Marquet, P. & Depeursinge, C. Spatial filtering for zero-order and twin-image elimination in digital off-axis holography. *Appl. Opt.* **39,** 4070. doi:10.1364/AO.39.004070 (Aug. 2000).

84. Molenberghs, G. & Verbeke, G. *Linear Mixed Models for Longitudinal Data* doi:10.1007/978-1-4419-0300-6 (Springer New York, New York, NY, 2000).

85. Zuur, A. F., Ieno, E. N., Walker, N., Saveliev, A. A. & Smith, G. M. *Mixed effects models and extensions in ecology with R* 13–29. doi:10.1007/978-0-387-87458-6 (Springer New York, New York, NY, 2009).

86. Gałecki, A. & Burzykowski, T. *Linear Mixed-Effects Models Using R Springer Texts in Statistics* **9-12,** 856–875. doi:10.1007/978-1-4614-3900-4 (Springer New York, New York, NY, Oct. 2013).

87. Herbig, M., Mietke, A., Müller, P. & Otto, O. Statistics for real-time deformability cytometry: Clustering, dimensionality reduction, and significance testing. *Biomicrofluidics* **12.** doi:10.1063/1.5027197 (2018).

88. R Core Team. *R: A Language and Environment for Statistical Computing* R Foundation for Statistical Computing (Vienna, Austria, 2020).

89. Bates, D., Mächler, M., Bolker, B. & Walker, S. Fitting Linear Mixed-Effects Models Using lme4. *Journal of Statistical Software* **67,** 1–48. doi:10.18637/jss.v067.i01 (2015).

90. Wilks, S. S. The Large-Sample Distribution of the Likelihood Ratio for Testing Composite Hypotheses. *Ann. Math. Stat.* **9,** 60–62. doi:10.1214/aoms/1177732360 (Mar. 1938).

91. R Core Team. *R: A Language and Environment for Statistical Computing* R Foundation for Statistical Computing (Vienna, Austria, 2020).

92. Yevick, H. G. & Martin, A. C. Quantitative analysis of cell shape and the cytoskeleton in developmental biology. *WIREs Dev. Biol.* **7,** 1–13. doi:10.1002/wdev.333 (Nov. 2018).

93. Saadaoui, M., Rocancourt, D., Roussel, J., Corson, F. & Gros, J. A tensile ring drives tissue flows to shape the gastrulating amniote embryo. *Science (80-.).* **367,** 453–458. doi:10.1126/science.aaw1965 (Jan. 2020).

94. Schöck, F. & Perrimon, N. Molecular Mechanisms of Epithelial Morphogenesis. *Annu. Rev. Cell Dev. Biol.* **18,** 463–493. doi:10.1146/annurev.cellbio.18.022602.131838 (Nov. 2002).

95. Ding, M., Woo, W.-M. & Chisholm, A. D. The cytoskeleton and epidermal morphogenesis in. *Exp. Cell Res.* **301,** 84–90. doi:10.1016/j.yexcr.2004.08.017 (Nov. 2004).

96. Cabeen, M. T. & Jacobs-Wagner, C. Bacterial cell shape. *Nat. Rev. Microbiol.* **3,** 601–610. doi:10.1038/nrmicro1205 (Aug. 2005).

97. Carthew, R. W. Adhesion proteins and the control of cell shape. *Curr. Opin. Genet. Dev.* **15,** 358–363. doi:10.1016/j.gde.2005.06.002 (Aug. 2005).

98. Keren, K. *et al.* Mechanism of shape determination in motile cells. *Nature* **453,** 475–480. doi:10.1038/nature06952 (May 2008).

99. Smith, L. G. Cytoskeletal control of plant cell shape: getting the fine points. *Curr. Opin. Plant Biol.* **6,** 63–73. doi:10.1016/S1369-5266(02)00012-2 (Feb. 2003).

100. Peura, M. & Iivarinen, J. *Efficiency of simple shape descriptors* in *Proc. Third Int. Work. Vis. Form, Capri, Italy, May 28–30* (1997), 443–451.

101. Pincus, Z. & Theriot, J. A. Comparison of quantitative methods for cell-shape analysis. *J. Microsc.* **227,** 140–156. doi:10.1111/j.1365-2818.2007.01799.x (2007).

102. Lobo, J., See, E. Y.-S., Biggs, M. & Pandit, A. An insight into morphometric descriptors of cell shape that pertain to regenerative medicine. *J. Tissue Eng. Regen. Med.* **10,** 539–553. doi:10.1002/term.1994. arXiv: NIHMS150003 (July 2016).

103. Uynuk-Ool, T. *et al.* The geometrical shape of mesenchymal stromal cells measured by quantitative shape descriptors is determined by the stiffness of the biomaterial and by cyclic tensile forces. *J. Tissue Eng. Regen. Med.* **11,** 3508–3522. doi:10.1002/term.2263 (2017).

104. Ducroz, C., Olivo-Marin, J.-C. & Dufour, A. *Characterization of cell shape and deformation in 3D using Spherical Harmonics* in *2012 9th IEEE Int. Symp. Biomed. Imaging* (IEEE, May 2012), 848–851. doi:10.1109/ISBI.2012.6235681.

105. Zhanwei, Y., Fuguo, L., Peng, Z. & Bo, C. Description of shape characteristics through Fourier and wavelet analysis. *Chinese J. Aeronaut.* **27,** 160–168. doi:10.1016/j.cja.2013.07.011 (Feb. 2014).

106. Lestrel, P. E. Method for analyzing complex two-dimensional forms: Elliptical Fourier functions. *Am. J. Hum. Biol.* **1,** 149–164. doi:10.1002/ajhb.1310010204 (1989).

107. Des Chênes, M.-A. P. Mémoire sur les séries et sur l'intégration complète d'une équation aux différences partielles linéaire du second ordre, à coefficients constants. *Mémoires présentés à l'Institut des Sciences, Lettres et Arts, par divers savants, et lus dans ses assemblées. Sciences, mathématiques et physiques. (Savants étrangers.)* **1,** 638–648 (1806).

108. Meek, A. T. *et al.* Real-time imaging of cellular forces using optical interference. *Nat. Commun.* **12,** 3552. doi:10.1038/s41467-021-23734-4 (Dec. 2021).

109. Park, K. *et al.* Measurement of adherent cell mass and growth. *Proc. Natl. Acad. Sci.* **107,** 20691–20696. doi:10.1073/pnas.1011365107 (Nov. 2010).

110. Corbin, E. A., Adeniba, O. O., Ewoldt, R. H. & Bashir, R. Dynamic mechanical measurement of the viscoelasticity of single adherent cells. *Appl. Phys. Lett.* **108,** 093701. doi:10.1063/1.4942364 (Feb. 2016).

111. Park, K., Mehrnezhad, A., Corbin, E. A. & Bashir, R. Optomechanical measurement of the stiffness of single adherent cells. *Lab Chip* **15,** 3460–3464. doi:10.1039/C5LC00444F (2015).

112. Bragg, W. The diffraction of short electromagnetic waves by crystal. *Proceedings of the Cambridge Philosophical Society* **17,** 43–57 (1913).

113. Lekavich, J. Basics of acousto-optic devices. *Lasers and Applications,* 59–64 (Apr 1986).

114. Verrier, N., Atlan, M. & Gross, M. Holographic vibrometry: Full field holographic vibrometry at ultimate limits. doi:10.1002/9781119091745. arXiv: 1506.05961 (June 2015).

115. Samson, B., Verpillat, F., Gross, M. & Atlan, M. Video-rate laser Doppler vibrometry by heterodyne holography. *Opt. Lett.* **36,** 1449. doi:10.1364/ol.36.001449. arXiv: 1103.3592 (2011).

116. Psota, P., Ledl, V., Dolecek, R., Erhart, J. & Kopecky, V. Measurement of piezoelectric transformer vibrations by digital holography. *IEEE Trans. Ultrason. Ferroelectr. Freq. Control* **59,** 1962–1968. doi:10.1109/TUFFC.2012.2414 (Sept. 2012).

117. Verrier, N., Gross, M. & Atlan, M. Phase-resolved heterodyne holographic vibrometry with a strobe local oscillator. *Opt. Lett.* **38,** 377. doi:10.1364/OL.38.000377 (Feb. 2013).

118. Bruno, F., Laurent, J., Royer, D. & Atlan, M. Holographic imaging of surface acoustic waves. *Appl. Phys. Lett.* **104,** 083504. doi:10.1063/1.4866390. arXiv: 1401.5344 (Feb. 2014).

119. Powell, R. L. & Stetson, K. A. Interferometric Vibration Analysis by Wavefront Reconstruction. *J. Opt. Soc. Am.* **55,** 1593. doi:10.1364/JOSA.55.001593 (Dec. 1965).

120. Aleksoff, C. C. Temporally Modulated Holography. *Appl. Opt.* **10,** 1329. doi:10.1364/AO.10.001329 (June 1971).

121. Picart, P., Leval, J., Mounier, D. & Gougeon, S. Time-averaged digital holography. *Opt. Lett.* **28,** 1900. doi:10.1364/OL.28.001900 (Oct. 2003).

122. Picart, P., Moisson, E. & Mounier, D. digitally recorded holograms. **42,** 1947–1957. doi:10.1364/AO.42.001947 (2003).

123. Guck, J. *et al.* Optical Deformability as an Inherent Cell Marker for Testing Malignant Transformation and Metastatic Competence. *Biophys. J.* **88,** 3689–3698. doi:10.1529/biophysj.104.045476 (May 2005).

124. Liang, X., Liu, A., Lim, C., Ayi, T. & Yap, P. Determining refractive index of single living cell using an integrated microchip. *Sensors Actuators A Phys.* **133,** 349–354. doi:10.1016/j.sna.2006.06.045 (Feb. 2007).

125. Du, G., Ravetto, A., Fang, Q. & Den Toonder, J. M. J. Cell types can be distinguished by measuring their viscoelastic recovery times using a micro-fluidic device. *Biomed. Microdevices* **13,** 29–40. doi:10.1007/s10544-010-9468-4 (2011).

126. Ullmann, A. & Brauner, N. Closure relations for the shear stress in two-fluid models for core-annular flow. *Multiphase Science and Technology* **16,** 355–387 (2004).

127. Drury, J. L. & Dembo, M. Aspiration of human neutrophils: Effects of shear thinning and cortical dissipation. *Biophys. J.* **81,** 3166–3177. doi:10.1016/S0006-3495(01)75953-X (2001).

128. Chen, S., Zhao, M., Wu, G., Yao, C. & Zhang, J. Recent advances in morphological cell image analysis. *Comput. Math. Methods Med.* **2012.** doi:10.1155/2012/101536 (2012).

129. Van Breukelen, F. & Martin, S. L. Invited Review: Molecular adaptations in mammalian hibernators: unique adaptations or generalized responses? *J. Appl. Physiol.* **92,** 2640–2647. doi:10.1152/japplphysiol.01007.2001 (June 2002).

130. Kulzer, E. Die Herztätigkeit bei lethargischen und winterschlafenden Fledermäusen. *Z. Vgl. Physiol.* **56,** 63–94. doi:10.1007/BF00333563 (1967).

131. Khmaladze, A. *et al.* Dual-wavelength linear regression phase unwrapping in three-dimensional microscopic images of cancer cells. *Opt. Lett.* **36,** 912. doi:10.1364/ol.36.000912 (2011).

7. Symbols and Abbreviations

c	speed of light, $c = 299\,792\,458\,\mathrm{m/s}$
E	Young's modulus
E	electric field amplitude
$\mathbf{E}$	complex electric field depending on space and time
f	frequency
i	index
j	imaginary unit
$J_n(z)$	nth Bessel function of the first kind with argument z
k	wave number ($2\pi/\lambda$)
$\vec{k}$	wave vector, wave vector magnitude is reflected by the wave number $\lvert\vec{k}\rvert = k$
k_B	Boltzmann constant, $k_B = 1.380\,649 \times 10^{-23}\,\mathrm{J \cdot K^{-1}}$
t	time
T	absolute temperature (K)
x, y, z	spatial coordinates
η	viscosity
λ	wavelength
σ	extensional stress
τ	characteristic time of an exponential decay
τ_s	shear stress
ω	angular frequency ($2\pi f$)

AC	alternating current
AFM	atomic force microscope
AOM	acousto-optic modulator
BS	beam splitter
CMOS	complementary metal-oxide-semiconductor
DC	direct current
DEHP	di(2-ethylhexyl)phthalate
DFT	discrete Fourier transformation
DINCH	diisononyl cyclohexane-1,2-dicarboxylate
DMSO	dimethyl sulfoxide
dRT-DC	dynamic real-time deformability cytometry
EDTA	ethylenediaminetetraacetic acid
FCS	fetal calf (or bovine) serum
FEM	finite element method
FFT	fast Fourier transformation
FM	frequency modulated
HLDV	holographic laser Doppler vibrometry
HVS	holographic vibration spectroscopy
iPSC	induced pluripotent stem cell
LDV	laser Doppler vibrometer
LED	light-emitting diode
LMM	linear mixed model
MEMS	micro-electro-mechanical system
MRE	magnetic resonance elastography
OCE	optical coherence elastography
OPL	optical path length
PBMC	peripheral blood mononuclear cell

PBS polarizing beam splitter

PDMS polydimethylsiloxane

RMSE Root-mean-square error

RT-DC real-time deformability cytometry

SEM standard error of the mean

SNR signal-to-noise ratio

VIPS vibration-induced phase shift

8. Author contributions

I. Article: Aurich, K., **Fregin, B.**, Palankar, R., Wesche, J., Hartwich, O., Biedenweg, B., Nguyen, T.H., Greinacher, A. and Otto, O. Label-free on chip quality assessment of cellular blood products using real-time deformability cytometry. *Lab Chip* 20, 2306–2316 (2020).

K.A. and O.O. conceived the project, developed the experimental setup, and wrote the manuscript. B.F., O.H., D.B. and O.O. designed and performed all RT-DC experiments. R.P. designed and performed the fluorescence experiments. J.W., O.H. and K.A. performed the platelet concentrate experiments. K.A. performed the red cell concentrate experiments. J.W. and K.A. performed human peripheral stem cell experiments. T.-H.N. performed magnetic labelling of platelets. K.A., B.F., R.P. and O.O. analyzed the data. A.G., R.P., and B.F. wrote the manuscript. R.P., A.G. and O.O. obtained the funding. All authors reviewed the final version of the manuscript.

II. Article: Panhwar, M.H., Czerwinski, F., Dabbiru, V. A. S., Komaragiri, Y., **Fregin, B.**, Biedenweg, D., Nestler, P., Pires, R. H. and Otto, O. High-throughput cell and spheroid mechanics in virtual fluidic channels. *Nat. Commun.* 11, 2190 (2020).

O.O. conceived the project. F.C. developed the experimental setup. F.C. performed finite element method simulations. F.C. and M.H.P. carried out rheological buffer characterization. P.N. analyzed interface stability. F.C., M.H.P., B.F. and D.B. designed and performed experiments on HL60 and HEK293T cells. V.A.D. and R.H.P. developed the spheroid assay. F.C. and M.H.P. carried out cell and spheroid experiments. Y.K. performed compound treatment. F.C., M.H.P., B.F. and O.O. performed statistical data analysis. O.O. supervised the project. F.C. and O.O. wrote the manuscript. All authors reviewed the manuscript.

III. Article: **Fregin, B.**, Czerwinski, F., Biedenweg, D., Girardo, S., Gross, S., Aurich, K. and Otto, O. High-throughput single-cell rheology in complex samples by dynamic real-time deformability cytometry. *Nat. Commun.* 10, 415 (2019).

O.O. conceived the project. B.F. developed the experimental setup and acquisition software. B.F. and D.B. designed and performed experiments on HL60 cells. B.F. and K.A. designed and performed experiments on peripheral blood cells. F.C. performed FEM simulations and rheological characterization. Sa.G. provided calibration beads and characterized the calibration reference. B.F. developed the algorithm for rheological cell characterization. B.F. and St. G. established and carried out the statistical data

analysis. O.O. and K.A. supervised the project. B.F. and O.O. wrote the manuscript. All authors reviewed the manuscript.

IV. Manuscript: **Fregin, B.**, Biedenweg, D. and Otto, O. Cellular shape descriptors determine the outcome of viscoelastic analyses in microfluidic systems . Submitted to *Biophysical Journal* (2021).

O.O. and B.F. designed the experimental assay. D.B. performed sample preparation. B.F. established and performed the measurements as well as data analysis. B.F. performed simulations. O.O. supervised the project. O.O. and B.F. wrote and reviewed the manuscript.

Greifswald, 2. September 2021

Prof. Dr. Oliver Otto

Bob Fregin

9. Publications

9.1. Peer-reviewed articles

I. Article: Label-free on-chip quality assessment of cellular blood products using real-time deformability cytometry

Aurich, K., **Fregin, B.**, Palankar, R., Wesche, J., Hartwich, O., Biedenweg, B., Nguyen, T.H., Greinacher, A. and Otto, O. Label-free on chip quality assessment of cellular blood products using real-time deformability cytometry. *Lab Chip* 20, 2306–2316. doi:10.1039/D0LC00258E (2020).

Published: May 20, 2020

II. Article: High-throughput cell and spheroid mechanics in virtual fluidic channels

Panhwar, M.H., Czerwinski, F., Dabbiru, V.A.S., Komaragiri, Y., **Fregin, B.**, Biedenweg, D., Nestler, P., Pires, R.H. and Otto, O. High-throughput cell and spheroid mechanics in virtual fluidic channels. *Nat. Commun.* 11, 2190. doi:10.1038/s41467-020-15813-9 (2020).

Published online: May 4, 2020

III. Article: High-throughput single-cell rheology in complex samples by dynamic real-time deformability cytometry

Fregin, B., Czerwinski, F., Biedenweg, D. Girardo, S., Gross, S., Aurich, K. and Otto, O. High-throughput single-cell rheology in complex samples by dynamic real-time deformability cytometry. *Nat. Commun.* 10, 415. doi:10.1038/s41467-019-08370-3 (2019).

Published online: January 24, 2019

This paper was acknowledged as the paper of the month in March 2019 by the German Centre for Cardiocascular Research (DZHK).

9.2. Submitted manuscript

IV. Manuscript: Cellular shape descriptors determine the outcome of viscoelastic analyses in microfluidic systems

Fregin, B., Biedenweg, D. and Otto, O. Cellular shape descriptors determine the outcome of viscoelastic analyses in microfluidic systems . Submitted to the *Biophysical Journal* (2021).

Submitted to the Biophysical Journal on September 1, 2021
Submission ID: BIOPHYSICAL-JOURNAL-D-21-00556

9.3. Further articles

Article: Wavefront shaping for imaging-based flow velocity measurements through distortions using a Fresnel guide star

Koukourakis, N., **Fregin, B.**, König, J., Büttner, L., and Czarske, J. W. Wavefront shaping for imaging-based flow velocity measurements through distortions using a Fresnel guide star. *Opt. Express* 24, 22074-22087. doi:10.1364/OE.24.022074 (2016).

Published: September 13, 2016

Article: Toxicity and Immunogenicity in Murine Melanoma following Exposure to Physical Plasma-Derived Oxidants

Bekeschus, S., Rödder, K., **Fregin, B.**, Otto, O., Lippert, M., Weltmann, K. D., Wende, K., Schmidt, A. and Gandhirajan, R. K. Toxicity and Immunogenicity in Murine Melanoma following Exposure to Physical Plasma-Derived Oxidants. *Oxid. Med. Cell. Longev.* 2017, 1–12. doi:10.1155/2017/4396467 (2017).

Published: June 27, 2017

9.4. Published abstracts

Czarske, J. W., Koukourakis, N., **Fregin, B.**, König, J. and Büttner, L. Adaptive flow-field measurements using digital holography. *Proc. SPIE 10074, Quantitative Phase Imaging III* 100740F. doi:10.1117/12.2252084 (21 February 2017).

Fregin, B., Czerwinski, F., Biedenweg, D., Girardo, S., Groß, S., Aurich, K. and Otto, O. Dynamic Real-Time Deformability Cytometry - Time-Resolved Mechanical Single Cell Analysis at 100 Cells/s. *Biophys. J.* 118, 605a. doi:10.1016/j.bpj.2019.11.3267 (7 February 2020).

Panhwar, M. H., Czerwinski, F., **Fregin, B.**, Dabbiru, V. A., Komaragiri, Y., Biedenweg, D., Pires, R. H. and Otto, O. Label-Free Cytometry in Virtual Fluidic Channels - High-Throughput Cell Rheology and Tissue Mechanics. *Biophys. J.* 118, 603a. doi:10.1016/j.bpj.2019.11.3257 (7 February 2020).

9.5. Conference talks

Fregin, B., Czerwinski, F., Aurich, K., Biedenweg, D. and Otto, O. dynamic RT-DC: time-resolved mechanical single cell analysis at 100 cells / second.
Spring Meeting of the German Physical Society. March 11 - 16, 2018, Berlin, Germany

Fregin, B., Czerwinski, F., Biedenweg, D., Girardo, S., Aurich, K. and Otto, O. Dynamic RT-DC: Time-resolved mechanical single cell analysis at 100 cells/s.
13th Winter Conference of the European Society for Molecular Imaging (ESMI), TOPIM 2019 on IMAGING the BIOMECHANICS of LIFE. January 13 - 18, 2019, Les Houches, France

Fregin, B., Czerwinski, F., Aurich, K., Biedenweg, D., Girardo, S., Gross, S. and Otto, O. Dynamic RT-DC: time-resolved mechanical single cell analysis at 100 cells / second.
Spring Meeting of the German Physical Society. March 31 - April 5, 2019, Regensburg, Germany

Fregin, B., Czerwinski, F., Biedenweg, D., Girardo, S., Gross, S., Aurich, K. and Otto, O. Dynamic Real-Time Deformability Cytometry: High-throughput multiparametric mechanical single cell analysis.
29th Annual Conference of the German Society for Cytometry. September 25 - 27, 2019, Berlin, Germany

Fregin, B., Czerwinski, F., Biedenweg, D., Girardo, S., Gross, S., Aurich, K. and Otto, O. Dynamic real-time deformability cytometry: High-throughput single cell rheology in complex samples.
Cell Pysics 2019. October 9 - 11, 2019, Saarbrücken, Germany

Fregin, B., Czerwinski, F., Biedenweg, D., Gross, S., Aurich, K., Kerth, G. and Otto, O. Red blood cell viscoelasticity as key regulator for hibernation in bats.
DZHK Christmas Cardio Lunch. December 2, 2019, Greifswald, Germany

Fregin, B., Czerwinski, F., Biedenweg, D., Gross, S., Aurich, K., Kerth, G. and Otto, O. 2-parametric mechanical phenotyping of peripheral blood cells.
Invited evening lecture at the local DZHK retreat 2020. March 4 - 5, 2020, Koserow, Germany

Fregin, B., Czerwinski, F., Biedenweg, D. Girardo, S., Gross, S., Aurich, K. and Otto, O. High-throughput single-cell rheology in complex samples by dynamic real-time deformability cytometry.
Invited presentation of the paper of the month at 8th DZHK Retreat. September 17 - 18, 2020, Online

Fregin, B., Czerwinski, F., Biedenweg, D., Girardo, S., Gross, S., Aurich, K. and Otto, O. Dynamic Real-Time Deformability Cytometry: Time-resolved mechanical single cell analysis at 100 cells/s.
Invited conference talk at the 65th Annual Meeting of the Biophysical Society. February 22 - 26, 2021, Online

9.6. Poster presentations

Fregin, B., Schmieder, F. and Czarske, J. W. Multi-mode laser-Doppler-anemometer for advance in fuel cell research.
Award ceremony from the Gisela and Erwin Sick Foundation: my student research project was awarded. October 10, 2012, Dresden, Germany

Fregin, B., Koukourakis, N., König, J., Czarske, J. W. and Otto, O. Wavefront-shaping for flow-field measurements.
Spring Meeting of the German Physical Society. March 19 - 24, 2017, Dresden, Germany

Fregin, B., Biedenweg, D., Harting, J. and Otto, O. Dynamic RT-DC: Time-resolved mechanical single cell analysis at 100 cells/s.
Gordon Research Conference, Physics & Chemistry of Microfluidics. June 4 - 9, 2017, Lucca (Barga), Italy

Fregin, B., Czerwinski, F., Biedenweg, D. and Otto, O. Dynamic RT-DC: Time-resolved mechanical single cell analysis at 100 cells/s
1st International School on Hemo Physics. May 15 - 18, 2018, Montpellier, France

Fregin, B., Czerwinski, F., Biedenweg, D., Girardo, S., Aurich, K. and Otto, O. Dynamic RT-DC: Time-resolved mechanical single cell analysis at 100 cells/s.
13th Winter Conference of the European Society for Molecular Imaging (ESMI), TOPIM 2019 on IMAGING the BIOMECHANICS of LIFE. January 13 - 18, 2019, Les Houches, France

Fregin, B., Czerwinski, F., Biedenweg, D., Girardo, S., Aurich, K. and Otto, O. Dynamic RT-DC: Time-resolved mechanical single cell analysis at 100 cells/s. 8th Biennal European Cell Mechanics Meeting (CellMech 2019). June 3 - 6, 2019, Milan, Italy

Fregin, B., Czerwinski, F., Biedenweg, D., Girardo, S., Gross. S., Aurich, K. and Otto, O. Dynamic RT-DC: Time-resolved mechanical single cell analysis at 100 cells/s. 64th Annual Meeting of the Biophysical Society. February 15 - 19, 2020, San Diego, USA

Fregin, B., Czerwinski, F., Aurich, K., Biedenweg, D., Gross, S., Kerth, G. and Otto, O. Dynamic RT-DC: red blood cell viscoelasticity as a label-free biomarker. Spring Meeting of the German Physical Society. March 22 - 24, 2021, Online

9.7. I. Article: Label-free on-chip quality assessment of cellular blood products using real-time deformability cytometry

Aurich, K., **Fregin, B.**, Palankar, R., Wesche, J., Hartwich, O., Biedenweg, B., Nguyen, T.H., Greinacher, A. and Otto, O. Label-free on chip quality assessment of cellular blood products using real-time deformability cytometry. *Lab Chip* 20, 2306–2316. doi:10.1039/D0LC00258E (2020).

Published: May 20, 2020

Supplementary Information is available at http://www.rsc.org/suppdata/d0/lc/d0lc00258e/d0lc00258e1.pdf

Lab on a Chip

PAPER

Cite this: *Lab Chip*, 2020, **20**, 2306

Label-free on chip quality assessment of cellular blood products using real-time deformability cytometry†

Konstanze Aurich, *[a] Bob Fregin, [bc] Raghavendra Palankar, [a] Jan Wesche, [a] Oliver Hartwich,‡[a] Doreen Biedenweg,[d] Thi-Huong Nguyen,§[a] Andreas Greinacher[a] and Oliver Otto[bc]

Without cellular blood products such as platelet concentrates (PC), red blood cell concentrates (RCC), and hematopoietic stem cells (HPSC) modern treatments in medicine would not be possible. An unresolved challenge is the assessment of their quality with minimal cell manipulation. Minor changes in production, storage conditions, or blood bag composition may impact cell function, which can have important consequences on product integrity. This is especially relevant for personalized medicine, such as autologous T-cell therapy. Today a robust methodology that globally determines cell status directly before transfusion or transplantation is lacking. We demonstrate that measuring viscoelastic characteristics of peripheral blood cells using real-time deformability cytometry (RT-DC) provides comprehensive information on product quality, which is not accessible using conventional quality control tests. In addition, RT-DC requires few cells, a minimal sample volume and has a rapid turnaround time. We compared RT-DC to standard *in vitro* quality assays assessing: i) PC after storage at 4 °C and room temperature; ii) magnetic nanoparticle labeled platelets; iii) RCC stored in blood bags with different plasticizers; iv) RCC after gamma irradiation; and v) HPSC after cryopreservation with 5% or 10% dimethyl sulfoxide, respectively. Additionally, we evaluated the engraftment time of patients' platelets and leukocytes after transplantation of HPSC products. Our results demonstrate that label-free mechano-phenotyping can be used as a potential biomarker for quality assessment of cell-based pharmaceutical products.

Received 12th March 2020,
Accepted 18th May 2020

DOI: 10.1039/d0lc00258e

rsc.li/loc

Introduction

Cellular blood products, such as platelet concentrates (PC), red blood cell concentrates (RCC), hematopoietic stem cells (HPSC), and advanced therapy medicinal products (ATMP) such as chimeric antigen receptor (CAR) T-cells, are medicinal products that are extracted from human donor blood. PC are transfused to prevent or treat bleeding in patients with severe thrombocytopenia or platelet function defects.[1] RCC are used to replace missing red blood cells (RBC) in acute or chronic anaemia (*e.g.* severe blood loss).[2] Transplantation of HPSC from a donor to a recipient or in an autologous setting is carried out in the case of malignant haematological diseases, since the patients' own remaining hematopoietic stem cells are insufficient. In addition, allogenic HPSC are able to attack remaining cancer cells, which are not detected or sufficiently combated by the patient's immune system.[3] Blood products are obtained from whole blood donations in blood bag systems that are regularly divided into their components by centrifugation and separation or by apheresis. This guarantees that patients receive a tailor-made therapy of the required blood component and in addition allows for extended shelf life of the single components. Platelets in PC react very sensitive to physico-chemical changes such as temperature, osmolality as well as pH and undergo rapid activation and aggregation.[4] Hence, conventionally PC are stored at room temperature (RT) in the presence of additive solutions entailing a limited shelf life of 4–7 days. While storage at 4 °C reduces bacterial proliferation and would extend shelf life, the *in vivo* survival of cold stored platelets

[a] *Transfusionsmedizin, Universitätsmedizin Greifswald, 17475 Greifswald, Germany. E-mail: konstanze.aurich@med.uni-greifswald.de*
[b] *Zentrum für Innovationskompetenz: Humorale Immunreaktionen bei kardiovaskulären Erkrankungen, Universität Greifswald, 17489 Greifswald, Germany*
[c] *Deutsches Zentrum für Herz-Kreislauf-Forschung e.V., Universitätsmedizin Greifswald, 17489 Greifswald, Germany*
[d] *Klinik für Innere Medizin B, Universitätsmedizin Greifswald, 17475 Greifswald, Germany*

† Electronic supplementary information (ESI) available. See DOI: 10.1039/d0lc00258e

‡ Present address: Universitätsmedizin Rostock, Apotheke, Ernst-Heydemann-Straße 7, 18057 Rostock, Germany.
§ Present address: Institut für Bioprozess- und Analysenmesstechnik e.V., Rosenhof, 37308 Heilbad Heiligenstadt, Germany.

after transfusion is strongly reduced.[4–7] In contrast to PC, RCC can withstand a storage temperature of 4 °C that prolongs shelf live up to 49 days while HPSC are cryopreserved by adding a cryoprotectant and thus can be stored in liquid nitrogen for an extended period of time.

To ensure patient safety and treatment efficacy, all transfused blood products must pass through highest level of quality assurance standards under strict regulatory control for providing biologically safe and physiologically viable cellular products according to good manufacturing practice (GMP) guidelines.[8] Methods currently used for routine quality control of PC include platelet aggregation by light transmission aggregometry assay (LTA) and analysis of surface activation markers by flow cytometry.[9] These standard methods also find application in product quality control during the introduction of new technologies such as pathogen inactivation or modified storage conditions that prolong the limited shelf life of PC. Another process that could influence platelet function is platelet labeling with contrast agents required for *in vivo* tracking of platelets during viability and survival studies.[10]

Similarly, for quality assessment of RCC, total and free hemoglobin, hemolysis rates and potassium levels are measured, which are released during storage as a result of cell degradation.[11] Measurements of aforementioned parameters are routinely performed on RCC treated with gamma irradiation used for avoiding transfusion-associated graft *versus* host disease (GvHD), resulting from the engraftment of residual allogenic donor leukocytes in immunosuppressive patients.[12] Furthermore, RCC are stored in polyvinyl chloride (PVC) blood bags plasticized with phthalate-based plasticizers. These plasticizers can leach into the RCC products and are known to be associated with impairment of the hormone status in the recipient.[13] Alternatively to commonly used plasticizer di(2-ethylhexyl)phthalate (DEHP), new generation of plasticizers such as diisononyl cyclohexane-1,2-dicarboxylate (DINCH) could potentially replace traditionally used phthalates and minimize interference with the endocrine system. However, DINCH is known to interact with the RBC membrane and thus increases hemolysis.[14]

HPSC products are characterized by CD34+ and CD3+ cell count and viability *via* flow cytometry or by analysis of reproducing cells in colony forming unit assays.[15] In cancer therapy transplantation typically involves infusing the collected HPSC product either fresh or after cryopreservation. As a cryoprotectant agent commonly dimethyl sulfoxide (DMSO) is used. Due to the dose-dependent side effects of DMSO after transplantation, currently efforts are underway to reduce the DMSO concentration in HPSC. Several studies have demonstrated that post thawing, HPSC had a similar or even better recovery rate reducing DMSO concentration from 10 to 5%.[16–19]

Changes in storage conditions, pathogen contamination or chemicals such as plasticizers from storage containers are known to affect the cellular cytoskeleton.[20–22] Cytoskeletal changes and thus many important cell functions, such as mitosis and migration are strongly linked to cell mechanical properties.[23–25] Thus, the inclusion of these parameters into the quality assessment of blood products would be highly desirable. While being a label-free parameter of high-potential that reflects cell integrity, mechanical properties are not applied on a routine basis in a translational environment as current methods like atomic force microscopy and optical stretching are time-consuming and technically demanding.[26–28]

Real-time deformability cytometry (RT-DC) as well as its recent extension real-time fluorescence and deformability cytometry (RT-FDC) are high-throughput methods for mechanical and fluorescent characterization of up to 1000 cells per second in real-time.[29,30] Here, a microfluidic chip with a central constriction is connected to a syringe pump driving a cell-containing sample fluid that is hydrodynamically focused by a sheath fluid (Fig. 1a). Inside the constriction the cells experience hydrodynamic shear and normal forces inducing cell deformation. A pulsed LED is used for image exposure while a CMOS camera (1000 frames per second) acquires a single snapshot per cell. Real-time image acquisition and analysis is synchronized with fluorescence detection, where fluorescence excitation can be carried out for three laser wavelengths. Avalanche photodiodes detect the emitted light allowing for

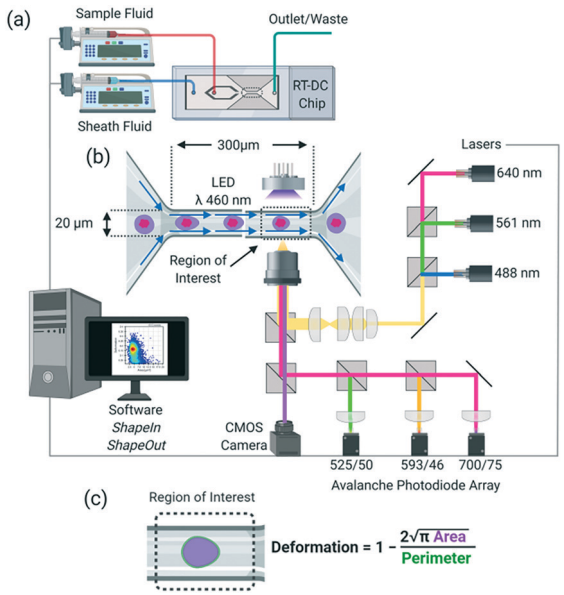

Fig. 1 Real-time fluorescence and deformability cytometry as a quality control tool for assessing therapeutic cellular blood products. The setup consists of (a) a microfluidic chip, with (b) a central constriction of 300 µm length and 15 µm × 15 µm (platelet concentrate) or 20 µm × 20 µm (red cell concentrate and hematopoietic stem cells) cross-section, where cells in the sample fluid are surrounded by a sheath fluid and deformed by shear and normal forces. In RT-FDC mechanical cell analysis is combined with lasers of different wave length and avalanche photodiodes for parallel fluorescence excitation and detection. (c) Deformation of cells is calculated from the circularity using ratio of cell area and perimeter.

simultaneous analysis of, *e.g.*, platelet deformation and activation (Fig. 1b). Cell deformation is analyzed from its circularity considering the ratio of cell area and perimeter (Fig. 1c).

In this work, we comprehensively evaluated RT-DC as a fast and robust quality control tool for assessing a wide range of therapeutic cellular blood products. We demonstrate for PC, RCC and HPSC that RT-DC enables monitoring of cell quality beyond the capacity of currently established methods (Fig. 2). Our results show that storage at different temperatures leads to a highly impaired platelet deformation, whereas labeling of platelets with nanoparticles has no impact on their mechanical cell properties. For RCC we highlight that the choice of the plasticizers in PVC blood bags affects the rheological properties of RBC, while gamma irradiation has no effect.

Finally, we turn to individualized products in regenerative medicine and tested if cryopreservation of HPSC with different DMSO concentration changes cell mechanics and the subsequent impact on stem cell engraftment after transplantation. Our results suggest a correlation between the deformation of hematopoietic stem cells and their viability.

Results and discussion

Effects of various storage conditions on platelet quality

PC are currently stored at RT, which significantly increases the risk for bacterial contamination and growth. While standard *in vitro* assays of platelet metabolism, morphology, or function do not differ considerably between storage at 4 °C or at RT, cold stored platelets have a functionally impaired *in vivo* survival.[5–7]

Here, we assessed whether mechanical phenotyping of PC stored at different temperatures can be used as a label-free marker for platelet function. Analysis of platelets by RT-DC not only confirms the known size differences between room

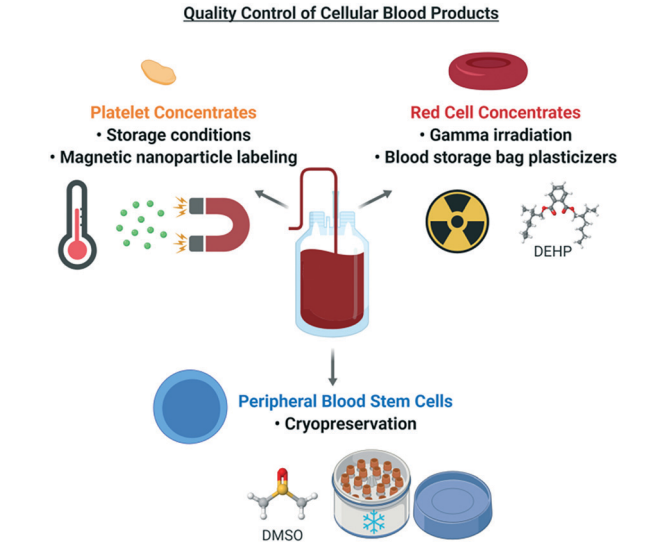

Fig. 2 Cellular blood products as platelet concentrates, red cell concentrates and hematopoietic stem cells require quality control. We used RT-DC to assess the quality of platelet concentrates after storage at different temperature and after magnetic labeling, of red cell concentrates stored in blood bags with different plasticizers and after gamma irradiation as well as of hematopoietic stem cells after cryopreservation with DMSO. DMSO = dimethyl sulfoxide, DEHP = di(2-ethylhexyl)phthalate.

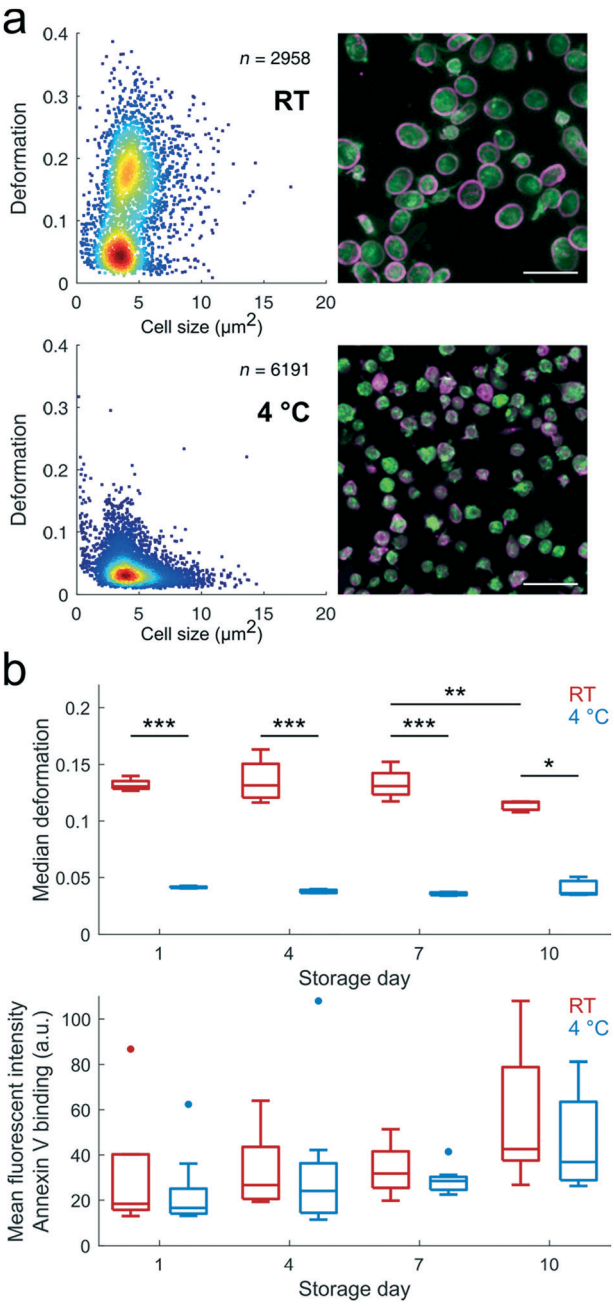

Fig. 3 (a) Real-time deformability cytometry (left panel) of platelets from platelet concentrates (PC) stored at room temperature (RT, top) and 4 °C (bottom) at storage day 1 shows a reduction in deformation and cell size. Confocal microscopy images (right panel) highlighting α-tubulin (magenta) and F-actin (green) distribution at RT (top) and cold storage (bottom). (b) Platelet deformation for 4 platelet concentrates monitored over 10 days at RT and 4 °C (top) and annexin V binding to phosphatidylserine measured by flow cytometry (bottom).

temperature and 4 °C stored platelets,[31] but also reveals a bimodal distribution at RT while a reduced deformation (*i.e.* increased stiffness) at 4 °C is observed (Fig. 3a, left panel). The decrease in cell deformation already manifests at day one of storage and can be linked at a cytoskeletal level to an increased coiling and disintegration of the circumferential marginal band of tubulin (Fig. 3a, right panel and S1a†).

We monitored median platelet deformation in PC stored at room temperature and 4 °C for up to 10 days (4 PC). PC stored at RT showed no significant changes in deformation at day 1, 4, and 7 while a significant decrease ($p < 0.01$) at day 10 was observed (Fig. 3b, upper panel). In contrast, storage at 4 °C leads to a significantly lower deformation over the entire study period (day 1, 4, 7, $p < 0.001$ and day 10, $p < 0.02$). In parallel, we assessed whether RT and 4 °C storage leads to expression of apoptotic markers by quantifying annexin V binding to phosphatidylserine (PS) expressed on platelet surface. Annexin V binding showed no significant differences for days 1, 4, and 7 (Fig. 3b, lower panel) while an increase in annexin V binding was observed at day 10 for both RT and.

Our data confirm that established *in vitro* assays like the annexin-V-binding-assay based on platelet metabolism, activation, and aggregation reveal no differences between RT and 4 °C storage.[5,32] In contrast, monitoring mechanical properties yield a significantly reduced deformation during cold storage. This finding can be linked to a reorganization of the platelet tubulin ring and is highly important in the light of platelet depletion from circulation after cytoskeletal changes.[9,33–35] Similarly, changes in mechanical properties indicate undesirable platelet activation. RT-FDC provides the possibility to assess whether observed differences in cell deformation are linked to platelet activation.[30]

We tested platelet activation, *e.g.* at sub-optimal PC storage conditions by addition of thrombin receptor activator peptide 6 (TRAP-6).[36] We gated our data and analyzed the sub-populations of activated platelets (which express CD62P) for their mechanical properties (Fig. 4a, left and center panel, ESI† Fig. S1c). Our data demonstrate that the decreased deformation (*i.e.* increased stiffness) is restricted to activated platelets (Fig. 4b) rendering this label-free biomarker a unique quality control for unfavourable storage conditions or pre-activation of therapeutic cells.

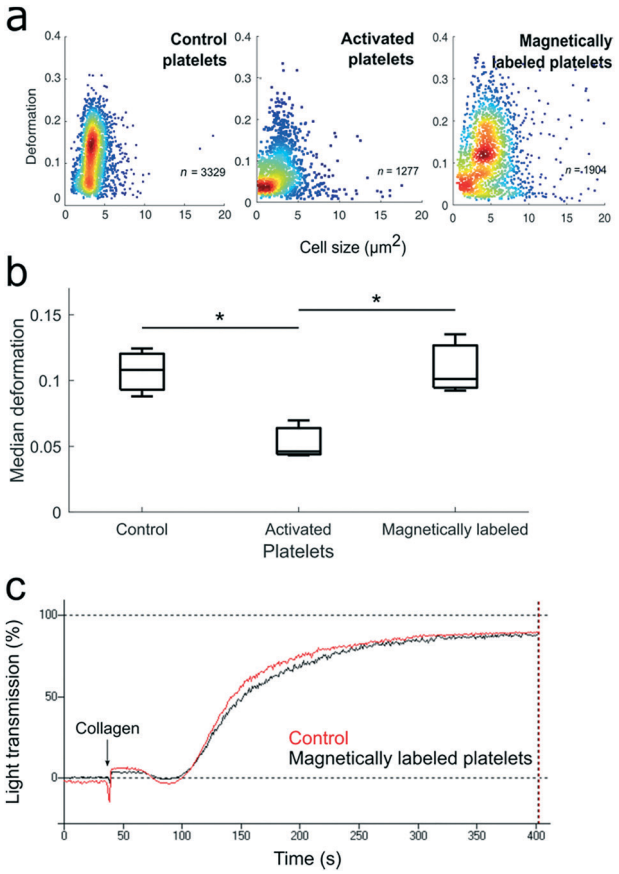

Fig. 4 Platelet activation of control platelets and after magnetic labeling. (a) Real-time deformability cytometry for control (left), Trap-6 activated (centre) and magnetically labeled platelets (right). (b) Median deformation of control platelets, TRAP-6 activated and magnetically labeled platelets (3 platelet concentrates). (c) Maximum aggregation after addition of collagen for control and magnetically labeled platelets in light transmission aggregation assay. Statistical analysis for RT-DC is performed using linear mixed models (*, $p < 0.05$).

Effect of magnetic nanoparticle labeling on platelet quality

We next expanded the application of RT-DC to assess mechanical properties of platelets labeled with superparamagnetic iron oxide nanoparticles (SPION).[10] This method has the potential to replace radioactive labeling of platelets to distinguish between the patient's own and transfused autologous platelets for assessment of platelet survival in clinical trials. Radioactive labeling of therapeutic blood cells is no longer ethically possible in the European Union, particularly for healthy volunteers.[10] Using SPION, particles bind to the platelet membrane, while some of them transfer from open canalicular system channels to another target inside platelets such as the α-granula.[37] RT-DC measurements show that labeled platelets exhibit comparable mechanical properties to non-labeled platelets (Fig. 4a, left and right panel and b). These findings agree with the standard quality parameters LTA revealing no major differences between both groups (Fig. 4c). Therefore, RT-DC demonstrates for the first time that uptake of magnetic nanoparticles by platelets does not impair their cell mechanical properties. This is a step towards introducing magnetic nanoparticles as an alternative to radioactive labeling for *in vivo* application in humans.

Quality assessment of red blood cells stored in blood bags with different plasticizers

Current methods used to assess the mechanical properties of red blood cells are time-consuming and complex, thus cannot be performed in real-time as it is required for most translational applications (*e.g.* in routine quality control of

blood products where results determine product release for transfusion, or assessment in patients).

We took advantage of the potential of RT-DC to identify differences in RBC mechanics caused by the application of blood containers with different plasticizers. The potentially harmful effects of phthalate plasticizers in blood containers are a matter of debate, due to their perceived hormone like and toxic effects.[38] Here, we compared RBC stored inside a DEHP and DINCH bag, respectively, where we find a decrease in mean deformation for the latter (Fig. 5a). Interestingly, this difference already manifests at day one of storage and is consistent over the full period of 49 days where an additional decrease in deformation for DINCH was observed (Fig. 5b). When comparing deformation to hemolysis from RBCs we find a clear correlation between both parameters, which highlights the potential of mechanical phenotyping to assess the quality of RCC label-free in a clinical setting (Fig. 5c).

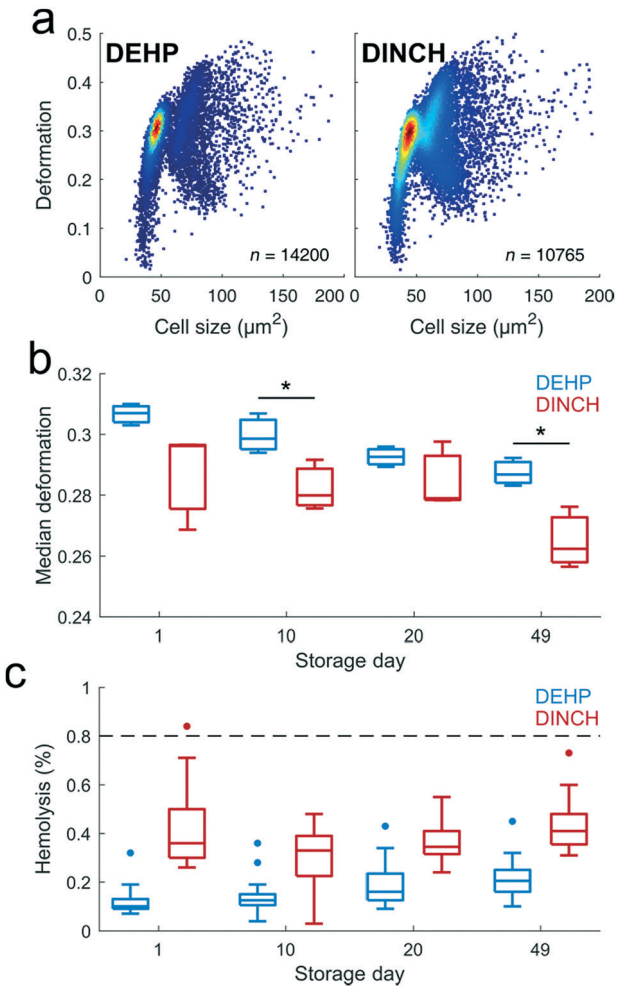

Fig. 5 Mechanical phenotype of red cell concentrate after storage with different plasticizers. (a) Real-time deformability cytometry red cell concentrates produced in DEHP (left) and DINCH bags (right) at storage day 49, (b) median deformation of DEHP and DINCH red blood cells (3 red cell concentrates) and (c) hemolysis during storage period of 49 days (16 red cell concentrates), dotted line = limit of hemolysis according to German hemotherapy guidelines (= 0.8%). DEHP = di(2-ethylhexyl)phthalate, DINCH = di-isononyl-cyclohexane-1,2-dicarboxylate. Statistical analysis for RT-DC is performed using linear mixed models, statistical analysis for hemolysis was performed using students *t*-test, (*, $p < 0.05$).

Quality assessment of red blood cells after gamma irradiation

RCC are irradiated to decrease the risk that residual donor T-lymphocytes induce fatal transfusion-associated GvHD in immune-compromised transfusion recipients.[39] However, it is known that gamma irradiation induces potassium release and the production of reactive oxygen species resulting in a viscosity increase that leads to impaired cell deformability.[40] A correlation between deformation and hemolysis was found in RCC after gamma irradiation with 30 Gy.

While short storage until day 10 did not yield a difference between irradiated and non-irradiated bags (day 10: deformation 0.299 ± 0.007 *vs.* 0.300 ± 0.004, $p = 0.919$, hemolysis: 0.145 ± 0.078% *vs.* 0.113 ± 0.158%, $p = 0.5$, non-irradiated *vs.* irradiated, Fig. 6a), RCC during extended storage of up to day 20 showed decreased deformation and increased hemolysis (deformation: 0.293 ± 0.003 *vs.* 0.298 ± 0.004, $p < 0.001$, hemolysis: 0.192 ± 0.095% *vs.* 0.303 ± 0.117, $p = 0.014$, non-irradiated *vs.* irradiated, Fig. 6b and c). These results were in accordance with previous studies and prove the reduced shelf life of irradiated RCC.[40,41]

Overall, the deformability of red blood cells is widely used for applications focused primarily on disease diagnosis such as malaria or sickle cell anaemia, since the impaired hemoglobin in these disease patterns leads to reduced deformability.[42,43] However, RBC mechanical properties can be also used for quality assessment of RCC units in blood banks. Aging of RBC causes storage lesions in RBC membranes leading to an increased stiffness and further to increased clearance of transfused RBC from circulation.[44,45]

Transfusion outcome is primarily co-determined by RCC quality. This underscores the translational potential of RT-DC for evaluation of minor variations in the production process of cellular blood components and is completely in line with a multitude of *in vitro* studies and *in vivo* observations on survival of irradiated red cells.[46]

Hematopoietic stem cells quality after cryopreservation with dimethyl sulfoxide

Hematopoietic stem cell transplantation is currently one of the mainstays of treatment of hematologic malignancies. For autologous stem cell therapy the patient's own stem cells have to be cryopreserved during the period of high-dose chemotherapy/whole body irradiation. Thereafter stem cells are re-transfused to restore the patient's own blood producing system, which had been irreversibly damaged by the preceding aggressive treatment.[47] Cryopreservation of HPSC with DMSO is the standard method for long-term storage at −80 °C or in liquid nitrogen below −160 °C. We analyzed the impact of liquid nitrogen storage at DMSO

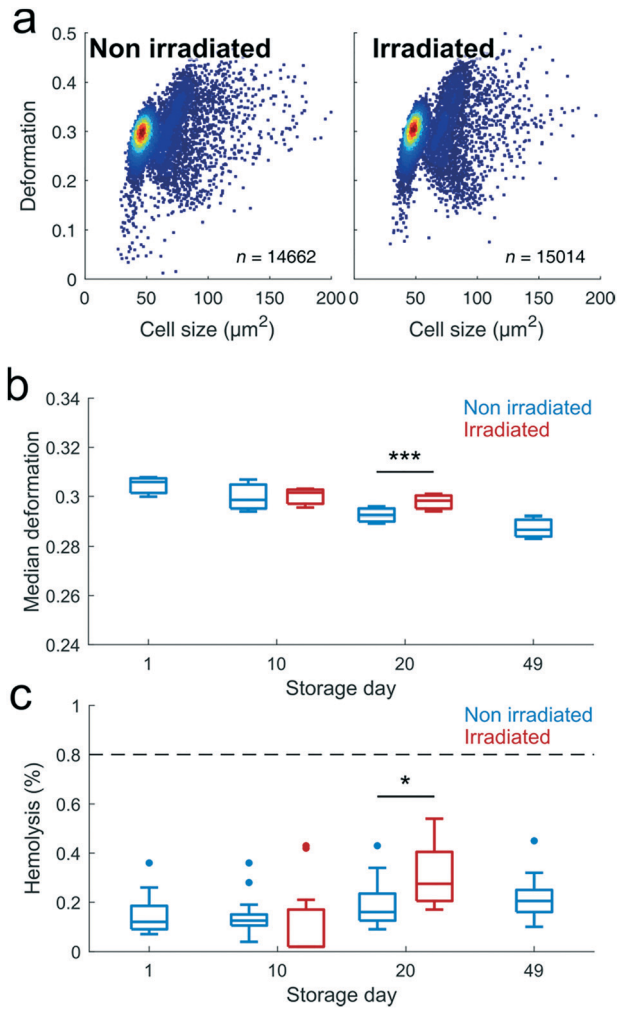

Fig. 6 Mechanical phenotype of red cell concentrates after gamma irradiation. (a) Real-time deformability cytometry of non-irradiated and irradiated red blood cells on storage day 20, (b) median of deformation for non-irradiated (blue) and irradiated (red) red cell concentrates (3 red cell concentrates) and (c) hemolysis during storage period of 49 days (16 red cell concentrates), dotted line = limit of hemolysis according to German hemotherapy guidelines (= 0.8%), DEHP = di(2-ethylhexyl)phthalate, DINCH = di-isononyl-cyclohexane-1,2-dicarboxylate. Statistical analysis for RT-DC is performed using linear mixed models (***, $p < 0.001$); statistical analysis for hemolysis was performed using students *t*-test (*, $p < 0.05$).

concentrations of 5% and 10% on stem cell mechanics, cell count, *in vitro* viability, and *in vivo* engraftment in humans.

First, a HPSC containing a mixture of leukocytes, red blood cells and platelets has been analyzed using RT-FDC. For HPSCs, deformation *versus* cell size scatter data revealed four distinct populations (Fig. 7a, left panel). Using a combination of viability and CD34+ fluorescence markers we found a homogeneous distribution of viable CD34+ cells by flow cytometry (ESI† Fig. S2b) and RT-FDC (Fig. 7a, center panel) which can now be described by size and deformation only (Fig. 7a, right panel).

Comparing HPSC before (2 HPSC) and after cryopreservation (4 HPSC) in liquid nitrogen with 5% and 10% DMSO resulted in a significant decrease in deformation from 0.052 ± 0.001 (before cryopreservation) to 0.035 ± 0.004 (after cryopreservation with 5% DMSO; $p < 0.0004$) and 0.041 ± 0.002 (after cryopreservation with 10% DMSO; $p < 0.01$; Fig. 7b, left panel). A small, but significant difference in deformation was found between 5% and 10% DMSO ($p < 0.05$). Freezing and DMSO concentration also impairs cell size (ESI† Fig. S2a). CD34+ cell count remained at the same level before and after cryopreservation (Fig. 7b, centre panel). However, HPSC viability was lower when 10% DMSO had been added for cryopreservation in comparison to 5% DMSO ($p = 0.026$; Fig. 7b, right panel).

Our results suggest that CD34+ viability might directly be linked to the mechanical cell properties and that deformation after cryopreservation could serve as a marker for human stem cell viability and function. Interestingly, the maximum in viability coincides with a minimum in cell deformation suggesting a direct link between mechanical properties and viability of hematopoietic stem cells.

As each HPSC product has to undergo quality control before release, this finding may have major relevance for label-free assessment of HPSC and for the evaluation of different preparation and storage conditions, also with regard to the implementation of advanced genetically modified cellular products.

In vivo engraftment of differently manufactured stem cell products

We compared regeneration of hematopoiesis in patients transplanted with autologous HPSC cryopreserved with either 5% or 10% DMSO. The limit of 50 000 platelets per μL was reached by 100% of involved patients (21 patients) at day 18 (5% DMSO) or day 17 (10% DMSO; $p = 0.53$, 29 patients) after transplantation (Fig. 8a). Reaching the leukocyte limit of 1000/μL differs between 5% and 10% DMSO concentration also by one day in average (day 15 with 5% DMSO and day 14 with 10% DMSO; $p = 0.01$; Fig. 8b).

That means the reduction of DMSO concentration from 10% to 5% hardly influenced hematopoietic recovery after autologous HPSC transplantation but resulted in improved tolerance of stem cell infusion.[18] Reducing the DMSO concentrations during cryopreservation of HPSCs would be a major advantage for patients due to reduced side effects. RT-DC results correlated very closely with the extensive biological studies performed to compare the effects of 5% and 10% DMSO and so RT-DC has the potential to become a real-time high-throughput tool for testing the quality of stem cell products.

Conclusion

This study introduces RT-DC as a quality control tool for a wide range of cellular blood products. We provide evidence that cell mechanical properties can be applied for rapid, label-free on-the-fly quality assessment of platelets, red blood cells and human peripheral blood stem cells avoiding cell

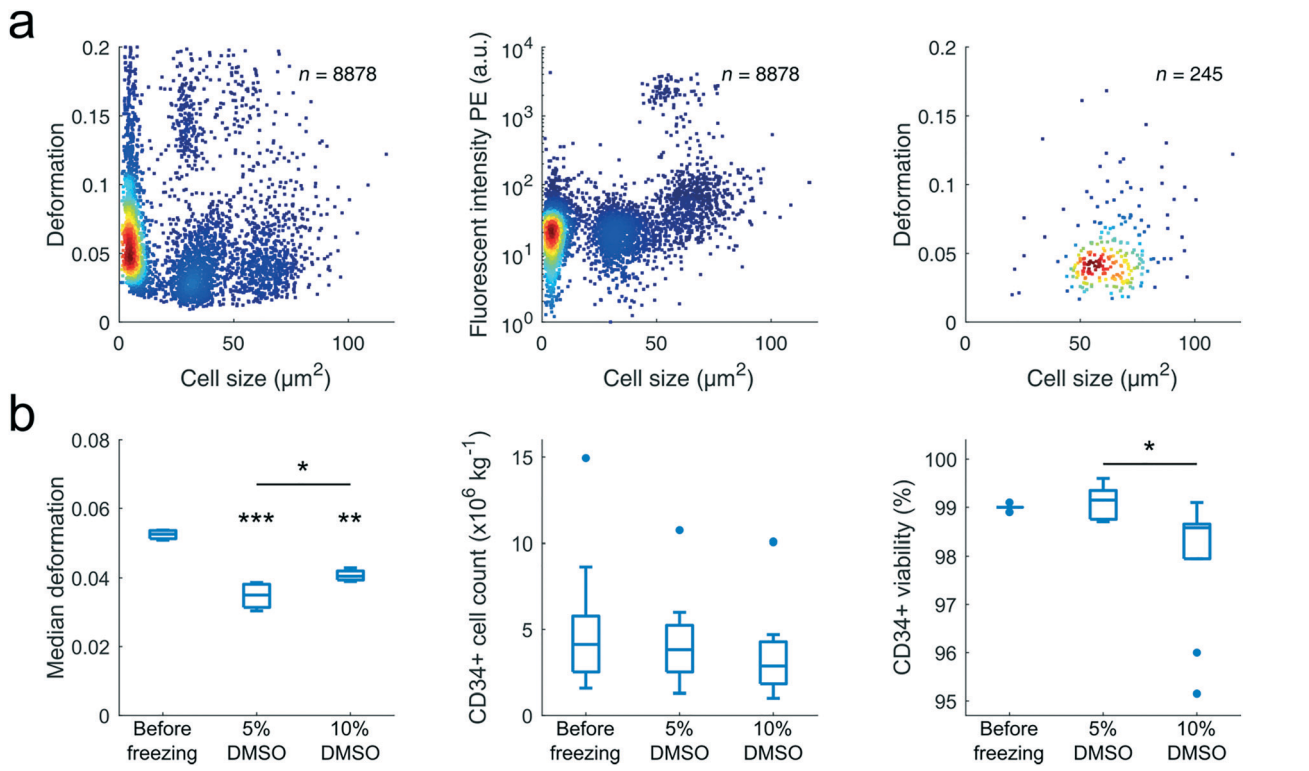

Fig. 7 Quality assessment of hematopoietic stem cells. (a) Real-time fluorescence and deformability cytometry on HPSC reveals four sub-populations (left). Fluorescence intensity of the HPSC cells after addition of anti-CD34-PE labeled antibody (centre) and deformation *vs.* cell size scatter plot (right) of viable CD34+ cells from (a) centre. (b) Deformation (left), cell count (centre) and viability of CD34+ stem cells (right) before freezing (2 hematopoietic stem cell products) and directly after thawing cryopreserved cells with 5 or 10% DMSO (4 hematopoietic stem cell products). Measurements have been carried out using a microfluidic chip having a constriction of 20 μm × 20 μm cross-section and 300 μm length. Statistical analysis for RT-DC is performed using linear mixed models (*, $p < 0.05$; **, $p < 0.01$; ***, $p < 0.001$).

manipulation which can cause cell damage and biased assay results.

We show that high-throughput mechanical phenotyping by RT-DC can be applied for quality assessment of pharmaceutical cellular blood products. Studying PC, RCC and HPSC under different, clinically relevant storage conditions, our results demonstrate that intrinsic mechanical properties reveal insights into cell function and predict cellular state in a robust way. With the rapidly evolving therapeutic options of engineered cell-based immunotherapies for leukaemia and other cancers, there is an urgent need for improved and practicable quality control measures with a rapid turnaround time. We propose RT-DC as a technology with the potential to innovate quality control measures of therapeutic cellular blood products.

Experimental

Apheresis platelet concentrates (PC) and (red cell concentrates) RCC were collected from healthy donors according to the German guidelines for hemotherapy with written ethical consent and under approval of University Medicine Greifswald.

Apheresis platelet concentrates

Eight individuals were recruited to donate 2 units of apheresis PC on a COM.Tec machine (Fresenius Kabi, Germany). Collected platelets were stored in platelet additive solution (PAS; SSP+, Maco Pharma, France). PAS was added to reach a final plasma concentration of 30%. After resting for 30 min at room temperature (RT) apheresis PCs were stored either at RT or at 4 °C under permanent agitation for 10 days (platelet agitator LPR1, Melco Engineering Corp., USA).

Magnetic labeling

Apheresis PC cell count was adjusted to 400 × 10^6/mL using SSP+ and the cell suspension was incubated with carboxydextran coated superparamagnetic iron oxide nanoparticles (2 mM final iron concentration, Ferucarbotran, Meito Sangyo, Japan) for 30 min at 37 °C. Platelets were washed to eliminate excess particles (650 g, 7 min, RT), resuspended in SSP+ and rested for 45 minutes at 37 °C before further use.

In vitro platelet function testing

Annexin V binding on phosphatidylserine was compared between RT and cold stored platelets by flow cytometry as a

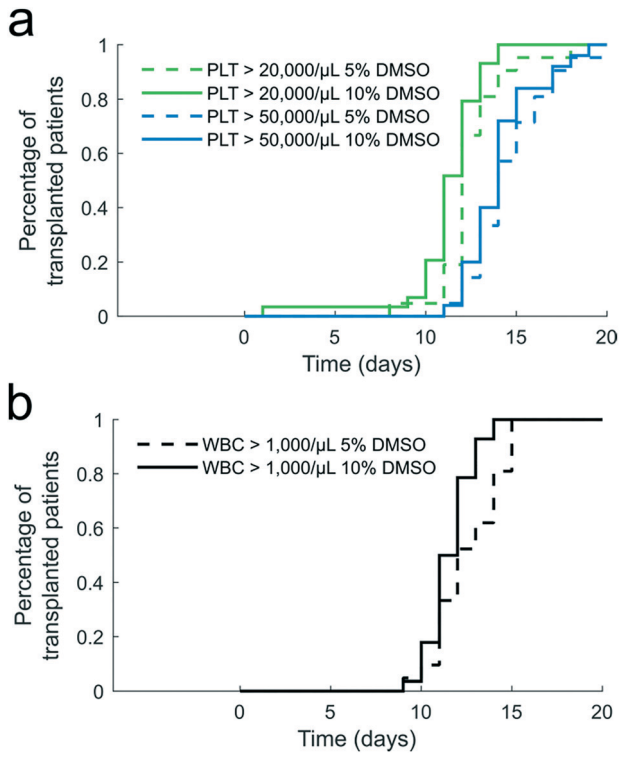

Fig. 8 Engraftment of platelet and white blood cell *in vivo*. Platelet engraftment (a) and white blood cell engraftment (b) after hematopoietic cells transplantation of HPSC cryopreserved with 5% (21 patients) and 10% DMSO (29 patients). PLT = platelets, WBC = white blood cells, DMSO = dimethyl sulfoxide.

measure for apoptosis. Therefore, platelets were incubated at a concentration of 300 × 10^6/mL for 10 min at 37 °C with 5 µL annexin V–allophycocyanine (APC; Biolegend, USA) after fixation by 0.5% paraformaldehyde (PFA, Sigma Aldrich, Germany), washed twice with wash buffer (2 mL phosphate buffered saline, PBS; 650 g, 7 min, RT) and analyzed by flow cytometry (FC500, Beckman Coulter, Germany; ESI† Fig. S1b). Platelet function was analyzed using light transmission platelet aggregation assay (LTA) and flow cytometry. Collagen (Horm collagen, NYCOMED Austria GmbH, Austria) was used as inductor. LTA was performed with a 4-channel-aggregometer (Labitec, Germany). Platelet aggregation was measured by turbidimetry induced by addition of 8 µg mL^{-1} collagen (final concentration; NYCOMED Austria). Platelet activation ability was determined for magnetically labeled platelets by measuring the CD62P expression after addition of TRAP-6. Therefore, platelets were incubated at a concentration of 300 × 10^6/mL for 15 min at 37 °C with 20 µM TRAP-6 (Hart Biologicals, USA), fixed (0.5% paraformaldehyde, Sigma Aldrich, Germany; 20 min; RT) and washed twice with wash buffer (2 mL PBS; 650 g, 7 min, RT). The pellet was resuspended in PBS and tested using flow cytometry. Platelets were gated using a mouse-anti-human CD41-PC5 labeled monoclonal antibody (P2, Beckman Coulter). Increase of CD62P exposure on CD41-positive events was determined using CD62P-FITC (CLBThromb/6, Beckman Coulter; ESI† Fig. S1d). The conformation changes upon activation of glycoproteins (GPs) IIb/IIIa complex analyzing expression at baseline and after activation by 20 µM TRAP-6.

Platelet cytoskeleton analysis

Platelets from PC were fixed in 2% PFA in PBS for 30 min at 4 °C. Excess PFA was removed by washing platelets twice in PBS followed by quenching for 5 min in 30 mM glycine/PBS, pH 7.5. For imaging, platelets were transferred onto microscopy slides by centrifugation for 5 min at 750 × *g* (Cytospin™ 4 Cytocentrifuge, Fisher scientific, USA). Tubulin was stained with a monoclonal anti-α-tubulin antibody produced in mouse (clone DM1A, ascites fluid, Sigma Aldrich, Germany) used at 1 : 500 dilution and detected by a donkey anti-mouse IgG (H + L) highly cross-adsorbed secondary antibody, Alexa Fluor 568 (Thermo Fisher, USA) at a dilution of 1 : 750. F-actin was detected by Phalloidin Atto 488 (Atto-Tec AD, Germany) used at 50 pM diluted in PBS. Confocal laser scanning microscopy was performed on Leica TCS SP5 Confocal Microscope (Leica, Germany) using a 40× oil immersion objective. Atto 488 was exited and Alexa Fluor 568 was exited at 488 nm and 575 nm and emission was collected at 520 nm and 605 nm, respectively.

Red blood cell concentrates

RCC were produced from whole blood of 3 individual donors. Whole blood was collected into DEHP or DINCH containing quadruple blood bag system T/B 500 mL, citrate phosphate dextrose solution (CPD) systems with phosphate–adenine–glucose–guanosin–saline–mannitol solution (PAGGS–M) as additive solution (Maco Pharma, France). After 1 h resting WB was centrifuged on a Roto Silenta RS centrifuge (4000*g*, 10 min; Hettich GmbH, Germany) and separated into plasma, buffy coat, and RCC by MacoPress Smart (Maco Pharma, France). RCC from DEHP bags were split into two bags, one of which was stored at 4 °C for 49 days and the other irradiated with 30 Gy (irradiation device IBL-437 C Type G, CIS, Germany) at storage day 10 and stored for another 10 days at 4 °C until day 20.

Hemolysis

Hemoglobin released by RBC was transformed into cyano methemoglobin using potassium hexacyanoferrate III and potassium cyanide (transformation reagent). Cell free supernatant was produced from 10 mL RBC by 2 centrifugation steps at 15 000*g* for 10 min (10 000 rpm; Heraeus Megafuge 1.0R, Heraeus GmbH, Germany). 1 mL of supernatant was incubated for 5 min with 4 mL of transformation reagent. 1 mL of this sample was transferred to a cuvette (thickness 1 cm) and a multi wavelength absorption analysis was performed at 540 nm (A1) and 680 nm (A2) in a UV-1600PC spectrophotometer (controlled by M. Wave Professional software V 1.0, VWR, Germany) which was blanked in advance with 1 mL of transformation reagent.

Free hemoglobin was calculated (1):

$$C_{\mathrm{FreeHemoglobin}} = (\mathrm{A1} - \mathrm{A2}) \times 454 \quad (1)$$

Hemolysis in % was calculated (2)

$$\mathrm{Hemolysis}\,[\%] = \frac{(100\% - \mathrm{Hematocrit}\,[\%]) \times C_{\mathrm{FreeHemoglobin}}}{C_{\mathrm{TotalHemoglobin}} \times 1000} \quad (2)$$

Hematopoietic stem cells

Cryopreservation of hematopoietic stem cells plays an important role in the therapy of malignancies of the hematopoietic system, since long term storage of these cells at deep temperatures is required. We used DMSO as a cryopreservant agent to avoid damage of stem cells due to ice crystallization. Cryopreserving solution of autologous plasma and DMSO in a concentration of either 10% or 20% (WAK Chemie, Germany) was added to the stem cell preparation at 4 °C in a ratio of 1 : 2 to achieve a final DMSO concentration of 5% or 10%. Thereafter the whole preparation was stored at −80 °C resulting in a cooling rate of 2 °C min^{-1} and after 24 h transferred in the vapor phase of liquid nitrogen at ≤160 °C.

Analysis of CD34+ or CD45+ cell count and viability by flow cytometry

Cell preparations were analyzed for their CD34+ or CD45+ content by flow cytometry on a FC500 (Beckmann Coulter, USA). Leukocyte concentration was adjusted to 15 000 cells per μL with PBS (Biochrom, Germany). For CD34+ and CD45+ cell count and viability in HPSC StemKit test kit (Beckman Coulter, USA) was used according to manufactures' instructions. Data were evaluated according to the International Society of Hemotherapy and Graft Engineering (ISHAGE) protocol (ESI† Fig. S2b).[48]

Real-time deformability cytometry

Real-time deformability cytometry is a high-throughput technology for mechanical cell phenotyping as published earlier.[29] Briefly, the setup is built around an inverted microscope (Observer A1, Zeiss, Germany) with a microfluidic chip assembled on the *xy*-stage for position control (AcCelerator, Zellmechanik Dresden, Germany). The microfluidic chip consists of a constriction of 15 μm × 15 μm cross-section (platelets) or 20 μm × 20 μm cross-section (red blood cells and human peripheral blood stem cells) with a length of 300 μm and is connected to a syringe pump (NemeSys, Cetoni, Germany). A cell suspension is driven through the chip at flow rates of 0.006 μL s^{-1} (platelets), 0.06 μL s^{-1} (red blood cells) as well as 0.06 μL s^{-1} and 0.08 μL s^{-1} (human peripheral blood stem cells), where cells deform inside the central channel by normal and shear forces only. Cell deformation D is calculated (3):

$$D = 1 - \frac{2\sqrt{\pi A}}{P} \quad (3)$$

where A is the projected cell area and P the perimeter detected by the software ShapeIn (Zellmechanik Dresden) in real-time exceeding 1000 cells per second.

Measurements are carried out in buffer Carrier B (Zellmechanik Dresden), which is composed of 0.6% (w/v) methylcellulose in PBS (without Ca^{2+} and Mg^{2+}). For RT-DC on platelets 50 μL of platelets in plasma were diluted in Carrier B to a final concentration of approximately 10×10^6 per mL. For RBCs and HPSCs 25 μL from RCC or HPSC concentrates were diluted in carrier B to a final concentration of approximately 1×10^6 per mL. In total, we analyzed a minimum of 1000 and up to 20 000 cells per sample depending on cell type, their abundance, and on the experiment. On an average the mean run time of 5.5 min was spent for per sample for each experiment.

For deformation analysis only cells are included where the actual cell area deviates less than 10% (platelets), 15% (RBCs) and 5% (all other cells) from the area tracked by the algorithm. Material properties are calculated using an analytical model to couple the hydrodynamic stress distribution on a cell surface to linear elasticity theory.[49] Calculations are performed at different flow rates representing different experimental conditions.

Simultaneous measurements of cell deformation and fluorescence is carried out using an extension of RT-DC, real-time fluorescence and deformability cytometry.[30]

For platelets studies, cells have first been exposed to thrombin receptor activator peptide 6 (TRAP-6, 20 μM final concentration) and second stained with 10 μL CD62P-FITC (5 μg mL^{-1}) as an activation marker. Our gating strategy consists of a negative control to define the fluorescence levels indicating cell activation. For CD34+ cells have first been labeled with anti-CD34-PE (Beckman Coulter, USA) by incubating for 10 minutes. Following two washing steps (600 g, 10 min) and resuspension in carrier B buffer, cells have been analysed in RT-FDC (Fig. 7a, centre panel) and fluorescence gate (intensity $>10^3$, a.u.) identifying CD34+ cells has been defined that allows to monitor HPSC deformation in heterogeneous samples after thawing.

Statistical data analysis

Statistical analysis of RT-DC data is done from independent experimental replicates using linear mixed models.[50] Briefly, the model separates observations between measurement quantities of two samples into random and fixed effects. While random effects account for random and systematic measurement bias, *e.g.* variations in buffer viscosity, fixed effects describe the actual change in an experimental observable, *e.g.* deformation or cell size. We compare two models, one with and one without the fixed effect by calculating the maximum likelihood ratio. Using the Wilks theorem, the corresponding p values are derived. Statistical analysis is performed using the software ShapeOut 0.8.6 (Zellmechanik Dresden).

For all other statistical data evaluation, we used Origin Pro 2018b. Statistical significances were calculated by 2 sample students *t*-test or logrank test.

Author contribution

K. A. and O. O. conceived the project, developed the experimental setup, and wrote the manuscript. B. F., O. H., D. B. and O. O. designed and performed all RT-DC experiments. R. P. designed and performed the fluorescence experiments. J. W., O. H. and K. A. performed the platelet concentrate experiments. K. A. performed the red cell concentrate experiments. J. W. and K. A. performed human peripheral stem cell experiments. T.-H. N. performed magnetic labelling of platelets. K. A., B. F., R. P. and O. O. analysed the data. A. G., R. P., and B. F. wrote the manuscript. R. P., A. G. and O. O. obtained the funding. All authors reviewed the final version of the manuscript.

Conflicts of interest

O. O. is co-founder of Zellmechanik Dresden GmbH distributing real-time deformability cytometry. All other authors do not report a conflict of interest. Maco Pharma International kindly provided the whole blood collection bags with DEHP and DINCH plasticizers.

Acknowledgements

We gratefully acknowledge financial support from the German Federal Ministry of Research and Education (ZIK HIKE grant to O. O. under grant agreement 03Z22CN11) and from the German Research Foundation (Project number 374031971 – TRR 240 to A. G., O. O. and R. P.). We thank Maria Geske, Jessica Fuhrmann, Robert Koch, and Tobias Oergel for excellent technical support.

References

1 R. R. Vassallo and S. Murphy, *Curr. Opin. Hematol.*, 2006, **13**, 323–330.
2 S. L. Rygard, L. B. Holst and A. Perner, *Crit. Care Clin.*, 2018, **34**, 299–311.
3 K. Heydari, A. Shamshirian, P. Lotfi-Foroushani, A. Aref, A. Hedayatizadeh-Omran, M. Ahmadi, G. Janbabei, S. Keyhanian, E. Zaboli, S. M. Ghasemzadeh and R. Alizadeh-Navaei, *Clin. Transl. Oncol.*, 2020, DOI: 10.1007/s12094-020-02322-w.
4 L. Waters, M. Cameron and M. P. Padula, *Vox Sang.*, 2018, **113**, 317–328.
5 I. Marini, K. Aurich, R. Jouni, S. Nowak-Harnau, O. Hartwich, A. Greinacher, T. Thiele and T. Bakchoul, *Haematologica*, 2018, 207–214, DOI: 10.3324/haematol.2018.195057.
6 P. Sandgren, M. Hansson, H. Gulliksson and A. Shanwell, *Vox Sang.*, 2007, **93**, 27–36.
7 K. M. Hoffmeister, *J. Thromb. Haemostasis*, 2011, **9**(Suppl 1), 35–43.
8 European medicines agency, *EU Guidelines to Good Manufacturing Practice Medicinal Products for Human and Veterinary Use*, 2020.
9 M. Shrivastava, *Transfus. Apher. Sci.*, 2009, **41**, 105–113.
10 K. Aurich, J. Wesche, R. Palankar, R. Schluter, T. Bakchoul and A. Greinacher, *ACS Appl. Mater. Interfaces*, 2017, **9**, 34666–34673.
11 D. J. Jenkins, C. W. Kendall, T. H. Nguyen, J. Teitel, A. Marchie, M. Chiu, A. Y. Taha, D. A. Faulkner, T. Kemp, J. M. Wong, R. de Souza, A. Emam, E. A. Trautwein, K. G. Lapsley, C. Holmes, R. G. Josse, L. A. Leiter and W. Singer, *Eur. J. Clin. Nutr.*, 2007, **61**, 483–492.
12 D. Xu, M. Peng, Z. Zhang, G. Dong, Y. Zhang and H. Yu, *J. Geophys. Res. Space Physics*, 2012, **10**, 321–330.
13 J. Sampson and D. de Korte, *Transfus. Med.*, 2011, **21**, 73–83.
14 J. W. Lagerberg, E. Gouwerok, R. Vlaar, M. Go and D. de Korte, *Transfusion*, 2015, **55**, 522–531.
15 M. J. Watts and D. C. Linch, *Br. J. Haematol.*, 2016, **175**, 771–783.
16 A. Smagur, I. Mitrus, S. Giebel, M. Sadus-Wojciechowska, J. Najda, T. Kruzel, T. Czerw, J. Gliwinska, M. Prokop, M. Glowala-Kosinska, A. Chwieduk and J. Holowiecki, *Vox Sang.*, 2013, **104**, 240–247.
17 I. Mitrus, A. Smagur, W. Fidyk, M. Czech, M. Prokop, A. Chwieduk, M. Glowala-Kosinska, T. Czerw, M. Sobczyk-Kruszelnicka, W. Mendrek, K. Michalak, M. Sadus-Wojciechowska, J. Najda, J. Holowiecki and S. Giebel, *Bone Marrow Transplant.*, 2018, **53**, 274–280.
18 C. A. Akkok, K. Liseth, I. Nesthus, T. Lokeland, K. Tefre, O. Bruserud and J. F. Abrahamsen, *Transfusion*, 2008, **48**, 877–883.
19 K. Liseth, E. Ersvaer, J. F. Abrahamsen, I. Nesthus, A. Ryningen and O. Bruserud, *Transfusion*, 2009, **49**, 1709–1719.
20 G. Berger, D. W. Hartwell and D. D. Wagner, *Blood*, 1998, **92**, 4446–4452.
21 E. M. Milford and M. C. Reade, *Transfusion*, 2016, **56**(Suppl 2), S140–S148.
22 M. Wiltshire, A. Meli, M. A. Schott, A. Erickson, N. Mufti, S. Thomas and R. Cardigan, *Transfus. Med.*, 2016, **26**, 208–214.
23 J. Guck and E. R. Chilvers, *Sci. Transl. Med.*, 2013, **5**, 212fs241.
24 D. Di Carlo, *J. Lab. Autom.*, 2012, **17**, 32–42.
25 A. F. Pegoraro, P. Janmey and D. A. Weitz, *Cold Spring Harbor Perspect. Biol.*, 2017, **9**(11), a022038.
26 P. H. Wu, D. R. Aroush, A. Asnacios, W. C. Chen, M. E. Dokukin, B. L. Doss, P. Durand-Smet, A. Ekpenyong, J. Guck, N. V. Guz, P. A. Janmey, J. S. H. Lee, N. M. Moore, A. Ott, Y. C. Poh, R. Ros, M. Sander, I. Sokolov, J. R. Staunton, N. Wang, G. Whyte and D. Wirtz, *Nat. Methods*, 2018, **15**, 491–498.
27 W. M. Weaver, P. Tseng, A. Kunze, M. Masaeli, A. J. Chung, J. S. Dudani, H. Kittur, R. P. Kulkarni and D. Di Carlo, *Curr. Opin. Biotechnol.*, 2014, **25**, 114–123.
28 L. Sachs, C. Denker, A. Greinacher and R. Palankar, *Res. Pract. Thromb. Haemostasis*, 2020, **4**, 386–401.
29 O. Otto, P. Rosendahl, A. Mietke, S. Golfier, C. Herold, D. Klaue, S. Girardo, S. Pagliara, A. Ekpenyong, A. Jacobi, M. Wobus, N. Topfner, U. F. Keyser, J. Mansfeld, E. Fischer-

Friedrich and J. Guck, *Nat. Methods*, 2015, **12**, 199–202, 194 p following 202.
30 P. Rosendahl, K. Plak, A. Jacobi, M. Kraeter, N. Toepfner, O. Otto, C. Herold, M. Winzi, M. Herbig, Y. Ge, S. Girardo, K. Wagner, B. Baum and J. Guck, *Nat. Methods*, 2018, **15**, 355–358.
31 T. M. Getz, *Transfus. Apher. Sci.*, 2019, **58**, 12–15.
32 I. P. Torres Filho, L. N. Torres, C. Valdez, C. Salgado, A. P. Cap and M. A. Dubick, *J. Thromb. Haemostasis*, 2017, **15**, 163–175.
33 B. Wood, M. P. Padula, D. C. Marks and L. Johnson, *Transfusion*, 2016, **56**, 2548–2559.
34 L. Johnson, S. Tan, B. Wood, A. Davis and D. C. Marks, *Transfusion*, 2016, **56**, 1807–1818.
35 J. G. White and W. Krivit, *Blood*, 1967, **30**, 625–635.
36 F. C. Chao, J. L. Tullis, D. M. Kenney, G. S. Conneely and J. R. Doyle, *Thromb. Diath. Haemorrh.*, 1974, **32**, 216–231.
37 T. H. Nguyen, N. Schuster, A. Greinacher and K. Aurich, *ACS Appl. Mater. Interfaces*, 2018, **10**, 28314–28321.
38 Y. Morishita, Y. Nomura, C. Fukui, T. Kawakami, T. Ikeda, T. Mukai, T. Yuba, K. I. Inamura, H. Yamaoka, K. I. Miyazaki, H. Okazaki and Y. Haishima, *PLoS One*, 2017, **12**(9), e0185737.
39 F. Adams, G. Bellairs, A. R. Bird and O. O. Oguntibeju, *Biomed. Res. Int.*, 2015, **2015**, 968302.
40 M. L. Barjas-Castro, M. M. Brandao, A. Fontes, F. F. Costa, C. L. Cesar and S. T. Saad, *Transfusion*, 2002, **42**, 1196–1199.
41 Y. Suzuki, N. Tateishi, I. Cicha, M. Shiba, M. Muraoka, K. Tadokoro and N. Maeda, *Clin. Hemorheol. Microcirc.*, 2000, **22**, 131–141.
42 S. M. Hosseini and J. J. Feng, *Biophys. J.*, 2012, **103**, 1–10.
43 M. M. Brandao, A. Fontes, M. L. Barjas-Castro, L. C. Barbosa, F. F. Costa, C. L. Cesar and S. T. Saad, *Eur. J. Haematol.*, 2003, **70**, 207–211.
44 G. Deplaine, I. Safeukui, F. Jeddi, F. Lacoste, V. Brousse, S. Perrot, S. Biligui, M. Guillotte, C. Guitton, S. Dokmak, B. Aussilhou, A. Sauvanet, D. Cazals Hatem, F. Paye, M. Thellier, D. Mazier, G. Milon, N. Mohandas, O. Mercereau-Puijalon, P. H. David and P. A. Buffet, *Blood*, 2011, **117**, e88–e95.
45 K. Matthews, M. E. Myrand-Lapierre, R. R. Ang, S. P. Duffy, M. D. Scott and H. Ma, *J. Biomech.*, 2015, **48**, 4065–4072.
46 P. D. Mintz and G. Anderson, *Ann. Clin. Lab. Sci.*, 1993, **23**, 216–220.
47 U. Zahid, F. Akbar, A. Amaraneni, M. Husnain, O. Chan, I. B. Riaz, A. McBride, A. Iftikhar and F. Anwer, *Curr. Hematol. Malig. Rep.*, 2017, **12**, 217–226.
48 D. R. Sutherland, L. Anderson, M. Keeney, R. Nayar and I. Chin-Yee, *J. Hematother.*, 1996, **5**, 213–226.
49 A. Mietke, O. Otto, S. Girardo, P. Rosendahl, A. Taubenberger, S. Golfier, E. Ulbricht, S. Aland, J. Guck and E. Fischer-Friedrich, *Biophys. J.*, 2015, **109**, 2023–2036.
50 M. Herbig, A. Mietke and O. Otto, *Biomicrofluidics*, 2018, **12**, 042214.

9.8. II. Article: High-throughput cell and spheroid mechanics in virtual fluidic channels

Panhwar, M.H., Czerwinski, F., Dabbiru, V.A.S., Komaragiri, Y., **Fregin, B.**, Biedenweg, D., Nestler, P., Pires, R.H. and Otto, O. High-throughput cell and spheroid mechanics in virtual fluidic channels. *Nat. Commun.* 11, 2190. doi:10.1038/s41467-020-15813-9 (2020).

Published online: May 4, 2020

Supplementary Information is available at https://www.nature.com/articles/s41467-020-15813-9#Sec22

nature COMMUNICATIONS

ARTICLE

https://doi.org/10.1038/s41467-020-15813-9 OPEN

High-throughput cell and spheroid mechanics in virtual fluidic channels

Muzaffar H. Panhwar[1,2], Fabian Czerwinski[1], Venkata A. S. Dabbiru[1,2], Yesaswini Komaragiri[1,2], Bob Fregin[1,2], Doreen Biedenweg[3], Peter Nestler[1], Ricardo H. Pires[1,2] & Oliver Otto[1,2]✉

Microfluidics by soft lithography has proven to be of key importance for biophysics and life science research. While being based on replicating structures of a master mold using benchtop devices, design modifications are time consuming and require sophisticated cleanroom equipment. Here, we introduce virtual fluidic channels as a flexible and robust alternative to microfluidic devices made by soft lithography. Virtual channels are liquid-bound fluidic systems that can be created in glass cuvettes and tailored in three dimensions within seconds for rheological studies on a wide size range of biological samples. We demonstrate that the liquid-liquid interface imposes a hydrodynamic stress on confined samples, and the resulting strain can be used to calculate rheological parameters from simple linear models. In proof-of-principle experiments, we perform high-throughput rheology inside a flow cytometer cuvette and show the Young's modulus of isolated cells exceeds the one of the corresponding tissue by one order of magnitude.

[1] Zentrum für Innovationskompetenz: Humorale Immunreaktionen bei kardiovaskulären Erkrankungen, Universität Greifswald, Fleischmannstr. 42, 17489 Greifswald, Germany. [2] Deutsches Zentrum für Herz-Kreislauf-Forschung e.V., Standort Greifswald, Universitätsmedizin Greifswald, Fleischmannstr. 42, 17489 Greifswald, Germany. [3] Klinik für Innere Medizin B, Universitätsmedizin Greifswald, Fleischmannstr. 8, 17475 Greifswald, Germany. ✉email: oliver.otto@uni-greifswald.de

Phenotyping of cells utilizing intrinsic material properties, i.e., elasticity and viscosity, is increasingly being recognized to be of key relevance in basic and applied life science research[1–3]. Early developments have mainly been driven by technologies like atomic force microscopy[4], micropipette aspiration[5] as well as optical stretching[6,7] and focused on the fundamental interplay between cytoskeletal protein structure and viscoelastic cell properties to combine physics and biology on a molecular as well as cellular scale[8–10]. In this field, mechanosensitivity has been found as an essential mechanism of how cells respond to and communicate with their environment[11].

The great success of mechanical phenotyping to study cell function paved the way toward applications in translational research but required an elevated sample throughput that could not be reached by established methods. One answer to this challenge was found in microfluidic devices[12–14]. Already decades ago, Hochmuth et al. utilized glass capillaries and high-speed video microscopy to study red blood cell deformation in flow[15–17]. In their pioneering work they carried out an extensive characterization of erythrocyte shape, orientation and viscosity. Glass capillaries share the advantages of all microfluidic systems, i.e., high-throughput and serial sample processing capabilities, but lack the flexibility to design and implement sophisticated fluid flows.

The introduction of soft lithography as a rapid prototyping technology revolutionized the way of creating microfluidic structures[18,19]. Using replicas of elastomers enabled benchtop production of lab-on-a-chip devices to access the nano- and microscale for single molecule and single-cell experiments[20–23]. For example, Gossett et al. demonstrated high-speed mechanical phenotyping of various cell lines and showed for embryonic stem cells a discrimination of their pluripotent state with sufficient statistical power[24]. The idea of stretching cells in an extensional flow has been expanded by Dudani et al. toward a pinched-flow geometry, where hydraulic circuit design is used to deform cells in multiple stretching modes[25]. Recently, mechanical cell characterization has also been complemented with real-time data analysis[26,27] as well as fluorescent labeling to combine the sensitivity of intrinsic material properties with the specificity of molecular markers[28].

While lab-on-a-chip devices are nowadays routinely being used in translational research to assess viscoelastic properties, e.g., for studying the onset of infectious diseases[29] and for monitoring patients' status over time[30,31], the high-throughput analysis of this label-free biomarker is currently limited to single cells and excludes multicellular structures. However, a detailed understanding of how mechanics impacts on tissue development and homeostasis would be highly relevant to establish 3D cell culture models that incorporate material properties into the field of tissue engineering[32,33]. Despite some initial work on spheroids using atomic force microscopy and micropipette aspiration current approaches lack the potential of simultaneous high-throughput characterization of cells and tissues applying a single experimental method[34,35].

A suitable microfluidic system for high-speed mechanical phenotyping of spheroids is a glass cuvette. Having a diameter of several hundred of micrometers these cuvettes are the main entity in fluorescence-based flow cytometers, where translocating cells are analyzed by laser excitation and detection of the emitted as well as the scattered light[36]. While providing sufficient confinement for spheroids, commercial flow cytometers are not capable to analyze single cells by their mechanical properties. One reason is found in the large cross-sectional area of the cuvette, which is needed to reduce blocking by debris but also results in low hydrodynamic stress amplitudes. Since determination of elasticity and viscosity requires, first, exposure of cells to sufficient shear as well as normal stresses and, second, detection of the corresponding cellular deformation, the large cuvette diameter effectively inhibits mechanical measurements.

Here, we introduce virtual fluidic channels to create microfluidic constrictions of variable cross-sections inside glass cuvettes of commercial flow cytometers. Virtual channels are liquid-bound microfluidic devices and are formed by co-flowing aqueous polymer solutions at low Reynolds numbers where a stabilizing sheath confines a sample flow between immiscible liquid phases. We demonstrate that virtual fluidic channel dimensions can be adjusted within seconds in real-time and enable high-throughput rheological measurements of biological samples of both, cells and spheroids.

Taking advantage of a simple scaling law defining a channel diameter, which depends on flow rates and viscosity but not on polymer composition, we investigate suspended cells in different degrees of virtual confinement. In contrast to bullet-like cells found in Poiseuille flows our results reveal a characteristic shape resembling an ellipsoid. This steady-state can be explained by a hydrodynamic stress originating from the viscosity mismatch at the liquid–liquid interface and we show its utilization for simple creep-compliance experiments that allow for an extraction of material properties.

We develop an analytical model and compare the interfacial stress to typical shear and normal stress distributions inside Poiseuille flows of laminar systems. Our results verify that cell deformation of small objects embedded in virtual channels inside large geometries, e.g., single cells in cuvettes, is governed by interfacial stress, while large objects, e.g., spheroids as a tissue model system in glass cuvettes, deform dominantly by shear stress.

We combine our technology with real-time deformability cytometry (RT-DC) for high-throughput characterization of biological samples. In proof-of-principle experiments we show that virtual channels can be applied to perform mechanical cell assays and to identify cytoskeletal alterations label-free. Finally, we investigate the role of single-cell mechanics for tissue stability. Virtual channels allow for direct comparison between the rheological properties of single cells and the corresponding tissues. Our results indicate that the elastic modulus of cells exceeds the one of tissue by an order of magnitude, while tissue stiffness increases with size.

Results

Virtual fluidic channels in microfluidic systems. Virtual channel formation is first demonstrated inside a polydimethylsiloxane (PDMS) microfluidic chip with a squared constriction of 30 µm × 30 µm cross-section and 300 µm length (Fig. 1a, upper half and Supplementary Fig. 1A). Confining a sample solution of 57 µM methylcellulose (MC) inside a sheath flow of 50 mM polyethylene glycol (PEG) 8000, both in PBS, leads to an interface, which is stable and immiscible on the experimental time scale (Supplementary Fig. 2 and Supplementary Movie 1). Inside the constriction both aqueous phases can be distinguished optically by a refractive index difference at the liquid–liquid interface that we use to define the width w of the virtual channel (Fig. 1a, top inset, white dashed line and Supplementary Movie 2). Finite element method (FEM) simulations of the full microfluidic geometry assuming a two-phase Stokes flow reveal the same binary concentration distribution of MC and PEG (Fig. 1a, lower half).

While the greater dynamic viscosity of the PEG solution effectively impedes flow and acts as a liquid wall inside the PDMS geometry, the MC phase with its lower viscosity tunnels through this confinement (Fig. 1a, top inset). The velocity profile is described by the superposition of two parabolic functions, for the

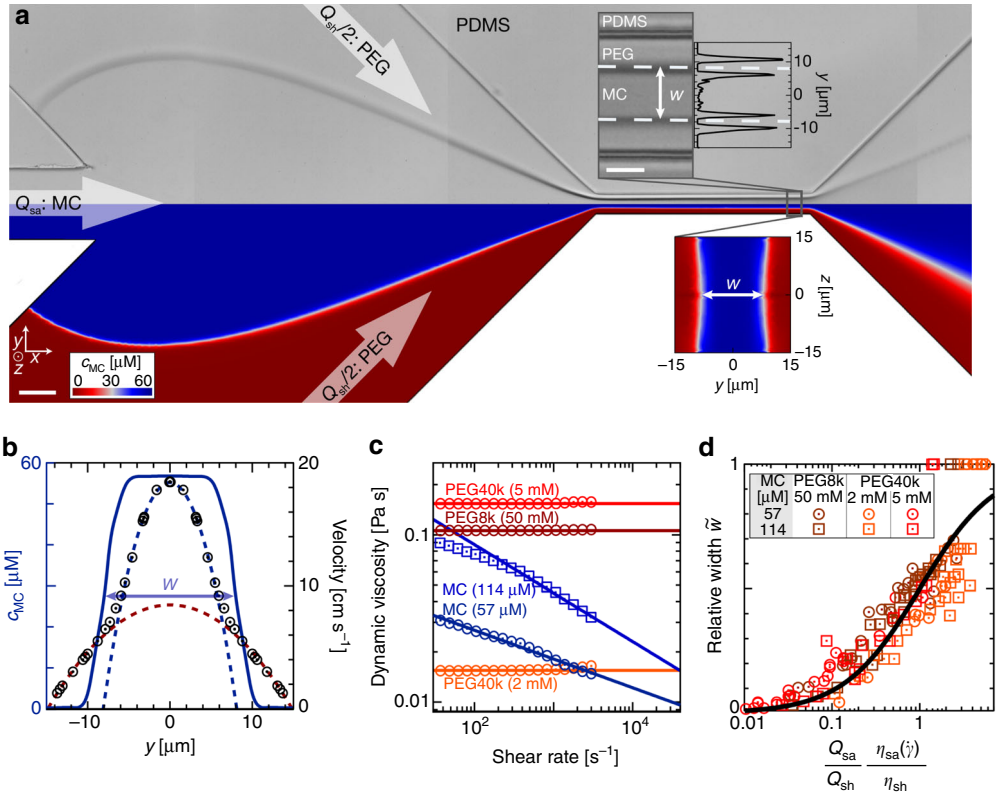

Fig. 1 Virtual fluidic channel inside microfluidic chip. a Microfluidic chip as stitched microscopy image (upper half) and as the concentration plot of a finite element method (FEM) simulation of the full geometry (lower half). Arrows indicate inflow of 57 µM methylcellulose in PBS (MC, flow rate Q_{sa} = 48 nl s^{-1}) and 50 mM polyethylene glycol 8000 in PBS (PEG8000, flow rate Q_{sh} = 8 nl s^{-1}) forming a stable virtual fluidic channel between two liquid–liquid interfaces represented in dark gray (upper half) and in white (lower half). Scale bar is 50 µm. Top inset shows a bright-field image of the central constriction and the projected squared intensity gradient (arb. units) across the full channel width. Virtual channel width corresponds to distance *w* (white dashed lines) between the center of both intensity maxima. Scale bar is 10 µm. Bottom inset shows a cross-sectional view of the calculated (FEM) polymer concentration inside the channel. **b** Velocity profile (black circles) inside the center of the constriction derived from FEM simulations with the corresponding MC concentration distribution (blue solid line) used to identify the virtual channel width *w*. The red and the blue dashed lines indicate the parabolic flow profiles of the outer and inner aqueous phases. **c** Dynamic viscosities of sample and sheath solutions as a function of shear rate. Virtual channel formation is performed using MC as sample buffer (blue) and PEG as sheath buffer (dark red, orange, bright red). Data points are measured and for shear rates greater than 3000 s^{-1} the shear-rate dependency is modeled as a power-law fluid (solid blue line) and as Newtonian fluid (solid orange and red lines). **d** Relative virtual channel width $\tilde{w}$ as a function of flow rate and viscosity ratios. The plot summarizes $n = 146$ experiments using different concentrations of MC, PEG8000 (PEG8K), and PEG40000 (PEG40K) for sample and sheath solution. The black curve is a solution to Eq. (1).

inner and outer aqueous phase (Fig. 1b, blue and red dashed line), respectively[37]. The velocity gradient of the resulting piecewise-defined Poiseuille flow (Fig. 1b, black circles) is given by the viscosity mismatch of both polymer solutions (Fig. 1c) where the MC phase corresponds to an effective (virtual) channel size smaller than the cross-section of the PDMS chip.

We investigated the impact of flow rate and viscosity on virtual channel width as these parameters allow for a precise adjustment of the liquid–liquid interface. Analyzing different polymers of various chain lengths and concentrations we confirm a simple functional relationship reported earlier[38,39]:

$$\frac{Q_{sa}}{Q_{sh}} \frac{\eta_{sa}(\dot{\gamma})}{\eta_{sh}} = \frac{\tilde{w}}{1-\tilde{w}}, \quad (1)$$

where Q_{sa} and Q_{sh} are the flow rates of sample as well as sheath, η_{sa} and η_{sh} are the corresponding viscosities and $\tilde{w}$ is the channel width relative to the diameter of the PDMS constriction (see Methods). The viscosity of sample solution is derived from a power law utilizing experimental shear rates $\dot{\gamma}$ while our sheath solution follows a Newtonian behavior (Fig. 1c, see Methods).

The fact, that the relative virtual channel width is only determined by the flow rate and viscosity ratios at the respective shear rates, qualifies well-defined flow conditions unconstrained by polymer length, concentration and the microfluidic chip (Fig. 1d). Considering the non-linear rheological properties of MC revealing a pronounced shear-thinning component, this simple relationship is unexpected in a complex hydrodynamic environment of co-flowing aqueous phases.

Cell mechanical phenotyping in virtual channels. Next, we study the capability of virtual channels as a confining constriction for probing mechanical properties of suspended cells. Using the myeloid precursor cell line HL60, RT-DC is performed in a standard PDMS chip of 20 µm × 20 µm cross-section[26] and results are compared with measurements inside a virtual channel of 21 µm width formed in a larger 30 µm x 30 µm chip (see Methods). Mechanical phenotyping in both, plastic chip and virtual channel, reveals similar distributions in cell size and deformation (Fig. 2a, b), cells display the typical bullet shape (Fig. 2a, b, insets) and only slightly perturb the MC-PEG interface (Fig. 2c).

Sensitivity of our system toward cytoskeletal modifications has been assessed by exposing HL60 cells to 1 µM cytochalasin D (CytoD, see Methods). For cells inside a PDMS channel the depolymerization of filamentous actin reveals the expected

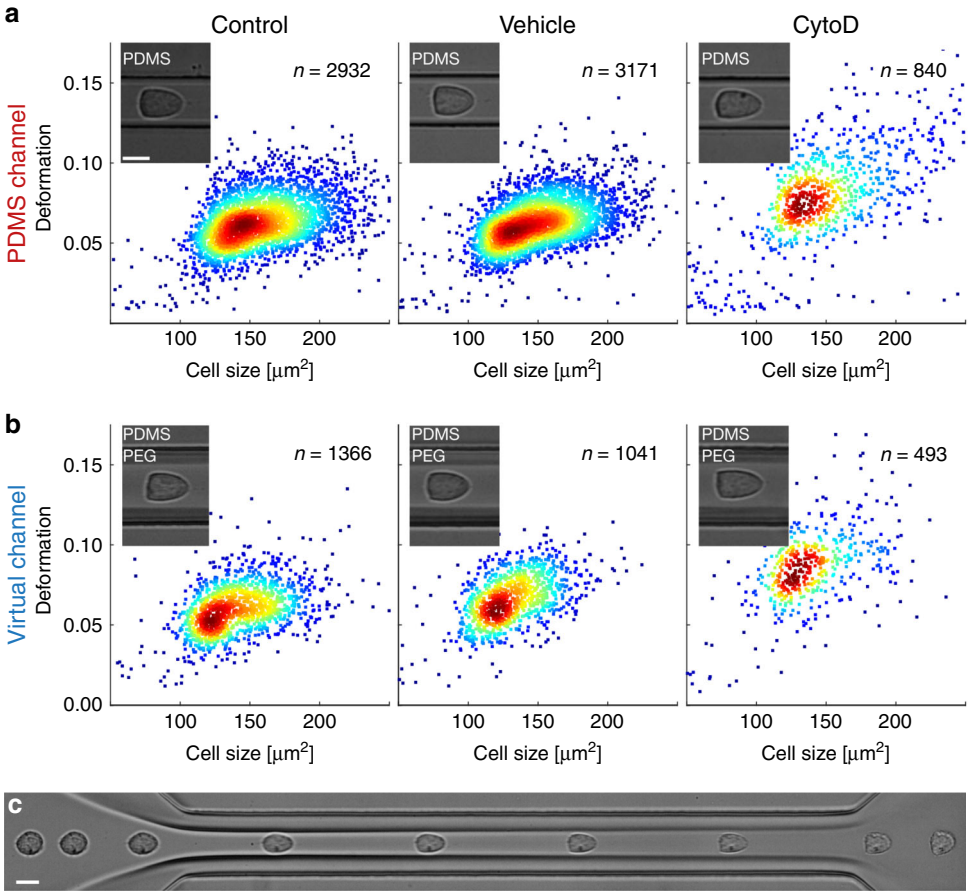

Fig. 2 Cell deformation in PDMS chip and virtual fluidic channel. a Real-time deformability cytometry (RT-DC) of HL60 cells in polydimethylsiloxane (PDMS) channel yielding scatter plots of deformation versus cell size for control cells (left), dimethyl sulfoxide (DMSO) vehicle control (0.25% (v/v), center) and 1 µM CytoD (right). Measurements have been done at a total flow rate of 40 nl s^{-1} in a PDMS chip with a 300 µm long channel and 20 µm × 20 µm squared cross-section using 57 µM MC for sample and sheath buffer, respectively. **b** RT-DC of HL60 cells in a virtual channel of 21 µm width and 30 µm height for control cells (left), DMSO vehicle control (0.25% (v/v), center) and 1 µM CytoD (right). Virtual channel is formed inside a PDMS chip with a 300 µm long channel and 30 µm × 30 µm squared cross-section using 57 µM MC (sample) as well as 50 mM PEG8000 (sheath). Measurements are taken at indicated position (Fig. 1a, gray rectangle) and a total flow rate of 94 nl s^{-1} (Q_{sa} = 90 nl s^{-1}, Q_{sh} = 4 nl s^{-1}). Insets show representative cell images. **c** Time series of single HL60 cell passing a virtual channel (sample 57 µM MC, Q_{sa} = 72 nl s^{-1}, sheath 50 mM PEG8000, Q_{sh} = 8 nl s^{-1}). Average cell velocity within the channel is ~20 cm s^{-1}. Scale bar is 10 µm. Recording of time series has been repeated five times. Color in scatter plots indicates a linear density scale from min (blue) to max (red).

increase in deformation d from $d = 0.062 \pm 0.016$ (median ± std. dev.) for the control sample and $d = 0.062 \pm 0.015$ for the vehicle control of 0.25% (v/v) dimethyl sulfoxide (DMSO) to $d = 0.080 \pm 0.030$ for the 1 µM CytoD treatment (Fig. 2a). Virtual channel measurements agree with these results and yield $d = 0.059 \pm 0.015$ (control), $d = 0.065 \pm 0.015$ (vehicle control of 0.25% (v/v) DMSO) as well as $d = 0.087 \pm 0.023$ (1 µM CytoD) where flow rates have been adjusted to match the stress distribution on the cell surface inside the PDMS chips (Fig. 2b and Supplementary Fig. 3).

A statistical analysis of three experimental replicates summarizes more than 20,000 single-cell measurements and confirms in both systems the expected significant increase in cell deformation and decrease in Young's modulus E relative to the vehicle control and control when cells are being exposed to 1 µM CytoD (Fig. 3, Supplementary Figs. 4 and 5). Importantly, we find no significant differences in deformation and Young's modulus E comparing results in PDMS and virtual channels. In contrast, a significant decrease in cell size is found when cells are confined by a MC-PEG interface. This observation can be attributed to the geometry of our microfluidic chip having a sheath current from two sides, both connected to the same inlet. The corresponding virtual channel is always aligned in the center of the constriction (Fig. 1a) confining the cells perpendicular to one direction of flow only and leaving the channel height of 30 µm unaltered (Fig. 1a, bottom inset).

Utilizing FEM simulations, we investigate the impact of a non-squared channel cross-section on the hydrodynamic stress distribution. While a 20 µm × 20 µm PDMS channel leads to a mean shear stress on the cell surface of 970 Pa (Supplementary Fig. 3, left), we find 908 Pa for a virtual channel having 21 µm width and a 30 µm height (Supplementary Fig. 3, right). With a difference below 10% our calculations suggest comparable microfluidic conditions, a conclusion which is supported by experimental results (Fig. 3).

Cell mechanics in mesofluidic systems. In a following step, we transfer our experimental framework to mesoscopic geometries on the centimeter scale. This approach would facilitate microfluidic assays controlled by flow rates and viscosities, fully unconstrained by (soft) lithography and other fabrication techniques. As a proof-of-principle experiment we use a standard flow cytometer glass cuvette of 2 cm length (Fig. 4a and Supplementary Fig. 1b). Although exceeding dimensions of standard

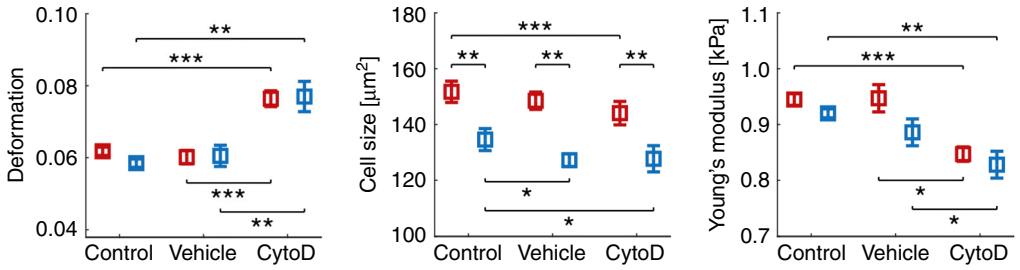

Fig. 3 Analysis of cytoskeletal alterations using virtual fluidic channels. Statistical analysis using linear mixed models of three independent biological replicates for cell deformation (left), cell size (center) and Young's modulus (right) inside a 20 µm × 20 µm PDMS chip (red) and 21 µm virtual fluidic channel inside a 30 µm × 30 µm PDMS chip (blue). Data compares control cells ($n = 8024$; PDMS and $n = 4040$; virtual channel), vehicle control ($n = 8948$; PDMS and $n = 2778$; virtual channel) as well as cells after treatment with 1 µM CytoD ($n = 4148$; PDMS and $n = 1237$; virtual channel). Data are presented as mean ± standard error of the mean (*$p < 0.05$; **$p < 0.01$; and ***$p < 0.001$).

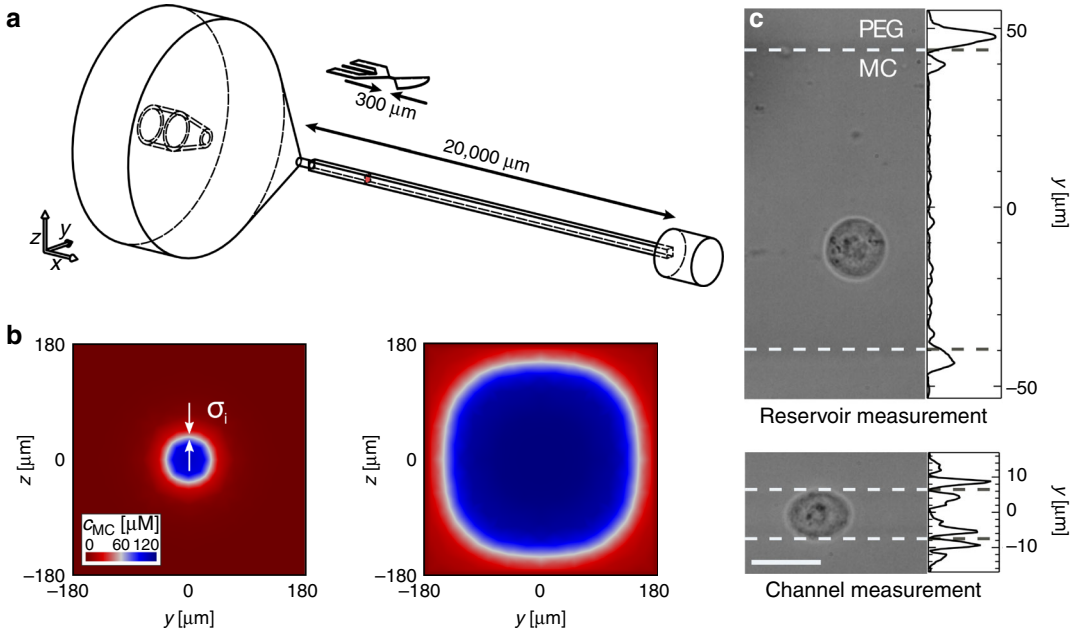

Fig. 4 Virtual channel formation inside a flow cytometer glass cuvette. a Technical drawing of glass cuvette and PDMS chip to scale for comparison. Arrows indicate length of constrictions of 2 cm for the cuvette and 300 µm for the PDMS device. **b** FEM simulations of concentration distribution for the cross-section of the cuvette performed for sample 114 µM MC at $Q_{sa} = 200$ nl s^{-1} and sheath 5 mM PEG40000 at $Q_{sh} = 1000$ nl s^{-1} yielding a 80 µm virtual channel (left). Arrows indicate the stress σ_i due to the viscosity mismatch at the interface. Adjusting the flow rates to $Q_{sh} = 50$ nl s^{-1} while keeping Q_{sa} constant, enables increasing the diameter of the constriction to 260 µm (right). **c** Representative image of a HL60 cell in a virtual channel of 88 µm diameter (sample 114 µM MC at $Q_{sa} = 200$ nl s^{-1}, sheath 5 mM PEG40000 at $Q_{sh} = 1000$ nl s^{-1}, top) and inside a virtual channel of 14 µm diameter (sample 114 µM MC at $Q_{sa} = 15$ nl s^{-1}, sheath 5 mM PEG40000 at $Q_{sh} = 1000$ nl s^{-1}, bottom). Projected line plots at top and bottom indicate the squared intensity gradient (arb. units) perpendicular to the flow direction while center between the maxima identify virtual channel interfaces (white dashed lines). Recording of cells and spheroids inside virtual channels has been repeated six times where a fluctuation in virtual channel size of 10% has been observed.

microfluidic chips by almost two orders of magnitude, a stable virtual channel of circular cross-section can be formed inside a squared constriction of 360 µm side length (Supplementary Fig 6). The existence of two steady co-flowing aqueous solutions can be predicted from FEM simulations on the full flow profile (Fig. 4b) and has been confirmed by experimental data (Fig. 4c).

Adapting Eq. (1) to the cuvette geometry demonstrates that the virtual constriction can be controlled by sample and sheath flow rates as well as viscosities (see Methods):

$$\frac{Q_{sa}}{Q_{sh}}\frac{\eta_{sa}(\dot{\gamma})}{\eta_{sh}} = \frac{\frac{\pi}{4}\tilde{w}^2}{1-\frac{\pi}{4}\tilde{w}^2}, \qquad (2)$$

where the channel diameter w can be adjusted between a few and more than one hundred micrometers (Fig. 4b, c). Here, $\tilde{w}$ is determined relative to the side length of the cuvette cross-section.

Having a dynamic size range exceeding one order of magnitude our microfluidic system can be applied to mechanically characterize cells in their reference state, i.e., in large virtual channels at low hydrodynamic stress (Fig. 4c, top) and under a finite hydrodynamic stress in narrow virtual channels (Fig. 4c, bottom)[27]. Interestingly, the sheath inside the constriction of the glass cuvette fully encloses the sample and enables a true three-dimensional cell confinement (Fig. 4b and Supplementary Fig. 7) and a homogeneous stress distribution on the cell surface mimicking the axial symmetric velocity profile (Supplementary Fig. 7, left panel). This is in contrast to standard PDMS chips, where virtual channels are limited to 2.5 dimensions with fixed feature heights given by the planar geometry of the master mold (Fig. 1a, bottom inset and Supplementary Fig. 7, right panel; see Methods). The different sheath flow geometries in the cuvette and

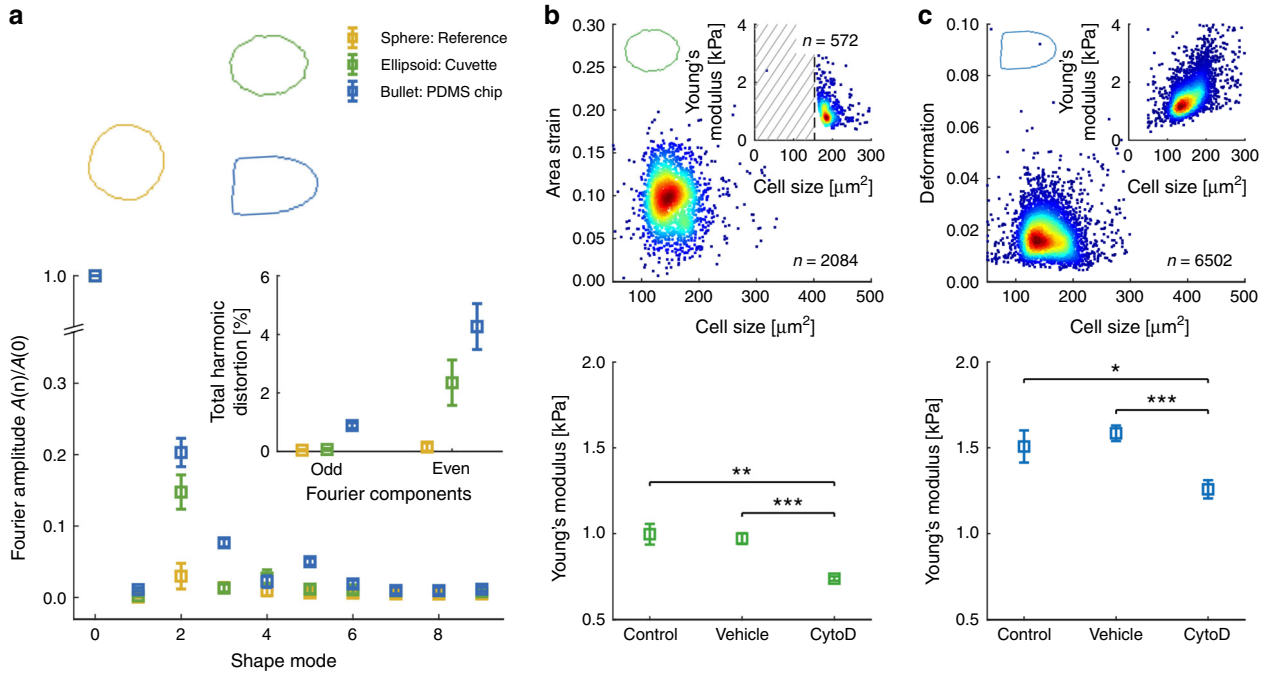

Fig. 5 High-throughput cell mechanics inside a flow cytometer glass cuvette. a Fourier amplitudes of cellular shape modes for $n = 25$ HL60 cells inside a $w = 88$ µm (yellow) and $w = 14$ µm (green) virtual channel of a glass cuvette as well as $n = 25$ HL60 cells inside the virtual channel of PDMS chip shown in Fig. 2 (blue). The inset represents the total harmonic distortion calculated for the cells inside the virtual channel of a cuvette (green), a PDMS chip (blue) and a reference measurement (yellow). Data are presented as mean ± standard deviation. **b** Area strain of HL60 cells inside a $w = 14$ µm virtual channel of a glass cuvette ($Q_{sa} = 15$ nl s^{-1} and $Q_{sh} = 1000$ nl s^{-1}, top). Inset shows Young's modulus distribution of HL60 cells calculated from area strain with $\sigma_i = 78$ Pa, shaded area indicates fraction of cells not confined by the virtual channel. Bottom graph compares the Young's modulus of three independent biological replicates of HL60 cells ($n = 2689$), a DMSO vehicle control (0.25% (v/v); $n = 3829$), and HL60 cells treated with 1 µM CytoD ($n = 3497$). **c** Deformation of HL60 cells inside a $w = 20$ µm virtual channel of a glass cuvette ($Q_{sa} = 20$ nl s^{-1} and $Q_{sh} = 1000$ nl s^{-1}, top). Inset shows Young's modulus distribution of HL60 cells calculated from a hydrodynamic model considering shear- and normal stress on cell surface in steady-state. Bottom graph compares Young's modulus of three independent biological replicates of HL60 cells ($n = 19{,}018$), a DMSO vehicle control (0.25% (v/v); $n = 23{,}612$) and HL60 cells treated with 1 µM CytoD ($n = 15{,}245$). Scale bar is 20 µm. Color in scatter plots indicates a linear density scale from min (blue) to max (red). Statistical data analysis is performed using linear mixed models and data are presented as mean ± standard error of the mean (*$p < 0.05$; **$p < 0.01$; ***$p < 0.001$).

PDMS system also explain the different scaling in relative virtual channel width $\tilde{w}$ of Eqs. (1) and (2).

Next, we ask if virtual channels inside a flow cytometer cuvette are suited to induce cell deformation. The answer is not obvious since cell surface stress scales with the velocity gradient between the maximum at channel center and zero velocity due to the no-slip boundary condition at the glass surface (Fig. 1b). Assuming typical experimental values for a cuvette of side length 360 µm and 3 cm s^{-1} cell velocity this results in shear rates in the order of 10^2 s^{-1}, which is in contrast to ~10^4 s^{-1} for cells inside a 20 µm PDMS chip at a velocity of 10 cm s^{-1}.

Despite two orders in magnitude difference in shear rate we do not only find the majority of cells inside the virtual channel of a cuvette deforming but also observe an ellipsoidal steady-state shape (Fig. 4c, bottom and Fig. 5a, green contour), which clearly deviates from the bullet shape in PDMS systems (Fig. 2c and Fig. 5a, blue contour) and from the circular reference state (Fig. 4c, top and Fig. 5a, yellow contour). Aiming to understand the physical origin of the alternating cell shapes, we perform a Fourier decomposition of the cell contour analyzing the amplitude of the first ten Fourier components[40].

For cells inside a virtual channel of a glass cuvette the second shape mode dominates (Fig. 5a, green) while cells inside the virtual channel of a PDMS chip possess significant contributions of the third and fifth mode (Fig. 5a, blue). Looking at the total harmonic distortion of the first ten Fourier components we find no contribution of the odd modes to ellipsoidal cell shape (Fig. 5a, inset), which implies a deformation inside the cuvette perpendicular to the direction of flow, only.

The fundamental difference in Fourier spectra points toward stress distributions on the cell surface that originate from different physical principles. We speculate that, while cell deformation in narrow channels, i.e., (virtual channels in) micrometer-sized systems, is mainly driven by shear, cells inside virtual channels of a cuvette are deformed by an interfacial stress σ_i originating from the liquid–liquid interface (Fig. 4b, left and Fig. 4c, bottom).

We investigate this hypothesis by calculating the hydrodynamic shear stress and normal stress on a cell surface inside a glass cuvette using FEM simulations (see Methods). Here, we assume a total flow rate of 1.02 µl s^{-1} ($Q_{sh} = 1000$ nl s^{-1}, $Q_{sa} = 20$ nl s^{-1}) and a constant viscosity of 11 mPa s. In geometries with a relative size $\lambda = r_{sphere}/R$, where r_{sphere} is the cell radius and R is the equivalent cuvette radius, peak stress increases with increasing λ for a fixed flow rate (Supplementary Fig. 8). While this relationship is valid for any laminar microfluidic system with a central spherical obstacle, we can show that virtual channels also possess a constant stress contribution at the interface resulting from the viscosity mismatch between the two co-flowing aqueous polymer phases. This effect has been described previously for systems where an annular flow of low viscosity, surrounds a core of high viscosity, e.g., oil, to reduce friction at

the oil-wall interface for power-effective transportation in pipes[41]. Under these conditions, σ_i can be derived from the simple expression:

$$\sigma_i = -\frac{8\,\eta_{sa}(\dot{\gamma})}{w}(u_c - 2u_a), \quad (3)$$

where $\eta_{sa}(\dot{\gamma})$ is the viscosity of the sample flow at shear rate $\dot{\gamma}$, w is the width of the virtual channel, u_c is the cell velocity inside the virtual channel and u_a the superficial velocity proportional to $\frac{Q_{sh}}{\pi R^2}$.

Utilizing experimental values for HL60 cells moving at a flow rate of 1.015 µl s^{-1} (Q_{sh} = 1000 nl s^{-1}, Q_{sa} = 15 nl s^{-1}) inside a w = 14 µm virtual channel of a cuvette with a side length of 360 µm we obtain a velocity of u_c = 2.8 cm s^{-1} and a stress at the liquid–liquid interface of σ_i = 78 Pa. In comparison to the hydrodynamic shear and normal stress, σ_i dominates (Supplementary Fig. 8) thus inducing cell deformation predominantly perpendicular to the direction of flow (Fig. 4c, bottom). For the calculation, viscosity values of $\eta_{sa}(\dot{\gamma})$ = 11 mPa s were taken from FEM simulations and independently confirmed using calibration beads with a fixed elastic modulus of $E = 1.5 \pm 0.5$ kPa (see Methods)[42].

Since Eq. (3) allows to consider the ellipsoidal cell shape as the steady-state response to a simple creep-compliance experiment with a constant interfacial stress $\sigma_i = E\,\varepsilon_c$, the Young's modulus can directly be calculated from the area strain ε_c of the cell (see Methods). Effectively, the liquid–liquid interface acts as a high-frequency liquid cantilever for probing global cell rheological properties on a millisecond time scale such that material properties can be extracted from simple linear models.

As a proof-of-principle experiment we characterize HL60 cells inside the virtual channel of a glass cuvette utilizing the parameters above. Assuming volume conservation the area strain can be calculated (see Methods) where a mean value of $\bar{\varepsilon}_c = 0.10 \pm 0.03$ (mean ± std. dev.) is obtained analyzing more than two thousand cells (Fig. 5b, top). From the single strain values ε_c the Young's modulus of each cell can be derived (Fig. 5b, top inset). Here, the shaded area defines an exclusion zone of cells being smaller than the virtual channel diameter, which are not probed by the interfacial stress and excluded for rheological analysis.

In a final step we perform measurements on HL60 cells after cytoskeletal modifications where we apply the liquid–liquid interface to induce cell deformation. Analyzing three biological replicates, we compare the Young's modulus of control cells (n = 2689), the corresponding DMSO control (0.25% (v/v); n = 3829), and cells after treatment with 1 µM CytoD (n = 3497). A statistical analysis reveals no difference between control ($E = 1.00 \pm 0.06$ kPa (mean ± SEM)) and vehicle ($E = 0.97 \pm 0.03$ kPa), but a significant reduction after treatment with CytoD ($E = 0.74 \pm 0.03$ kPa) compared with the control ($p < 0.0065$) and the DMSO control ($p < 0.0006$; Fig. 5b, lower graph and Supplementary Fig. 9).

For verification of our results, we adjust the virtual channel diameter inside the glass cuvette to w = 20 µm utilizing a total flow rate 1.02 µl s^{-1} (Q_{sa} = 20 nl s^{-1} and Q_{sh} = 1000 nl s^{-1}). With a mean diameter of HL60 cells smaller than w, cellular stress is governed by hydrodynamic shear and normal forces and not by the liquid–liquid interface. Analyzing more than 6000 cells, we find a median cell deformation $d = 0.017 \pm 0.007$ (median ± std. dev.; Fig. 5c, top graph), which enables applying the analytical model published earlier to predict the Young's modulus by solving the full flow profile around the cell inside the microfluidic chip[27]. We obtain $E = 1.37 \pm 0.55$ kPa (Fig. 5c, top inset). A statistical analysis of three experimental replicates for control (n = 19,018 cells), DMSO vehicle (0.25% (v/v); n = 23,612), and 1 µM CytoD (n = 15,245) reveals no difference between the control ($E = 1.5 \pm 0.1$ kPa (mean ± SEM)) and the vehicle ($E = 1.58 \pm 0.05$ kPa), but a significant reduction in the elastic modulus for cells treated with CytoD ($E = 1.25 \pm 0.06$ kPa) compared with the control ($p < 0.04$) and the DMSO control ($p < 0.0004$; Fig. 5c, lower graph and Supplementary Fig. 10).

High-throughput tissue mechanics. We reveal the full potential of virtual fluidic channels by studying the impact of single-cell mechanics on tissue properties. Such a comparative analysis is of high importance, e.g., to understand emergent effects in cellular co-culture systems in regenerative medicine. This has so far only been possible using atomic force microscopy with its ability to bridge length scales from a few micrometers to a millimeter scale. Here, we aim to utilize the capability of virtual channels to modify the constriction diameter and to tailor the hydrodynamic stress distribution toward high-throughput characterization of HEK293T cells and spheroids inside the glass cuvette of a commercial flow cytometer.

Spheroids have been cultured for multiple days in agarose micro-molds with an initial seeding density of ~30 cells per well. We observe an average spheroid diameter of 82 ± 23 µm (mean ± std. dev.; n = 5) at day 1, which increases to 134 ± 19 µm (n = 13) at day 4 (Fig. 6a, left). Approximating the number of cells inside the spheroids from the volume allows to fit an exponential growth curve to our data, where we find a doubling time of 32 h (Fig. 6a, right).

For studying the contribution of single cells to tissue stiffness we first adjust the diameter of the virtual channel inside the cuvette to w = 16 µm to probe single HEK293T cells by interfacial stress (Fig. 6b, left panel; 114 µM MC sample and 5 mM PEG40000 sheath) yielding $\varepsilon_c = 0.09 \pm 0.03$ (median ± std. dev.; Fig. 6b, center panel and Supplementary Fig. 11). The cellular Young's modulus E is calculated under steady-state conditions applying the interface model. Utilizing experimental parameters of u_c = 2.8 cm s^{-1} and η_{sa} = 11 mPa s yields an interfacial stress of σ_i = 66 Pa, which exceeds the stress originating from Poiseuille flow (Supplementary Fig. 8). From the stress–strain relationship we obtain a mean Young's modulus of $E = 0.73 \pm 0.38$ kPa for single HEK293T cells (Fig. 6b, right panel).

Finally, virtual fluidic channels are applied for high-throughput mechanical characterization of HEK293T spheroids as a 3D-tissue model. Cells are cultured into spheroids with a diameter of ~130 µm using agarose micro-molds, where each spheroid contains an average of 650 cells (Fig. 6a, right, blue box plot; see Methods). Taking advantage of the simple relationship between Q_{sa}, Q_{sh}, η_{sa}, and η_{sh}, stable virtual channels of 190 µm mean diameter are established inside the constriction of the cuvette (Eq. (2) and Fig. 6c, left panel). While suspended spheroids slightly perturb the liquid–liquid interface during translocation, the low Reynolds number regime ensures a fast recovery within less than two spheroid diameters. The spheroids show the typical bullet-like shape with a mean deformation of 0.038 ± 0.027 (mean ± std. dev.; Fig. 6c, center panel), which is significantly higher than the undeformed reference state at 260 µm virtual channel width (Supplementary Fig. 12).

For estimating the elastic modulus of spheroids, we first calculate σ_i from Eq. (3) utilizing experimental parameters Q_{sh} = 330 nl s^{-1}, u_c = 1.67 cm s^{-1}, and w = 190 µm as stated above. Assuming a viscosity η_{sh} = 53 mPas from FEM simulations of the full hydrodynamic geometry yields an interfacial stress of σ_i = 20 Pa. With a magnitude much smaller than the hydrodynamic shear and normal stress, spheroid deformation is dominated by the parabolic flow profile and the elastic modulus is obtained from the analytical model published earlier[27,43]. This yields $E = 86 \pm 36$ Pa (mean ± std. dev.; Fig. 6c, right panel). Analyzing three biological replicates of more than 700 spheroids

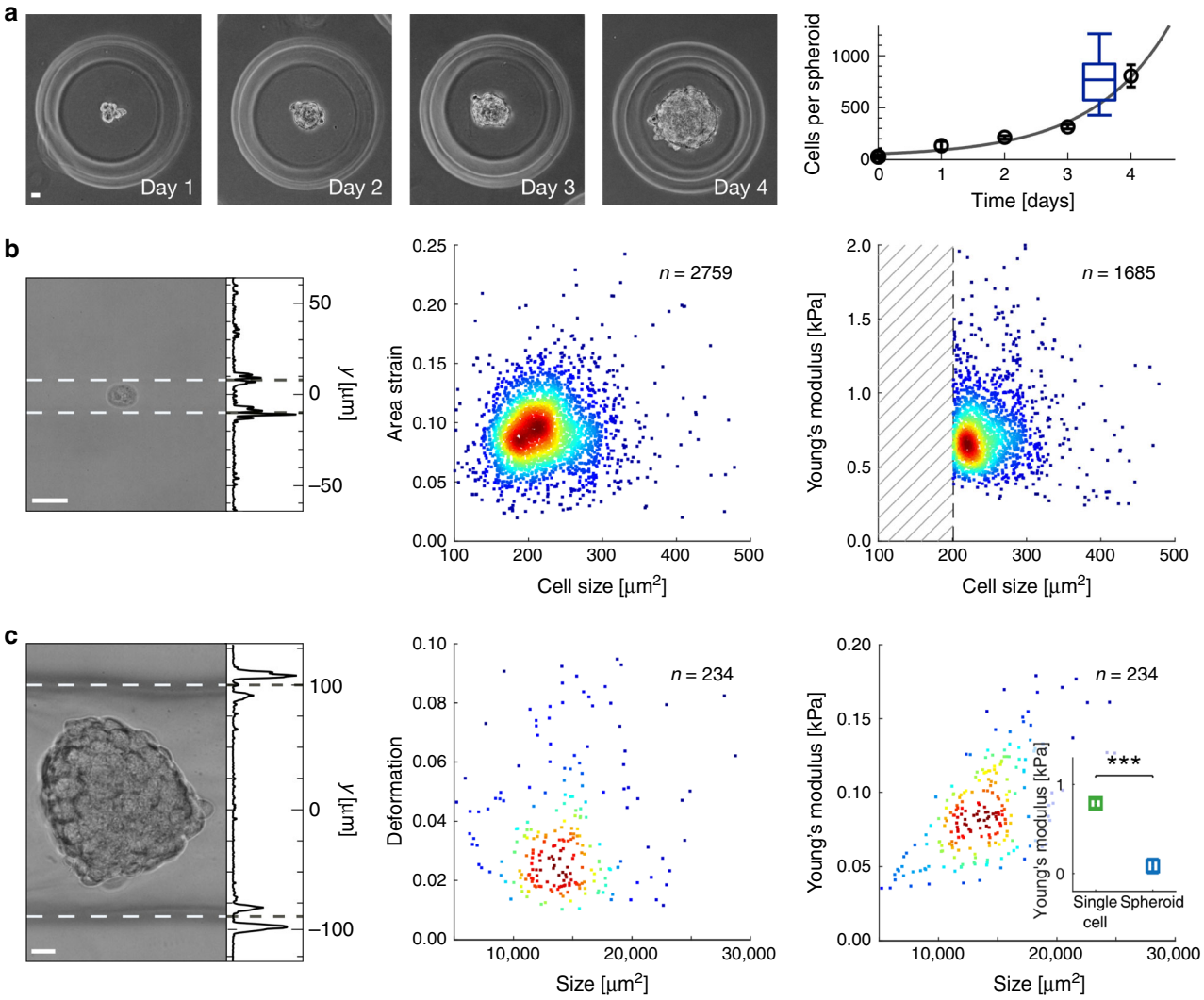

Fig. 6 High-throughput cell and tissue mechanics inside glass cuvette. a Bright-field images of HEK293T spheroids obtained at four subsequent days inside agarose mold. Initial seeding density is ~30 cells per micro well (left). Exponential fit (solid line) to the mean cell number (black circles) per spheroid yields a doubling time of ~32 h. Time series has been recorded twice. Distribution of cell number per spheroid indicated in (**c**, center panel) is represented in blue box plot showing median (center line), 25 and 75 percentiles (lower and upper box bound) as well as 10 and 90 percentiles (whiskers). **b** Representative image of a HEK293T cell in virtual channel of 16 µm diameter (sample 114 µM MC at $Q_{sa} = 20$ nl s^{-1}, sheath 5 mM PEG40000 at $Q_{sh} = 1000$ nl s^{-1}, left). Corresponding scatter plots of area strain (center) and Young's modulus (right) versus HEK293T cell size. Young's modulus is calculated from area strain assuming an interfacial stress of 66 Pa. Shaded area indicates cells not confined inside the virtual channel. **c** Representative image of HEK293T spheroid in virtual channel of 190 µm width (sample 114 µM MC at $Q_{sa} = 330$ nl s^{-1}, sheath 5 mM PEG40000 at $Q_{sh} = 200$ nl s^{-1}, left). Projected line plots in (**b**) and (**c**) indicate the squared intensity gradient (arb. units) perpendicular to the flow direction while centers of the intensity maxima identify the virtual channel interfaces (dashed white lines). Corresponding scatter plots of deformation (center) and Young's modulus (right) versus HEK293T spheroid size. Inset in right graph compares Young's modulus of single cells ($E = 0.79 \pm 0.06$ kPa) and spheroids ($E = 84 \pm 78$ Pa) from three independent biological replicates consisting of $n = 2433$ single-cell and $n = 762$ spheroid measurements ($p = 0.0003$). Scale bar is 20 µm. Color in scatter plots indicates a linear density scale from min (blue) to max (red). Statistical data analysis is performed using linear mixed models and data are represented as mean ± standard error of the mean (***$p < 0.001$).

and 2000 cells, we derive an apparent Young's modulus of 84 ± 78 Pa (mean ± SEM), which is a factor of ten smaller than single cells cultured in a 2D plastic culture dish with 0.79 ± 0.06 kPa (Fig. 6c, right panel inset).

Discussion

Microfluidics has shown great impact in fundamental and applied biochemical, biomedical as well as biophysical research[21,30,44]. The possibility to control nanoliter sample volumes to perform quantitative molecular and cellular assays of highest sensitivity is one of the great promises of fluidic microtechnology and aims to replace bulk experimental assays[23]. Recent examples include single molecule and protein sensing, chemical reactions for analyte diagnostics, fluorescence cytometry as well as mechanical cell characterization[21,24,45,46].

In the low Reynolds number regime laminar systems can be categorized into single and multiple phase flows[47–51]. While single aqueous phases have mainly been used to study material properties of molecules and cells[24–26,52], multiphase flows allow to tailor the total reaction volume to the analyte of interest, e.g., to control diffusive processes or for spatiotemporal alignment of particles and cells[21,38]. Interestingly, a combination of both approaches, i.e., modifying the system size and tailoring the hydrodynamic stress distribution to perform rheological

characterization of biological matter across various scales, has not been achieved before.

The latter would be of high importance for the growing field of 3D-tissue assays. In contrast to two-dimensional cell culture systems using plastic petri dishes, 3D models allow to mimic a physiological environment that can be used, e.g., for drug discovery[53], to study thrombi formation in vitro[54] as well as cardiac tissue regeneration[55]. While recent research was focusing on generation of 3D cell cultures, e.g., using hanging drop microplates or spheroid microplates with ultra-low attachment coating, high-throughput characterization of tissue function mainly focused on molecular labels or genomics as well as transcriptomics potentially altering the sample[56].

In contrast to standard assays in cell biology, methods utilizing intrinsic material properties of tissues provide a label-free access to biological function. Originally, these methods have been limited to single cells[6,8] and were mainly based on the interaction between an acoustic, optical or physical probe[57,58]. Recently, atomic force microscopy and micropipette aspiration have been extended toward 3D-tissue assays where they probe mechanical properties locally by integrating over a limited number of cells[59]. However, a high-throughput assay able to impose a homogeneous stress distribution on a tissue that integrates cell-cell and cell-matrix interactions into the stress–strain response remained elusive.

By introducing virtual fluidic channels, we establish a simple, fast and highly flexible method to perform microfluidic experiments independent of chip material and chip geometry. We demonstrate that only two parameters, volumetric flow rate and medium viscosity, are sufficient for on-the-fly modifications of channel cross-sections resulting in constrictions with fluid dynamics comparable to systems built from soft lithography.

Virtual fluidic channels can be formed inside classic microfluidic systems, e.g., PDMS chips, but also inside mesoscopic geometries of centimeter size. Using a glass cuvette from a commercial flow cytometer, we show the formation of a stable liquid-bound constriction with cross-sections that can be changed from a few microns to hundreds of micrometers within seconds.

As one potential application we performed mechanical characterization of HL60 cells in both systems. Proof-of-principle experiments in PDMS chips using real-time deformability cytometry revealed an elasticity of 0.95 ± 0.01 kPa (mean ± SEM) and 0.92 ± 0.02 kPa for solid and fluid confinement, respectively, showing no significant differences. Next, we repeated our assay using virtual channels created in a large glass cuvette where we obtained a slightly elevated Young's modulus of 1.5 ± 0.1 kPa. The observed differences potentially originate from different levels in deformation amplitudes present in both systems. In fact, the deformation inside the glass cuvette is so small that deviations of the initial cell shape from an ideal circle (circularity = 1) might impede application of the analytical model that requires finite cell shape changes in shear flow[27,43].

For solving this discrepancy, we demonstrate that the viscosity mismatch at the liquid–liquid interface leads to an interfacial stress resulting in a cellular strain that allows for extracting material properties from simple creep-compliance experiments. For HL60 cells probed by this liquid–liquid interface of a virtual channel inside a glass cuvette we obtain an elastic modulus of 0.97 ± 0.03 kPa, which is in good agreement not only with our PDMS results based on shear flow but also with data published earlier[27,40]. In fact, our proof-of-principle experiments demonstrate that a virtual channel acts like a liquid cantilever that exposes biological samples to a homogeneous 3D stress distribution for probing biological matter on a millisecond scale. In contrast to atomic force microscopy or microconstrictions virtual fluidic channels enable a label-free analysis without any cell-wall interaction and at high-throughput.

We highlight further potential applications of virtual fluidic channels and provide the first high-throughput rheological characterization of spheroids inside the cuvette of a commercial flow cytometer. Spheroids have gained an increasing importance as in vitro 3D cell culture models in biology closely mimicking in vivo conditions during development[10,32]. In addition, the mechanical microenvironment in a tissue-like structure might also be of importance to understand immune-specific cell response to external stimuli, e.g., during inflammation[60]. While our data on this tissue model confirms previous studies of small sample size[34,35], virtual fluidic channels additionally enable comparative single-cell and tissue rheology of sufficient statistical power appropriate for large-scale sample screenings.

In summary, virtual fluidic channels allow for on-the-fly generation of nearly arbitrary hydrodynamic environments inside large fluidic geometries, e.g., commercial glass cuvettes. We demonstrate that our method provides simultaneous access to material properties of biological samples across various length scales from single cells to tissues, which could be highly relevant for a functional evaluation of engineered tissue grafts in regenerative applications. Ultimately, our approach renders microfluidic experiments independent of soft lithography and extends the parameter space of classical fluorescence-based flow cytometry toward an unbiased cell and tissue analysis utilizing intrinsic material properties.

Methods

Sample and sheath fluid. Sample solution is used as cell as well as spheroid carrier and is made of methylcellulose (MC, approximate molecular weight 88 kDa, Sigma) in PBS−/− (without Mg^{2+} and Ca^{2+}). Briefly, MC concentrations of 0.5% (w/v), respectively, 57 µM, and 1.0% (w/v), respectively, 114 µM, are dissolved at room temperature by agitation overnight. The osmolarity of MC solutions is measured to be stable at a physiological range between 275 and 295 mOsm (Fiske 210 Osmometer). The sheath fluid is used to establish a liquid confinement of the sample and is made of polyethylene glycol (PEG) in PBS−/− with a molecular weight of 8000 Da (AppliChem) or 40,000 Da (Serva Electrophoresis). Experiments have been carried out at concentrations of 50 mM (PEG8000) and 2 mM as well as 5 mM (PEG40000).

The shear-rate dependent viscosities of our buffers are obtained from a full rheological characterization using a rheometer in cone-plate geometry (MCR502, Anton Paar). MC solutions reveal a concentration-dependent shear-thinning behavior and the dynamic viscosities follow a simple power law (Fig. 1c):

$$\eta_{\mathrm{MC}}(\dot{\gamma}) = n_{1|2} \cdot \left(\frac{\dot{\gamma}}{\dot{\gamma}_0}\right)^{(m_{1|2}-1)} \quad (4)$$

where $\eta_{\mathrm{MC}}(\dot{\gamma})$ is the dynamic viscosity of 57 and 114 µM MC at the hydrodynamic shear rate $\dot{\gamma}$, respectively. Here, n denotes a consistency parameter with $n_{57\,\mu\mathrm{M}} = 0.078$ Pa s and $n_{114\,\mu\mathrm{M}} = 0.60$ Pa s, m is the flow behavior index with $m_{57\,\mu\mathrm{M}} = 0.79$ and $m_{114\,\mu\mathrm{M}} = 0.64$, while $\dot{\gamma}_0 = 1\,\mathrm{s}^{-1}$ for reference.

All PEG solutions can be described by a Newtonian behavior (Fig. 1c) with a constant viscosity of $\eta_{\mathrm{PEG8000\,(50\,mM)}} = 0.106$ Pa s, $\eta_{\mathrm{PEG40000\,(2\,mM)}} = 0.015$ Pa s and $\eta_{\mathrm{PEG40000\,(5\,mM)}} = 0.154$ Pa s over the entire relevant shear-rate range from 100 to 50,000 s^{-1}.

All buffers are sterile filtered (pore size 0.2 µm, VWR) prior to experiments.

Virtual channel formation. We use two major geometries to establish virtual channels in fluidic devices: a microfluidic chip assembled from polydimethylsiloxane (PDMS) and sealed with a glass cover slide as well as a mesoscopic glass cuvette commonly used in commercial flow cytometers.

The microfluidic chip is produced using soft lithography (Zellmechanik Dresden) and consists of two inlets, which are connected to a syringe pump (NemeSys, Cetoni). An outlet is used for recollection of cells for potential downstream analysis. Prior to an experiment, two 1-ml syringes (Luer-Lock syringe, BD) with MC solution (sample) and PEG solution (sheath) are assembled on the syringe pump system, which is controlled by the ShapeIn2 software (version 2.0.5, Zellmechanik Dresden). The PDMS chip is first filled with the MC buffer through the sample inlet at 100 nl s^{-1} and subsequently the PEG solution is added through the sheath inlet at 50 nl s^{-1} (Supplementary Fig. 1A). The virtual channel forms immediately inside the squared central constriction of 300 µm length and 30 µm × 30 µm cross-section, can be adjusted by controlling flow rates as well as buffer viscosities and is stable throughout the entire duration of the experiment.

In a second set of experiments, a standard flow cytometry glass cuvette (Sysmex) is used. With a length of 2 cm and a quadratic 360 µm × 360 µm cross-section the constriction of the cuvette exceeds the dimensions of our microfluidic chip by almost a factor of 100. In contrast to the planar geometry in the PDMS system, the sheath flow completely surrounds the sample and results in a three-dimensional confinement (Fig. 4b, left panel). Both inlets are connected to a syringe pump (NemeSys, Cetoni) and 114 µM MC solution (1 ml Luer-Lock syringe, BD) as well as 5 mM PEG40000 solution (10 ml Luer-Lock syringe, BD) are used for sample and sheath, respectively (Supplementary Fig. 1B). For initiating experiments, the cuvette was simultaneously filled with MC at 200 nl s^{-1} through the sample inlet and PEG at 1000 nl s^{-1} through the sheath inlet. The virtual channel forms immediately upon contact and remains stable throughout the entire experiment. The sample flow is not in contact with the surface of the cuvette as it is completely surrounded and confined by sheath buffer.

Finite element method simulations. Numerical finite element method (FEM) simulations have been performed using Comsol Multiphysics (version 5.4, Comsol Group) and its computational fluid dynamics and transport packages. For the microfluidic chip the full layout is reconstructed, and one quadrant used for hydrodynamic simulations taking advantage of the two symmetry axes through the center line of the design (Fig. 1a and Supplementary Fig. 1A)[40]. The layout of the glass cuvette is reconstructed following the manufacturer's documentation, and one eighth of the entire structure is simulated utilizing the four symmetry axes through the center line of the design (Fig. 4a and Supplementary Fig. 1B).

FEM simulations are carried out using physics-controlled meshes of an extra fine element size defined by the meshing algorithm. For the microfluidic chip this leads to a meshed volume of ~6×10^6 elements with an average element radius of 1.2 µm, for the glass cuvette to ~1×10^6 elements with an average element radius of 14.3 µm. For all experiments, the fluid is set to be incompressible and solid walls are defined by a no-slip boundary condition. The fluid is modeled as a superposition of the respective MC and PEG solution material features, normalized to the local concentrations. While laminar inflow at sample and sheath inlet are assigned flow rates under constant pressure conditions, backflow is suppressed, reflecting experimental conditions. Parametric and material sweeps supporting the derivation of the scaling law in Eq. (1) are performed for all sample and sheath materials as well as flow rate combinations and channel geometries (Supplementary Table 1).

FEM simulations to determine the shear stress on a sphere's surface are carried out by simulating a steady-state condition minimizing the difference of the integrated shear stress and the pressure acting on the sphere following ref. [27]. The whole system is set to move by the velocity of the interface u_i found in full-geometry simulations. Simulation of surface stresses as a function of relative cell size λ is conducted in the very same manner using respective parameters (Supplementary Table 1).

Virtual channel characterization. In both major geometries, PDMS chip and glass cuvette, we use the squared grayscale intensity gradient to identify the interfaces between MC and PEG solutions in the focal plane of our bright-field images. Having a region-of-interest of 250 pixels in length and sufficient height, to capture the entire virtual channel, the mean pixel intensity is calculated for each pixel line. From this one-dimensional intensity distribution perpendicular to the flow direction the squared intensity gradient is derived yielding two local maxima. These are identified as the optical interface position (Fig. 1a, top inset) and are chosen to coincide with the half-maximum MC concentration found by FEM simulations (Fig. 1b) to describe the distinct phases accordingly:

$$c_{\mathrm{MC}}(y) \geq \frac{c_{\mathrm{MC,max}}}{2} \Leftrightarrow |y| \leq \tilde{w} y_{\max} \tag{5}$$

or, equivalently:

$$c_{\mathrm{MC}}(y) < \frac{c_{\mathrm{MC,max}}}{2} \Leftrightarrow |y| > \tilde{w} y_{\max} \tag{6}$$

with $-y_{\max} \leq y \leq y_{\max}$ and $0 \leq \tilde{w} \leq 1$, $c_{\mathrm{MC}}(y)$ is the methylcellulose concentration distribution while $-y_{\max}$ and $y_{\max}$ are the lateral boundaries of the solid constriction inside the microfluidic chip or cuvette, respectively. The relative width $\tilde{w}$ of the virtual channel is thus defined by the half-maximum concentration $\frac{1}{2} c_{\mathrm{MC,max}}$ (Fig. 1a, b).

A simple linear proportionality analysis allows to describe $\tilde{w}$ in our PDMS chip (Fig. 1a, top inset)[38]:

$$\frac{Q_{\mathrm{sa}}}{Q_{\mathrm{sh}}} = \frac{A_{\mathrm{sa}}}{A_{\mathrm{sh}}} \frac{u_{\mathrm{sa}}}{u_{\mathrm{sh}}} = \frac{\tilde{w}}{1-\tilde{w}} \frac{u_{\mathrm{sa}}}{u_{\mathrm{sh}}} \propto B \frac{\tilde{w}}{1-\tilde{w}} \frac{\eta_{\mathrm{sh}}}{\eta_{\mathrm{sa}}(\dot{\gamma})} \Rightarrow \frac{Q_{\mathrm{sa}}}{Q_{\mathrm{sh}}} \frac{\eta_{\mathrm{sa}}(\dot{\gamma})}{\eta_{\mathrm{sh}}} = B \frac{\tilde{w}}{1-\tilde{w}} \tag{7}$$

with the flow rates Q_{sa} and Q_{sh}, the dynamic viscosities η_{sa} and η_{sh}, the cross-sections of the aqueous phases A_{sa} and A_{sh}, the mean velocities u_{sa} and u_{sh}, and the linear proportionality factor B. We fit Eq. (7) to our experimental data (Fig. 1d) with an open parameter B yielding $B = 0.994 \pm 0.047$ (99% confidence interval). Therefore, we safely set $B = 1$, which simplifies Eq. (7) to:

$$\frac{Q_{\mathrm{sa}}}{Q_{\mathrm{sh}}} \frac{\eta_{\mathrm{sa}}(\dot{\gamma})}{\eta_{\mathrm{sh}}} = \frac{\tilde{w}}{1-\tilde{w}}. \tag{1}$$

Interestingly, this simple equation is completely independent from the specific polymers, chain lengths, molecular weights, and concentrations.

An analysis of the entire flow rate and viscosity range for sample and sheath yields $0.05 < \frac{Q_{\mathrm{sa}}}{Q_{\mathrm{sh}}} \frac{\eta_{\mathrm{sa}}}{\eta_{\mathrm{sh}}} < 2$, where a stable interface can be observed. Beyond this range either sample or sheath flow may completely dominate.

In a similar way, a description can be derived for a circular virtual channel inside a rectangular cross-section:

$$\frac{Q_{\mathrm{sa}}}{Q_{\mathrm{sh}}} = \frac{A_{\mathrm{sa}}}{A_{\mathrm{sh}}} \frac{u_{\mathrm{sa}}}{u_{\mathrm{sh}}} = \frac{\frac{\pi \tilde{w}^2}{4}}{1-\frac{\pi \tilde{w}^2}{4}} \frac{u_{\mathrm{sa}}}{u_{\mathrm{sh}}} \propto B \frac{\tilde{w}}{1-\tilde{w}} \frac{\eta_{\mathrm{sh}}}{\eta_{\mathrm{sa}}(\dot{\gamma})} \Rightarrow \frac{Q_{\mathrm{sa}}}{Q_{\mathrm{sh}}} \frac{\eta_{\mathrm{sa}}(\dot{\gamma})}{\eta_{\mathrm{sh}}} = B \frac{\frac{\pi \tilde{w}^2}{4}}{1-\frac{\pi \tilde{w}^2}{4}}, \tag{8}$$

which simplifies to Eq. (2) for $B = 1$. Notably, Eqs. (2) and (8) show a quadratic behavior for the relative width due to the specific boundary conditions.

Characterization of interface stability has been done by analyzing the diffusion of both polymers, MC and PEG, in PBS. Diffusion coefficients of MC, PEG8000 and PEG40000 in PBS were measured by dynamic light scattering (DLS, Zetasizer Nano-ZS, Malvern Instruments). DLS analyzes the autocorrelation function of back-scattered intensity fluctuations over time. The diffusion coefficients are $D_{\mathrm{MC}} = 8 \times 10^{-12}$ m^2 s^{-1}, $D_{\mathrm{PEG8000}} = 2 \times 10^{-10}$ m^2 s^{-1}, and $D_{\mathrm{PEG40000}} = 3 \times 10^{-11}$ m^2 s^{-1}, respectively. Measurements were carried out at 25 °C at a scatter angle of 173°. Average diffusive displacement of dissolved polymers can be calculated using the solution to Fick's second law $\Delta x = \sqrt{2 D t_{\mathrm{passage}}}$ and is <1 µm for each polymer (using typical time to traverse a microfluidic chip constriction t_{passage} = channel length/flow velocity ≈ 2 ms).

Cell culture. HL60 cells, a myeloid precursor cell line (courtesy of Dan and Ada Olins) are cultured in RPMI-1640 medium (BioWest) with 10% FCS (Gibco), 1% penicillin/streptomycin (BioWest), and 2 mM L-Glutamin (BioWest) in an incubator at 37 °C under 5% CO_2 and 95% ambient air. Every 48 h cells are centrifuged at 200 × g for 5 min (Allegra X-15R, Beckman Coulter), the supernatant is discarded, and cells are resuspended to a concentration of ~1.5×10^5 cells per milliliter. Experiments are carried out ~36 h after splitting during log-phase. Cells have been checked for Mycoplasma infection, and viability is assessed prior to experiments to ~95% using Trypan Blue.

HEK293T cells as a model system for adherent cells are cultured in DMEM high glucose medium (BioWest) with 10% FCS (Gibco) and 2 mM L-Glutamine (BioWest) in an incubator at 37 °C under 5% CO_2 and 95% ambient air. After reaching a confluency of 80%, cells are detached from T25 culture flasks enzymatically by exposure to 1× Trypsin (BioWest) for 2 min, centrifuged at 200 × g for 5 min (Allegra X-15R, Beckmann Coulter), and the supernatant is discarded. Cells are resuspended in cell culture medium to a final amount of 0.8×10^6 cells per flask. Cells have been checked for Mycoplasma infection and viability is assessed prior to experiments to ~95% using Trypan Blue.

Spheroid culture. HEK293T spheroids as a tissue model system are cultured in agarose micro-molds following the manufacturer protocol (Microtissues). Briefly, after autoclaving the micro-molds, 2% (w/v) agarose (Biozym Scientific) is dissolved in 0.9% (w/v) sterile saline and boiled in a microwave oven. After cooling to 60–70 °C, 500 µl molten agarose is added into a 12-series micro-mold, removed after gelation and transferred to a 12-well culture plate and equilibrated with medium.

Cells are initially grown in a T75 culture flask with a seeding density of 2×10^6 cells. After reaching a confluency of 60–80%, cells are detached enzymatically by exposure to 1× Trypsin (BioWest) for 5 min, centrifuged at 200 × g for 5 min (Allegra X-15R, Beckmann Coulter) and 7000 cells are resuspended in a total volume of 120 µl of cell culture medium inside the agarose micro-mold containing 256 wells. Cells are grown for 3 days reaching a mean spheroid diameter of ~130 µm inside the wells. Each spheroid consists of 650 single cells on average.

The agarose micro-molds are flipped upside down and the spheroids are collected in a 12-well plate submerged in PBS−/− and centrifuged at 50 × g for 5 min (Allegra X-15R, Beckmann Coulter). After collection in a falcon tube and a further centrifugation at 50 × g for 5 min, the pellet is resuspended in MC buffer to a concentration of 1000 spheroids per 200 µl prior to experiments.

Real-time deformability cytometry. Real-time deformability cytometry (RT-DC) is used for high-throughput mechanical cell and spheroid characterization. The system is built on a commercial solution (AcCellerator, Zellmechanik Dresden) consisting of an inverted microscope (Axio Observer A.1, Zeiss), a CMOS camera (MC1362, Mikrotron), a microsecond-pulsed LED illumination (L1, Zellmechanik Dresden), and a dedicated syringe pump (NemeSys, Cetoni).

Either a microfluidic chip or a glass cuvette is assembled on the xy-stage of the microscope. Cells or spheroids translocate through a constriction and deform by hydrodynamic shear and normal stress[26,27]. Image acquisition and analysis are performed in real-time with a throughput exceeding 1000 cells or 10 spheroids per second (depending on initial concentration) and deformation is quantified using the circularity of each particle:

$$\text{Deformation} = 1 - \text{Circularity} = 1 - \frac{2\sqrt{\pi\,\text{Area}}}{\text{Perimeter}}. \tag{9}$$

Measurements on single cells are performed using a 40x objective (PDMS chip: Apochromat, Zeiss; glass cuvette: LD Plan Neofluar, Zeiss) with an optical resolution of 0.34 µm per pixel, and on spheroids using a 20x objective (LDC, Zeiss) with 0.68 µm per pixel.

Measurement protocol. Prior to RT-DC experiments using microfluidic chips, the entire fluidic system is first filled via the sample inlet using 57 μM MC solution at a flow rate of 100 nl s^{-1}. Next, 50 mM PEG8000 solution is added through the sheath inlet at a flow rate of 50 nl s^{-1}. Upon contact of both aqueous phases in the entrance region of the constriction, a distinctive virtual channel forms immediately, which can be identified by the optical phase difference at the interface (Fig. 1a). After stabilizing the fluid flow for 3 min, sample and sheath are adjusted to the experimental flow rates and equilibrated for 2 min.

In a typical RT-DC experiment, inlet tubing is detached after virtual channel formation and 100 μl of cell suspension in MC buffer at a concentration of ~10^6 cells per milliliter are drawn using the syringe pump. The tube is reconnected and the experimental flow rates are applied. RT-DC of single cells is performed as published[26]. Briefly, deformation and size of several thousand single cells inside the virtual channel are analyzed. Measurements are carried out at flow rates of Q_{sa} = 10 nl s^{-1} and Q_{sh} = 30 nl s^{-1} (sample and sheath MC (57 μM), 20 μm × 20 μm cross-section PDMS chip), Q_{sa} = 90 nl s^{-1} (sample MC (57 μM)) and Q_{sh} = 4 nl s^{-1} (sheath PEG8000 (50 mM), virtual channel of 21 μm × 30 μm cross-section in the constriction of PDMS chip of 30 μm × 30 μm cross-section). In addition, a reservoir measurement, i.e., before entering the (virtual) channel, is taken for reference.

Prior to experiments using the glass cuvette, the full fluidic system is cleaned manually by flushing both inlets with 10 ml of 70% isopropanol and de-ionized water. This procedure also ensures a complete degassing of the system, which is an essential requirement for stable virtual channels. Next, the glass cuvette is simultaneously filled with 114 μM MC at 200 nl s^{-1} via the sample and 5 mM PEG40000 at 1000 nl s^{-1} via sheath inlet. Upon virtual channel formation inside the central constriction, the system is stabilized for 10 min before experimental flow rates are applied and then equilibrated for additional 2 min.

In a typical RT-DC experiment, the sample is resuspended in 1 ml of 114 μM MC to a concentration of ~10^6 cells per milliliter or 5×10^3 spheroids per milliliter. Long-term virtual channel stability is achieved by preparing a biological sample solution in a separate syringe/tubing system and replacing the initial set manually. RT-DC measurement are carried out 3 mm inside the constriction of the cuvette and by controlling the flow rates to tune the virtual channel to a diameter of 20 μm using flow rates Q_{sa} = 20 nl s^{-1} and Q_{sh} = 1000 nl s^{-1} (cells) and to a diameter of 190 μm using flow rates Q_{sa} = 330 nl s^{-1} and Q_{sh} = 200 nl s^{-1} (spheroids). In addition, a reservoir measurement is conducted in a virtual channel of 88 μm width for single-cell samples and of 260 μm width for spheroid samples as a reference. For each condition several thousand cells and hundreds of spheroids are analyzed, respectively.

Data acquisition, image analysis, and the control of the syringe pump are performed by using the ShapeIn2 software (version 2.0.5, Zellmechanik Dresden).

Compound treatment of HL60 cells. The HL60 cells were treated with cytochalasin D (CytoD) to inhibit filamentous actin polymerization (Sigma-Aldrich). Cell concentration was adjusted to 10^6 cells in 100 μl of 57 μM MC and CytoD dissolved in dimethyl sulfoxide (DMSO; Sigma-Aldrich) was added to a final concentration of 1 μM[61] . Prior to the experiment cells were incubated for 20 min at 37 °C (5% CO_2 and 95% ambient air). During measurement DMSO and CytoD concentration is maintained constant to avoid the reversibility of the effect[62].

Analytical models for cell mechanical properties. For determining the elastic properties of cells and spheroids inside the glass cuvette we model the full virtual channel inside a cross-section of 360 μm side length. The relative diameter $\tilde{w}$ of the virtual channel is obtained from experimental data (Fig. 1a, top inset), the velocity at the liquid–liquid interface is extracted from FEM simulations assuming Stokes flow and used as a moving wall boundary condition. Placing a sphere of radius r_{sphere}, representing either a cell or a spheroid, in the centre of the virtual channel allows for extracting a mean surface shear rate for all experimental conditions. The dynamic viscosity of the MC solution is then determined by using Eq. (4).

For deriving the elastic modulus of cells and spheroids, respectively, we provide two different analytical models.

The first approach is based on an analytical model introduced earlier[27]. Briefly, for a moving object inside the (virtual) channel we assume a steady-state defined by the balance of shear and normal forces on its surface. Expansion of the Stokes equation in the appropriate geometry and coupling to linear elasticity theory allows to predict surface displacement of an initially round object. Our model shows for a given relative size $\lambda = r_{sphere}/R$, where r_{sphere} is the object's radius and R is the (equivalence) radius of the constriction, that the characteristic stress scales with the viscosity of the surrounding medium as well as with object velocity and is a function of the surface position. Since deformation is governed by shear and normal forces originating from the Poiseuille flow inside the microfluidic channel, the steady-state object shape resembles a bullet with finite front radius, which is best characterized by its circularity. Assuming objects of varying bulk elastic modulus E, cell deformation can be predicted for a given characteristic stress and be used to generate a lookup table to solve the inverse problem, i.e., to predict E from cell deformation.

The second model is based on the reduction of viscous friction for material transport in pipes and is described by an interfacial stress σ_i at the liquid–liquid interface of co-flowing solutions[41]. Here, we use σ_i to impose a surface stress on objects confined in a virtual channel and to induce a deformation with an amplitude that depends on the elastic modulus of the object, its velocity, the virtual channel radius and medium viscosity (Eq. (3)). In contrast to the above model utilizing hydrodynamic shear and normal forces where deformation is quantified by circularity, the interfacial stress acts perpendicular to the direction of flow and leads to an ellipsoidal deformation, that can be described by an area strain.

The area strain ε_c is calculated from the cross-sectional area of the deformed cell $A(t)$. Assuming volume conservation and a spherical reference cell shape the area of the undeformed cell A_0 can be approximated and the strain obtained from:

$$\varepsilon_c = \frac{A(t) - A_0}{A_0}. \quad (10)$$

The one-dimensional elongation in the direction of flows allows to consider the shape as the steady-state strain in a Kelvin–Voigt model and the elastic modulus can be calculated from $\sigma_i = E\,\varepsilon_c$.

In principle both, the interfacial stress model and the Stokes equation in combination with linear elasticity theory, can be used to extract elastic properties from RT-DC measurements. Our results suggest that the applicability depends on the relative object size λ inside the constriction. While for large λ, e.g., cells inside a PDMS channel, surface stress is dominated by the hydrodynamic shear and normal forces originating from Poiseuille flow, deformation in geometries with small λ is governed by the interfacial stress only and shear stress can be neglected.

We investigate the dependency of hydrodynamic shear and interfacial stress on λ by performing FEM simulations for different flow rates of 0.53 and 1.02 μl s^{-1} and the corresponding viscosities of 53 and 11 mPa s for spheroid and cell measurements, respectively (Supplementary Fig. 8). While the interfacial stresses (dashed lines) do not depend on λ, we find an increasing peak stress for increasing relative object size. Here, σ_i has been derived from Eq. (3) utilizing typical experimental parameters of w = 14 μm, u_c = 2.8 cm s^{-1}, and u_a = 0.8 cm s^{-1} for single HL60 cells (blue dotted line) and w = 190 μm, u_c = 1.67 cm s^{-1}, and u_a = 0.38 cm s^{-1} for spheroids (black dotted line), respectively. For single cells, we find that $\sigma_s > \sigma_i$ for $\lambda > 0.9$, where σ_s is the hydrodynamic shear stress, while for spheroids we obtain $\sigma_s > \sigma_i$ for $\lambda > 0.5$.

For choosing a relative size ratio where σ_i dominates, we postulate that the interfacial stress has to exceed the hydrodynamic stress by a factor of 10 or higher. Applying the experimental conditions stated above this results into a threshold of $\lambda < 0.4$ for single cells while spheroid deformation is always governed by shear stress.

Viscosity calibration. Viscosity calibration was performed by using beads of fixed elastic modulus $E = 1.5 \pm 0.5$ kPa[42]. Measuring cell deformation inside a virtual channel of w = 16 μm and utilizing the stress–strain relationship $\sigma_i = E\varepsilon_c$ allows to calculate η_{sa} from Eq. (3).

Statistical data analysis. Statistical significance is calculated based on independent experimental replicates using linear mixed models[63]. Here, a pairwise comparison between two groups is utilized to attribute differences in an observable to random and fixed effects, respectively. Random effects represent systematic and stochastic measurement bias, e.g., alterations in virtual channel width, while fixed effects account for the actual effect size, i.e., the increase or decrease in an experimental quantity. Statistical significance is obtained assuming two models, one with and one without the fixed effect and the maximum likelihoods are calculated. Using the likelihood ratio and applying Wilks' theorem, stating that the distribution of the test statistic −2 log (likelihood ratio) approaches a χ^2 distribution with a number of degrees of freedom corresponding to the dimensionality difference of the two models, the corresponding p-values are determined[64].

Sample pairing is performed by utilizing experimental replicates from different measurement days or, if carried out at the same day, linear mixed model analysis is combined with a permutation test of all samples where the p-value with the lowest significance is reported. Multiple comparisons are not corrected for as parameters are not analyzed in parallel.

All experiments have been repeated at least three times independently with a sample size of $n > 100$ for spheroids and $n > 1000$ for cell measurements. The corresponding p-values are reported in Supplementary Table 2.

Reporting summary. Further information on research design is available in the Nature Research Reporting Summary linked to this article.

Data availability

The datasets generated in this study are available from the corresponding author upon reasonable request. The file formats of the raw rata are AVI for videos, TDMS and RTDC (HDF5) for RT-DC data, and MPH for Comsol Multiphysics simulations.

Code availability

Statistical data analysis was performed using the software ShapeOut (version 0.8.7, Zellmechanik Dresden, https://github.com/ZELLMECHANIK-DRESDEN/ShapeOut) and Matlab (version R2017a, Mathworks). The source code for FEM simulations and analysis (Comsol Multiphysics, version 5.4 and Matlab version R2017a, Mathworks) is available from the corresponding author upon reasonable request.

Received: 18 April 2019; Accepted: 25 March 2020;
Published online: 04 May 2020

References

1. Di Carlo, D. A mechanical biomarker of cell state in medicine. *J. Lab. Autom.* **17**, 32–42 (2012).
2. Ayad, N. M. E., Kaushik, S. & Weaver, V. M. Tissue mechanics, an important regulator of development and disease. *Philos. Trans. R. Soc. B Biol. Sci.* **374**, 20180215 (2019).
3. Ganai, N., Buscher, T., Gompper, G. & Elgeti, J. Mechanics of tissue competition: Interfaces stabilize coexistence. *N. J. Phys.* **21**, 063017 (2019).
4. Haase, K. & Pelling, A. E. Investigating cell mechanics with atomic force microscopy. *J. R. Soc. Interface* **12**, 20140970 (2015).
5. Hochmuth, R. M. Micropipette aspiration of living cells. *J. Biomech.* **33**, 15–22 (2000).
6. Guck, J. et al. The optical stretcher: a novel laser tool to micromanipulate cells. *Biophys. J.* **81**, 767–784 (2001).
7. Lincoln, B. et al. Deformability-based flow cytometry. *Cytom. A* **59**, 203–9 (2004).
8. Trepat, X. et al. Universal physical responses to stretch in the living cell. *Nature* **447**, 592–595 (2007).
9. Pelling, A. E. & Horton, M. A. An historical perspective on cell mechanics. *Pflug. Arch.* **456**, 3–12 (2008).
10. Trepat, X. & Sahai, E. Mesoscale physical principles of collective cell organization. *Nat. Phys.* **14**, 671–682 (2018).
11. Janmey, P. A. & McCulloch, C. A. Cell mechanics: integrating cell responses to mechanical stimuli. *Annu. Rev. Biomed. Eng.* **9**, 1–34 (2007).
12. Stone, H. A., Stroock, A. D. & Ajdari, A. Engineering flows in small devices. *Annu. Rev. Fluid Mech.* **36**, 381–411 (2004).
13. Zheng, Y. & Sun, Y. Microfluidic devices for mechanical characterisation of single cells in suspension. *Micro Nano Lett.* **6**, 327 (2011).
14. Weaver, W. M. et al. Advances in high-throughput single-cell microtechnologies. *Curr. Opin. Biotechnol.* **25**, 114–23 (2014).
15. Hochmuth, R., Marple, R. & Sutera, S. Capillary blood flow—1. Erythrocyte deformation in glass capillaries. *Microvasc. Res.* **2**, 409–419 (1970).
16. Sutera, S., Seshadri, V., Croce, P. & Hochmuth, R. Capillary blood flow—2. Deformable model cells in tube flow. *Microvasc. Res.* **2**, 420–433 (1970).
17. Sheshadri, V., Hochmuth, R., Croce, P. & Sutera, S. Capillary blood flow— 3. Deformable model cells compared to erythrocytes in vitro. *Microvasc. Res.* **2**, 434–442 (1970).
18. Xia, Y. & Whitesides, G. M. Soft Lithography. *Annu. Rev. Mater. Sci.* **28**, 153–184 (1998).
19. Qin, D., Xia, Y. & Whitesides, G. M. Soft lithography for micro- and nanoscale patterning. *Nat. Protoc.* **5**, 491–502 (2010).
20. Agresti, J. J. et al. Ultrahigh-throughput screening in drop-based microfluidics for directed evolution. *Proc. Natl Acad. Sci. USA* **107**, 4004–4009 (2010).
21. Dudani, J. S., Go, D. E., Gossett, D. R., Tan, A. P. & Di Carlo, D. Mediating millisecond reaction time around particles and cells. *Anal. Chem.* **86**, 1502–1510 (2014).
22. Pagliara, S. et al. Auxetic nuclei in embryonic stem cells exiting pluripotency. *Nat. Mater.* **13**, 638–644 (2014).
23. Sackmann, E. K., Fulton, A. L. & Beebe, D. J. The present and future role of microfluidics in biomedical research. *Nature* **507**, 181–189 (2014).
24. Gossett, D. R. et al. Hydrodynamic stretching of single cells for large population mechanical phenotyping. *Proc. Natl. Acad. Sci. USA* https://doi.org/10.1073/pnas.1200107109 (2012).
25. Dudani, J. S., Gossett, D. R., Tse, H. T. K. & Di Carlo, D. Pinched-flow hydrodynamic stretching of single-cells. *Lab Chip* **13**, 3728–34 (2013).
26. Otto, O. et al. Real-time deformability cytometry: on-the-fly cell mechanical phenotyping. *Nat. Methods* **12**, 199–202 (2015).
27. Mietke, A. et al. Extracting cell stiffness from real-time deformability cytometry: theory and experiment. *Biophys. J.* **109**, 2023–2036 (2015).
28. Rosendahl, P. et al. Real-time fluorescence and deformability cytometry. *Nat. Methods* **15**, 355 (2018).
29. Koch, M. et al. Plasmodium falciparum erythrocyte-binding antigen 175 triggers a biophysical change in the red blood cell that facilitates invasion. *Proc. Natl Acad. Sci. USA* **114**, 4225–4230 (2017).
30. Guck, J. & Chilvers, E. R. Mechanics meets medicine. *Sci. Transl. Med.* **5**, 212fs41 (2013).
31. Toepfner, N. et al. Detection of human disease conditions by single-cell morpho-rheological phenotyping of blood. *Elife* **7**, e29213 (2018).
32. Eyckmans, J. & Chen, C. S. 3D culture models of tissues under tension. *J. Cell Sci.* **130**, 63–70 (2017).
33. Zuppinger, C. 3D Cardiac cell culture: a critical review of current technologies and applications. *Front. Cardiovasc. Med.* **6**, 1–9 (2019).
34. Jaiswal, D. et al. Stiffness analysis of 3D spheroids using microtweezers. *PLoS One* **12**, e0188346 (2017).
35. Blumlein, A., Williams, N. & McManus, J. J. The mechanical properties of individual cell spheroids. *Sci. Rep.* **7**, 7346 (2017).
36. Adan, A., Alizada, G., Kiraz, Y., Baran, Y. & Nalbant, A. Flow cytometry: basic principles and applications. *Crit. Rev. Biotechnol.* **37**, 163–176 (2016).
37. Li, J., Sheeran, P. S. & Kleinstreuer, C. Analysis of multi-layer immiscible fluid flow in a microchannel. *J. Fluids Eng.* **133**, 111202 (2011).
38. Knight, J. B., Vishwanath, A., Brody, J. P. & Austin, R. H. Hydrodynamic focusing on a silicon chip: Mixing nanoliters in microseconds. *Phys. Rev. Lett.* **80**, 3863–3866 (1998).
39. Wu, Z. & Nguyen, N. T. Hydrodynamic focusing in microchannels under consideration of diffusive dispersion: Theories and experiments. *Sens. Actuators, B Chem.* **107**, 965–974 (2005).
40. Fregin, B. et al. High-throughput single-cell rheology in complex samples by dynamic real-time deformability cytometry. *Nat. Commun.* **10**, 415 (2019).
41. Ullmann, A. & Brauner, N. Closure relations for the shear stress in two-fluid models for core-annular flow. *Multiph. Sci. Technol.* **16**, 355–387 (2004).
42. Girardo, S. et al. Standardized microgel beads as elastic cell mechanical probes. *J. Mater. Chem. B* **6**, 6245–6261 (2018).
43. Mokbel, M. et al. Numerical simulation of real-time deformability cytometry to extract cell mechanical properties. *ACS Biomater. Sci. Eng.* **3**, 2962–2973 (2017).
44. Amini, H., Lee, W. & Di Carlo, D. Inertial microfluidic physics. *Lab Chip* **14**, 2739–61 (2014).
45. Bell, N. A. W. & Keyser, U. F. Digitally encoded DNA nanostructures for multiplexed, single-molecule protein sensing with nanopores. *Nat. Nanotechnol.* **11**, 645–651 (2016).
46. Blasi, T. et al. Label-free cell cycle analysis for high-throughput imaging flow cytometry. *Nat. Commun.* **7**, 10256 (2016).
47. Dittrich, P. S. & Manz, A. Lab-on-a-chip: microfluidics in drug discovery. *Nat. Rev. Drug Discov.* **5**, 210–8 (2006).
48. Vanapalli, S. A., Duits, M. H. G. & Mugele, F. Microfluidics as a functional tool for cell mechanics. *Biomicrofluidics* **3**, 12006 (2009).
49. Teixeira, A. G. et al. Emerging biotechnology applications of aqueous two-phase systems. *Adv. Healthc. Mater.* **7**, 1–19 (2018).
50. Zhao, C. X. & Middelberg, A. P. J. Two-phase microfluidic flows. *Chem. Eng. Sci.* **66**, 1394–1411 (2011).
51. Song, Y., Sauret, A. & Shum, H. C. All-aqueous multiphase microfluidics. *Biomicrofluidics* **7**, 1–12 (2013).
52. Shaqfeh, E. S. G. The dynamics of single-molecule DNA in flow. *J. Non-Newton.* **130**, 1–28 (2005).
53. Langhans, S. A. Three-dimensional in vitro cell culture models in drug discovery and drug repositioning. *Front. Pharm.* **9**, 1–14 (2018).
54. Paniccia, R., Priora, R., Liotta, A. A. & Abbate, R. Platelet function tests: a comparative review. *Vasc. Health Risk Manag* **11**, 133–148 (2015).
55. Hansen, A. et al. Development of a drug screening platform based on engineered heart tissue. *Circ. Res.* **107**, 35–44 (2010).
56. Frey, O., Misun, P. M., Fluri, D. A., Hengstler, J. G. & Hierlemann, A. Reconfigurable microfluidic hanging drop network for multi-tissue interaction and analysis. *Nat. Commun.* **5**, 4250 (2014).
57. Kollmannsberger, P. & Fabry, B. Linear and nonlinear rheology of living cells. *Annu. Rev. Mater. Res.* **41**, 75–97 (2011).
58. Nijenhuis, N., Zhao, X., Carisey, A., Ballestrem, C. & Derby, B. Combining AFM and acoustic probes to reveal changes in the elastic stiffness tensor of living cells. *Biophys. J.* **107**, 1502–1512 (2014).
59. Diz-Muñoz, A., Weiner, O. D. & Fletcher, D. A. In pursuit of the mechanics that shape cell surfaces. *Nat. Phys.* **14**, 648–652 (2018).
60. Tietze, S. et al. Spheroid culture of mesenchymal stromal cells results in morphorheological properties appropriate for improved microcirculation. *Adv. Sci.* https://doi.org/10.1002/advs.201802104 (2019).
61. Golfier, S. et al. High-throughput cell mechanical phenotyping for label-free titration assays of cytoskeletal modifications. *Cytoskeleton* **74**, 283–296 (2017).
62. Stevenson, B. R. & Begg, D. A. Concentration-dependent effects of cytochalasin D on tight junctions and actin filaments in MDCK epithelial cells. *J. Cell Sci.* **107**, 367–375 (1994).
63. Herbig, M., Mietke, A., Müller, P. & Otto, O. Statistics for real-time deformability cytometry: clustering, dimensionality reduction, and significance testing. *Biomicrofluidics* **12**, 042214 (2018).
64. Wilks, S. S. The large-sample distribution of the likelihood ratio for testing composite hypothesis. *Ann. Math. Stat.* **9**, 60–62 (1938).

Acknowledgements

We thank Paula Büttner, Sophie Schilling and Patrick Bohn for experimental support and are grateful for valuable discussions with Mihaela Delcea. We kindly thank Jochen

Guck for the glass cuvette loan. We gratefully acknowledge financial support from the German Federal Ministry of Research and Education (ZIK grant to O.O. under grant agreement 03Z22CN11) and the German Center for Cardiovascular Research (postdoc startup grant 81X3400107 to O.O.). This work has also been funded by the Deutsche Forschungsgemeinschaft (DFG, German Research Foundation) 231396381/GRK1947.

Author contributions

O.O. conceived the project. F.C. developed the experimental setup. F.C. performed finite element method simulations. F.C. and M.H.P. carried out rheological buffer characterization. P.N. analyzed interface stability. F.C., M.H.P., B.F. and D.B. designed and performed experiments on HL60 and HEK293T cells. V.A.D. and R.H.P. developed the spheroid assay. F.C. and M.H.P. carried out cell and spheroid experiments. Y.K. performed compound treatment. F.C., M.H.P., B.F. and O.O. performed statistical data analysis. O.O. supervised the project. F.C. and O.O. wrote the manuscript. All authors reviewed the manuscript.

Competing interests

M.H.P., P.N., V.A.D., D.B., R.H.P., and Y.K. declare no competing interest. O.O. is shareholder of Zellmechanik Dresden GmbH distributing real-time deformability cytometry. F.C., B.F., and O.O. filed a patent application for virtual fluidic channels (Applicant: University Greifswald; inventors: Fabian Czerwinski, Bob Fregin, and Oliver Otto; PCT Application; application number: PCT/EP2018/075605).

Additional information

Supplementary information is available for this paper at https://doi.org/10.1038/s41467-020-15813-9.

Correspondence and requests for materials should be addressed to O.O.

Peer review information *Nature Communications* thanks Dino Di Carlo and the other, anonymous, reviewer(s) for their contribution to the peer review of this work. Peer reviewer reports are available.

Reprints and permission information is available at http://www.nature.com/reprints

Publisher's note Springer Nature remains neutral with regard to jurisdictional claims in published maps and institutional affiliations.

9.9. III. Article: High-throughput single-cell rheology in complex samples by dynamic real-time deformability cytometry

Fregin, B., Czerwinski, F., Biedenweg, D. Girardo, S., Gross, S., Aurich, K. and Otto, O. High-throughput single-cell rheology in complex samples by dynamic real-time deformability cytometry. *Nat. Commun.* 10, 415. doi:10.1038/s41467-019-08370-3 (2019).

Published online: January 24, 2019

Supplementary Information is available at https://static-content.springer.com/esm/art%3A10.1038%2Fs41467-019-08370-3/MediaObjects/41467_2019_8370_MOESM1_ESM.pdf

nature COMMUNICATIONS

ARTICLE

https://doi.org/10.1038/s41467-019-08370-3 OPEN

High-throughput single-cell rheology in complex samples by dynamic real-time deformability cytometry

Bob Fregin [1], Fabian Czerwinski [1], Doreen Biedenweg[2], Salvatore Girardo [3], Stefan Gross [2,4], Konstanze Aurich [2] & Oliver Otto [1,4]

In life sciences, the material properties of suspended cells have attained significance close to that of fluorescent markers but with the advantage of label-free and unbiased sample characterization. Until recently, cell rheological measurements were either limited by acquisition throughput, excessive post processing, or low-throughput real-time analysis. Real-time deformability cytometry expanded the application of mechanical cell assays to fast on-the-fly phenotyping of large sample sizes, but has been restricted to single material parameters as the Young's modulus. Here, we introduce dynamic real-time deformability cytometry for comprehensive cell rheological measurements at up to 100 cells per second. Utilizing Fourier decomposition, our microfluidic method is able to disentangle cell response to complex hydrodynamic stress distributions and to determine viscoelastic parameters independent of cell shape. We demonstrate the application of our technology for peripheral blood cells in whole blood samples including the discrimination of B- and CD4+ T-lymphocytes by cell rheological properties.

[1] Zentrum für Innovationskompetenz: Humorale Immunreaktionen bei kardiovaskulären Erkrankungen, Universität Greifswald, Fleischmannstr. 42, 17489 Greifswald, Germany. [2] Universitätsmedizin Greifswald, Fleischmannstr. 8, 17489 Greifswald, Germany. [3] Biotechnology Center, Center for Molecular and Cellular Bioengineering, Technische Universität Dresden, Tatzberg 47/49, 01307 Dresden, Germany. [4] Deutsches Zentrum für Herz-Kreislauf-Forschung e. V., Standort Greifswald, Universitätsmedizin Greifswald, Fleischmannstr. 42, 17489 Greifswald, Germany. Correspondence and requests for materials should be addressed to O.O. (email: oliver.otto@uni-greifswald.de)

With the potential for label-free phenotyping of cellular states and functions, the mechanical properties of cells have gained an increasing importance over the last years[1–3]. Being sensitive to cytoskeletal and nuclear alterations, this biomarker has been used to track the stability, passaging, and differentiation of stem cells, to follow the activation of immune cells, and to characterize metabolic states[4–8]. As mechanical phenotyping is based on intrinsic cell material properties, it serves as a complementary approach to traditional molecular biology methods and is of an increasing importance in fundamental and applied research, where molecular markers are not wanted or not available. However, a broad translation of mechanical phenotyping into life science applications had so far been hampered by lack of a fast and robust measurement technique. While traditional methods like atomic force microscopy, micropipette aspiration, and optical stretching were limited to analysis rates of less than 100 cells per hour[9–11], the introduction of microfluidic concepts increased the throughput by several orders of magnitude[12,13]. The serial deformation of cells in a hydrodynamic environment allows for throughput rates on the order of 100–10,000 cells per second, which is a prerequisite for screening applications, e.g., the combination of biophysical and molecular analysis or the characterization of highly potent skeletal stem cells in regenerative medicine[14,15].

In contrast to well established cell biology techniques, like flow cytometry, the parameter space of mechanical cell characterization cannot simply be extended by additional molecular markers, but is limited to any information that can be extracted from acoustical, mechanical, or optical measurements[16–18]. However, cells are far away from a thermal equilibrium. Their response to an external mechanical load in the form of creep or stress relaxation is highly nonlinear and driven by both, an active and a passive intrinsic remodeling, which has to be explored to link cytoskeletal properties to cell function[19–21]. While rheological experiments and the determination of a frequency-dependent complex modulus have initially been performed on adherent cells[2,22], microfluidic systems in combination with high-speed video microscopy enabled an increase in throughput and an extension to suspended cells[23,24].

Using a parallel array of micron-sized constrictions, Lange et al. utilize the confinement of suspended cells in a microfluidic channel to estimate cell elasticity and fluidity from flow speed, residence time, and driving pressure. Power-law rheology explains the collapsing of data from multiple cell lines and under multiple conditions onto a master curve and is in agreement with the theory of soft glassy materials[25,26]. Quantitative deformability cytometry extends this concept by introducing calibrated microspheres to extract quantitative information and allows for potential comparison to reference methods like micropipette aspiration[27].

In contrast to micro-constrictions, methods like deformability cytometry (DC), real-time deformability cytometry (RT-DC) and real-time fluorescence and deformability cytometry (RT-FDC) are contactless and utilize solely hydrodynamic stress to deform cells[24,28,29]. In addition, RT-DC and RT-FDC are capable to perform image acquisition and analysis on-the-fly, which allows for a label-free screening of heterogeneous cell samples of virtually unlimited size and the identification of sub-populations based on mechanical properties. However, in real-time data analysis, image acquisition and data evaluation have been limited to a single snapshot per cell and, thus only steady-state material parameters as the Young's modulus can be derived[30,31].

Here, we introduce dynamic RT-DC (dRT-DC) for single cell rheological measurements in heterogeneous samples where we capture the full dynamics of suspended cells passing the central constriction of a microfluidic channel on-the-fly. We show that Fourier analysis of cellular shape modes allows to disentangle the complex cell response to time-dependent and time-independent hydrodynamic stress distributions, which are typical for almost any microfluidic system. The symmetry of the Fourier modes can be used to extract the stress-strain relationship and to determine viscoelastic cell parameters directly by applying simplest model assumptions. We show that our approach is independent of cellular shape. Using a cell line as well as primary blood cells, we demonstrate that dynamic RT-DC is capable to determine an apparent Young's modulus as well as an apparent viscosity with throughput rates of up to 100 cells per second. Interestingly, this technology allows for a rheological comparison amongst cells in a single measurement of whole blood. In addition, we show a label-free statistical discrimination of major cell types including B- and CD4+ T-lymphocytes based on material properties. The latter has previously only been possible using multi-dimensional machine learning techniques[32,33].

Results

High-throughput single cell rheology. The high-throughput single cell rheology setup is based on the platform of real-time deformability cytometry (RT-DC), which has been published earlier[28]. The main experimental design consists of a microfluidic chip where suspended cells are driven through a central channel and deform due to shear and normal stresses only (Fig. 1a). By using on-the-fly image acquisition and simultaneous analysis of projected surface area A and cell perimeter P, RT-DC is capable to calculate a deformation parameter d based on the circularity c of a cell inside a microfluidic channel:

$$d = 1 - c = 1 - \frac{2\sqrt{\pi A}}{P}. \quad (1)$$

An analytical model which has recently been extended numerically allows for extracting an Young's modulus E as a material parameter[30,31]. However, RT-DC is limited to a static region-of-interest (ROI) at the rear part of the microfluidic channel, relies on the assumption of steady-state deformations as well as an initially spherical cell shape, and cannot track the dynamics of shape changes. This would be a prerequisite to derive elastic and viscous material properties of single cells.

Here, we introduce dynamic RT-DC (dRT-DC), a real-time and high-throughput method, to perform single cell rheology of suspended cells on a millisecond timescale. The full field of view of the camera is adjusted to a ROI that covers the entire length of a microfluidic channel, while a moving sub-ROI is used to track the trajectory of cells inside the constriction (Fig. 1a). In its current implementation and by using standard computer hard- and software, dRT-DC is capable to follow more than 100 cells per second in real time. Each single cell trace can consist of more than 100 data points (Fig. 1b and Supplementary Figure 1).

For a cell approaching the channel, we observe an increase in deformation reaching a maximum directly at the inlet (Fig. 1c, top). Interestingly, two distinct dynamic processes are apparent inside the constriction. First, cell deformation approaches a minimum before, second, it increases again and the cell shape adapts a bullet-like steady state given by the Poiseuille flow profile[30]. Both processes can be approximated by an exponential fit function (yellow and green line in Fig. 1c, top) and qualitatively understood considering the hydrodynamic stress distribution inside our microfluidic system. The velocity gradient in flow direction at the inlet and outlet (Supplementary Figure 2a and b) leads to a peak stress σ_{inlet} while a smaller stress amplitude $\sigma_{\mathrm{channel}}$ is found inside the channel (Fig. 1c, bottom and Supplementary

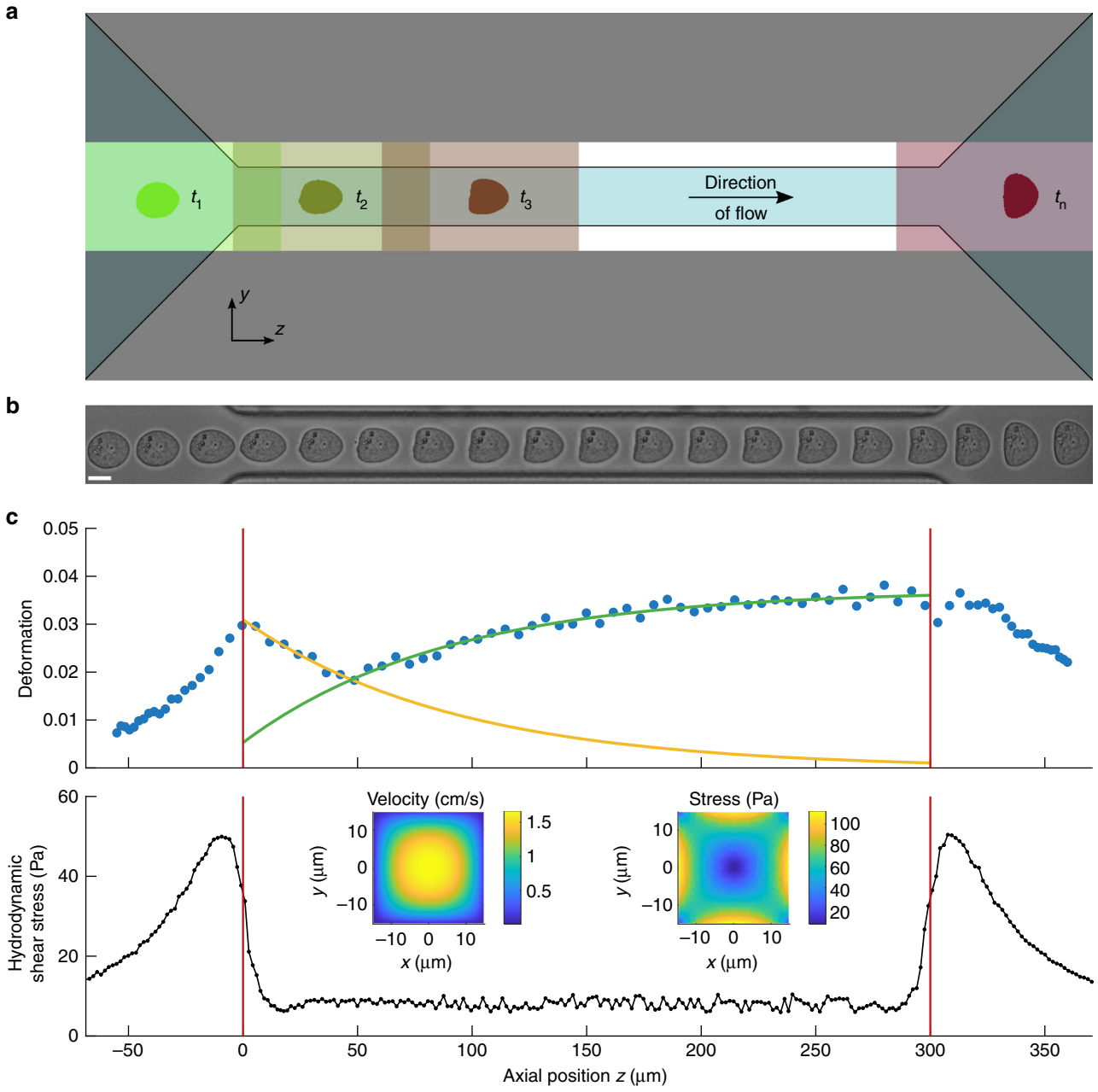

Fig. 1 Dynamic RT-DC. **a** Sketch of experimental setup showing microfluidic channel with translocating cell and corresponding region-of-interests at selected time points t_1, t_2, t_3, and t_n. **b** Time series of a suspended cell while translocating a 30 µm × 30 µm channel of 300 µm length. Length of the scale bar is 10 µm. **c** Deformation (1-circularity) trace of 92 single cell measurements along axial position z in the channel (blue dots). The yellow and green line originate from an exponential fit characterizing two apparent cell relaxation modes (top). The red vertical lines indicate channel inlet and outlet position. Finite element method (FEM) calculations of hydrodynamic shear stress profile along the same microfluidic channel axis at a flow rate of 8 nl s^{-1} in the absence of cells (bottom). Insets show velocity and stress distribution of the channel cross-section

Figure 2c). Apparently, the response of the cell is governed by both, a slow increase in hydrodynamic stress outside the channel towards a maximum at the inlet and a sudden but smaller step stress inside the constriction.

Shape modes disentangle hydrodynamic stress and cell strain. Next, we would like to answer the question how the two dynamic processes of decreasing and increasing cell deformation inside the channel can be disentangled and understood quantitatively. This is of fundamental importance to extract material properties from RT-DC data since simple rheological models, e.g., a Kelvin-Voigt model, require measurements of cell deformation as a response to a well-defined stress or vice-versa[20,34]. Using Fourier analysis, we determined the principal modes of each cell shape from its contour (Fig. 2a and Supplementary Figure 3a) and calculated the first ten Fourier coefficients at each position along the trajectory of the cell inside our microfluidic system (Fig. 2b and Supplementary Figure 3b).

Shape mode analysis was performed for more than 1000 HL60 cells and the results were normalized to the first Fourier coefficient a_0 representing the cell radius. Observing the mean (yellow line in Fig. 2b) over channel position reveals a maximum at the inlet (left red line in Fig. 2b and

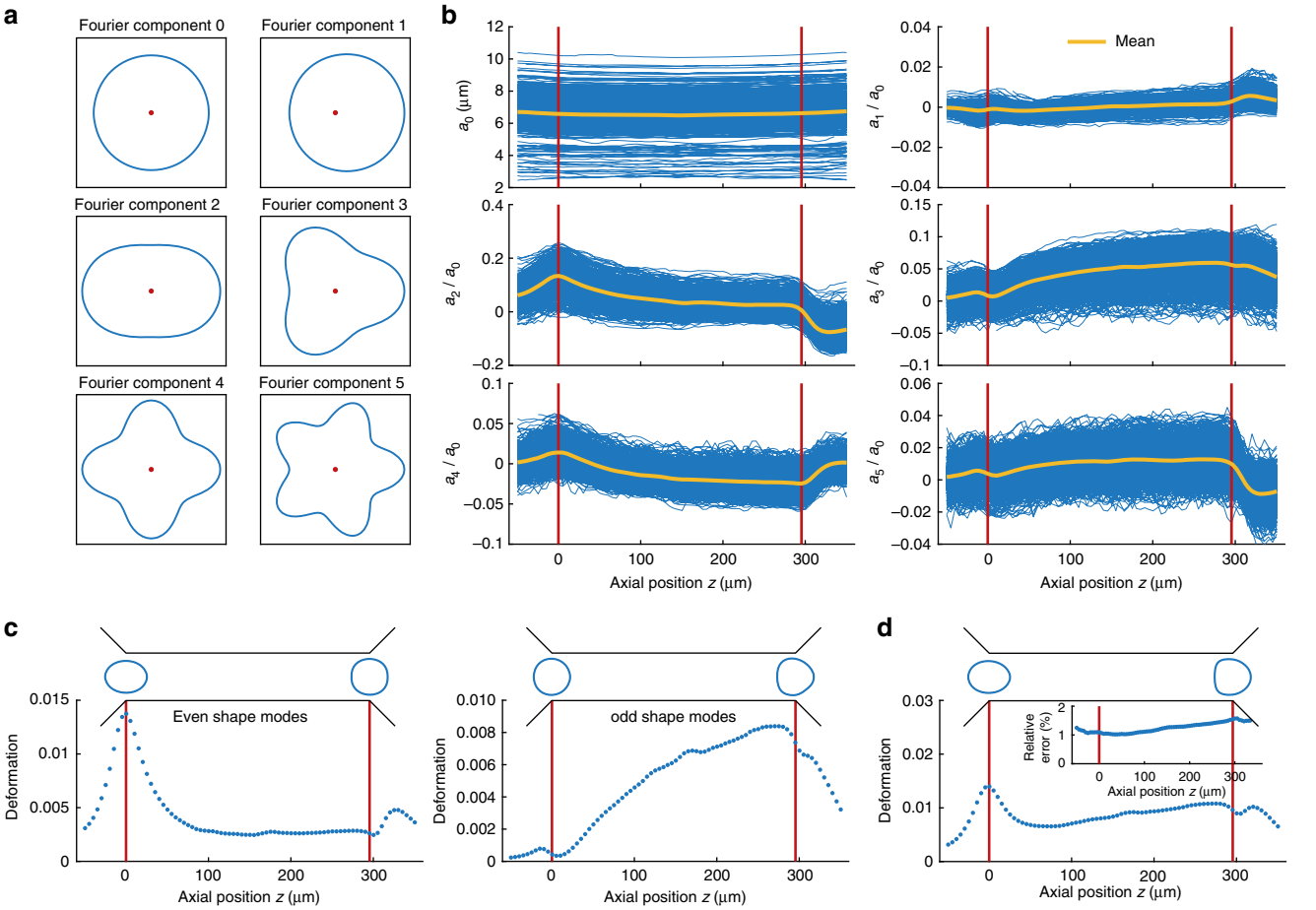

Fig. 2 Fourier decomposition of cell shape. **a** First six components of radial Fourier function (shape modes) including component zero, red dots indicate the origin. **b** Shape mode analysis applied to dynamic measurements of HL60 cells arranged for even and odd coefficients. Each blue trace represents the amplitude of a Fourier component of a single cell over the axial position z in the channel ($n = 1580$ cells). The yellow lines indicate the mean over all traces whereas the red vertical lines visualize the inlet and outlet position. **c** Reconstruction of cell deformation from first four even (left panel) and first five odd (right panel) Fourier coefficients and a_0 with mean cell shapes at channel inlet and outlet (top). **d** Reconstruction of cell deformation from first ten Fourier coefficients, including mean cell shapes (top). Inset shows the relative error in circularity of the reconstructed traces relative to the original dataset. Measurements have been carried out in a 30 × 30 µm channel at a flow rate of 8 nl s^{-1}

Supplementary Figure 3b) for all even Fourier coefficients followed by a relaxation into a steady state while odd coefficients increase from zero amplitude to a maximum at the end of the channel (right red line in Fig. 2b and Supplementary Figure 3b). These dynamics can be understood when transforming both, the even (a_2, a_4, a_6 and a_8) including (a_0), and the odd coefficients (a_1, a_3, a_5, a_7 and a_9) including (a_0) respectively, back into the deformation measure introduced in Equation 1. Of note, Fourier coefficients b_k represent the angular orientation of a cell inside the channel revealing a mean value close to zero and are of importance for single cells which are slightly displaced from the channel center (Supplementary Figure 3c).

For the even Fourier coefficients we find a peak in the reconstructed deformation trace d_{even} at the channel inlet followed by a relaxation into a steady state close to zero deformation (left panel in Fig. 2c). This behavior originates from the fluid velocity gradient in flow direction (Supplementary Figure 2b) yielding a maximum in hydrodynamic stress at the inlet (Fig. 1c and Supplementary Figure 2c). The corresponding contour of an elongated cell possesses the same symmetry of shape changes along the channel axis as the even shape modes (a_0), a_2 … a_8 (Fig. 2a and left panel in Fig. 2c). In contrast, a deformation trace reconstructed from only the first five odd Fourier coefficients displays a continuous increase from $d_{\mathrm{odd}} \approx 0$ at the inlet to $d_{\mathrm{odd}} = \max.$ at the outlet. The characteristic bullet contour reveals the same symmetry of shape changes as the odd shape modes (a_0), a_1 … a_9 (Fig. 2a and right panel in Fig. 2c). Reconstruction of the complete trace from the first ten Fourier components (Fig. 2d) resembles the original data while the relative error in deformation magnitude is around 1% or slightly above (Fig. 2d, inset).

In summary, shape mode analysis allows to disentangle the cell response to the inlet peak stress σ_{inlet} from the channel stress $\sigma_{\mathrm{channel}}$ (Fig. 1c). This implies that d_{even} can be seen as the deformation trace d_{inlet} representing shape dynamics caused by σ_{inlet} while d_{odd} can be understood as the deformation trace d_{channel} due to the constant stress $\sigma_{\mathrm{channel}}$ (Fig. 2c). The latter can be approximated by a step-function and is given by the hydrodynamic stress around the cell inside the constriction (Supplementary Figure 4). Applying an analytical model published earlier d_{channel} enables to establish a stress-strain relationship[30]. Therewith, rheological parameters can directly be determined from the channel data representing a creep-compliance experiment[35].

Single-cell rheology on cell line and primary cells. For performing rheology on single cells we extract four parameters from

dRT-DC data after Fourier decomposition and reconstructing the deformation versus time trace from even and odd Fourier coefficients separately. The cell response to the peak stress at the channel inlet d_{inlet} is reconstructed from the first four even shape modes and a_0 representing the cell radius. For this inlet deformation trace, the local maximum defines the peak deformation $\hat{d}_{inlet}$ while the relaxation into a steady state is quantified by the corresponding time constant τ_{inlet} (Fig. 3a, top). The response of the cell $d_{channel}$ to the constant stress $\sigma_{channel}$ inside the constriction is reconstructed from a_0 and the first five odd shape modes. Reaching a maximum at the channel outlet, $d_{channel}$ is described by the steady-state deformation $\hat{d}_{channel}$ relative to the inlet and the characteristic time constant $\tau_{channel}$ (Fig. 3a, bottom). Both timescales, τ_{inlet} and $\tau_{channel}$, originate from an exponential fit to our reconstructed data traces (yellow lines in Fig. 3a) assuming a linear cell response (Methods).

In a first set of experiments HL60 cells have been used as a model system and we studied the sensitivity of dRT-DC towards cytoskeletal alterations. Treatment with 1 µM cytochalasin D (CytoD), which depolymerizes filamentous actin, leads to an increase in τ_{inlet} and $\tau_{channel}$ (Fig. 3b) as well as in both deformation measures $\hat{d}_{inlet}$ and $\hat{d}_{channel}$ (Fig. 3c) relative to the wildtype and the corresponding DMSO control (0.25% (v/v)). Between the latter two no differences are observed.

A statistical analysis over three biological replicates each consisting of ~1000 single cell rheological experiments or more was carried out using linear mixed models (see Methods) and confirms the observed trend. Both, τ_{inlet} and $\tau_{channel}$, are significantly increased relative to the DMSO control as well as to the wildtype (Fig. 3d). Also, the deformation measures $\hat{d}_{inlet}$ and $\hat{d}_{channel}$ rise significantly when exposing HL60 cells to 1 µM CytoD (Fig. 3e). A direct comparison between the DMSO sample and the wild-type reveals no effect on τ_{inlet} and $\tau_{channel}$ as well as on $\hat{d}_{inlet}$ and $\hat{d}_{channel}$ (Fig. 3d, e).

Next, we use the channel deformation trace to extract rheological parameters from our data. For traces of $d_{channel}$ revealing a steady state (Fig. 3a, bottom), an analytical model can be used to obtain an apparent Young's modulus E[30,31] and an apparent viscosity η assuming linear viscoelasticity (see Methods)[20]. Briefly, finite element method (FEM) simulations are carried out to obtain the hydrodynamic surface stress distribution of a cell moving in a microfluidic channel (Supplementary Figure 4). For a cell moving within a 30 × 30 µm channel at a flow rate of 8 nl/s a mean surface shear stress of 142 Pa (dashed line in Fig. 3a, bottom) is determined. Using this stress distribution the cell deformation can be predicted and mapped to an apparent Young's modulus[30].

Applying our analytical model to biological replicates, HL60 cells exposed to 1 µM CytoD are found with $E = 0.28 \pm 0.03$ kPa, which is significantly reduced compared to the wildtype and DMSO control with an apparent Young's modulus of $E = 0.40 \pm 0.02$ kPa and $E = 0.43 \pm 0.01$ kPa, respectively (Fig. 3f).

The constant stress inside the constriction is not only a requirement of our analytical model to determine E, but also enables the interpretation of $\tau_{channel}$ as a cell response to a simple step stress. Under the assumption of a linear response following a Kelvin-Voigt model, the characteristic time $\tau_{channel} = \eta/E$ allows to calculate an apparent cell viscosity[20]. Here, we find a slight increase from $\eta = 3.43 \pm 0.16$ Pa s for the wildtype to $\eta = 3.67 \pm 0.05$ Pa s for the DMSO control, which reveals a significant reduction to $\eta = 2.76 \pm 0.2$ Pa s after CytoD treatment (Fig. 3g).

A re-evaluation of our HL60 wild-type data with respect to power-law rheology and a subsequent comparison to a Kelvin-Voigt model shows a smaller root-mean-square error for fitting an exponential function (Supplementary Figure 5a). This result might be linked to the fact that our time traces extend only over two orders of magnitude in time[35]. Interestingly, the absolute value in apparent Young's modulus for both models differs by less than 20% — a result which supports our experimental and analysis framework (Supplementary Figure 5b).

Next, we perform single cell rheology experiments on primary cells and assess the potential of dRT-DC for characterization of blood cells from different lineages, including sub-populations. Comparing typical individual traces of erythrocytes, granulocytes, and peripheral blood mononuclear cells (PBMCs) in whole blood, we find qualitative differences in deformation as well as translocation dynamics. While red blood cell rheology is dominated by the peak stress at the inlet of the microfluidic channel, leukocyte dynamics reveal a longer relaxation time in the channel and are thus largely affected by the steady-state parabolic flow profile (Fig. 4a).

Interestingly, dRT-DC allows for the extraction of rheological cell properties independent of cell shape. As simple analytical models require spherical cells for deriving material properties from RT-DC measurements[30,31], non-spherical cells, e.g., erythrocytes and activated cells, could not be characterized. Dynamic RT-DC overcomes this limitation by applying the symmetry of the Fourier components and by reconstructing the deformation trace from only odd shape modes. Here, the initial deformation value by means of circularity is always equal to zero corresponding to a spherical contour before cell response to the hydrodynamic stress (Fig. 4b).

For biological replicates of erythrocytes and purified granulocytes, PBMCs, and lymphocytes from three different donors, we determine the characteristic deformations as well as relaxation times (Supplementary Figure 6) and extract the apparent Young's modulus and the apparent viscosity as described above. Of note, purification of leukocytes (see Methods) has been carried out to obtain a sufficient sample number and to reduce the impact of changing material properties over time, but rheological characterization could be equally well performed on a single cell level in whole blood.

For erythrocytes, we find an apparent Young's modulus of $E = 0.10 \pm 0.01$ kPa while granulocytes ($E = 0.43 \pm 0.05$ kPa) and PBMCs ($E = 0.62 \pm 0.04$ kPa) are significantly stiffer (Fig. 4c). Estimation of the apparent viscosity from the characteristic times $\tau_{channel}$ also yields statistically significant differences between $\eta = 0.24 \pm 0.18$ Pa s for erythrocytes, $\eta = 5.22 \pm 0.34$ Pa s for granulocytes and $\eta = 8.70 \pm 0.45$ Pa s for PBMCs (Fig. 4d).

Dynamic RT-DC also allows for a discrimination of B- and CD4+ T-lymphocytes based on material properties. Interestingly, only minor differences are observed in the channel deformation measure $\hat{d}_{channel}$ (Fig. 4c, inset) and its derived parameters, the apparent Young's modulus (Supplementary Figure 6b top, inset) as well as the apparent viscosity (Supplementary Figure 6b bottom, inset). In contrast, an analysis of the inlet deformation trace reveals a significant increase in $\hat{d}_{inlet}$ for CD4+ T-cells (Fig. 4d, inset). In fact, lymphocytes are the only blood cells included in this study where sub-populations can better be identified based on the inlet dynamics.

Finally, we use a logistic model to assess the capability of dRT-DC to discriminate leukocytes on a single cell level. Following a multivariate approach incorporating cell size A, apparent Young's modulus E, and apparent viscosity η the Akaike information criterion (AIC) is used for model selection (see Methods). Comparing granulocytes and peripheral blood mononucleated cells we find a two-parametric model of A and η having the lowest AIC, which identifies PBMCs with a sensitivity exceeding 80% and an area under the curve AUC = 0.88 (Supplementary Figure 7a and Supplementary Table 1). For classification of CD4+ T cells we have been analyzing logistic models of cell size

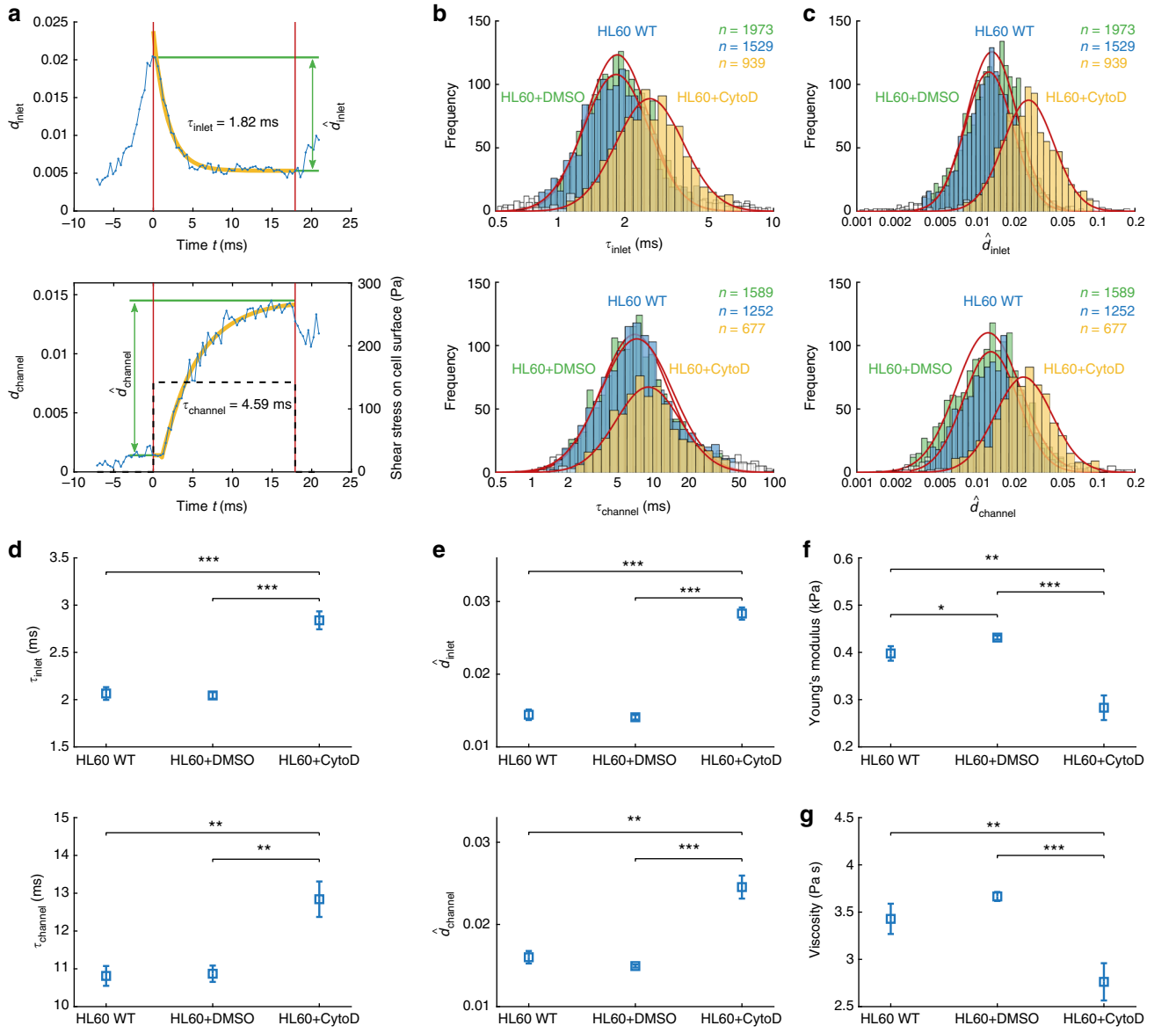

Fig. 3 Single-cell rheology on HL60 cells. **a** Reconstructed deformation trace d_{inlet} (top) and $d_{channel}$ (bottom) from first four even (top) and first five odd (bottom) cell shape modes including a_0, respectively (blue). Graphs show relaxation times τ_{inlet} and $\tau_{channel}$ (yellow) as well as peak deformations $\hat{d}_{inlet}$ and $\hat{d}_{channel}$ (green). Dashed line (bottom) represents mean shear stress on cell surface. The red vertical lines indicate channel inlet and outlet position. **b** Histograms of characteristic times τ_{inlet} and $\tau_{channel}$ are binned logarithmically and show wild-type cells (blue), cells after treatment with 1 µM CytoD (yellow) and the corresponding DMSO control (0.25% (v/v), green). **c** Histograms of peak deformation $\hat{d}_{inlet}$ and $\hat{d}_{channel}$ are binned logarithmically and show wild-type cells (blue), cells after treatment with 1 µM CytoD (yellow) and the corresponding DMSO control (green). In **b** and **c** data in a confidence interval of 3σ have been taken into account for the log-normal fit (red line), others are considered as outliers (white bins). **d**–**g** Statistical analysis for three biological replicates comparing wild-type cells ($n = 3382$), cells after treatment with 1 µM CytoD ($n = 2643$) and corresponding DMSO control ($n = 3965$) for characteristic timescales τ_{inlet} and $\tau_{channel}$ **d**, for peak deformation $\hat{d}_{inlet}$ and $\hat{d}_{channel}$ **e**, for Young's modulus E **f** and viscosity η **g**. Measurements have been carried out in a 30 × 30 µm channel at a flow rate of 8 nl s^{-1}. The mean shear rate of 5100 s^{-1} and the mean shear stress of 142 Pa on the cell surface has been derived from finite element method simulations considering the full microfluidic geometry. Statistical significance has been calculated from linear mixed models and error bars represent standard error of the mean (*$p < 0.05$; **$p < 0.01$; ***$p < 0.001$)

A, the peak deformation $\hat{d}_{inlet}$ and the inlet relaxation time τ_{inlet}. Here, a two-parametric model of $\hat{d}_{inlet}$ and τ_{inlet} reveals the lowest AIC with a sensitivity of 76% and an AUC = 0.62 (Supplementary Figure 7b and Supplementary Table 2).

Discussion

Rheological cell properties provide essential insights into biological functions regarding health and disease. Being label free, this biomarker allows for an unbiased phenotyping of cells as well as cellular sub-populations and is complementary to established assays in molecular biology. The latter always require an apriori knowledge about the molecular target of interest.

Within the existing technologies for rheological cell phenotyping, dynamic RT-DC fulfills the unmet requirement for high-throughput real-time analysis of heterogeneous samples with accompanying derivation of material properties from simplest model assumptions while being independent of cell shape.

The decomposition of cell shape into Fourier modes reveals two dynamic processes for a suspended cell passing a microfluidic

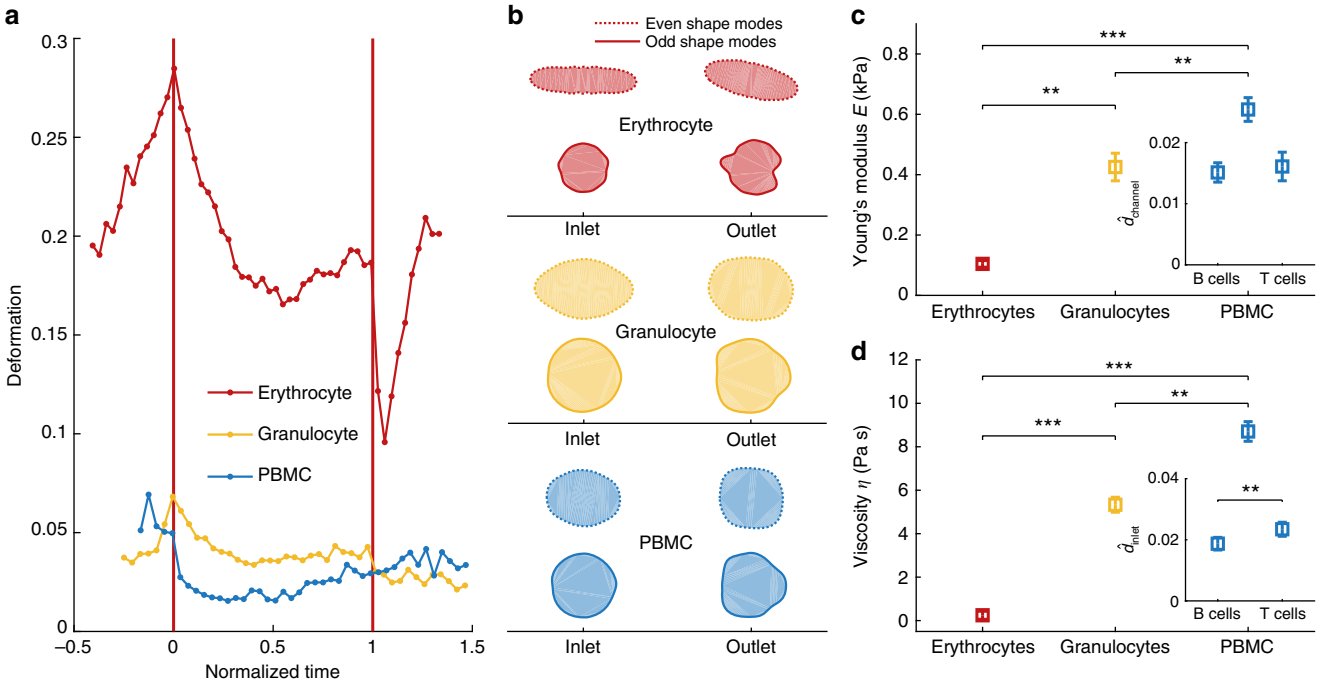

Fig. 4 Single cell rheology on peripheral blood cells. **a** Dynamic RT-DC traces of individual cells in whole-blood showing erythrocytes (red), granulocytes (yellow) and peripheral blood mononuclear cells (PBMC, blue). Translocation time has been normalized to account for different velocities. **b** Cell shapes of typical blood cells reconstructed from even (dashed line) and odd (solid line) shape modes showing erythrocytes (red), granulocytes (yellow) and PBMCs (blue). **c** Apparent Young's modulus E and **d** apparent viscosity η of purified cell samples. Insets show a comparison of the peak channel deformation $\hat{d}_{\mathrm{channel}}$ **c** and the peak deformation $\hat{d}_{\mathrm{inlet}}$ **d** for B cells and CD4+ T cells at the inlet. Statistical analysis in **c** and **d** includes data of three biological replicates from $n = 381$ erythrocytes, $n = 243$ granulocytes, $n = 130$ PBMCs, $n = 737$ B cells and $n = 3079$ CD4+ T cells. Experiments have been carried out in a 20 × 20 µm channel at a flow rate of 4 nl s^{-1}. The mean shear rate of 9700 s^{-1} and a mean stress of 216 Pa on the cell surface (granulocytes and PBMCs) as well as the mean shear rate of 8600 s^{-1} and a mean stress of 128 Pa on cell surface (erythrocytes) has been derived from finite element method simulations considering the full microfluidic geometry. Statistical significance has been calculated from linear mixed models and error bars represent standard error of the mean (**$p < 0.01$; ***$p < 0.001$)

channel. Even Fourier modes reflect a symmetry parallel as well as perpendicular to the channel axis and cell shapes reconstructed only from these components describe the cell response to the time-dependent flow profile of the inlet region. In contrast, odd Fourier modes are sensitive to shape changes perpendicular to the channel axis, only. Reconstruction of cell shape from these components reveals a dynamic process of zero deformation at the channel inlet and maximum deformation at the channel outlet as a response to the constant shear flow inside the constriction. Since this separation between even and odd Fourier modes is entirely based on symmetry arguments, dynamic RT-DC extends its parameter space to two deformation measures and two characteristic times within one experimental assay.

For a given cell type, these parameter pairs reveal similar experimental magnitudes supporting the model assumption of a linear homogeneous material. As a consequence, the deformation reconstructed from the odd shape modes can be considered as the strain response to a constant stress inside the channel. The characteristic time to reach the steady state can be analyzed using a simple Kelvin-Voigt model. It yields, together with an analytical model published earlier[30], an apparent Young's modulus and an apparent viscosity. Remarkably, the application of Fourier decomposition allows for rheological cell characterization fully independent of cell shape, because traces reconstructed from odd Fourier modes always start with zero deformation, which is a requirement of simple mechanical models[31].

We applied our experimental framework to HL60 cells as a model system and determined an apparent Young's modulus of ~0.4 kPa, which is in agreement with previously published results[27], but lower than earlier RT-DC data[30]. This deviation potentially originates from strain-stiffening effects[2] and the feature of dRT-DC that specifically takes into account the initial cell shape and does not rely on ensemble averages to correct for non-spherical objects.

Depolymerization of filamentous actin by CytoD leads to a reduction in the apparent Young's modulus as reported earlier for HL60 and 3T3 cells[27,36]. Although these previous studies successfully captured changes in elasticity by applying power-law rheology no significant differences in the fluidity were observed. Here, using dRT-DC and applying a linear viscoelastic model also allows to link actin depolymerization to a reduction in the apparent viscosity. Interestingly, the apparent viscosity of ~4 Pa s is almost two orders of magnitude lower than previously published, which might be due to shear-thinning effects in the cytoskeleton[37]. In fact, experimental and theoretical studies on the cytoplasmic viscosity of leukocytes revealed a shear-rate dependency following a power-law[38].

Finally, we have performed dRT-DC on peripheral blood and determined viscoelastic properties for erythrocytes, granulocytes, and peripheral blood mononuclear cells within a single measurement. This has not been possible before as state-of-the-art approaches always required purification of the cell type of interest[39,40]. However, sample preparation and cell isolation potentially alter cellular state and function, e.g. by using fluorescent labels. The capability of dRT-DC to identify and characterize cells in heterogeneous samples independent of their shape might be highly relevant to understand immune response during chronic diseases. Here, it has been shown that infections

with mycobacteria, Plasmodium, and hepatitis are known to increase susceptibility to other pathogens, but the underlying processes are largely unknown[41]. A direct and unbiased cell analysis based on single cell rheology within a complex sample as whole blood would therefore provide a complementary approach to study these coinfections.

Previous experiments using RT-DC have already demonstrated a correlation between malaria parasite infection and reduction of host cell membrane bending modulus[8,42]. An extension of this analysis from a specific cell type towards a mechanoprofile of interacting immune cells in whole blood might shed new light on these bystander effects during coinfections and help to elucidate novel infections mechanisms.

In this context, we provide evidence that dRT-DC is capable to discriminate between isolated leukocytes of different lineages including B- and CD4+ T-lymphocytes with statistical significance and a sensitivity of 76%. Therefore, dRT-DC is to the best of our knowledge the only technology that can distinguish between those cells without any external labeling or machine-learning framework. This is of essential importance for cell enrichment based on intrinsic material properties which require real-time operation at high throughput. Moving towards this need, dynamic RT-DC integrates the identification of material properties from simplest model assumptions into on-the-fly high-throughput mechanical phenotyping and bridges the gap between molecular and rheological analysis of cells.

Methods

Experimental setup. The dynamic RT-DC setup is based on the real-time deformability cytometry system[28]. Briefly, a microfluidic chip is assembled on the Accellerator (Zellmechanik Dresden) which consists of an inverted microscope with CMOS camera, a dedicated syringe pump, a microsecond pulsed LED illumination, and a dedicated acquisition software. The microfluidic chip is made out of poly-dimethylsiloxane (PDMS) and glass, has two inlets (one for the sample solution and one for sheath) and one outlet. Inlets and outlet are connected by a central constriction of 300 µm length and a cross-section of 20 µm × 20 µm or 30 µm × 30 µm, respectively.

To enable a continuous high-throughput tracing of dynamic cell changes, the RT-DC acquisition software has been adapted and a new analysis software has been developed. The field of view (1280 × 80 pixels) covers the full length and width of our channel including the inlet and outlet area (Fig. 1a, b) where our camera (MC1362, Mikrotron) takes images at frame rates between 2000 and 6000 frames per second (fps). Detection of a cell is based on image binarization and a border following algorithm as published earlier. Once a cell appears in the inlet region, our algorithm crops a region-of-interest (ROI) of 250 × 80 pixels around the cell, which moves along the channel until the outlet is reached (rectangles in Fig. 1a). Decision of ROI motion is based on the cell center-of-mass. For positions exceeding 70% of ROI length, the ROI moves by 48% ensuring that slow and fast cells can be tracked during their passage through the microfluidic channel. The small size of the ROI ensures that cell tracking is stable and not interfering with other cells in the channel.

In each iteration our algorithm calculates the position of the cell within the ROI and the channel, deformation and cell size. The current optical resolution of our system of 0.34 µm per pixel allows for the analyses of 100 cells per second where each trace consists of at least 14 data points. Cell velocities of up to 24 cm s^{-1} are achievable. The use of a high-viscous cell carrier that enables considerable cell deformation already at low flow rates effectively increases the number of data points per trace (Supplementary Figure 1).

Shape mode analysis. Shape mode analysis is based on a custom Matlab R2017a script (Mathworks) where the convex hull contour is extracted from a single cell image. The contour is described by a closed polygon ($x_{\mathrm{cont},n}$, $y_{\mathrm{cont},n}$) with $n = 0, 1, \ldots, N-1$ where N represents the number of contour points and ($x_{\mathrm{cont},N}$, $y_{\mathrm{cont},N}$) = ($x_{\mathrm{cont},0}$, $y_{\mathrm{cont},0}$).

In the first step of our algorithm the contour is piecewise linearly interpolated by 49 points between each pair of contour points resulting in the interpolated tuple of vectors (x_n, y_n). Next, each contour is transformed into polar coordinates (r_n,φ_n) with respect to its center-of-mass (x_{com}, y_{com}):

$$r_n = \sqrt{(x_n - x_{\mathrm{com}})^2 + (y_n - y_{\mathrm{com}})^2}, \varphi_n = \arctan2(y_n - y_{\mathrm{com}}, x_n - x_{\mathrm{com}}), \quad (2)$$

with

$$x_{\mathrm{com}} = \frac{1}{6A}\sum_{n=0}^{N-1}(x_n + x_{n+1})(x_n y_{n+1} - x_{n+1}y_n),$$
$$y_{\mathrm{com}} = \frac{1}{6A}\sum_{n=0}^{N-1}(y_n + y_{n+1})(x_n y_{n+1} - x_{n+1}y_n),$$
$$A = \frac{1}{2}\sum_{n=0}^{N-1}(x_n y_{n+1} - x_{n+1}y_n).$$

The interpretation as an angle dependent radius function $r_n(\varphi_n)$ allows for applying a discrete Fourier transformation (DFT) with Fourier coefficients a_k and b_k:

$$\begin{aligned} a_k &= \frac{1}{\pi}\sum_{n=0}^{N-1} r_n \cos(k\varphi_n)\Delta\varphi_n, k \geq 0 \\ b_k &= \frac{1}{\pi}\sum_{n=0}^{N-1} r_n \sin(k\varphi_n)\Delta\varphi_n, k \geq 1 \end{aligned}, \quad (3)$$

with

$$\Delta\varphi_n = \frac{1}{2}(\varphi_n - \varphi_{n-1}) + \frac{1}{2}(\varphi_{n+1} - \varphi_n).$$

In our system b_k represent the angular orientation of the cell inside the channel and their mean magnitude is expected to be zero due to shape symmetry in the direction of flow. In experiments b_k are statistically distributed with an expectation value close to zero (Supplementary Figure 3c). For cell contour reconstruction, the first ten Fourier coefficients a_k ($k \leq 9$) are sufficient. Whereas a_0 is a measure of cell size, a_1 gives eccentricity, and a_2 represents ellipticity. Higher shape modes describe shapes near to a s-pointed star, where s is the order of the Fourier coefficient (Fig. 2a and Supplementary Figure 3a). A size-invariant representation of the contour is achieved by a normalization of all Fourier coefficients to a_0. To distinguish between the peak stress response at the inlet and the response to the steady-state stress inside the channel, the two subsets of shapes are reconstructed separately, $r_{\mathrm{rec,even}}(\varphi_{\mathrm{rec}})$ for even coefficients and $r_{\mathrm{rec,odd}}(\varphi_{\mathrm{rec}})$ for odd coefficients:

$$\begin{aligned} r_{\mathrm{rec,even}}(\varphi_{\mathrm{rec}}) &= \frac{a_0}{2} + \sum_{k=1}^{4}\left[a_{2k}\cos(2k\varphi_{\mathrm{rec}}) + b_{2k}\sin(2k\varphi_{\mathrm{rec}})\right], \\ r_{\mathrm{rec,odd}}(\varphi_{\mathrm{rec}}) &= \frac{a_0}{2} + \sum_{k=0}^{4}\left[a_{2k+1}\cos((2k+1)\varphi_{\mathrm{rec}}) + b_{2k+1}\sin((2k+1)\varphi_{\mathrm{rec}})\right] \end{aligned}. \quad (4)$$

From the reconstructed cell shape, deformations can be derived using Equation 1, resulting in d_{inlet} and d_{channel}.

Cell culture. *HL60 cells*, a myeloid precursor cell line, is used as a model system for suspended cells (courtesy of Dan and Ada Olins). Cells are cultured in RPMI-1640 medium (BioWest) with 10% FCS (Gibco), 1% penicillin/streptomycin (BioWest) and 2 mM L-Glutamin (BioWest) using a standard incubator at 37 °C, 5% CO_2 and 95% air. Every 48 h cells are centrifuged at 200 rcf for 5 min. (Allegra X-15R, Beckman Coulter), the supernatant discarded and re-suspended to a concentration of approximately 1.5×10^5 cells per milliliter. All experiments have been carried out during log phase, ~36 h after splitting. Viability of cells has been assessed to ~95% using Trypan Blue. Cells have been checked for Mycoplasma infection.

Peripheral blood cells have been obtained from healthy blood donors with written consent and under approval of the Universitätsmedizin Greifswald. Blood samples are withdrawn with a 20-gauge multifly needle into a S-monovette of 6 ml sodium citrate by vacuum aspiration (BD). In whole blood measurements, blood is diluted 1:18 in phosphate buffered saline (PBS−/−, without Ca^{2+}/Mg^{2+}, BioWest) being supplemented with 1% (w/v) methylcellulose (Sigma-Aldrich). For measurements of erythrocytes, blood is diluted 1:180 in Cell Carrier B (PBS−/− and 0.6% methylcellulose, Zellmechanik Dresden) to reduce cell concentration and shear stress.

Granulocyte isolation has been performed using the EasySep Direct Human Pan-Granulocyte Isolation Kit (StemCell). Buffy coats from whole-blood donations of healthy blood donors (Department for Transfusion Medicine, Universitätsmedizin Greifswald) are mixed 1:1 with PBS−/− before negative magnetic bead isolation according to supplier instruction. Following a final centrifugation at 200 rcf for 5 min (Allegra X-15R, Beckman Coulter), cells are re-suspended in 100 µl PBS−/− and 1% (w/v) methylcellulose to a final concentration of approximately 0.5×10^7 cells per milliliter. Purity of granulocytes (91.8%) has been confirmed using flow cytometry (LSRII, BD, Supplementary Figure 8a).

Peripheral blood mononuclear cells (PBMCs) have been isolated using Ficoll gradient centrifugation. Briefly, whole blood from buffy coats (Department for Transfusion Medicine, Universitätsmedizin Greifswald) is mixed 1:1 with PBS−/−. Next, 10 ml of Ficoll (GE Healthcare) in 50 ml falcon tubes is carefully overlaid with 30 ml of buffy coats/PBS−/− mixture. After an initial centrifugation at 400 rcf for 40 min. (no breaks, Allegra X-15R, Beckman Coulter), the interphase is removed and transferred into a new 50 ml falcon tube. In the following, 50 ml of PBS−/− are added and the suspension is centrifuged at 300 rcf for 10 min. In two

iterations, the supernatant is discarded, the pellet is re-suspended in 50 ml PBS−/− and centrifuged at 200 rcf for 10 min. PBMCs are re-suspended in PBS−/− and 1% (w/v) methylcellulose to a final concentration of approximately 0.5×10^7 cells per milliliter.

Isolation of T- and B-lymphocytes has been carried out from PBMCs using the EasySep Human CD4+ T-cell and B-cell enrichment kit (StemCell), respectively. Briefly, isolated PBMCs are adjusted to a final concentration of 5×10^7 cells per milliliter in PBS−/− and isolation for T-lymphocytes and B-lymphocytes has been performed according to supplier instruction. After a final centrifugation at 200 rcf for 5 min. cells are re-suspended to 100 µl PBS−/− supplemented with 1% (w/v) methylcellulose to a final concentration of 0.5×10^7 cells per milliliter. For reducing systematic measurement error from time-dependent deformation changes, purification of B- and T-lymphocytes has been carried out sequentially and the measurement sequence has been altered between experimental replicates. Purity of T-lymphocytes (99.5%) and B-lymphocytes (99.9%) has been confirmed using flow cytometry (LSRII, BD, Supplementary Figure 8b and 8c).

Drug treatment of HL60 cells. Inhibition of polymerization of filamentous actin has been done using cytochalasin D (Sigma-Aldrich) capping the plus end of the filaments. Cells are aliquoted at a concentration of 1×10^6 cells per milliliter and cytochalasin D (CytoD) dissolved in dimethylsulfoxid (DMSO) is added to a final concentration of 1 µM[43]. After an incubation at 37 °C for 10 min cells are centrifuged at 200 rcf for 5 min and re-suspended in PBS−/− and 1% (w/v) methylcellulose as a measurement medium. Control measurements have been carried out using the wild-type cells and the corresponding DMSO control at 0.25% (v/v) concentration.

Dynamic RT-DC measurement procedure. Prior to measurement, polymer tubing which connects the syringe pump and the microfluidic chip is flushed extensively with de-ionized water and ethanol. Next, 1 ml syringes (1 ml Luer-Lock syringe, BD) are filled with a measurement buffer, connected to the polymer tubing and the entire system is equilibrated at a flow rate of 100 nl s^{-1} for several minutes. As measurement buffer PBS−/− with 0.6% (w/v) for erythrocytes and 1% (w/v) methylcellulose for all other cells has been used. Addition of methylcellulose increases hydrodynamic stress at low flow rates, thus leading to an improved temporal and spatial resolution at a given frame rate.

In a typical experiment 100 µl of cell suspension is drawn into the tubing, which is then connected to the microfluidic chip. After first cells arrive at central constriction in the field of view, flow rate is reduced to 4 nl s^{-1} and the system is again equilibrated for 10 min. Dynamic RT-DC is carried out at flow rates of 4 nl s^{-1} and 8 nl s^{-1}, respectively. One measurement at a given flow rate is usually composed of several thousand data points. While one flow rate is sufficient for full rheological analysis of our samples, initial characterization is usually done for multiple conditions. For experimental comparison, we rescale the flow rate to the average cell surface stress. The stress is obtained from FEM calculations of steady-state cells in our microfluidic channel applying the shear-rate dependency of the measurement buffer viscosity (Supplementary Figure 9).

Hydrodynamic simulations. For numerical simulations, we use the standard as well as the CFD packages of COMSOL Multiphysics 5.3a. Neglecting inertial, turbulent, and gravitational terms, the steady-state Navier-Stokes equation simplifies to Stokes flow.

The fluid is set to be incompressible and to the measured density of 1065 kg m^{-3} (DMA4500, Anton Paar). The shear-rate-dependent viscosities $\eta_{1/2}(\dot{\gamma})$ of our measurement buffers have been characterized using a rheometer (MCR502, Anton Paar) and then modeled for PBS−/− with 0.6% (w/v) methylcellulose by a simple power law to:

$$\eta_1(\dot{\gamma}) = K_1 \cdot \left(\frac{\dot{\gamma}}{\dot{\gamma}_0}\right)^{(n_1-1)}, \quad (5)$$

where K_1 is a consistency coefficient with $K_1 = 0.16$ Pa s and n_1 is the flow behavior index with $n_1 = 0.74$.

For PBS−/− with 1% (w/v) methylcellulose we find:

$$\eta_2(\dot{\gamma}) = K_2 \cdot \left(\frac{\dot{\gamma}}{\dot{\gamma}_0}\right)^{(n_2-1)}, \quad (6)$$

with $K_2 = 0.60$ Pa s and $n = 0.64$. In both equations $\dot{\gamma}$ denotes the hydrodynamic shear rate and $\dot{\gamma}_0 = 1\ s^{-1}$ (Supplementary Figure 9). This shear-thinning behavior is expected from a polymer solution of methylcellulose and has been reported before[44,45]. In our microfluidic system, viscosities in the order of 10 mPa s have been determined from the relevant shear rate regime.

The simulations are carried out on physics-controlled meshes of an extra fine element size defined by the COMSOL backend. Parametric and material sweeps are performed for numerous conditions with respect to sample and sheath flow, channel geometry and object sizes (Supplementary Table 3). The layout of the microfluidic chips has been reconstructed, and one quadrant simulated, thus, taking advantage of the two symmetry axes through the center line of the design. Walls have been simulated using the no-slip boundary condition, and laminar flows entering the inlets of sample and sheath were assigned specific rates under constant pressure conditions. At the outlet, backflow is suppressed, reflecting the experimental conditions.

To estimate the shear stress on a cell's surface, a sphere has been modeled inside a 100 µm long channel of 20 µm × 20 µm, respectively 30 µm × 30 µm cross-section, as previously described[30]. The boundary conditions of the channel have been chosen to balance net normal pressure and hydrodynamic shear stress on the sphere's surface (Supplementary Figure 4) within numerical precision.

Analytical model. Cell response to the peak stress at the channel inlet is described by the deformation trace d_{inlet} from even Fourier modes while cell response to the constant stress inside the channel is illustrated by the deformation trace d_{channel} reconstructed from odd Fourier modes. Using a custom Matlab R2017a script (Mathworks), the characteristic time for reaching the steady state is found by fitting the following exponential function to each trace:

$$d(t) = d_0 + \hat{d}e^{-\frac{t}{\tau}}, \quad (7)$$

where $d(t)$ is the deformation given by cell circularity (Equation 1), d_0 is a free fit parameter characterizing the steady-state deformation after relaxation of all time-dependent processes, $\hat{d}$ is the deformation amplitude with $\hat{d}_{\mathrm{inlet}} = \hat{d}$ and $\hat{d}_{\mathrm{channel}} = -\hat{d}$ and τ is the characteristic relaxation time τ_{inlet} or τ_{channel}, respectively.

Quality of the fit is determined by the coefficient of correlation r^2 which is defined by:

$$r^2 = 1 - \frac{\mathrm{SS}_{\mathrm{res}}}{\mathrm{SS}_{\mathrm{tot}}} = 1 - \frac{\sum_i (y_i - f_i)^2}{\sum_i (y_i - \bar{y})^2}, \quad (8)$$

where y_i represents the data points, f_i the function values of the fit and $\bar{y}$ the mean of datapoints. For all data we use a cutoff of $r^2 \geq 0.6$ (Supplementary Figure 10).

For calculation of cell rheological properties, we use the channel deformation trace d_{channel} only. Here, cells reach a steady-state deformation $\hat{d}_{\mathrm{channel}}$, which is defined by the balance of normal and shear forces inside the constriction. In this steady state we derive the cellular surface stress using FEM simulations as described above. The apparent Young's modulus E is then calculated using an analytical model published earlier[30]. Briefly, by coupling the hydrodynamic stress distribution in the channel to linear elasticity theory the deformation of a suspended spherical object can be predicted. Carrying out this analysis for a range of cell sizes and Young's modulus allows for generation of a look-up table, where experimental and predicted deformations can be compared. The stress distribution on the cell surface is derived from flow rate, channel diameter and viscosity for the mean size of each cell type presented in this study including flow-rate dependency and accompanying shear-thinning behavior of the surrounding medium.

While d_{channel} does not represent a simple strain function, e.g. $\varepsilon = \Delta l/l$, due to the parabolic hydrodynamic stress distribution, it is sufficient to represent the dynamic response of the cell to the step stress inside the channel and to derive a relaxation time from the fit of the channel deformation trace d_{channel} to Equation 7.

This relaxation time τ_{channel} can be considered the characteristic time for the creep-compliance response of the cell to a constant stress $\sigma_{\mathrm{channel}}$ (dashed line in Fig. 3a, bottom) inside the channel. Here, an apparent viscosity η can be calculated using a simple Kelvin-Voigt model with:

$$\tau_{\mathrm{channel}} = \frac{\eta}{E}, \quad (9)$$

where E is the apparent Young's modulus.

Application of these simple models to calculate the Young's modulus and viscosity requires an alignment of the cells in the center of the channel[30]. We verified this condition by analyzing the apparent Young's modulus and the apparent viscosity as a function of the cell displacement from the channel center and find a standard deviation $\sigma < 1$ µm for all conditions. Using a Spearman rank correlation test we find correlation coefficients of $\rho < 0.09$ for all conditions which confirms that there is no correlation between the rheological parameters and lateral cell position (Supplementary Figure 11).

Calibration of dynamic RT-DC. Calibration of dRT-DC has been carried out using standardized elastic poly-acrylamide microgel beads from ref. [46]. The rheology of beads with a mean diameter of 15.2 ± 0.8 µm and an elastic modulus of 1.5 ± 0.5 kPa has been characterized in 20 µm × 20 µm and 30 µm × 30 µm channels at a flow rate of 16 nl s^{-1} and 128 nl s^{-1}, respectively. Using the peak channel deformation $\hat{d}_{\mathrm{channel}}$ and applying our analytical model we obtain an apparent Young's modulus of 2.20 ± 0.03 kPa and 2.00 ± 0.04 kPa (Supplementary Figure 12). The slight deviation from the calibration standard is still within or close to the standard error of the mean and could be attributed to batch-to-batch variation as discussed in ref. [46]. Interestingly, the authors from Girardo et al. also performed measurements on the relaxation time using ensemble averages over hundreds of beads. They find a

value of 0.12 ± 0.02 ms, which is remarkably close to 0.36 ± 0.01 ms (20 µm × 20 µm channel) and 0.12 ± 0.01 ms (30 µm × 30 µm channel) for single beads.

Power-law rheology. A comparison between Kelvin-Voigt and power-law rheology was performed by fitting the following creep function to dRT-DC data

$$J(t) = \frac{1}{E} \cdot \left(\frac{t}{t_0}\right)^{\beta}, \quad (10)$$

where $J(t)$ is the creep compliance defined by the ratio of the time-dependent strain $\varepsilon_{\mathrm{channel}}$ and the stress $\sigma_{\mathrm{channel}}$ inside the channel, E is the Young's modulus and β is the fluidity (Supplementary Figure 5). A reference time of $t_0 = 1$ s was used. For approximating the cellular strain $\varepsilon_{\mathrm{channel}}$ inside the channel, the ratio between maximal cell surface displacement and radius was estimated to 10% and used to derive the creep compliance.

Statistical data analysis. Statistical significance has been calculated using linear mixed models (LMM) on three experimental replicates carried out on separate measurement days or using biological replicates[47]. For LMM, a pair-wise comparison is performed where the observed change in an observable is split into a fixed effect, a random effect and random fluctuations. While the random effect and random fluctuations account for systematic and random measurement bias, e.g., change in temperature or donor to donor variability, the fixed effect describes the statistical difference between two groups, e.g., control and compound treatment. Two models, one with L_{Model} and one without the fixed effect term $L_{\mathrm{NullModel}}$, are fit to the data and the maximum likelihood is calculated. The likelihood ratio indicates how well each model fits the data and the corresponding p-value is computed by the Wilks theorem and by using the software ShapeOut (Zellmechanik Dresden).

The predictive potential of dRT-DC has been estimated based on the parameters: cell size A, apparent Young's modulus E, apparent viscosity η, the peak inlet deformation $\dot{d}_{\mathrm{inlet}}$ and inlet relaxation time τ_{inlet} using logistic regression models. By considering all possible parameter combinations of A, E, and η for the classification of granulocytes and PBMCs and all combinations of A, $\dot{d}_{\mathrm{inlet}}$ and τ_{inlet} for the classification of B- and CD4+ T-cells model selection is based on Akaike's information criterion (AIC)[48]. For models describing the discrimination between (a) granulocytes and PBMCs as well as between (b) B- and CD4+ T-cells AICs are reported in Supplementary Material (Supplementary Table 1 and 2). The model with the lowest AIC is considered the best model while preference is given to the model with the lower number of parameters if the differences in AIC is less than two. Receiver operating characteristics (ROC) including the area under the ROC curve (AUC) are derived for each model and optimal cutoff values for sensitivity and specificity have been calculated for the intersection in the ROC curve where sensitivity equals specificity[49]. Data are always presented for the model yielding the lowest AIC.

Code availability. The source code for data acquisition (LabView 2016) and analysis (COMSOL Multiphysics 5.3a and Matlab R2017a) is available from the corresponding author upon reasonable request.

Data availability

The datasets generated in this study are available from the corresponding author upon reasonable request. The file format of the raw data is TDMS which can be read and analysed with Matlab or ShapeOut.

Received: 17 June 2018 Accepted: 8 January 2019
Published online: 24 January 2019

References

1. Guck, J. & Chilvers, E. R. Mechanics meets medicine. *Sci. Transl. Med.* **5**, 212fs41 (2013).
2. Trepat, X. et al. Universal physical responses to stretch in the living cell. *Nature* **447**, 592–595 (2007).
3. Deng, L. et al. Fast and slow dynamics of the cytoskeleton. *Nat. Mater.* **5**, 636–640 (2006).
4. Pagliara, S. et al. Auxetic nuclei in embryonic stem cells exiting pluripotency. *Nat. Mater.* **13**, 638–644 (2014).
5. Maloney, J. M. et al. Mesenchymal stem cell mechanics from the attached to the suspended state. *Biophys. J.* **99**, 2479–2487 (2010).
6. Lautenschläger, F. et al. The regulatory role of cell mechanics for migration of differentiating myeloid cells. *Proc. Natl Acad. Sci. USA* **106**, 15696–15701 (2009).
7. Munder, M. C. et al. A pH-driven transition of the cytoplasm from a fluid- to a solid-like state promotes entry into dormancy. *elife* **5**, e09347 (2016).
8. Koch, M. et al. Plasmodium falciparum erythrocyte-binding antigen 175 triggers a biophysical change in the red blood cell that facilitates invasion. *Proc. Natl Acad. Sci. USA* **114**, 4225–4230 (2017).
9. Fletcher, D. A. & Mullins, R. D. Cell mechanics and the cytoskeleton. *Nature* **463**, 485–492 (2010).
10. Worthen, G. S., Schwab, B., Elson, E. L. & Downey, G. P. Mechanics of stimulated neutrophils: cell stiffening induces retention in capillaries. *Science* **245**, 183–186 (1989).
11. Guck, J. et al. The optical stretcher: a novel laser tool to micromanipulate cells. *Biophys. J.* **81**, 767–784 (2001).
12. Gossett, D. R. et al. Label-free cell separation and sorting in microfluidic systems. *Anal. Bioanal. Chem.* **397**, 3249–3267 (2010).
13. Dudani, J. S., Go, D. E., Gossett, D. R., Tan, A. P. & Di Carlo, D. Mediating millisecond reaction time around particles and cells. *Anal. Chem.* **86**, 1502–1510 (2014).
14. Shaw Bagnall, J. et al. Deformability-based cell selection with downstream immunofluorescence analysis. *Integr. Biol.* **8**, 654–664 (2016).
15. Xavier, M. et al. Mechanical phenotyping of primary human skeletal stem cells in heterogeneous populations by real-time deformability cytometry. *Integr. Biol.* **8**, 616–623 (2016).
16. Hwang, J. Y. et al. Cell deformation by single-beam acoustic trapping: a promising tool for measurements of cell mechanics. *Sci. Rep.* **6**, 27238 (2016).
17. Nitsan, I., Drori, S., Lewis, Y. E., Cohen, S. & Tzlil, S. Mechanical communication in cardiac cell synchronized beating. *Nat. Phys.* **12**, 472–477 (2016).
18. Guck, J., Ananthakrishnan, R., Moon, T. J., Cunningham, C. C. & Käs, J. Optical deformability of soft biological dielectrics. *Phys. Rev. Lett.* **84**, 5451–5454 (2000).
19. Shokef, Y. & Safran, S. A. Scaling laws for the response of nonlinear elastic media with implications for cell mechanics. *Phys. Rev. Lett.* **108**, 178103 (2012).
20. Kollmannsberger, P. & Fabry, B. Linear and nonlinear rheology of living cells. *Annu. Rev. Mater. Res.* **41**, 75–97 (2011).
21. Pegoraro, A. F., Janmey, P. & Weitz, D. A. Mechanical properties of the cytoskeleton and cells. *Cold Spring Harb. Perspect. Biol.* **9**, a022038 (2017).
22. Rigato, A., Miyagi, A., Scheuring, S. & Rico, F. High-frequency microrheology reveals cytoskeleton dynamics in living cells. *Nat. Phys.* **13**, 771–775 (2017).
23. Wan, J., Ristenpart, W. D. & Stone, H. A. Dynamics of shear-induced ATP release from red blood cells. *Proc. Natl Acad. Sci. USA* **105**, 16432–16437 (2008).
24. Gossett, D. R. et al. Hydrodynamic stretching of single cells for large population mechanical phenotyping. *Proc. Natl Acad. Sci. USA* **109**, 7630–7635 (2012).
25. Lange, J. R. et al. Microconstriction arrays for high-throughput quantitative measurements of cell mechanical properties. *Biophys. J.* **109**, 26–34 (2015).
26. Lange, J. R. et al. Unbiased high-precision cell mechanical measurements with microconstrictions. *Biophys. J.* **112**, 1472–1480 (2017).
27. Nyberg, K. D. et al. Quantitative deformability cytometry: rapid, calibrated measurements of cell mechanical properties. *Biophys. J.* **113**, 1574–1584 (2017).
28. Otto, O. et al. Real-time deformability cytometry: on-the-fly cell mechanical phenotyping. *Nat. Methods* **12**, 199–202 (2015).
29. Rosendahl, P. et al. Real-time fluorescence and deformability cytometry. *Nat. Methods* **15**, 355–358 (2018).
30. Mietke, A. et al. Extracting cell stiffness from real-time deformability cytometry: theory and experiment. *Biophys. J.* **109**, 2023–2036 (2015).
31. Mokbel, M. et al. Numerical simulation of real-time deformability cytometry to extract cell mechanical properties. *ACS Biomater. Sci. Eng.* **3**, 2962–2973 (2017).
32. Tatsumi, K., Haizumi, K., Sugimoto, K. & Nakabe, K. Analysis of lymphocytes deformation in microchannel flows using compound drop model. *J. Phys. Conf. Ser.* **530**, 012012 (2014).
33. Yoon, J. et al. Identification of non-activated lymphocytes using three-dimensional refractive index tomography and machine learning. *Sci. Rep.* **7**, 6654 (2017).
34. Fabry, B. et al. Scaling the microrheology of living cells. *Phys. Rev. Lett.* **87**, 148102 (2001).
35. Desprat, N., Richert, A., Simeon, J. & Asnacios, A. Creep function of a single living cell. *Biophys. J.* **88**, 2224–2233 (2005).
36. Guillou, L. et al. Measuring cell viscoelastic properties using a microfluidic extensional flow device. *Biophys. J.* **111**, 2039–2050 (2016).
37. Ekpenyong, A. E. et al. Viscoelastic properties of differentiating blood cells are fate- and function-dependent. *PLoS ONE* **7**, e45237 (2012).
38. Drury, J. L. & Dembo, M. Aspiration of human neutrophils: effects of shear thinning and cortical dissipation. *Biophys. J.* **81**, 3166–3177 (2001).
39. Nguyen, J., Wei, Y., Zheng, Y., Wang, C. & Sun, Y. On-chip sample preparation for complete blood count from raw blood. *Lab Chip* **15**, 1533–1544 (2015).

40. Lee, D., Nam, S. M., Kim, J. A., Di Carlo, D. & Lee, W. Active control of inertial focusing positions and particle separations enabled by velocity profile tuning with coflow systems. *Anal. Chem.* **90**, 2902–2911 (2018).
41. Stelekati, E. & Wherry, E. J. Chronic bystander infections and immunity to unrelated antigens. *Cell Host Microbe* **12**, 458–469 (2012).
42. Toepfner, N. et al. Detection of human disease conditions by single-cell morpho-rheological phenotyping of blood. *eLife* **7**, e29213 (2018).
43. Golfier, S. et al. High-throughput cell mechanical phenotyping for label-free titration assays of cytoskeletal modifications. *Cytoskeleton* **74**, 283–296 (2017).
44. Nasatto, P. L. et al. Methylcellulose, a cellulose derivative with original physical properties and extended applications. *Polymers* **7**, 777–803 (2015).
45. Herold, C. Mapping of deformation to apparent Young's modulus in real-time deformability cytometry. Preprint at https://arxiv.org/abs/1704.00572 (2017).
46. Girardo, S. et al. Standardized microgel beads as elastic cell mechanical probes. *J. Mater. Chem. B* **6**, 6245–6261 (2018).
47. Herbig, M., Mietke, A., Müller, P. & Otto, O. Statistics for real-time deformability cytometry: clustering, dimensionality reduction, and significance testing. *Biomicrofluidics* **12**, 042214 (2018).
48. Burnham, K. P. & Anderson, D. R. *Model Selection and Multimodel Inference*. (Springer-Verlag, New York, 2002).
49. Greiner, M. Two-graph receiver operating characteristic (TG-ROC): a Microsoft- Excel template for the selection of cut-off values in diagnostic tests. *J. Immunol. Methods* **185**, 145–146 (1995).

Acknowledgements

We thank Andreas Greinacher, Volkmar Liebscher and Ricardo Pires for valuable discussions. We gratefully acknowledge support from the German Federal Ministry of Education and Research (ZIK grant to O.O. under grant agreement 03Z22CN11) and the German Research Foundation (project number 374031971 – TRR240).

Author contributions

O.O. conceived the project. B.F. developed the experimental setup. F.C. performed FEM simulations and rheological characterization. D.B. and B.F. designed and performed experiments on HL60 cells. B.F. and K.A. designed and performed experiments on peripheral blood cells. Sa.G. provided calibration beads and characterized the calibration reference. B.F. developed the algorithm for rheological cell characterization. B.F. and St. G. established and carried out the statistical data analysis. O.O. and K.A. supervised the project. B.F. and O.O. wrote the manuscript. All authors reviewed the manuscript.

Additional information

Supplementary Information accompanies this paper at https://doi.org/10.1038/s41467-019-08370-3.

Competing interests: B.F., F.C., K.A., D.B., Sa.G. and St.G. declare no competing interest. O.O. is shareholder of Zellmechanik Dresden GmbH distributing real-time deformability cytometry; Zellmechanik Dresden GmbH owns a patent for Real-Time Deformability Cytometry (RT-DC): EU patent under the number EP 30 036 520 B1.

Reprints and permission information is available online at http://npg.nature.com/reprintsandpermissions/

Journal peer review information: *Nature Communications* thanks the anonymous reviewers for their contribution to the peer review of this work. Peer reviewer reports are available.

Publisher's note: Springer Nature remains neutral with regard to jurisdictional claims in published maps and institutional affiliations.

9.10. IV. Manuscript: Cellular shape descriptors determine the outcome of viscoelastic analyses in microfluidic systems

Fregin, B., Biedenweg, D. and Otto, O. Cellular shape descriptors determine the outcome of viscoelastic analyses in microfluidic systems . Submitted to the *Biophysical Journal* (2021).

Submitted to the Biophysical Journal on September 1, 2021
Submission ID: BIOPHYSICAL-JOURNAL-D-21-00556

Cellular shape descriptors determine the outcome of viscoelastic analyses in microfluidic systems

Running title: Cells shape descriptors define mechanics

Bob Fregin, Doreen Biedenweg, and Oliver Otto

Keywords: microfluidics, deformation, shape descriptor, cell mechanics, single cell analyses

Abstract

The capability to parameterize shapes is of essential importance in biomechanics to identify cells, to track their motion and to quantify deformation. While various shape descriptors have already been investigated to study morphology and migration of adherent cells, little is known of how the mathematical definition of a contour impacts on the outcome of rheological experiments on cells in suspension. In microfluidic systems, hydrodynamic stress distributions induce time-dependent cell deformation that need to be quantified to determine viscoelastic properties. Here, we compared nine different shape descriptors to characterize the deformation of suspended cells in an extensional as well as shear flow using dynamic real-time deformability cytometry. While stress relaxation depends on the amplitude and duration of stress, our results demonstrate that steady-state deformation can be predicted from single cell traces even for translocation times shorter than the characteristic time. Interestingly, shape dynamics is not necessarily governed by an exponential behavior, which would be expected from linear rheological models. Implementing an analytical simulation, performing experiments and testing various data analysis strategies, we compared single cell and ensemble studies to address the question of computational costs versus experimental accuracy. Results indicate that high-throughput viscoelastic measurements of cells in suspension can be performed on an ensemble scale as long as the characteristic time matches the dimensions of the microfluidic system. Finally, we introduced a score to evaluate the shape descriptor-dependent effect size for cell deformation after cytoskeletal modifications. We provide evidence that single cell analysis in an extensional flow provides highest sensitivity independently of shape parametrization, while inverse Haralick's circularity is mostly applicable to study cells in shear flow.

Statement of Significance

The capability to parameterize shapes is of essential importance in biomechanics. While various shape descriptors have already been investigated to study morphology and migration of adherent cells, little is known about cell rheological experiments in microfluidic systems. Here, hydrodynamic stress distributions induce time-dependent cell deformation that needs to be quantified to determine viscoelastic properties. We compared nine different shape descriptors to characterize the deformation of cells in an extensional as well as shear flow using dynamic real-time deformability cytometry. Our results demonstrate that steady-state deformation can be predicted from incomplete single cell traces, that shape dynamics is not necessarily described by an exponential behavior and that the effect size of mechanical changes after cytoskeletal modifications depends on the shape descriptor.

Introduction

Mechanical properties of biological systems, e.g., cells and tissues, provide a direct link to their function and can be seen as a biomarker[1–5] in cell development, cell state determination and disease screening[2,4–7]. As rheological tests base on the application of external stresses while monitoring strain, a correct definition of cell deformation is of key importance[5,8,9]. Various shape descriptors enable for parametric analyses based on geometrical features like size, perimeter, circularity and membrane curvature. Their potential has already been demonstrated in establishing a link between cell function and shape for the migration of adherent cells and to investigate the potential of morphological features for a quantitative analysis of cell microscopy images in general[8,9]. In contrast, a systematic analysis of shape descriptors for cells in suspension is currently elusive.

Earlier work investigated red blood cell (RBC) shapes and dynamics in microchannels of different size and at different flow rates[10]. Experiments have been compared to simulations assuming the RBC membrane as a triangulated network of springs where fluid flow has been modeled by dissipative particle dynamics. While simulations predict well-defined RBC states at given hydrodynamic conditions, experimental data show a broad distribution of shapes. The role of deformation and shape of RBCs has also been investigated for patients suffering from diabetes with normal and high levels of cholesterol where Babu *et al.* report that deformation is reduced in individuals with hyper cholesterol[11]. Membrane bending of RBCs is also highly relevant for the investigation of malaria disease pathogenesis. Here, Koch *et al.* could demonstrate that the malaria parasite locally reduces the bending modulus to facilitate invasion[12].

In our work, we compared nine different shape descriptors to characterize deformation of suspended cells in an extensional as well as shear flow, which are microfluidic geometries found in almost any lab-on-chip design. A detailed understanding of how hydrodynamics and shape parametrization impacts on stress distribution and strain quantification, respectively, is of utmost importance for the interpretation of data from any rheological assay that investigates cells in motion. We previously shed light on the role of hydrodynamic stress for the shape evolution of cells[13] and introduced a framework for statistical data evaluation[14]. Now we expand our analyses towards the comparison of nine parameters describing cell shape that are being used in stress-relaxation or creep-compliance experiments[3,5,15–19]. Those descriptors include cell area, front radius, axes ratio, Taylor deformation, principal axes ratio, rescaled circularity, inverse Haralick's circularity, circular variance and inertia ratio.

Within the present study, we first monitored the evolution of cell shape in response to an extensional as well as shear flow. While stress relaxation dynamics differ for all shape descriptors, our results demonstrate that steady-state deformation can be predicted from single cell traces even for translocation times shorter than its characteristic time. This is an essential requirement to extract material properties from stress-strain experiments. Second, we compared single cell vs. ensemble studies to address the question of computational effort vs. experimental accuracy. Our data indicates the necessity of analyzing single cell traces for short or unknown characteristic times, i.e., for cells with unknown material properties. Finally, we induced cytoskeletal modifications by inhibiting actin polymerization

and investigated the effect size for different shape descriptors and in extensional as well as shear flow, respectively. Single cell analysis in response to an extensional flow provides highest sensitivity independent how deformation is quantified while inverse Haralick's circularity provides highest score in effect size for cells in shear flow.

Materials and Methods

Experimental setup

A microfluidic system described in ref. [13,18] is used. Briefly, a narrow microfluidic channel of 30 µm x 30 µm cross-section and 300 µm length fabricated facilitating soft-lithography is assembled on a standard inverted microscope as part of the AcCellerator system (Zellmechanik Dresden). While cells in suspension are passing the constriction, they are illuminated by a high-power pulsed LED (L1, Zellmechanik Dresden) and imaged using a high-speed CMOS camera (MC1362, Mikrotron) as well as a 40x objective (A-Plan, NA 0.65, Zeiss) leading to a resolution of 0.34 µm per pixel. Sample suspension as well as a sheath flow for hydrodynamic focusing into the channel are connected via tubing to and controlled by a two-channel syringe pump (neMESYS, Cetoni). An outlet is connected to a waste reservoir.

Cell shape analysis

Cell deformation analysis is carried out in a custom software for dynamic cell tracking[13] adopted from ref. [18]. The camera acquires images at 3000 frames per second within a field of view of 1280 x 100 pixels, equivalent to 435 x 34 µm, covering the complete channel length including inlet and outlet region (Fig. 1a). To reduce processing bandwidth, the tracking algorithm analyzes a smaller region-of-interest (ROI) within the full field of view by cropping of 250 x 100 pixel around the moving cell. This moving ROI encapsulating the tracked cell starts at the left boundary and is shifted stepwise by 120 pixels to the right (with increasing *x*) if cell's center of mass (COM) passes a threshold in the cropped image at approximately 70% of ROI width. Image acquisition and processing is implemented in LabView (LabView 2018, National Instruments) utilizing functions of the computer vision library OpenCV (https://opencv.org/) compiled into dynamic link libraries. After background subtraction, a binary image is generated by comparing the 8-bit image to a threshold of gray-scale value 6. The binarized image enables first, a border-following algorithm[20] and second, a convex hull algorithm[21] to find contour coordinates which are saved and used to calculate a rescaled circularity c^* as a deformation measure

$$c^* = 1 - c = 1 - \frac{2\sqrt{\pi A}}{P}, \tag{1}$$

where c, A and P represent the circularity, the projected cell area and the perimeter, respectively. Image acquisition, processing and cell shape analysis is done in real-time during the experiment.

Before entering the channel, cells move slowly and consequently, shear forces are small resulting into undeformed cell shapes close to a circle ($c^* \approx 0$), whereas cells are stretched

into an ellipsoidal shape at the inlet due to an acceleration in the direction of flow (Fig. 1b). Inside the channel, cells follow the Poiseuille flow profile and mimic a bullet-shaped steady-state at channel end or beyond.

For each cell and at each position within the field of view, the brightfield images, contour coordinates as well as area and circularity are stored during the experiment for later analysis. In a post-processing step, cell contour coordinates are used to calculate time traces of the remaining shape descriptors.

Cell shape descriptors

Deformation of a cell is quantified by multiple shape descriptors. In the following, we present the definition of cell area, the normalized front radius, the axes ratio, the Taylor deformation, the principal axes ratio, the rescaled circularity, inverse Haralick's circularity, circular variance and the inertia ratio[9,22].

All calculations are based on a convex hull cell contour described by a closed polygon (x_n, y_n) with N points where $n = 0, 1, \dots, N-1$ and $(x_N, y_N) = (x_0, y_0)$. The cell is aligned in the direction of flow which we assign the x-direction (Fig. 1a).

During image acquisition, cell contour is initially stored in Cartesian coordinates. For shape descriptors principal axes ratio, inverse Haralick's circularity, and circular variance the contour is interpreted as angle-dependent radius function $r(\varphi)$ and needs to be transformed into polar coordinates. To ensure equidistant sampling in φ space, the contour is piecewise linearly interpolated to 500 points in total over 2π in Cartesian coordinates$(x_{\mathrm{interp},k}, y_{\mathrm{interp},k})$. Interpolation is necessary, to ensure that calculation of shape descriptors is insensitive against the number of contour points. Here, a 500 points interpolation yields an error below 0.1% (Supplementary Fig. 1). Interpolated points are transformed into polar coordinates $r_{\mathrm{interp},k}(\varphi_{\mathrm{interp},k})$

$$\begin{aligned} r_{\mathrm{interp},k} &= \sqrt{\left(x_{\mathrm{interp},k} - x_{\mathrm{COM}}\right)^2 + \left(y_{\mathrm{interp},k} - y_{\mathrm{COM}}\right)^2}\,, \\ \varphi_{\mathrm{interp},k} &= \arctan2\left(y_{\mathrm{interp},k} - y_{\mathrm{COM}}, x_{\mathrm{interp},k} - x_{\mathrm{COM}}\right), \end{aligned} \tag{2}$$

where $(x_{\mathrm{COM}}, y_{\mathrm{COM}})$ represents the coordinates of center of mass with

$$\begin{aligned} x_{\mathrm{COM}} &= \frac{1}{6A}\sum_n (x_n + x_{n+1})(x_n y_{n+1} - x_{n+1} y_n)\,, \\ y_{\mathrm{COM}} &= \frac{1}{6A}\sum_n (y_n + y_{n+1})(x_n y_{n+1} - x_{n+1} y_n)\,, \\ \text{with Area } A &= \frac{1}{2}\sum_n (x_n y_{n+1} - x_{n+1} y_n)\,. \end{aligned} \tag{3}$$

Area: Cell area A is defined as the cell area enclosed by its convex hull contour (Eq. 3).

Normalized front radius: The normalized front radius R_{f}^{-1} represents the curvature of the cell's front part in the direction of flow (Fig. 1a). For calculation, contour points under an angle of 90° of the leading part relative to the center of mass are considered ($-45° \leq \varphi_n \leq 45°$, Fig. 2a). A least square approximation enables calculating the center $(x_{\mathrm{c}}, y_{\mathrm{c}})$ of the corresponding circle, from which the front radius r_{f} can be derived

$$\begin{aligned} r_n(x_{\mathrm{c}}, y_{\mathrm{c}}) &= \sqrt{(x_n - x_{\mathrm{c}})^2 + (y_n - y_{\mathrm{c}})^2}\,, \\ \min_{x_{\mathrm{c}}, y_{\mathrm{c}}} \sum_n &(r_n(x_{\mathrm{c}}, y_{\mathrm{c}}) - \overline{r_n}(x_{\mathrm{c}}, y_{\mathrm{c}}))^2\,, \\ r_{\mathrm{f}} &= \overline{r_n}(x_{\mathrm{c}}, y_{\mathrm{c}})\,. \end{aligned} \tag{4}$$

If the minimization algorithm fails to find the global minimum which is examined from a comparison of the returned r_{f} with an upper threshold, set to $10\sqrt{A/\pi}$, the front radius at the current cell position needs to be excluded.

For a size-independent representation, front radius is normalized to the equivalent radius of a cell with circular shape and of same size ($\sqrt{A/\pi}$). The front radius has a local minimum at inlet in contrast to all other shape descriptors but Haralick's circularity. For comparison, we analyze the inverse normalized front radius here, referred to as the normalized front radius R_{f}^{-1}

$$R_{\mathrm{f}}^{-1} = \frac{\sqrt{\frac{A}{\pi}}}{r_{\mathrm{f}}}\,. \tag{5}$$

Axes ratio: The axes ratio R_{a} is defined by the side lengths of the bounding box fully enclosing the cell (Fig. 2a) and is calculated from length L_{x} along the axis in direction of flow divided by length L_{y} along the perpendicular axis

$$R_{\mathrm{a}} = \frac{L_{\mathrm{x}}}{L_{\mathrm{y}}} = \frac{\max(x_n) - \min(x_n)}{\max(y_n) - \min(y_n)}\,. \tag{6}$$

Taylor deformation: Taylor deformation d_{T} is defined as the difference of the two axis lengths of the bounding box divided by their sum (Fig. 2a)

$$d_{\mathrm{T}} = \frac{L_{\mathrm{x}} - L_{\mathrm{y}}}{L_{\mathrm{x}} + L_{\mathrm{y}}}\,. \tag{7}$$

Principal axes ratio: The principal axes ratio R_{pa} is defined by the two principal axes of a cell contour and is calculated from a covariance matrix C based on the contour points relative to the center of mass. Since calculation of principal axes ratio depends on the radial distribution of contour points, the interpolated points equidistantly sampled in φ space are chosen as data basis (cf. Eq. 2)

$$\begin{aligned} \vec{x} &= x_{\mathrm{interp},k} = [x_0 \quad x_1 \quad \dots \quad x_{499}]^{\mathrm{T}}\,, \\ \vec{y} &= y_{\mathrm{interp},k} = [y_0 \quad y_1 \quad \dots \quad y_{499}]^{\mathrm{T}}\,, \\ C &= \frac{1}{500}[\vec{x} - x_{\mathrm{COM}} \quad \vec{y} - y_{\mathrm{COM}}]^{\mathrm{T}} \cdot [\vec{x} - x_{\mathrm{COM}} \quad \vec{y} - y_{\mathrm{COM}}] = \begin{bmatrix} C_{xx} & C_{xy} \\ C_{yx} & C_{yy} \end{bmatrix}. \end{aligned} \tag{8}$$

R_{pa} is defined as the ratio of both eigenvalues $\lambda_{1,2}$ of C. To ensure correct assignment of both eigenvalues, corresponding eigenvectors are filtered for their orientation.

Here, the principal axes ratio is calculated as the eigenvalue corresponding to the eigenvector dominated by the axis in direction of flow (x) divided by its perpendicular counterpart (y)

$$C\vec{v}_i = \lambda_i \vec{v}_i\,, \qquad \vec{v}_i = [v_{i,x} \quad v_{i,y}]^{\mathrm{T}}\,, \qquad i = 1{,}2\,,$$
$$R_{\mathrm{pa}} = \begin{cases} \dfrac{\lambda_1}{\lambda_2}, & |v_{1,x}| > |v_{2,x}| \\ \dfrac{\lambda_2}{\lambda_1}, & \text{else} \end{cases}. \tag{9}$$

Rescaled circularity: The rescaled circularity c^* is calculated from the cell circularity c according to Eq. 1. For a completely circular cell, the rescaled circularity is equal to zero.

Inverse Haralick's circularity: The Haralick's circularity c_{H} is based on the radial distribution of all cell contour points and is calculated from the mean of the interpolated radii $r_{\mathrm{interp},k}$ divided by their standard deviation[23] (cf. Eq. 2). In contrast to most shape descriptors, c_{H} possesses a local minimum at the channel inlet and we therefore, use the inverse Haralick's circularity c_{H}^{-1} in this work (Fig. 2b)

$$c_{\mathrm{H}}^{-1} = \frac{\sigma(r_{\mathrm{interp}})}{\mu(r_{\mathrm{interp}})},$$
$$\sigma(r_{\mathrm{interp}}) = \sqrt{\frac{1}{499}\sum_k (r_{\mathrm{interp},k} - \bar{r}_{\mathrm{interp}})^2}\,, \qquad \mu(r_{\mathrm{interp}}) = \bar{r}_{\mathrm{interp}} = \frac{1}{500}\sum_k r_{\mathrm{interp},k}\,. \tag{10}$$

Circular variance: The circular variance c_{var} relates the radial variance to the squared radii mean (Eq. 2)

$$c_{\mathrm{var}} = \frac{\mathrm{Var}(r_{\mathrm{interp}})}{\mu^2(r_{\mathrm{interp}})},$$
$$\mathrm{Var}(r_{\mathrm{interp}}) = \sigma^2(r_{\mathrm{interp}})\,. \tag{11}$$

Circular variance is the square of inverse Haralick's circularity.

Inertia ratio: The inertia ratio R_{i} relates the area moment of inertia along the two axes of minimal and maximal moment of area (Fig. 2a, depicted are the 4th roots since moment of inertia has the dimension length to the power of four). First, the area moments of inertia I_{xx}, I_{yy} and I_{xy}, related to the x-axis, y-axis, and their diagonal, respectively, are calculated for contour points relative to their center of mass $(\tilde{x}_n, \tilde{y}_n) = (x_n - x_{\mathrm{COM}}, y_n - y_{\mathrm{COM}})$

$$I_{xx} = \frac{1}{12}\sum_n (\tilde{x}_n\tilde{y}_{n+1} - \tilde{x}_{n+1}\tilde{y}_n)(\tilde{y}_n^2 + \tilde{y}_n\tilde{y}_{n+1} + \tilde{y}_{n+1}^2)\,,$$
$$I_{yy} = \frac{1}{12}\sum_n (\tilde{x}_n\tilde{y}_{n+1} - \tilde{x}_{n+1}\tilde{y}_n)(\tilde{x}_n^2 + \tilde{x}_n\tilde{x}_{n+1} + \tilde{x}_{n+1}^2)\,, \tag{12}$$
$$I_{xy} = \frac{1}{24}\sum_n (\tilde{x}_n\tilde{y}_{n+1} - \tilde{x}_{n+1}\tilde{y}_n)(\tilde{x}_n\tilde{y}_{n+1} + 2\tilde{x}_n\tilde{y}_n + 2\tilde{x}_{n+1}\tilde{y}_{n+1} + \tilde{x}_{n+1}\tilde{y}_n)\,.$$

The eigenvalues and eigenvectors of the area moment of inertia Tensor T are determined (describing minimal and maximal moment of area and corresponding axes).

For correct assignment of extremal axes of inertia ratio, the corresponding eigenvectors are filtered for orientation with respect to direction of flow. R_i is then calculated as inertia dominated by axis in the direction of flow (x) divided by its perpendicular counterpart (y).

$$
\begin{gathered}
T = \begin{bmatrix} I_{xx} & -I_{xy} \\ -I_{xy} & I_{yy} \end{bmatrix}, \\
T\vec{v}_i = \lambda_i \vec{v}_i\,, \qquad \vec{v}_i = [v_{i,x} \quad v_{i,y}]^\mathrm{T}\,, \qquad i = 1{,}2\,, \\
R_\mathrm{i} = \begin{cases} \dfrac{\lambda_2}{\lambda_1}, & |v_{1,x}| > |v_{2,x}| \\ \dfrac{\lambda_1}{\lambda_2}, & \text{else} \end{cases}.
\end{gathered}
\tag{13}
$$

Cell culture

All experiments have been performed using the model system HL60, a myeloid precursor suspension cell line (courtesy of Dan and Ada Olins). Cells are cultured in RPMI-1640 medium (BioWest) with 10% FCS (Gibco), 1% penicillin/streptomycin (BioWest) and 2 mM L-Glutamin (BioWest) in a standard incubator at 37 °C, 5% CO_2 and 95% air. Cells are split approximately every 48 h by centrifugation for 5 min at 200 rcf (Allegra X-15R, Beckman Coulter). The supernatant is discarded and cells are re-suspended in medium. Concentration is adjusted to approximately 1.5 x 10^5 cells per milliliter. Measurements were performed during log phase, approximately 36 hours after splitting. Viability of cells has been assessed to ~95% using Trypan Blue. Cells responded negatively to a test for Mycoplasma infection (MycoSPY®, Biontex).

Data filtering strategy

The tracking algorithm derives a convex hull contour of the cell from every raw image. Goodness of the contour fit is determined by comparing the convex hull area to the raw cell area (Fig. 2a, first panel). A cell trace is considered to be valid if at least 80% of all images from a cell inside the channel possess a convex hull area that is not more than 5% bigger than the raw cell area. If a cell trace does not cover the entire length of the channel, it is excluded from data analysis.

Cells are filtered for projected cell areas between [75, 300] µm² in order to exclude debris as well as cell clusters. Since the stress on cell surface depends on cell velocity, only cells with a mean velocity $v \pm 3\sigma$ are considered for analysis, with standard deviation σ. With all our experiments being carried out at a flow rate of 8 nl·s^{-1} we find a range of 17.6 mm·s^{-1} ± 1.8 mm·s^{-1} for a typical experiment with 1,806 cells acquired. After filtering for cell size and velocity, 1,766 cells remain in the sample. This corresponds to 2.2 % of the cells being excluded (Fig. 3a, b).

Fourier analysis

The shape dynamics of a cell translocating a microfluidic channel shows a superimposed response to an inlet stress due to its initial acceleration and to a constant stress inside the constriction. Shape mode decomposition utilizing Fourier transformation published earlier enables to disentangle cellular response to both contributions[13]. Briefly, cell contours are transformed from Cartesian into polar coordinates with respect to their center of mass. From the Fourier transformation of this angle-dependent radius function the first ten Fourier coefficients (FC) are considered. By symmetry arguments only, it was shown that cell response to inlet stress is reflected by the even Fourier components, whereas, the odd Fourier components represent cellular response to the stress inside the channel. To discriminate between the two responses, the shapes are reconstructed from even and odd FC subset (including FC zero) separately. Consequently, every cell shape of a cell at any position can be decomposed into two contours representing the response to inlet and channel stresses.

Time-dependent shape descriptor analysis

Time-dependent deformation traces $d(t)$, with d being a time-dependent scalar representing all shape descriptors considered in this work, are the basis for characteristic time analysis, which is needed, e.g., to calculate viscoelastic material properties.

Here, we extract the characteristic time τ by fitting an exponential function to the time-dependent deformation $d(t)$ using a custom script implemented in Matlab R2018b (Mathworks)

$$d_{\mathrm{fit}}(t) = \hat{d}\,\exp\left(-\frac{t}{\tau}\right) + d_0\,, \tag{14}$$

with time t and free fitting parameters $\hat{d}$, τ and d_0 representing the deformation amplitude of any shape descriptor discussed in this work, the characteristic time and the steady-state offset deformation, respectively. The exponential behavior with characteristic time τ of the fit follows the response of a Kelvin-Voigt model in presence of a step stress. The model is used for fitting of traces independently of the respective analysis strategy, i.e., direct ensemble, ensemble analysis of inlet or channel effects, and single cell analysis of both effects.

For direct ensemble analysis, we overlay all single traces into a master curve by calculating the median at each point in time inside the channel, using interpolation to synchronize between uneven sampling times of the traces. Fitting the master curve is performed for points in time within a range between 0% and 95% inside the channel to ensure that characteristic times are not affected by the outlet (cf. Fig. 3b). Of note, since position is defined by the center of mass, a cell can be considered inside the channel while the leading edge already crosses the outlet.

For ensemble analysis of inlet effects, we overlay all single traces into a master curve after Fourier decomposition and reconstruction from even FC. Subsequently fitting according to Equation 14 is performed as described above. Channel traces reconstructed from odd FC require introduction of a lag time corresponding to 10% of the translocation time for fitting.

Here, shape descriptors stay constant for a couple of frames before a response to channel stress is observed (Fig. 3b).

Single cell analysis is performed for traces reconstructed from even and odd FC analog to the ensemble traces described above. However, begin and end point for fitting need to be found for every single trace individually because the responses vary in their behavior over time. For inlet traces the position of the minimum (if applicable) is determined by a moving median filter of 3 points before and after the current time point, i.e., with a length of 7 points. Traces are fitted from channel inlet until minimum position or channel end if no minimum exists. For channel stress traces, the initial lag phase is searched dynamically and traces are fitted from the end of the lag phase until channel outlet.

Quality of fit is assessed from coefficient of determination r^2, where we consider all traces with $r^2 \geq 0.6$ for data analysis[13]. The coefficient of determination relates the residual sum of squares (SS_{res}) to the total sum of squares (SS_{tot})

$$r^2 = 1 - \frac{SS_{\mathrm{res}}}{SS_{\mathrm{tot}}} = \frac{\sum_i (d_i - d_{\mathrm{fit},i})^2}{\sum_i (d_i - \bar{d})^2}, \tag{15}$$

where d_i is the i-th data point, $d_{\mathrm{fit},i}$ corresponding fit function value and $\bar{d}$ the data mean.

Statistical analysis

For statistical analysis a linear mixed-effects model (LMM) is fitted to the dataset consisting of three biological replicates with paired control (control or DMSO vehicle) and treatment (CytoD), as introduced earlier[14]. First, a linear mixed-effects model is used considering the treatment as the fixed effect and differences between replicates as random effect. A second model including random effects only, represents the null hypothesis. Utilizing a model comparison by maximizing the likelihood function, a p-value can be extracted. This strategy is used for statistical analysis of single cell measurements where datasets consist of thousands of cells. The error of effect sizes is estimated from errors for intercept and treatment from LMM. Propagation of uncertainty is implemented utilizing a first order Taylor expansion.

Statistical analysis for ensemble measurements is performed by a t-test as the number of observations is not sufficient for fitting a linear mixed-effects model. Effect size is represented by normalizing the treatment parameter (CytoD) by the vehicle parameter (control or DMSO). Effect size diminished by unity is expected to be zero for no effect. A one-parametric t-test on this difference is used to test against zero and provides the corresponding p-value.

Results

Cellular shape descriptors reveal characteristic dynamics

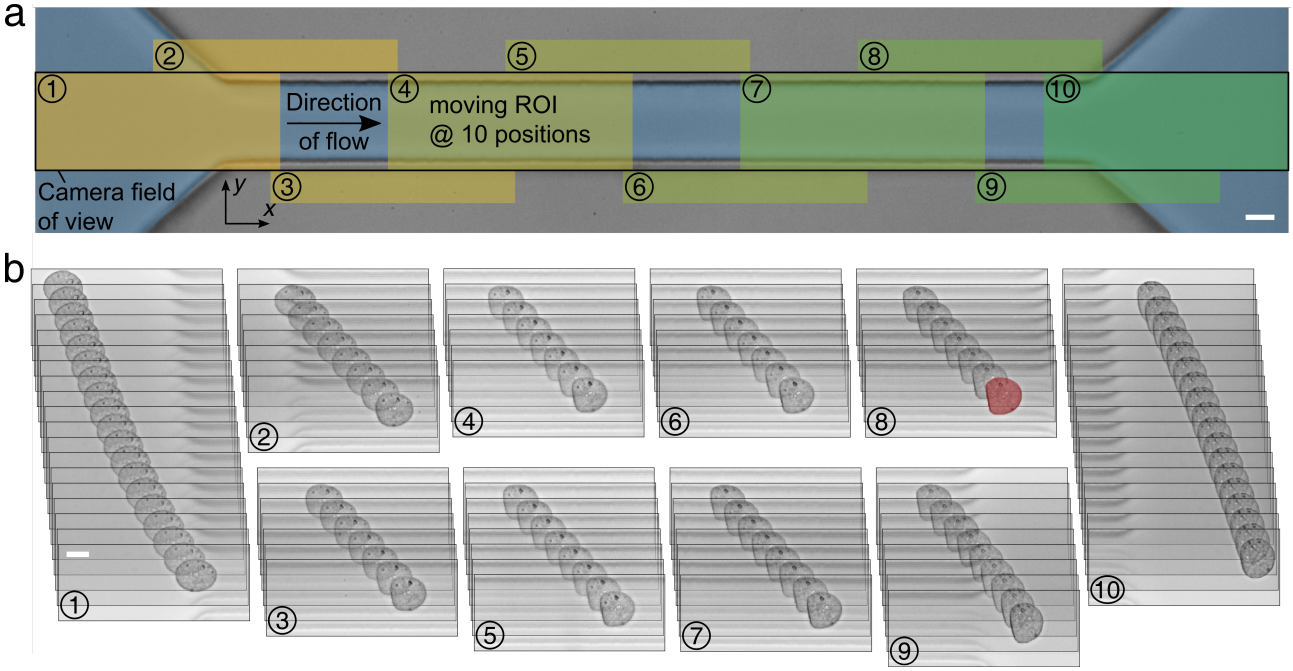

Fig. 1 Dynamic tracking of single cells in a microfluidic channel. **a)** Image of a 30 µm x 30 µm microfluidic channel of 300 µm length. Overlaid sketch demonstrates principle of dynamic cell tracking. Camera field of view is indicated by a black rectangle covering the complete length of channel as well as inlet and outlet region. A moving cell is tracked by a moving region-of-interest (ROI, 250 pix x 100 pix) shifted stepwise in the direction of flow depending on the cell position inside the channel (ROI positions 1 to 10 are highlighted). **b)** Image sequence of a tracked HL60 cell captured over time consisting of 98 consecutive frames. The trace was captured at the 10 different ROI positions indicated in (a). The cell shape at the end of the channel is highlighted in red and scale bars are 10 µm. Flow rate was set to 8 nl·s^{-1}.

For investigating how different shape descriptors affect the calculation of mechanical properties, suspended cells are monitored during the translocation of a microfluidic channel (Fig. 1a). We use dynamic real-time deformability cytometry (dRT-DC) to analyze cell shape within a moving region-of-interest (ROI) at ten different positions between channel inlet and outlet[13] (see Methods). The high temporal resolution of our experimental system enables to observe the dynamic cell response to the hydrodynamic stress distribution with a resolution of 98 frames at a typical flow rate of 8 nl·s^{-1} (Fig. 1b). The number of acquired frames differs for individual cells and depends strongly on the flow rate.

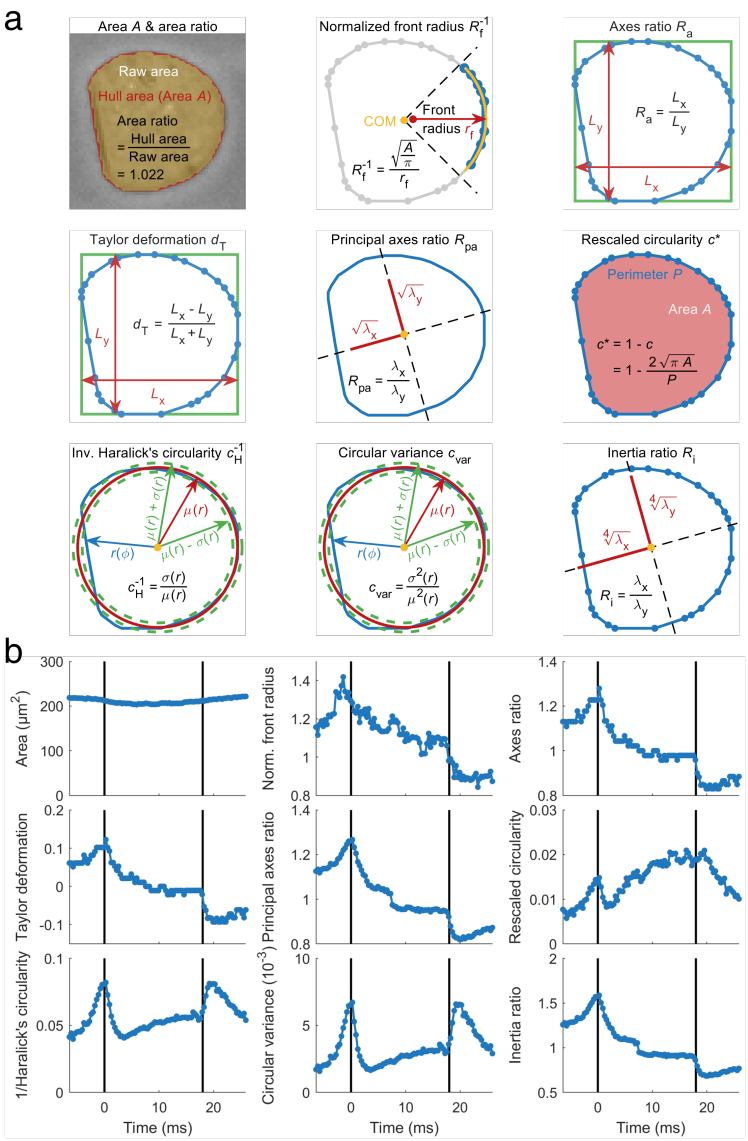

Fig. 2 Shape descriptors reveal varying cell response. **a)** Nine shape descriptors are introduced and applied to the steady-state shape of a HL60 cell (highlighted cell shape at channel end in Fig. 1b). Cell shape is represented by blue contour points and connecting line segments. **b)** Time-dependent traces of deformation represented by the different shape descriptors introduced in (a) and applied to the deformed shapes of a representative HL60 cell passing a 30 μm x 30 μm channel of 300 μm length at a flow rate of 8 nl·s^{-1}.

Derivation of cell material properties from strain requires knowledge of the stress distribution inside our microfluidic system. While stress on a cell can be obtained from an analytical as well as numerical model[6,24], there are multiple shape descriptors to quantify strain. Within this work, we investigated nine shape descriptors as a measure for cell deformation: projected cell area, normalized front radius, Taylor deformation, axes ratio, principal axes ratio, rescaled circularity, inverse Haralick's circularity, circular variance and inertia ratio (Fig. 2a, see Methods). All of these are geometric parameters for characterizing two-dimensional shapes by a scalar, represent different shape features, and possess different properties. Cell rotation inside the channel, e.g., impacts on normalized front radius, Taylor deformation, and axes ratio whereas the other shape descriptors are rotational invariant, either by definition like area, rescaled circularity, inverse Haralick's circularity, and circular variance, or due to reference to principal axes of cell orientation like principal axes ratio and inertia ratio.

When monitoring the translocation of a single HL60 cell through a microfluidic constriction, the nine shape descriptors reveal characteristic dynamics (Fig. 2b). Whereas area stays constant over time as expected, shape descriptors based on cell axes like axes ratio, Taylor deformation, principal axes ratio, and inertia ratio show a maximum at inlet position and are monotonous decreasing towards the channel outlet. We also observe a decrease in normalized front radius, indicating that curvature of the leading part of a cell decreases, and, hence, radius increases inside channel. In contrast, rescaled circularity, inverse Haralick's circularity, and circular variance reveal a minimum amplitude between the maximum at channel inlet and steady-state at channel outlet. Here, we define the steady-state as a condition where cell deformation is time-independent.

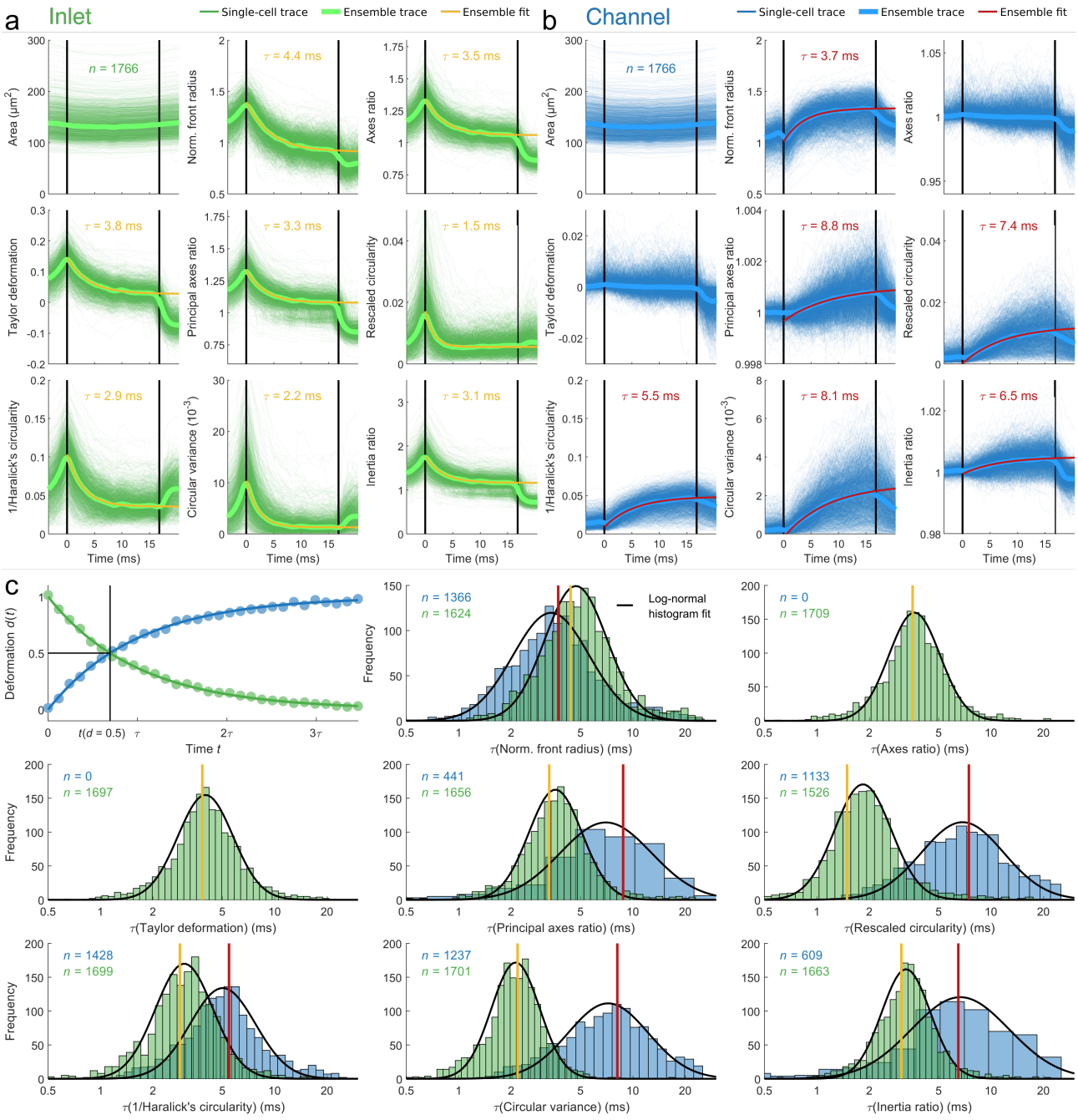

Fig. 3 Dynamics of shape descriptors for reconstructed Fourier traces. **a, b)** Cell shapes are decomposed by Fourier transformation and reconstructed from two subsets of first 10 Fourier coefficients (FC): even FC representing inlet effects (a, green traces) and odd FC including coefficient zero representing channel effects

(b, blue traces). Deformation dynamics are shown for 1766 HL60 cells passing a 30 µm x 30 µm channel of 300 µm length at a flow rate of 8 nl·s^{-1}. Ensemble response (median) of all cells was calculated (bold green and bold blue lines) while yellow (a) and red lines (b) represent an exponential fit to median traces. Vertical black lines indicate channel inlet and outlet. **c)** Exemplary sketch of deformation $d(t)$ representing an inlet (green dots) and channel (blue dots) trace as well as corresponding exponential fits (top left panel, solid lines). Single cell analysis is performed by fitting an exponential function to the data, calculation of characteristic times (τ) and filtering the resulting traces for a minimal amplitude fraction of α_{min} = 0.5 as well as plotting histograms on logarithmic scale. Distributions are filtered for validity of the fit ($r^2 \geq 0.6$). Solid black lines indicate a log-normal fit to the histograms filtering data for ± 1.96 σ (95%) with respect to median to reject outliers. Vertical red and yellow lines show a comparison to relaxation times from ensemble fit in (a) and (b). Area, Taylor deformation (channel) and axes ratio (channel) show no exponential stress response.

Characteristic times depend on cellular shape descriptors

A cell responds to two different stress distributions inside a microfluidic channel: a peak stress at the inlet due to a reduction in cross-section and subsequent acceleration, as well as a constant stress inside the channel originating from the Stokes flow[13]. This superposition results in complex cellular dynamics reflected in the behavior of the geometrical descriptors.

In general, shape descriptors can be discriminated in quantities revealing a minimum in their deformation trace and those with a monotonic behavior (Fig. 2b). Focusing on a deformation measure derived from circularity, we have recently shown that Fourier decomposition of shape modes enables to disentangle the cell response to the inlet stress from the effect of the channel stress[13]. Here, we expanded that analytical framework to all nine shape descriptors introduced above (Fig. 2a). Performing dRT-DC, traces from more than 4800 HL60 cells in three biological replicates were acquired, shapes decomposed and reconstructed from even and odd Fourier components individually representing cell response to inlet and channel stress, respectively (see Methods).

Shape descriptors reconstructed from only even Fourier coefficients reveal a peak at the channel entrance and a constant amplitude towards the outlet (Fig. 3a & Supplementary Fig. 2a). In contrast, most shape descriptors reconstructed from only odd Fourier coefficients possess a constant magnitude at channel inlet, which increases until the cell leaves the constriction (Fig. 3b & Supplementary Fig. 2b). Remarkably, axes ratio and Taylor deformation are both insensitive to channel stress and stay constant around one and zero, respectively. As expected, projected cell area does not change as a function of time and is therefore excluded from further analysis.

We analyzed the traces of all shape descriptors, first, by obtaining an ensemble average and second, on a single cell level. The ensemble average has been calculated from the median over all single cell traces (Fig. 3a green traces and Fig. 3b blue traces) for each of the 85 interpolated positions of a cell within the microfluidic system and separated for inlet and channel effects (Fig. 3a bold green line and Fig. 3b bold blue line). Fitting an exponential function (Eq. 14) to the ensemble trace yields two characteristic times, one for the cell response to inlet stress (τ_{inlet}, Fig. 3a yellow lines) and one for the cell response to the constant channel stress (τ_{channel}, Fig. 3b red lines). For the latter, τ_{channel} can be interpreted as the viscoelastic response

$$\tau = \frac{\eta}{E} \tag{16}$$

to a creeping-flow experiment exploiting a Kelvin-Voigt model[19,25–27]. For τ_{inlet} the analytical stress is unknown, but nevertheless it characterizes a relaxation process. Both, τ_{inlet} and τ_{channel} represent two material parameters and are investigated in this work.

Next, we analyzed our data on a single cell level (Fig. 3a and b, green and blue traces) by fitting an exponential function (Eq. 14) to every inlet and channel trace (Fig. 3c, top left panel). Goodness of the exponential fit is assessed by the coefficient of determination (r^2, see Methods). Only fits with $r^2 \geq 0.6$ are included in our analysis, as we already demonstrated that this threshold provides a good data representation[13]. Comparison between different conditions further requires that experimental timescales given by the channel translocation time t_{channel} match characteristic timescales τ_{inlet} and τ_{channel} of individual cells. This is specifically of importance when analyses require cells being in steady-state, which corresponds to five times the characteristic time (equivalent to more than 99% of asymptotic value of an exponential function for $t \to \infty$). This implies that a relaxation time of, e.g., 5 ms requires a translocation time of 25 ms.

For investigating the steady-state condition, we introduced an amplitude fraction α as the ratio between the shape descriptor amplitude at channel outlet $d(t_{\mathrm{channel}})$ and the steady-state amplitude $d(t \to \infty)$, both corrected for the amplitude at the channel inlet $d(t = 0)$, all obtained from the exponential fit:

$$\alpha = \frac{d(t_{\mathrm{channel}}) - d(t = 0)}{d(t \to \infty) - d(t = 0)}. \tag{17}$$

If the amplitude fraction of an experiment exceeds $\alpha \geq \alpha_{\mathrm{min}}$, the characteristic time from the fit is considered to be a valid representation of cell's relaxation time. Utilizing the exponential dependency between the amplitude and time domain, Eq. 17 can be rewritten by means of the relevant time scales (Supplementary Equations 1-5):

$$\tau \leq \tau_{\mathrm{threshold}}\,, \qquad \tau_{\mathrm{threshold}} = \frac{t_{\mathrm{channel}}}{-\ln(1 - \alpha_{\mathrm{min}})}. \tag{18}$$

Eq. 18 enables the definition of an upper threshold $\tau_{\mathrm{threshold}}$ of valid characteristic times for single cells by measuring a median translocation time and imposing a minimal amplitude fraction.

In a typical experimental setting with a 300 µm long channel and applying a flow rate of 8 nl·s^{-1}, we find a mean cell velocity of 17.6 mm·s^{-1} for HL60 cells and a channel translocation time of 17.0 ms. For α_{min} = 0.5, i.e., at least 50% of a given steady-state amplitude is found inside the channel (Fig. 3c, top left panel), the threshold in characteristic time is given by $\tau_{\mathrm{threshold}} = 1.44 \cdot t_{\mathrm{channel}}$, which corresponds to the condition $t_{\mathrm{channel}} \geq 0.69 \cdot \tau_{\mathrm{channel/inlet}}$ (Eq. 18).

In our work, we analyzed n = 4845 single cell traces from three biological replicates by Fourier decomposition, subsequent shape reconstruction from odd as well as even coefficients and calculation of eight shape descriptors introduced above (excluding cell size). Applying a minimal amplitude fraction α_{min} = 0.5 as a selection criterion for valid exponential fits, the resulting characteristic times are described by a log-normal distribution (Fig. 3c, one

replicate is presented). In general, we find $\tau_{\mathrm{channel}} > \tau_{\mathrm{inlet}}$, which can be explained by the short peak stress at the inlet and the longer constant stress in the channel. Interestingly, traces described by the normalized front radius demonstrate an opposite behavior, i.e., $\tau_{\mathrm{channel}} < \tau_{\mathrm{inlet}}$, a result that potentially originates from its sensitivity towards cell contour curvature in the direction of flow. In contrast, traces quantified by axis ratio and Taylor deformation are nearly insensitive towards the constant channel stress and the amplitude of the shape descriptors remains unaltered (Fig. 3b).

Finally, we compare the single cell analyses to the results from the ensemble fit and find that the ensemble characteristic time is equal or smaller than the mode of the single cell distribution in case of the inlet response (Fig. 3c, yellow lines) while the channel traces reveal an opposite trend (Fig. 3c, red lines). These qualitative differences can be understood from the different filtering strategies. While single cell analysis enables evaluation of every single trace, the individual steady-state information is hidden in the intrinsic averaging for the ensemble mean. However, on an ensemble level Eq. 18 must be fulfilled as well, which is true for all presented conditions assuming α_{min} = 0.5 (Fig. 3a, b). In a next step, we investigate within a simulation framework the impact of single cell and ensemble analysis on the gained results as well as the differences between both strategies.

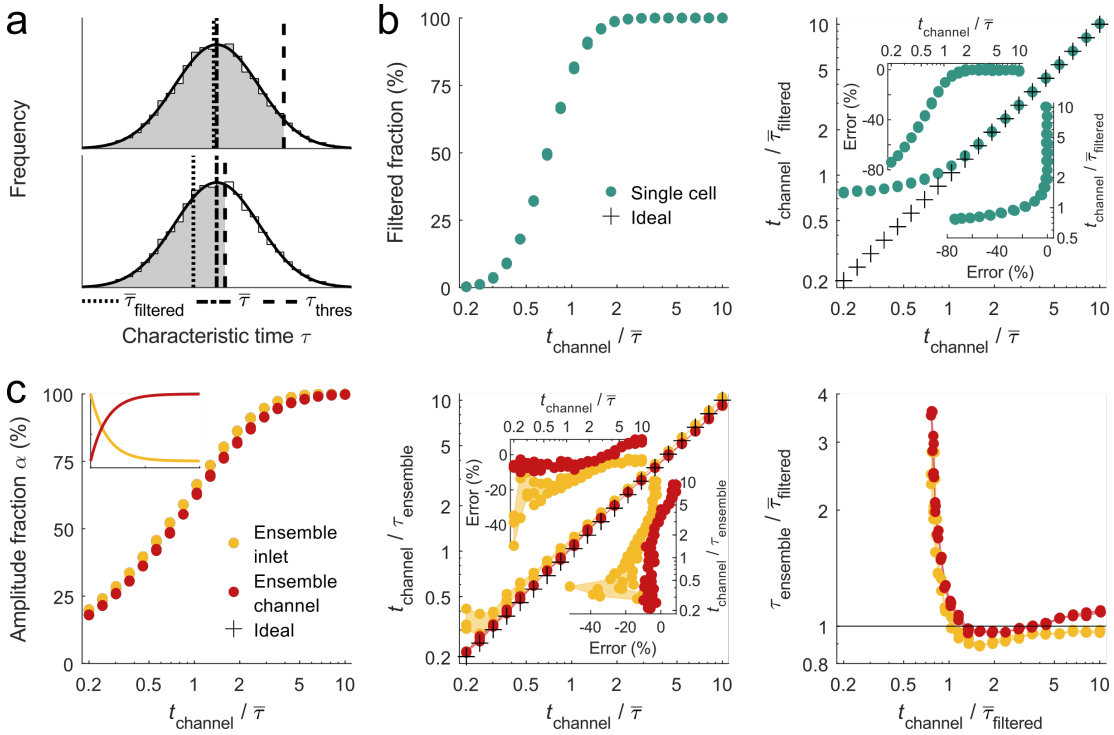

Fig. 4 Characteristic time simulation for cell shape dynamics. **a)** Log-normal distribution of 10^4 characteristic times τ with $\bar{\tau}$ = 5 ms and $\sigma(\log_{10}\tau/\tau_0)$ = 0.2 ($\bar{\tau}$ and σ have been estimated from experimental data, τ_0 is set to 1 ms). In experiments, $\bar{\tau}$ is usually not accessible due to finite channel length and is replaced by $\bar{\tau}_{\mathrm{filtered}}$, which depends on the upper limit of accessible characteristic times $\tau_{\mathrm{threshold}}$. **b)** Filtered fraction of single cell characteristic time distribution as function of channel translocation time normalized to $\bar{\tau}$ (left panel) and comparison between t_{channel} normalized to $\bar{\tau}_{\mathrm{filtered}}$ and $\bar{\tau}$ (right panel), respectively. Insets show error $(\bar{\tau}_{\mathrm{filtered}} - \bar{\tau})/\bar{\tau}$ for projections of x- and y-axis, respectively. **c)** Amplitude fraction as function of normalized channel translocation time for ensemble analysis of inlet (yellow) and channel data (red). Inset shows exemplary deformation traces for inlet (yellow) and channel (red) shape dynamics. Centre panel describes t_{channel} normalized to ensemble characteristic time as a function t_{channel} normalized to the median characteristic time from single cell analysis. The right panel compares $\tau_{\mathrm{ensemble}}/\bar{\tau}_{\mathrm{filtered}}$ to $t_{\mathrm{channel}}/\tau$ since experimental data does not allow accessing the full characteristic time distribution. Crosses indicate ideal case without any bias. For every set of parameters, three simulation runs are shown.

Measurement bias introduced by single cell analysis

We analyzed the impact of different filtering strategies on characteristic times from single cell traces captured inside the channel. As stated above, traces with $\tau_{\mathrm{inlet/channel}} > \tau_{\mathrm{threshold}}$ are excluded from the analysis. This leads to a shift in the median characteristic time $\bar{\tau}$ towards a lower value $\bar{\tau}_{\mathrm{filtered}}$ and introduces a systematic error into single cell analysis. Depending on $\tau_{\mathrm{threshold}}$ the bias can be smaller (Fig. 4a, left panel, top) or bigger (Fig. 4a, left panel, bottom).

We investigated this effect by simulating a characteristic time distribution defined by a log-normal function of median time $\bar{\tau}$ = 5 ms and a standard deviation of $\sigma(\log_{10}\tau/\tau_0)$ = 0.2, with τ_0 = 1 ms (Supplementary Fig. 3a). Varying the translocation time t_{channel} and normalization to $\bar{\tau}$ enables calculation of the filtered fraction of the sample distribution, which corresponds to 50% of all events of the full distribution for $t_{\mathrm{channel}} = 0.7\bar{\tau}$ and to 99% of all events for $t_{\mathrm{channel}} = 2\bar{\tau}$ (Fig. 4b, left panel). Here, we assumed a minimal amplitude fraction of α_{min} = 0.5. A comparison between $t_{\mathrm{channel}}/\bar{\tau}_{\mathrm{filtered}}$ and $t_{\mathrm{channel}}/\bar{\tau}$, where $\bar{\tau}$ is experimentally not accessible, reveals an apparent deviation for $t_{\mathrm{channel}} < 2\bar{\tau}$ (Fig. 4b, right panel). Filtering for traces in single cell analysis with translocation times t_{channel} equal to at least the median relaxation time $\bar{\tau}$ can lead to errors of up to 10% while we find an error of only 1.5% for $t_{\mathrm{channel}} \geq 2\bar{\tau}$ (Fig. 4b, right panel, top inset).

From these calculations, the measurement bias in single cell analysis can be estimated. An evaluation of the experimentally-observed median characteristic times from the eight shape descriptors indicates a range of 1.8 ms ≤ $\bar{\tau}_{\mathrm{filtered}}$ ≤ 4.8 ms for inlet data and 3.5 ms ≤ $\bar{\tau}_{\mathrm{filtered}}$ ≤ 7.2 ms for channel response (Fig. 3c). Normalizing a typical translocation time t_{channel} = 17 ms to each median characteristic time yields a ratio from 3.5 to 9.2 for inlet and 2.4 to 4.9 for channel response. This results in an error in single cell analysis between -1.5 % and 0.9 % (Fig. 4a, right panel, right inset).

Interestingly, for $t_{\mathrm{channel}} \geq \bar{\tau}_{\mathrm{filtered}}$ or $t_{\mathrm{channel}} \geq 0.7\bar{\tau}$ we obtain an error of approximately 20%, which has the same magnitude as the estimated experimental error, e.g., due to pixilation effects of our image acquisition[28]. Practically, these considerations imply first that the systematic bias due to the inaccessibility of the true median value of the characteristic time is independent of the shape descriptor and can be neglected. Second, our simulations verify that the steady-state of a cell can be extrapolated from translocation times as short (and even shorter) as the characteristic time and that the Young's modulus can be calculated from such traces.

Measurement bias introduced by ensemble analysis

Next, we investigated the conditions under which the ensemble average is a good representation of the underlying single cell distribution. Although single cell traces are characterized by an exponential function, the median or mean of many such exponential functions does not necessarily possess exponential behavior. In fact, summation of non-linear functions does not result in a function of the same type without loss of generality.

In a simulation, we addressed this issue and generated characteristic time distributions as described above. Corresponding amplitude values of the traces were taken from a log-normal distribution with center at unity and standard deviation of $\sigma(\log_{10} A) = 0.2$ (Supplementary Fig. 3b). From each pair of characteristic times and deformation amplitudes, an exponential curve is created, either with negative (Fig. 4c, left panel, inset, yellow line) or positive slope (Fig. 4c, left panel, inset, red line), representing inlet and channel response, respectively. An ensemble response is calculated from the median over all traces. When calculating the amplitude fraction α of the ensemble response while varying the translocation time t_{channel} relative to the median characteristic time $\bar{\tau}$ of the single trace distribution, we observe for an increasing translocation time or channel length an increase in α (Fig. 4b, left panel). For $t_{\mathrm{channel}} \geq \bar{\tau}$ we obtain $\alpha \geq 61\%$, or if we impose $\alpha_{\mathrm{min}} = 0.5$, meaning that at least 50% of deformation amplitude are supported by acquired data points within channel, the translocation time of cells should be chosen to be at least approx. 70% of the expected median relaxation time.

In line with experimental assays, we extract the ensemble relaxation time τ_{ensemble} by fitting an exponential function to the median response. Comparing the ensemble relaxation time $t_{\mathrm{channel}}/\tau_{\mathrm{ensemble}}$ to the median of the real single trace characteristic time distribution $t_{\mathrm{channel}}/\bar{\tau}$, both with respect to t_{channel}, we find in almost all conditions a small but obvious underestimation of τ_{ensemble} (Fig. 4c, center panel). In general, this effect is more pronounced for the inlet response, in particular, for short translocation times. An absolute error below 11% or 9% is observed for the response to inlet or channel stress, respectively, if t_{channel} is kept between $2\bar{\tau}$ and $10\bar{\tau}$ (Fig. 4c center panel, top inset). The fact of having a finite error even for long translocations times and the apparent differences between inlet and channel computations originates from the non-trivial problem of summation over non-linear functions.

Looking at experimental data, we find ensemble characteristic times for all eight shape descriptors of 1.5 ms ≤ τ_{ensemble} ≤ 4.4 ms for inlet and 3.7 ms ≤ τ_{ensemble} ≤ 8.8 ms for channel stress response (Fig. 3c). Normalization of the translocation time to each ensemble characteristic time yields a ratio from 3.9 to 11.3 for inlet and from 1.9 to 4.6 for channel response. This results in an absolute error below 5 % for inlet and from -5 % to 4 % for channel, respectively (Fig. 4c, center panel, right inset). A comparison of these values to the systematic error introduced by excluding traces from single cell analysis shows that ensemble averaging results in larger bias but still well below other uncertainties, e.g., pixilation effects.

Since experiments do not permit access to the full characteristic time distribution in single cell analysis nor obtaining the unbiased ensemble characteristic time, we finally compare $\tau_{\mathrm{ensemble}}/\bar{\tau}_{\mathrm{filtered}}$ to the normalized translocation time $t_{\mathrm{channel}}/\bar{\tau}_{\mathrm{filtered}}$ (Fig. 4c, right panel). For $t_{\mathrm{channel}}/\bar{\tau}_{\mathrm{filtered}} < 1$, i.e., for short translocation times, we find an overestimation of τ_{ensemble} compared to single cell analysis as many traces are included in the ensemble characteristic time that do not reach the minimal amplitude fraction. For long translocation times, we find little deviation between the ensemble average and the filtered median of the single cell analysis, as expected. Interestingly, for intermediate translocation times, $1.2 \leq t_{\mathrm{channel}}/\bar{\tau}_{\mathrm{filtered}} \leq 4$, τ_{ensemble} is slightly smaller than $\bar{\tau}_{\mathrm{filtered}}$ for both inlet and channel measurements.

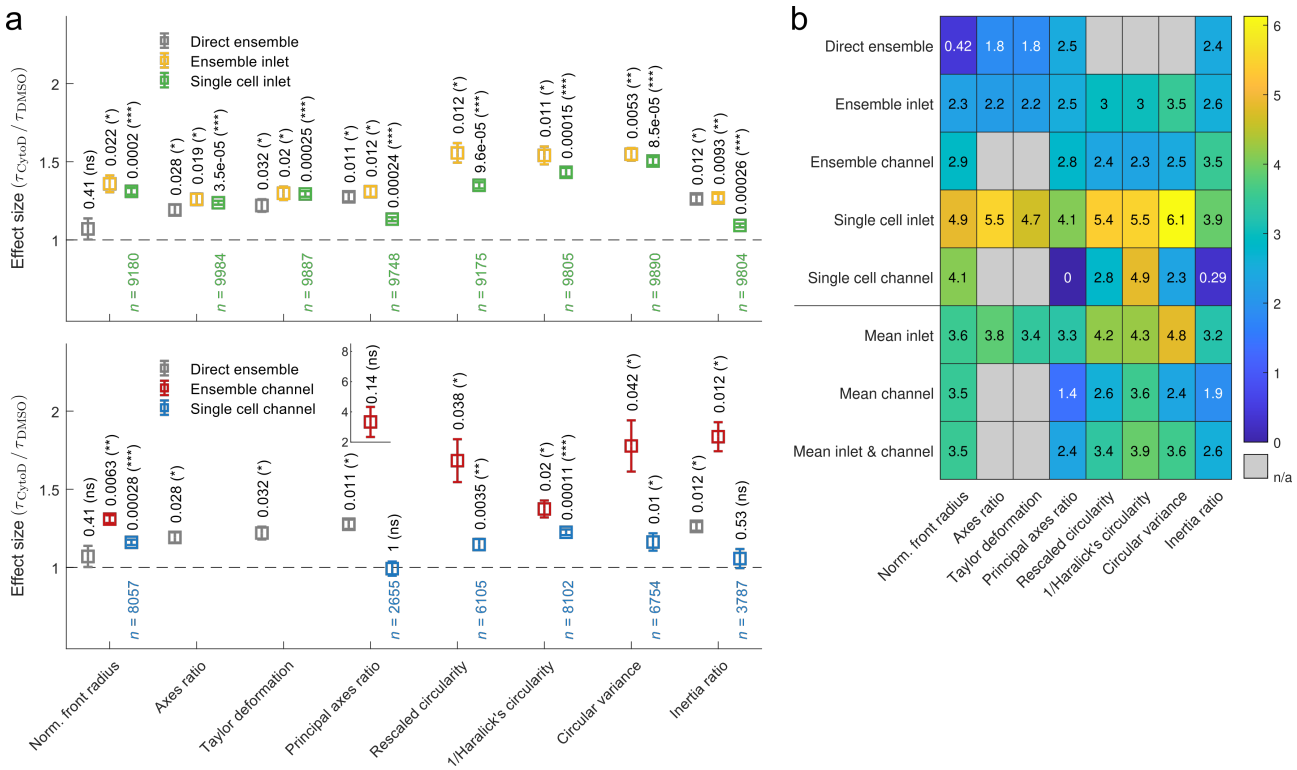

Fig. 5 Effect size calculated for shape descriptors after cell exposure to CytoD. **a)** Effect size for characteristic times of inlet traces (top) and channel traces (bottom) calculated from the ratio of characteristic times of cells treated with 1 µM CytoD and the respective 0.25% (v/v) DMSO vehicle control. Analysis has been performed by fitting an exponential function to the median trace reconstructed from even (yellow) and odd (red) Fourier coefficients (ensemble analysis) as well as by fitting an exponential function to each individual cell trace reconstructed from even (green) and odd (blue) Fourier coefficients (single cell analysis). The grey data points represent a direct ensemble cell analysis without Fourier decomposition. For ensemble analysis statistical significance has been obtained from a one-parametric t-test while for single cell analysis statistical significance has been obtained by linear mixed-effect models. The resulting *p*-values are reported on top of data points. Error bars represent standard error of the mean. **b)** Heat map: $\text{score} = -\text{effect size} \cdot \log_{10}(p\text{-value})$ to combine effect size and significance level into scalar (ns, not significant $p \geq 0.05$, * $p < 0.05$, ** $p < 0.01$, *** $p < 0.001$).

Impact of shape descriptors on effect size after cytoskeletal modifications

Utilizing the results on comparing single cell and ensemble analysis for all eight shape descriptors, we perform measurements on HL60 cells treated with cytochalasin D (CytoD) inhibiting actin polymerization. Cells were incubated with 1 µM CytoD and the corresponding vehicle control (0.25% (v/v) DMSO), respectively (see Methods). Data was acquired by dRT-DC and evaluated as described above (Supplementary Fig. 4-7). For comparison, also a direct analysis of all time traces, i.e., without Fourier decomposition and reconstruction, was performed (Fig. 5a, grey data points). Here, the cell traces were averaged yielding one ensemble response of deformation expressed by a shape descriptor (Supplementary Fig. 8). The latter approach is computational less expensive than all other analyses and yields results rapidly but does not allow for a discrimination of inlet and channel effects. Since rescaled circularity, inverse Haralick's circularity, and circular variance reveal a minimum in amplitude inside channel, data cannot be processed for these shape descriptors without Fourier decomposition.

We define the effect size of cytoskeletal modifications as the ratio between the characteristic times after CytoD treatment and the vehicle control, where $\tau_{\mathrm{CytoD}}/\tau_{\mathrm{DMSO}}$ = 1 indicates no effect. With the exception of the single cell channel data represented by the principal axes ratio (Fig. 5a, lower panel, blue data points), all shape descriptors yield an effect size > 1 of varying amplitude and statistical significance. For the direct ensemble and Fourier-based ensemble analysis of the channel, principal axes ratio reveals the largest effect size, while ensemble analysis of the inlet data is best described by rescaled circularity. In contrast, single cell data after Fourier reconstruction from the inlet and channel have the largest effect size when being evaluated by circular variance and inverse Haralick's circularity, respectively. In general, we find that shape descriptors calculated from ensemble data reveal larger effect sizes than single cell data for inlet (Fig. 5a, upper panel, yellow and green data points) as well as for channel measurements (Fig. 5a, lower panel, red and blue data points).

Finally, we combine the results of our effect size analysis and define a score for each shape descriptor:

$$\mathrm{score} = -\mathrm{effect\ size} \cdot \log_{10}(p\text{-value})\,, \tag{19}$$

which takes into account the magnitude of the effect size and the significance level given by the p-value. The score provides a measure, how well a combination of shape descriptor and analysis strategy is suited for probing characteristic times for compound screening. Comparing all approaches presented in this work yields the highest score for single cell analysis at the inlet, a result which could originate from the peak stress at channel entrance (Fig. 5b). Interestingly, tracking and evaluating individual traces inside the channel also reveals higher scores compared to ensemble averages and emphasizes the importance of single cell analysis to extract quantitative information from compound-response assays. Being computational less expensive, we also compare inlet and channel characteristic times calculated from ensemble averages. Here, higher scores for traces representing inlet effects were observed.

A detailed look at the different shape descriptors indicates that ensemble analysis at the inlet is best be performed using circular variance (score 3.5) and the corresponding channel evaluation should be done by inertia ratio (score 3.5). In contrast, all shape descriptors with the exception of inertia ratio yield high scores for single cell analysis at the inlet (scores between 4.1 and 6.1) while channel traces should be evaluated using normalized front radius (score 4.1) and inverse Haralick's circularity (score 4.9). Ensemble analysis without shape mode decomposition yields the highest scores for principal axes ratio (score 2.5) and inertia ratio (score 2.4) with amplitudes that are equal or lower than scores using Fourier decomposition and symmetry-based shape reconstruction.

Assessing how well a shape descriptor is suited for the interpretation of cell mechanical measurements independently of the type of analysis, a mean score of analysis strategies was calculated for inlet and channel effects individually and also combined (Fig. 5b). Circular variance (score 4.8) and inverse Haralick's circularity (score 4.3) yield the largest mean score for inlet stress, whereas impact of channel stress is best described by inverse Haralick's circularity (score 3.6) and normalized front radius (score 3.5). The highest overall mean score is reached by inverse Haralick's circularity (score 3.9) and circular variance (score 3.6).

Discussion

Utilizing dynamic real-time deformability cytometry (dRT-DC), we captured the dynamics of cells passing a microfluidic channel and their deformation in response to two overlapping stress distributions[13]. The resulting image sequences allow to extract various time-dependent parameters from dRT-DC data[14], which we limited within this work to scalar quantities[9]. Typical examples of these shape descriptors are axes ratio[3,16,17] and circularity[18,19] that represent cellular strain and are thus suitable to determine mechanical properties if the corresponding hydrodynamic stress distribution can be estimated.

While a detailed comparison of shape descriptors for suspended cells in microfluidic systems is elusive, adherent cells have already been characterized in great detail[8,9]. Here, a link between morphology and cell function was established by shape and motion analysis of motile cells in combination with a standardization of shape parameters. For example, for keratocytes, a close correlation between cell state, shape and the speed of motion has been found that depends on the self-organization of the membrane and the cytoskeleton. In consequence, cell shape can be predicted by a model based only on cell area, membrane tension and actin content[8]. Shape descriptors further allow for quantitative analysis of microscopy images to study cell morphological features in general[9].

Our study aims to expand shape analysis to suspended cells inside an extensional as well as in a shear flow. In total nine different shape descriptors have been analyzed and compared: cell area, front radius, axes ratio, Taylor deformation, principal axes ratio, rescaled circularity, inverse Haralick's circularity, circular variance and inertia ratio. We utilized Fourier decomposition of cellular shape modes and reconstruction from even and odd coefficients separately to disentangle the superposition of an extensional (inlet) and Poiseuille flow (constriction) inside a microfluidic channel of finite length. In both hydrodynamic geometries cell response follows an exponential function with characteristic times and amplitudes depending on the respective shape descriptor.

Within this analytical framework we addressed three questions: First, we investigated the conditions required for cells to reach a steady-state deformation while translocating the microfluidic channel, which is a precondition to determine cell elasticity[6,24]. The steady-state essentially depends on the viscoelastic property of a cell, i.e., the characteristic time τ that is *a-priori* unknown. Since constriction length is usually fixed in microfluidic systems, the only possibility (at least for volumetric flows of constant viscosity) to control the position of steady-state deformation is by translocation time t_{channel} via changing the flow rate. However, flow rates can only be controlled in a narrow range to ensure sufficiently high shear stress to induce cell deformation and sufficiently small cell velocities to allow dynamic tracking and reduce image blurring. Here, we introduced an amplitude fraction α as a measure how much of the steady-state amplitude is found inside the constriction. By performing dRT-DC and analyzing the resulting dynamics for different shape descriptors in combination with analytical simulations, we find for α = 0.5 the error in τ being below 20%. This implies that steady-state deformation of cells can be predicted from dRT-DC traces for translocation times even shorter than the characteristic time. For $t_{\mathrm{channel}} = 2\tau$ the error is only 11% and smaller.

Second, we compared single cell vs. ensemble studies, which is relevant to estimate the experimental and computational effort vs. data accuracy. For short translocation times, i.e., $t_{\mathrm{channel}}/\bar{\tau} < 1$ we find an overestimation of the ensemble characteristic time as traces are included into $\bar{\tau}_{\mathrm{ensemble}}$ that do not reach a steady-state. That emphasizes the need for single cell analyses if $\bar{\tau}$ of the sample is unknown. In contrast, for long translocation times little differences are found between single cell and ensemble studies. When comparing experimental characteristic times for HL60 cells in this study to typical translocation times, we find a ratio of approximately 5 (depending on the shape descriptor), which results in an error of 5% for ensemble and 1.5% for single cell data, which is far below other systematic errors, e.g., due to finite pixel size of our camera system.

Finally, we performed a drug-response assay using cytochalasin D and investigated the effect size for different shape descriptors and for single cell as well as ensemble analysis at the inlet and inside the channel. We demonstrated that single cell analysis at the inlet provides highest sensitivity almost independent how deformation is quantified. In contrast, when measurements are limited to the constant flow profile inside the channel to compute elasticity and viscosity, inverse Haralick's circularity provides the highest score in effect size.

Conclusion

In summary, we have demonstrated the potential of different shape descriptors for quantifying the dynamics of a cell passing a microfluidic constriction. Analysis has been performed under different conditions in response to a drug inhibiting actin polymerization. We performed the data analysis on three different levels of depth, spanning a range from directly calculating the shape descriptors to performing Fourier analysis to disentangle inlet and channel contributions before investigating ensemble and single-cell response, separately. Importantly, our studies demonstrate that a steady-state deformation of cells is not required to compare the stress response of cells under different conditions, e.g., drug treatment, as along as a sufficient part of the shape dynamics inside a microfluidic channel is known and can be quantified.

Author Contributions

O.O. and B.F. designed the experimental assay. D.B. performed sample preparation. B.F. established and performed the measurements as well as data analysis. B.F. performed simulations. O.O. supervised the project. O.O. and B.F. wrote and reviewed the manuscript.

Conflict of interest

O.O. is co-founder of Zellmechanik Dresden distributing the technology for real-time deformability cytometry. All other authors do not report a conflict of interest.

Acknowledgments

We gratefully acknowledge support from the German Federal Ministry of Education and Research (ZIK grant to O.O. under grant agreement 03Z22CN11), the German Centre for Cardiovascular Research (Postdoc start-up grant to O.O under grant agreement 81X3400107) and the German Research Foundation (project number 374031971 – TRR240).

References

1. Ekpenyong, A. E. *et al.* Viscoelastic Properties of Differentiating Blood Cells Are Fate- and Function-Dependent. *PLoS One* **7**, e45237 (2012).

2. Di Carlo, D. A Mechanical Biomarker of Cell State in Medicine. *J. Lab. Autom.* **17**, 32–42 (2012).

3. Gossett, D. R. *et al.* Hydrodynamic stretching of single cells for large population mechanical phenotyping. *Proc. Natl. Acad. Sci.* **109**, 7630–7635 (2012).

4. Darling, E. M. & Di Carlo, D. High-Throughput Assessment of Cellular Mechanical Properties. *Annu. Rev. Biomed. Eng.* **17**, 35–62 (2015).

5. Urbanska, M. *et al.* A comparison of microfluidic methods for high-throughput cell deformability measurements. *Nat. Methods* **17**, 587–593 (2020).

6. Mietke, A. *et al.* Extracting Cell Stiffness from Real-Time Deformability Cytometry: Theory and Experiment. *Biophys. J.* **109**, 2023–2036 (2015).

7. Adamo, A. *et al.* Microfluidics-Based Assessment of Cell Deformability. *Anal. Chem.* **84**, 6438–6443 (2012).

8. Keren, K. *et al.* Mechanism of shape determination in motile cells. *Nature* **453**, 475–480 (2008).

9. Lobo, J., See, E. Y.-S., Biggs, M. & Pandit, A. An insight into morphometric descriptors of cell shape that pertain to regenerative medicine. *J. Tissue Eng. Regen. Med.* **10**, 539–553 (2016).

10. Reichel, F. *et al.* High-Throughput Microfluidic Characterization of Erythrocyte Shapes and Mechanical Variability. *Biophys. J.* **117**, 14–24 (2019).

11. Babu, N. Influence of hypercholesterolemia on deformability and shape parameters of erythrocytes in hyperglycemic subjects. *Clin. Hemorheol. Microcirc.* **41**, 169–177 (2009).

12. Koch, M. *et al.* Plasmodium falciparum erythrocyte-binding antigen 175 triggers a biophysical change in the red blood cell that facilitates invasion. *Proc. Natl. Acad. Sci.* **114**, 4225–4230 (2017).

13. Fregin, B. *et al.* High-throughput single-cell rheology in complex samples by dynamic real-time deformability cytometry. *Nat. Commun.* **10**, 415 (2019).

14. Herbig, M., Mietke, A., Müller, P. & Otto, O. Statistics for real-time deformability cytometry: Clustering, dimensionality reduction, and significance testing. *Biomicrofluidics* **12**, (2018).

15. Moreno-Flores, S., Benitez, R., Vivanco, M. d. M. & Toca-Herrera, J. L. Stress relaxation microscopy: Imaging local stress in cells. *J. Biomech.* **43**, 349–354 (2010).

16. Lee, S. S., Yim, Y., Ahn, K. H. & Lee, S. J. Extensional flow-based assessment of red blood cell deformability using hyperbolic converging microchannel. *Biomed. Microdevices* **11**, 1021–1027 (2009).

17. Pagliara, S. *et al.* Auxetic nuclei in embryonic stem cells exiting pluripotency. *Nat. Mater.* **13**, 638–644 (2014).

18. Otto, O. *et al.* Real-time deformability cytometry: on-the-fly cell mechanical phenotyping. *Nat. Methods* **12**, 199–202 (2015).

19. Nyberg, K. D. *et al.* Quantitative Deformability Cytometry: Rapid, Calibrated Measurements of Cell Mechanical Properties. *Biophys. J.* **113**, 1574–1584 (2017).

20. Suzuki, S. & Abe, K. Topological structural analysis of digitized binary images by border following. *Comput. Vis. Graph. Image Process.* **30**, 32–46 (1985).

21. Sklansky, J. Finding the convex hull of a simple polygon. *Pattern Recognit. Lett.* **1**, 79–83 (1982).

22. Peura, M. & Iivarinen, J. Efficiency of simple shape descriptors. in *Proceedings of the Third International Workshop on Visual Form, Capri, Italy, May 28–30* 443–451 (1997).

23. Haralick, R. M. A Measure for Circularity of Digital Figures. *IEEE Trans. Syst. Man Cybern.* **SMC-4**, 394–396 (1974).

24. Mokbel, M. *et al.* Numerical Simulation of Real-Time Deformability Cytometry To Extract Cell Mechanical Properties. (2017) doi:10.1021/acsbiomaterials.6b00558.

25. Kirby, M. A. *et al.* Optical coherence elastography in ophthalmology. *J. Biomed. Opt.* **22**, 1 (2017).

26. Corbin, E. A., Adeniba, O. O., Ewoldt, R. H. & Bashir, R. Dynamic mechanical measurement of the viscoelasticity of single adherent cells. *Appl. Phys. Lett.* **108**, 093701 (2016).

27. Laurent, V. M. *et al.* Assessment of Mechanical Properties of Adherent Living Cells by Bead Micromanipulation: Comparison of Magnetic Twisting Cytometry vs Optical Tweezers. *J. Biomech. Eng.* **124**, 408–421 (2002).

28. Herold, C. Mapping of Deformation to Apparent Young's Modulus in Real-Time Deformability Cytometry. *arXiv* (2017).

Supplementary Material

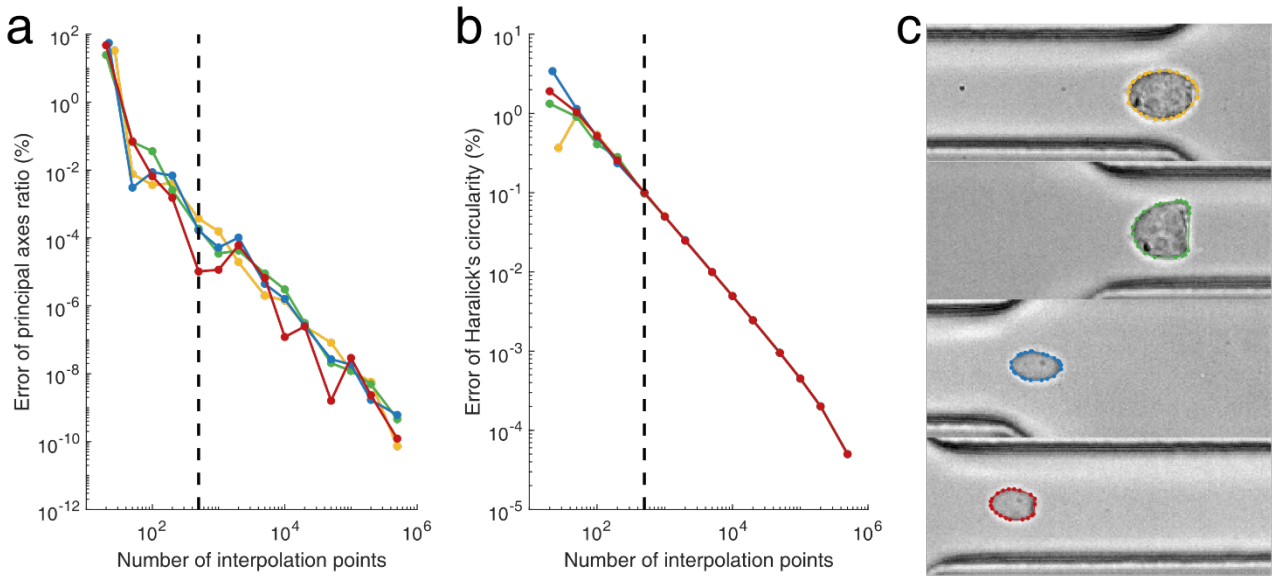

Fig. 1 Interpolation of cell contour points. **a, b)** Principal axes ratio (a) and Haralick's circularity (b) depend on the number and distribution of cell contour points. Interpolated points are equidistantly sampled in angle φ. To estimate the error from a finite number of interpolation points, results are referenced to 10^6 interpolation points. For shape descriptor calculation, 500 interpolation points are chosen yielding an error of 0.1% or below. The error estimation is done for 2 cells at 2 positions (inlet and outlet) each. **c)** Corresponding cell shapes for the four traces in (a) and (b).

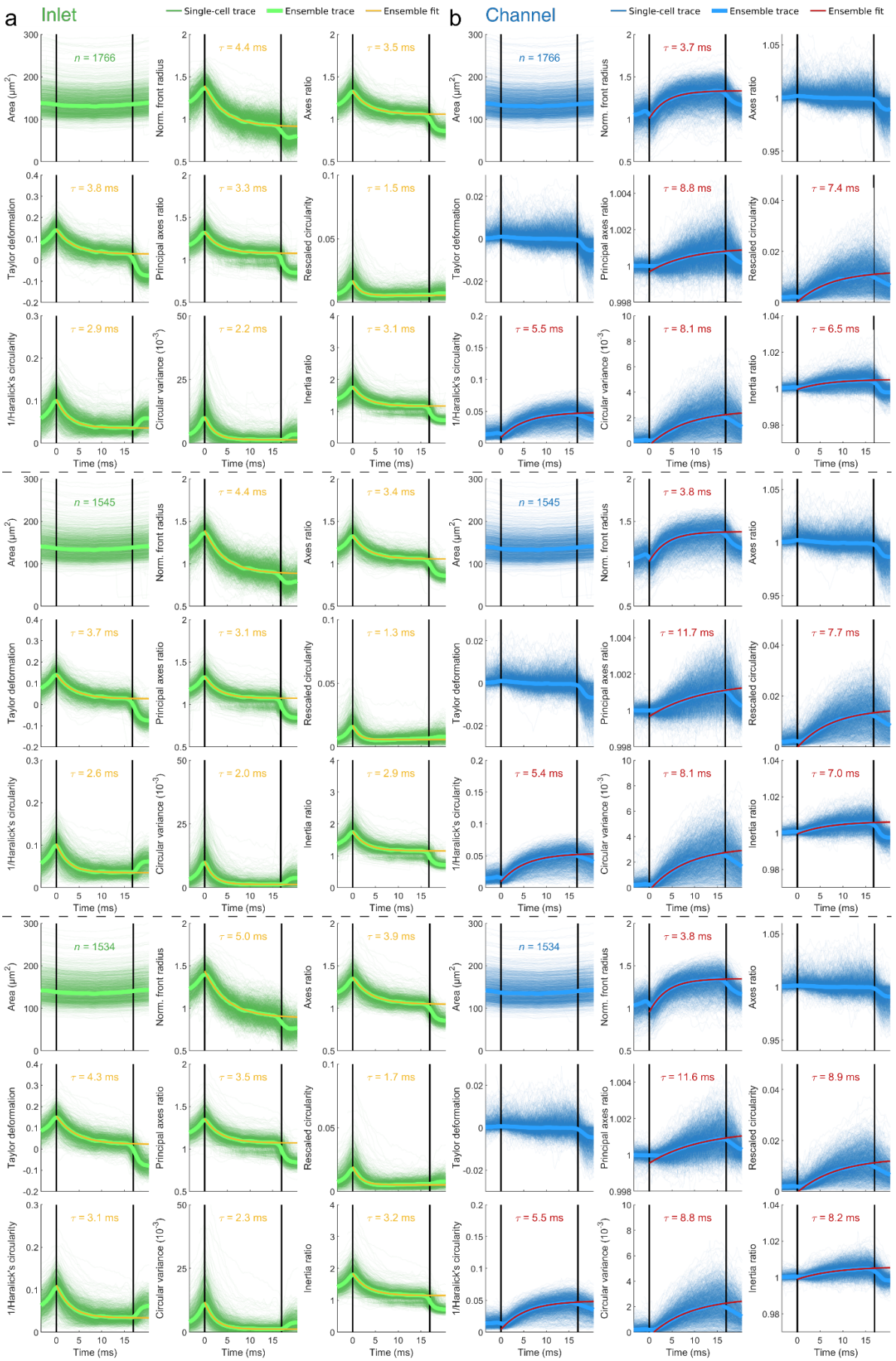

Fig. 2 Three biological replicates (top, center, bottom) of single cell traces of HL60 cells without treatment reconstructed from even FC (a) and odd FC (b), representing inlet and channel effects, respectively. Measurements were performed in a 30 μm x 30 μm channel of 300 μm length at a flow rate of 8 nl·s^{-1}. Replicates are separated by dashed lines.

Fit validity criterion is based on amplitude fraction α, a ratio of deformation amplitude at channel outlet and steady-state deformation, derived from an exponential fit. For a channel deformation response (odd FC) of type

$$d(t) = \hat{d}\left[1 - \exp\left(-\frac{t}{\tau}\right)\right], \tag{1}$$

with amplitude $\hat{d}$ and characteristic time τ, amplitude fraction α is

$$\alpha = \frac{d(t_{\text{channel}})}{d(t \to \infty)}. \tag{2}$$

For a response to inlet stress (even FC) deformation is

$$d(t) = \hat{d}\exp\left(-\frac{t}{\tau}\right) \tag{3}$$

and the amplitude fraction has the form

$$\alpha = \frac{\hat{d} - d(t_{\text{channel}})}{\hat{d} - d(t \to \infty)}. \tag{4}$$

For both cases, a threshold with respect to the characteristic time can be derived, if a minimal amplitude fraction $\alpha_{\min}$ is applied

$$\tau \leq \frac{t_{\text{channel}}}{-\ln(1 - \alpha_{\min})}. \tag{5}$$

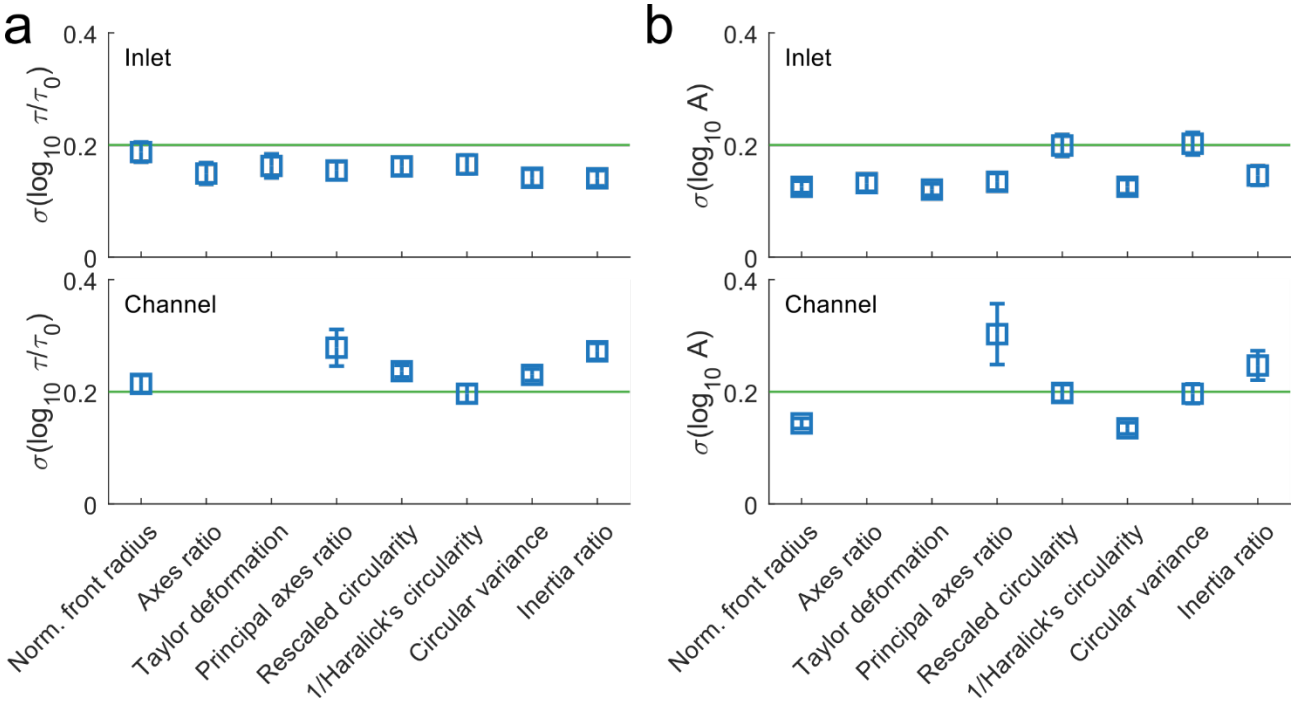

Fig. 3 Broadness of the log-normal distributions of characteristic time and deformation amplitude gained from fits to single cell traces. **a, b)** Standard deviation σ of logarithmized distributions of characteristic time $\log_{10}\tau/\tau_0$ with τ_0 = 1 ms (a) and amplitude $\log_{10} A$ (b) from nine measurement conditions: untreated HL60 cells and cells treated with DMSO and CytoD with three replicates each. Mean ± SEM over all conditions is presented. A level of 0.2 is indicated (green line), as it represents the standard deviation of most shape descriptors, which is used for simulated characteristic time and amplitude distributions (Fig. 4).

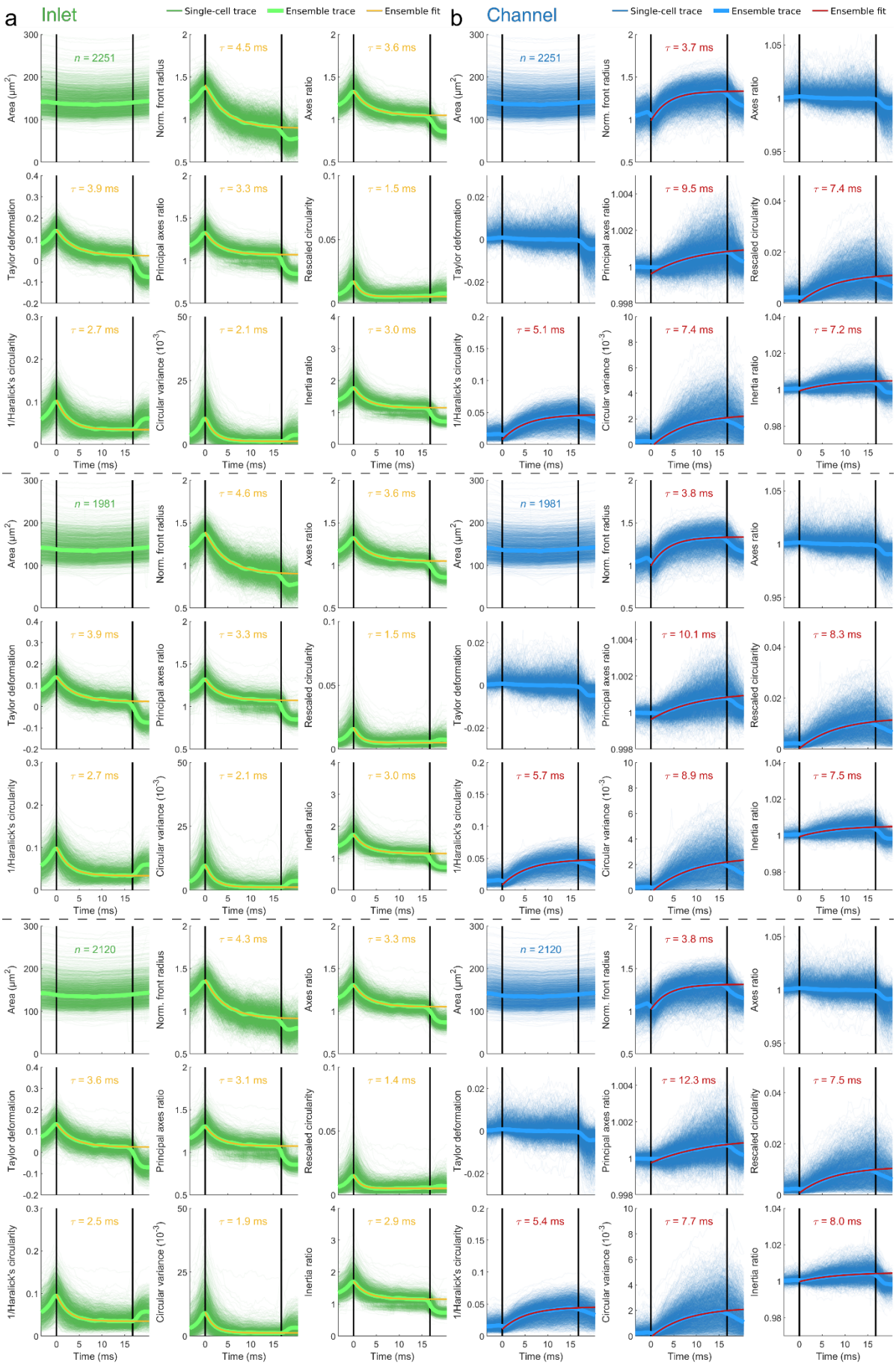

Fig. 4 Three biological replicates (top, center, bottom) of single cell traces of DMSO vehicle (0.25 % (v/v) DMSO) reconstructed from even FC (a) and odd FC (b), representing inlet and channel effects, respectively. Experimental conditions are the same as in Supplementary Fig. 2. Replicates are separated by dashed lines.

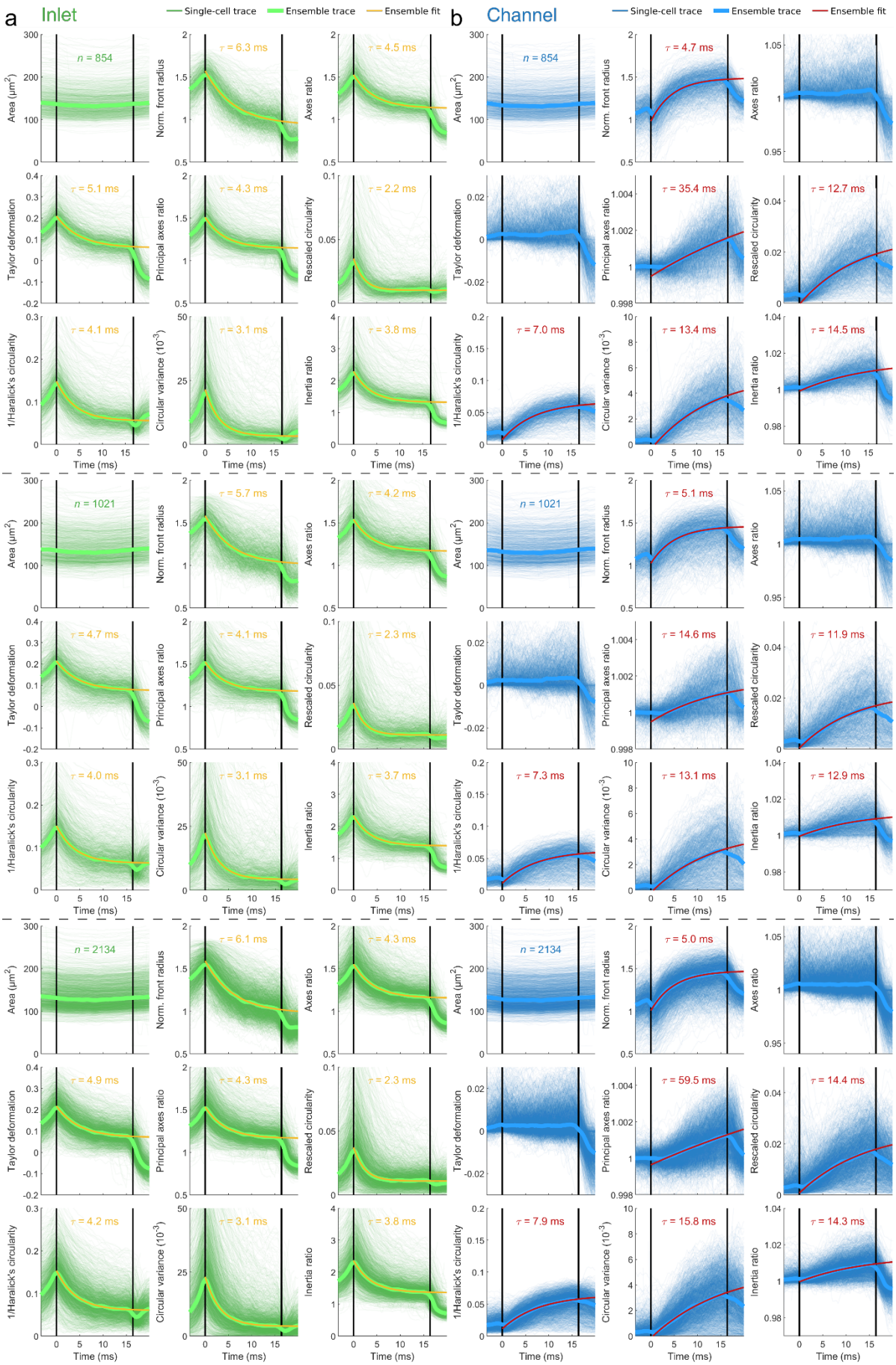

Fig. 5 Three biological replicates (a - c) of single cell traces of HL60 cells treated with Cytochalasin D (1 μM) reconstructed from even FC (a) and odd FC (b), representing inlet and channel effects, respectively. Experimental conditions are the same as in Supplementary Fig. 2. Replicates are separated by dashed lines.

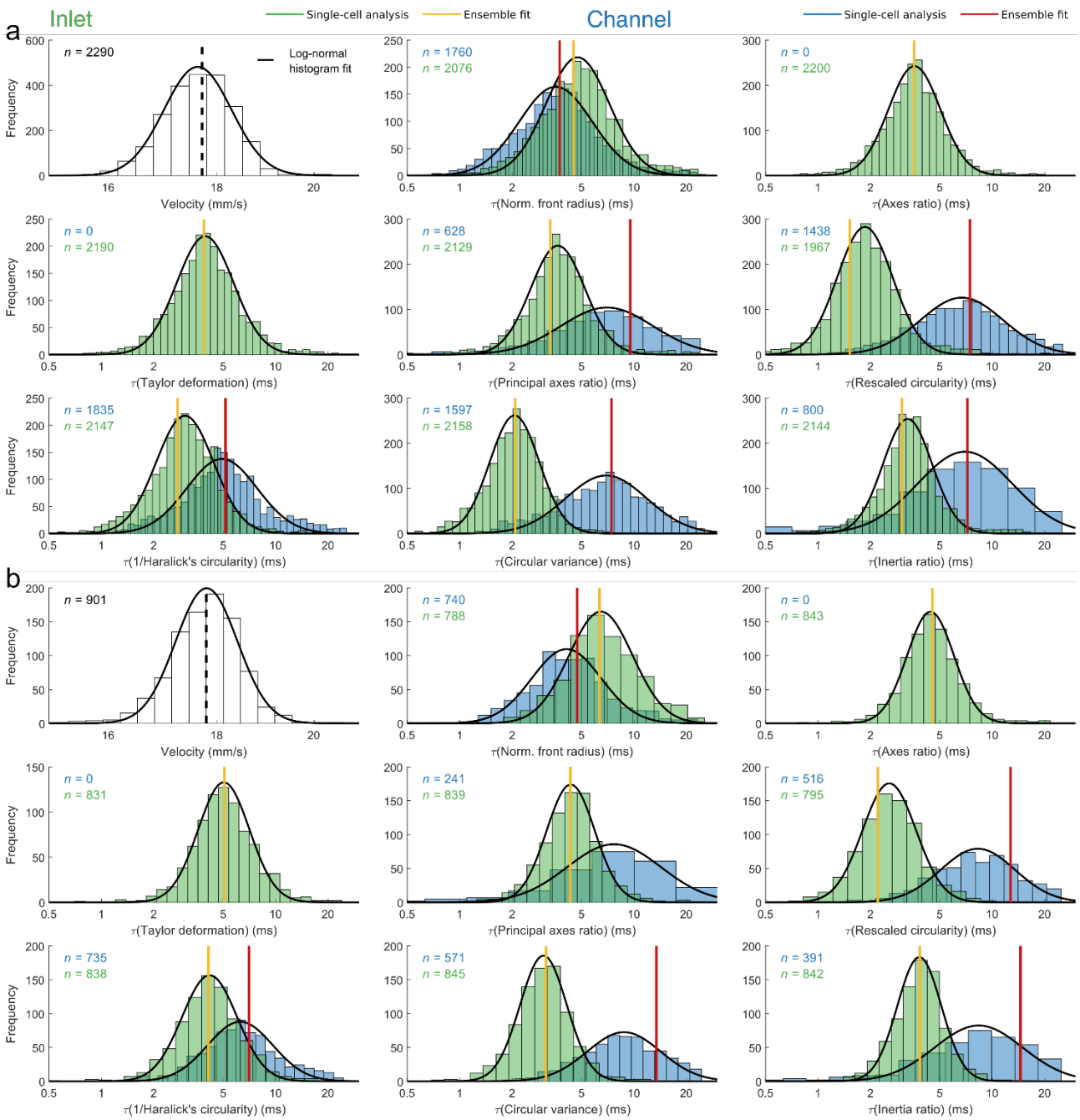

Fig. 6 Relaxation time analysis on single cell level for HL60 cells passing a 30 µm x 30 µm channel of 300 µm length at a flow rate of 8 nl·s^{-1}. **a)** Cells are treated with DMSO and **b)** cytochalasin D (CytoD). One out of three biological replicates is presented as an example (cf. Fig. 3c). Characteristic time (τ) distributions on a logarithmic axis extracted from an exponential fit to single-cell traces for odd and even Fourier coefficient subset shown in blue and green, respectively. Distributions are filtered for validity of the fit ($r^2 \geq 0.6$ and $\tau \leq 24.4$ ms for DMSO or $\tau \leq 24.3$ ms for CytoD, details are described in the text). Solid black lines indicate a log-normal histogram fit filtering data for ± 1.96 σ (95%) with respect to median to reject outliers and vertical red and yellow lines show a comparison to ensemble fit (cf. Fig. 3a, b). Since cell area shows no exponential stress response, a velocity histogram is presented instead, revealing a narrow distribution. For Taylor deformation and axes ratio, no response from odd Fourier components exists.

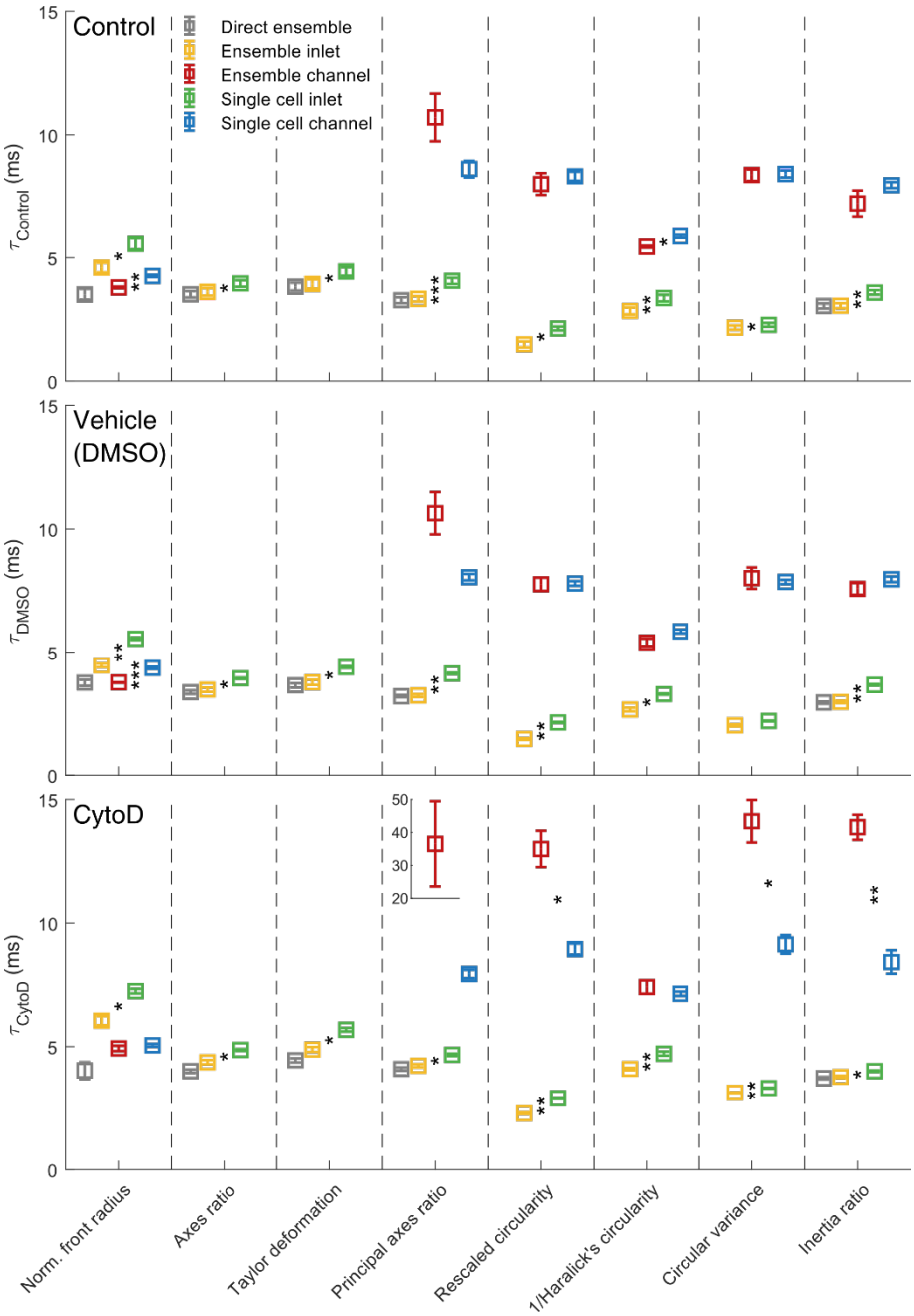

Fig. 7 Comparison of characteristic times over the three studies: direct ensemble, ensemble and single cell analysis of inlet and channel effects, showing mean ± SEM of three biological replicates for control (untreated HL60 cells), vehicle (0.25% (v/v) DMSO treatment) and 1 µM cytochalasin D treatment (CytoD). Statistical analysis is done utilizing a paired t-test comparing ensemble vs single cell analysis for inlet and channel, respectively. Measurement have been performed in a 30 µm x 30 µm channel of 300 µm length at a flow rate of 8 nl·s^{-1}. (* $p < 0.05$, ** $p < 0.01$, *** $p < 0.001$)

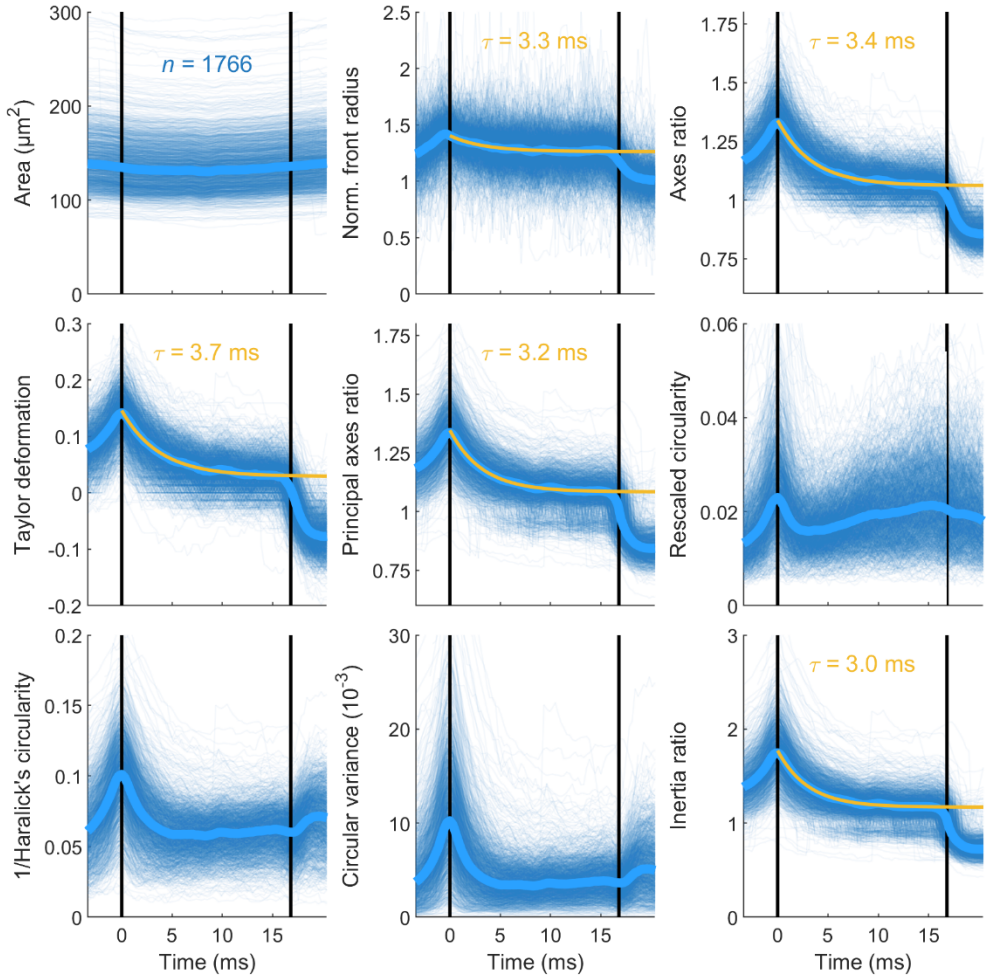

Fig. 8 Ensemble response of deformation expressed by nine shape descriptors. Single cell response traces of more than 1700 HL60 cells (blue traces) and ensemble (median) over all cells (bold blue lines) are shown. Characteristic times are extracted from an exponential fit to the ensemble (yellow curves). Since adapted circularity, inverse Haralick's circularity and circular variance reveal a minimum no exponential curve is fitted. Measurements have been performed in a 30 μm x 30 μm channel of 300 μm length at a flow rate of 8 nl·s^{-1}.

A. Appendix

A.1. Parameter selection for spectral analysis of holographic laser Doppler vibrometry

A.1.1. DFT of sampled time-dependent intensity

The demodulated sampled intensity signal with frequency components at bands m is (Equation 2.29)

$$\frac{I_{\mathrm{dem},i}}{\epsilon c} = E_{\mathrm{ref}}^2 + E_{\mathrm{obj}}^2 + 2E_{\mathrm{ref}}E_{\mathrm{obj}} \sum_{m=-\infty}^{\infty} J_m(\Phi_{\mathrm{vib}}) \cos(\varphi_{\mathrm{vib}}) \ , \tag{A.1}$$

$$\text{with } \Phi_{\mathrm{vib}} = 4\pi \frac{\hat{z}_{\mathrm{vib}}}{\lambda_0} \ ,$$

$$\varphi = 2\pi \frac{i}{N}\Big(\delta N(m_{\mathrm{sel}} - m) - 1\Big) + \varphi_{\mathrm{const}} - m\frac{\pi}{2} - m\varphi_{\mathrm{vib}} \ .$$

The DFT of this signal gives complex Fourier coefficients $\hat{a}_k$

$$\hat{a}_k = \frac{1}{N} \sum_{i=0}^{N-1} \exp\Big(-2\pi j \frac{ik}{N}\Big) \frac{I_{\mathrm{dem},i}}{\epsilon c} \ , \tag{A.2}$$

with $k = 0, ..., \frac{N}{2}$ (the spectrum is symmetric since the input signal is real). Plugging in Equation A.1 yields

$$\begin{aligned} \hat{a}_k = {} & \frac{1}{N}\Big(E_{\mathrm{ref}}^2 + E_{\mathrm{obj}}^2\Big) \sum_{i=0}^{N-1} \exp\Big(-2\pi j \frac{ik}{N}\Big) \qquad (A.3) \\ & + \frac{2}{N} E_{\mathrm{ref}}E_{\mathrm{obj}} \sum_{i=0}^{N-1} \sum_{m=-\infty}^{\infty} J_m(\Phi_{\mathrm{vib}}) \frac{1}{2}\Big[\exp(j\varphi) + \exp(-j\varphi)\Big] \exp\Big(-2\pi j \frac{ik}{N}\Big) \\ = {} & \frac{1}{N}\Big(E_{\mathrm{ref}}^2 + E_{\mathrm{obj}}^2\Big) \sum_{i=0}^{N-1} \exp\Big(-2\pi j \frac{ik}{N}\Big) \qquad (A.4) \\ & + \frac{1}{N} E_{\mathrm{ref}}E_{\mathrm{obj}} \sum_{m=-\infty}^{\infty} J_m(\Phi_{\mathrm{vib}}) \sum_{i=0}^{N-1} \exp\Big(j\varphi - 2\pi j \frac{ik}{N}\Big) \\ & + \frac{1}{N} E_{\mathrm{ref}}E_{\mathrm{obj}} \sum_{m=-\infty}^{\infty} J_m(\Phi_{\mathrm{vib}}) \sum_{i=0}^{N-1} \exp\Big(-j\varphi - 2\pi j \frac{ik}{N}\Big) \ , \end{aligned}$$

utilizing the trigonometric identity $\cos(\alpha) \equiv \frac{1}{2}\Big(\exp(j\alpha) + \exp(-j\alpha)\Big)$.

The first term (top) in Equation A.4, representing the DC fraction of the spectrum, can be simplified to

$$\hat{a}_0 = E_{\text{ref}}^2 + E_{\text{obj}}^2 \ , \tag{A.5}$$

since the sum over the exponential function yields only a non-zero result in case of $k = 0$. For $k \neq 0$ the exponential term represents the N roots of unity whose sum is zero.

The second term (center) in Equation A.4 contributes to the AC fraction and can be formulated as

$$\begin{aligned} \hat{a}_{k,1} = \frac{1}{N} E_{\text{ref}} E_{\text{obj}} \sum_{m=-\infty}^{\infty} J_m(\Phi_{\text{vib}}) \exp\left(j\left(\varphi_{\text{const}} - m\frac{\pi}{2} - m\varphi_{\text{vib}}\right)\right) \\ \cdot \sum_{i=0}^{N-1} \exp\left(2\pi j \frac{i}{N}(\delta N(m_{\text{sel}} - m) - 1 - k)\right) \ . \end{aligned} \tag{A.6}$$

Again, the exponential function (the second one) represents the N roots of unity, unless its argument becomes zero, or an integer multiple of 2π. Since the sum over the N roots of unity is zero, only for $k = k_1$ with

$$\delta N(m_{\text{sel}} - m) - 1 - k_1 = e \cdot N \ , \qquad e \in \mathbb{Z} \tag{A.7}$$

$$k_1 = \delta N(m_{\text{sel}} - m) - 1 - e \cdot N \tag{A.8}$$

$\hat{a}_{k_1} = \hat{a}_{k_1,1}$ is non-zero

$$\hat{a}_{k_1} = E_{\text{ref}} E_{\text{obj}} \sum_{m=-\infty}^{\infty} J_m(\Phi_{\text{vib}}) \exp\left(j\left(\varphi_{\text{const}} - m\frac{\pi}{2} - m\varphi_{\text{vib}}\right)\right) \ . \tag{A.9}$$

The third term (bottom) in Equation A.4 also contributes to the AC spectrum fraction and is very similar to the second one. The complex Fourier amplitudes $\hat{a}_{k_2}$ can be derived

$$\hat{a}_{k_2} = E_{\text{ref}} E_{\text{obj}} \sum_{m=-\infty}^{\infty} J_m(\Phi_{\text{vib}}) \exp\left(j\left(-\varphi_{\text{const}} + m\frac{\pi}{2} + m\varphi_{\text{vib}}\right)\right) \ , \tag{A.10}$$

$$\text{with } k_2 = -\Big(\delta N(m_{\text{sel}} - m) - 1\Big) - e \cdot N \ . \tag{A.11}$$

The spectrum received from the DFT has the coefficients

$$\hat{a}_k = \hat{a}_0 + \hat{a}_{k_1} + \hat{a}_{k_2} \ . \tag{A.12}$$

As seen from k_1 and k_2 (Equations A.8 and A.11, respectively) spectral components are repeated infinitely in positive and negative direction of frequency axis ($e \in \mathbb{Z}$) due to aliasing, a fundamental property of sampling. Due to sampling with a rate of f_{cam}, the resulting spectrum is band-limited within $f_{\text{DFT}} \in [0, f_{\text{cam}}/2]$. All higher

frequencies are folded into this spectral range. This can be observed from the DFT result. The spectral band of index m can be found at the discrete spectral index $k = k_1$ or $k = k_2$

$$k_1 = \Big(\delta N(m_{\text{sel}} - m) - 1\Big)\%N \ , \qquad \text{if } k_1 \in \left[0, \frac{N}{2}\right] \ , \tag{A.13}$$

$$k_2 = \Big(-\delta N(m_{\text{sel}} - m) + 1\Big)\%N \ , \qquad \text{if } k_2 \in \left[0, \frac{N}{2}\right] \ , \tag{A.14}$$

with $k = N f_{\text{DFT}}/f_{\text{cam}}$. Since k_2 has the same but negative value as k_1 before modulo operation with N, k can be combined into

$$k = \left| \left(\delta N(m_{\text{sel}} - m) - 1 + \frac{N}{2}\right)\%N - \frac{N}{2} \right| . \tag{A.15}$$

The spectral magnitude of the DC term and of band m are (Equations A.5, A.9 and A.10)

$$|\hat{a}_0| = E_{\text{ref}}^2 + E_{\text{obj}}^2 \ , \tag{A.16}$$

$$|\hat{a}_k| = |E_{\text{ref}} E_{\text{obj}} J_m(\Phi_{\text{vib}})| \ . \tag{A.17}$$

Spectral phase, however, depends on the selected on whether k_1 or k_2 falls within $[0, N/2]$ and, hence

$$\angle \hat{a}_0 = 0 \ , \tag{A.18}$$

$$\angle \hat{a}_k = \begin{cases} \varphi_{\text{const}} - m\dfrac{\pi}{2} - m\varphi_{\text{vib}} + \pi(J_m(\Phi_{\text{vib}}) < 0), & \text{if } k_1 \in \left[0, \dfrac{N}{2}\right] \\ -\varphi_{\text{const}} + m\dfrac{\pi}{2} + m\varphi_{\text{vib}} + \pi(J_m(\Phi_{\text{vib}}) < 0), & \text{else} \end{cases} . \tag{A.19}$$

Since $J_m(\Phi_{\text{vib}})$ can be negative, a phase shift of π has to be incorporated in that case.

A.1.2. Considerations for selection of experimental acquisition parameters N and δ

From the theoretical frequency decomposition (Section A.1.1) the expected spectral response from an experiment can be simulated (Figure A.1). Since an infinite number of vibration bands exist (m ranges from $-\infty$ to ∞), bands are overlapping. With higher order, however, their amplitude and hence, their contribution to the superpositioned spectral response, decreases (Figure 2.5 and Equation 2.35). Bands of higher order overlapping the bands $m = 0$ and $m = +1$ or $m = -1$ which are used for vibration parameter extraction, will, depending on their magnitude, impact on the reconstruction result. By a beneficial selection of experimental acquisition parameters N and δ, those errors can be minimized.

Figure A.1 shows two examples of selected parameters for $m_{\text{sel}} = 1$, $N = 16$ points and $\delta N = 4$ or $\delta N = 5$ over increasing Φ_{vib}, i.e., increasing vibration amplitudes $\hat{z}_{\text{vib}}$.

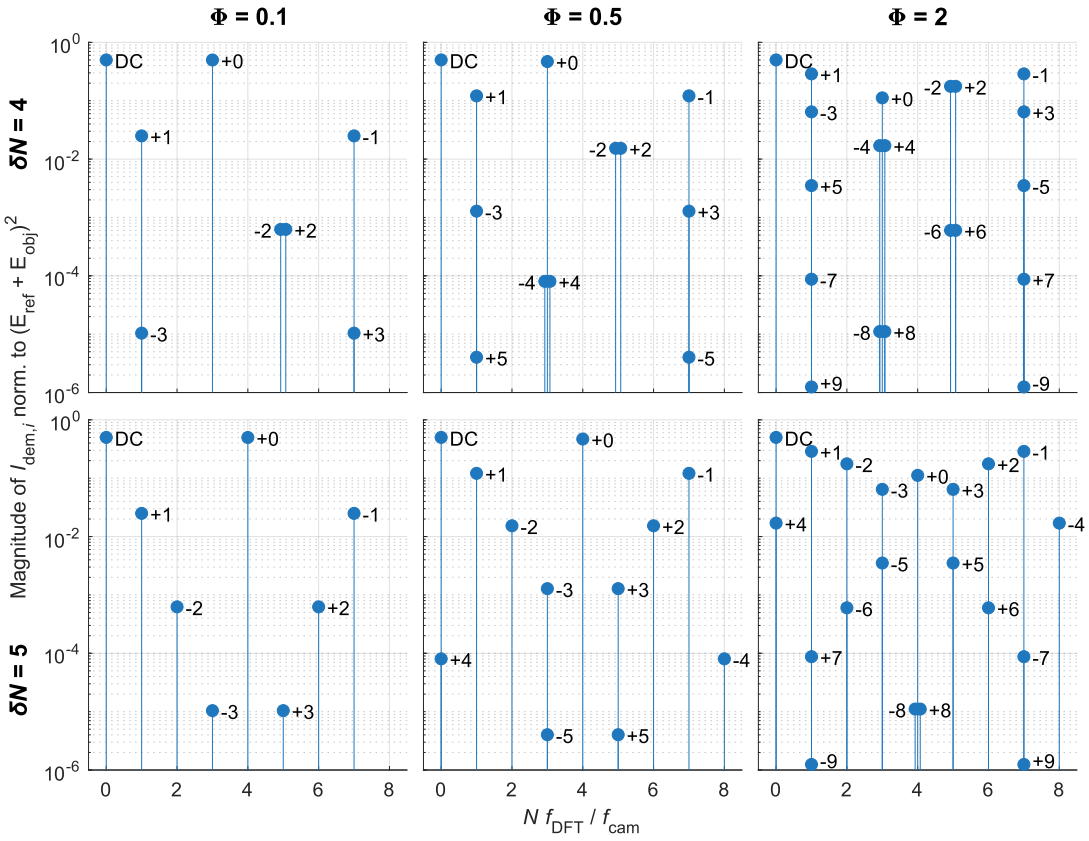

Figure A.1.: One-sided power spectra of the intensity signal in Equation 2.29 reveals all contributing frequency components superimposing into a total spectrum, accessible by experiments. Spectra are shown for $m_{\mathrm{sel}} = 1$, $N = 16$ points, $\delta N = 4$ (top) and $\delta N = 5$ (bottom), and amplitudes of modulation of $\Phi_{\mathrm{vib}} = 0.1$ (left), $\Phi_{\mathrm{vib}} = 0.5$ (center) and $\Phi_{\mathrm{vib}} = 2$ (right) corresponding to vibration amplitudes $\hat{z}_{\mathrm{vib}}$ of 5.3 nm, 26.3 nm and 105 nm, respectively, for $\lambda_0 = 660\,\mathrm{nm}$. Intensities in reference and object beam path are equal ($E_{\mathrm{ref}} = E_{\mathrm{obj}}$) and spectral intensity magnitude is normalized to total intensity $(E_{\mathrm{ref}} + E_{\mathrm{obj}})^2$. Next to the frequency components the sideband index m is shown. If two components are overlapping, e.g., for $m = \pm 2$, they are spatially separated for improved visibility. Due the sampling with f_{cam}, all high-frequency sidebands are mirrored into the spectrum ranging from $f_{\mathrm{DFT}} = 0$ to $f_{\mathrm{cam}}/2$.

Sideband magnitude increases with increasing vibration amplitude and hence, impacts on a band with which it overlaps. Parameter extraction is disturbed if the magnitude of overlapping band is high compared to the bands of interest at $m = 0$ and $m = \pm 1$. For $\delta N = 5$ a much better band separation can be observed. This means that even for the same number of acquired points N, i.e., the same throughput, parameter extraction can be improved by carefully selecting δN.

When selecting N and δ the following requirements have to be satisfied. The number of frames N is an integer and at $N \geq 3$ samples have to be acquired for phase-shifting evaluation utilized here (see Section 1.4.3). The fractional part δ of the frequency ratio $f_{\mathrm{vib}}/f_{\mathrm{cam}}$ is within the range $0 < \delta < 1$. $\delta = 0$ has to be excluded because all sidebands

would fall into $k = 1$ in this case (Equation A.15). And since the bands should be at discrete frequencies in the calculated spectrum (at least bands used for parameter reconstruction should not fall between two k's), δN needs to be an integer (Equation A.15). For maximizing the throughput of the technique, N should be as low as possible as vibrational parameters are extracted from a set of N frames, corresponding to a timeframe of N/f_{cam}.

From those requirements one can conclude that $\delta N \geq 2$. For $\delta N = 2$, however, the only possible N is 3 yielding a spectrum with two components only, which makes it impossible to separate the bands $m = 0$ and $m = +1$ or $m = -1$ from the DC contribution. Hence, for experiments parameters have to be at least $N \geq 4$ and $\delta N \geq 3$.

The following iterative procedure can be of help for selecting experimental parameters:

1. Start with $N = 4$ and $\delta N = 3$. Decide for one band m_{sel} optically selected by the setup, typically $m_{\mathrm{sel}} = 1$.

2. Calculate spectral positions of the baseband $m = 0$ and sidebands $m = \pm 1$ (Equation A.15)

$$k = N\frac{f_{\mathrm{DFT}}}{f_{\mathrm{cam}}} = \left|\left(\delta N(m_{\mathrm{sel}} - m) - 1 + \frac{N}{2}\right)\%N - \frac{N}{2}\right| . \tag{A.15}$$

3. Determine overlapping bands at the calculated spectral position k from (derived from Equations A.13 and A.14)

$$m_{\mathrm{ovrlp},1} = m_{\mathrm{sel}} - \frac{k + 1 + eN}{\delta N} \quad \text{if } m_{\mathrm{ovrlp},1} \in \mathbb{N}, m_{\mathrm{ovrlp},1} \in \left[0, \frac{N}{2}\right] , \tag{A.20}$$

$$m_{\mathrm{ovrlp},2} = m_{\mathrm{sel}} + \frac{k - 1 + eN}{\delta N} \quad \text{if } m_{\mathrm{ovrlp},1} \in \mathbb{N}, m_{\mathrm{ovrlp},1} \in \left[0, \frac{N}{2}\right] , \tag{A.21}$$

   with $e \in \mathbb{Z}$. Of note, for $k = 0$ and $k = N/2$ both equations yield the same result, due to frequency component mirroring at those frequencies.

4. Estimate the amplitude of the overlapping bands compared to the one of the band of interest for expected vibration amplitude $\hat{z}_{\mathrm{vib}}$.

5. Repeat for all δN available for recent N. If the impact by overlaying bands is to high for the expected vibration amplitudes, increase N by one and continue.

In Table A.1.2 the sideband indices of the band with highest amplitude overlapping bands at $m = 0$ and $m = \pm 1$ are tabulated for $m_{\mathrm{sel}} = 1$ and $4 \leq N \leq 20$.

Table A.1.: Overview of experimental parameters N and δ for spectral evaluation of HVS for $m_{\mathrm{sel}} = 1$ (focusing optically on the first vibration band).

N	δN	$N f_{\mathrm{DFT}}/f_{\mathrm{cam}}$			overlapping band m_{ovrlp} with highest amplitude			note
		$m=-1$	$m=0$	$m=+1$	$m=-1$	$m=0$	$m=+1$	
4	3	1	2	1	+1	±4	−1	*
5	3	0	2	1	DC	−2	+2	+2
5	4	2	2	1	0	−1	−2	*
6	3	1	2	1	+1	±2	−1	*
	4	1	3	1	+1	±3	−1	*
	5	3	2	1	+5	−2	±3	+2, +5
7	3	2	2	1	0	−1	−2	*
	4	0	3	1	DC	−2	−3	
	5	2	3	1	−3	+3	+2	+3
	6	3	2	1	−2	−3	+3	+3
8	3	3	2	1	−3	±4	+3	+3, ±4
	4	1	3	1	+1	±2	−1	*
	5	1	4	1	+1	±8	−1	*
	6	3	3	1	0	−1	±2	*
	7	3	2	1	−3	±4	+3	+3, ±4
9	3	4	2	1	+2	±3	−2	
	4	2	3	1	−2	−3	−4	
	5	0	4	1	DC	−2	−3	
	6	2	4	1	+2	±3	−2	
	7	4	3	1	+4	+3	+2	
	8	3	2	1	−4	+4	+3	+4
10	3	5	2	1	+9	−2	−3	
	4	3	3	1	0	−1	−2	*
	5	1	4	1	+1	±2	−1	*
	6	1	5	1	+1	±5	−1	*
	7	3	4	1	−3	−4	±5	+4, ±5
	8	5	3	1	+4	−2	+2	
	9	3	2	1	±5	+4	+3	+4, ±5
11	3	5	2	1	−5	+5	+4	+5
	4	4	3	1	−3	−4	−5	
	5	2	4	1	−4	−5	+5	+5
	6	0	5	1	DC	−2	−3	
	7	2	5	1	−2	−3	−4	
	8	4	4	1	0	−1	−2	*
	9	5	3	1	+4	+3	+2	
	10	3	2	1	+5	+4	+3	
12	3	5	2	1	+3	±4	−3	
	4	5	3	1	+2	±3	−2	

N	δN	$Nf_{\mathrm{DFT}}/f_{\mathrm{cam}}$			overlapping band m_{ovrlp} with highest amplitude			note
		$m=-1$	$m=0$	$m=+1$	$m=-1$	$m=0$	$m=+1$	
	5	3	4	1	+5	+4	+3	
	6	1	5	1	+1	±2	−1	*
	7	1	6	1	+1	±12	−1	*
	8	3	5	1	+2	±3	−2	
	9	5	4	1	+3	±4	−3	
	10	5	3	1	−2	±3	+2	
	11	3	2	1	+5	+4	+3	
13	3	5	2	1	−2	−3	−4	
	4	6	3	1	−4	−5	−6	
	5	4	4	1	0	−1	−2	*
	6	2	5	1	−6	+6	+5	+6
	7	0	6	1	DC	−2	−3	
	8	2	6	1	+6	+5	+4	
	9	4	5	1	−3	−4	−5	
	10	6	4	1	−5	−6	+6	+6
	11	5	3	1	+4	+3	+2	
	12	3	2	1	+5	+4	+3	
14	3	5	2	1	±7	+6	+5	+6, ±7
	4	7	3	1	+6	−2	−3	
	5	5	4	1	−3	−4	−5	
	6	3	5	1	−2	−3	+3	
	7	1	6	1	+1	±2	−1	*
	8	1	7	1	+1	±7	−1	*
	9	3	6	1	−5	−6	±7	+6, ±7
	10	5	5	1	0	−1	−2	*
	11	7	4	1	+13	−2	−3	
	12	5	3	1	−3	+3	+2	
	13	3	2	1	+5	+4	+3	
15	3	5	2	1	+4	±5	−4	
	4	7	3	1	−5	−6	−7	+6, +7
	5	6	4	1	+2	±3	−2	
	6	4	5	1	+4	±5	−4	
	7	2	6	1	+7	+6	+5	+6, +7
	8	0	7	1	DC	−2	−3	
	9	2	7	1	+4	±5	−4	
	10	4	6	1	+2	±3	−2	
	11	6	5	1	−4	−5	−6	
	12	7	4	1	+4	±5	−4	
	13	5	3	1	+4	+3	+2	
	14	3	2	1	+5	+4	+3	
16	3	5	2	1	−3	−4	−5	

N	δN	$Nf_{\mathrm{DFT}}/f_{\mathrm{cam}}$			overlapping band m_{ovrlp} with highest amplitude			note
		$m=-1$	$m=0$	$m=+1$	$m=-1$	$m=0$	$m=+1$	
	4	7	3	1	+3	±4	−3	
	5	7	4	1	−7	±8	+7	+7, ±8
	6	5	5	1	0	−1	−2	*
	7	3	6	1	+5	+4	+3	
	8	1	7	1	+1	±2	−1	*
	9	1	8	1	+1	±16	−1	*
	10	3	7	1	−2	−3	±4	
	11	5	6	1	−3	−4	−5	
	12	7	5	1	+3	±4	−3	
	13	7	4	1	−7	±8	+7	+7, ±8
	14	5	3	1	±4	+3	+2	
	15	3	2	1	+5	+4	+3	
17	3	5	2	1	+8	+7	+6	
	4	7	3	1	−6	−7	−8	
	5	8	4	1	+6	+5	+4	
	6	6	5	1	−3	−4	−5	
	7	4	6	1	−7	−8	+8	+8
	8	2	7	1	+7	+6	+5	
	9	0	8	1	DC	−2	−3	
	10	2	8	1	−4	−5	−6	
	11	4	7	1	−8	+8	+7	+8
	12	6	6	1	0	−1	−2	*
	13	8	5	1	−5	−6	−7	
	14	7	4	1	−2	−3	−4	
	15	5	3	1	+4	+3	+2	
	16	3	2	1	+5	+4	+3	
18	3	5	2	1	+5	±6	−5	
	4	7	3	1	−2	−3	−4	
	5	9	4	1	+17	−2	−3	
	6	7	5	1	+2	±3	−2	
	7	5	6	1	−5	−6	−7	
	8	3	7	1	−4	+4	+3	
	9	1	8	1	+1	±2	−1	*
	10	1	9	1	+1	±9	−1	*
	11	3	8	1	−7	−8	±9	+8, ±9
	12	5	7	1	+2	±3	−2	
	13	7	6	1	+7	+6	+5	
	14	9	5	1	+8	−2	−3	
	15	7	4	1	+5	±6	−5	
	16	5	3	1	+4	+3	+2	
	17	3	2	1	+5	+4	+3	

N	δN	$Nf_{\mathrm{DFT}}/f_{\mathrm{cam}}$			overlapping band m_{ovrlp} with highest amplitude			note
		$m=-1$	$m=0$	$m=+1$	$m=-1$	$m=0$	$m=+1$	
19	3	5	2	1	-4	-5	-6	
	4	7	3	1	-7	-8	-9	
	5	9	4	1	-5	-6	-7	
	6	8	5	1	$+9$	$+8$	$+7$	
	7	6	6	1	0	-1	-2	*
	8	4	7	1	-2	-3	-4	
	9	2	8	1	$+7$	$+6$	$+5$	
	10	0	9	1	DC	-2	-3	
	11	2	9	1	$+8$	$+7$	$+6$	
	12	4	8	1	$+6$	$+5$	$+4$	
	13	6	7	1	-3	-4	-5	
	14	8	6	1	-8	-9	$+9$	$+9$
	15	9	5	1	-6	-7	-8	
	16	7	4	1	-9	$+9$	$+8$	$+9$
	17	5	3	1	$+4$	$+3$	$+2$	
	18	3	2	1	$+5$	$+4$	$+3$	
20	3	5	2	1	$+9$	$+8$	$+7$	
	4	7	3	1	$+4$	± 5	-4	
	5	9	4	1	$+3$	± 4	-3	
	6	9	5	1	-4	± 5	$+4$	
	7	7	6	1	-3	-4	-5	
	8	5	7	1	$+4$	± 5	-4	
	9	3	8	1	$+5$	$+4$	$+3$	
	10	1	9	1	$+1$	± 2	-1	*
	11	1	10	1	$+1$	± 20	-1	*
	12	3	9	1	$+4$	± 5	-4	
	13	5	8	1	$+9$	$+8$	$+7$	
	14	7	7	1	0	-1	-2	*
	15	9	6	1	$+3$	± 4	-3	
	16	9	5	1	$+4$	± 5	-4	
	17	7	4	1	-3	-4	-5	
	18	5	3	1	$+4$	$+3$	$+2$	
	19	3	2	1	$+5$	$+4$	$+3$	

notes: 1) for conditions marked with * no extraction of vibration amplitude and phase is possible

2) numbers indicate favorable conditions and represent overlapping bands with highest amplitudes selected for vibration amplitude and phase extraction ($m=-1$ and $m=0$ or $m=0$ and $m=+1$).